FACTORS CONTROLLING ENANTIOMER-SELECTIVE AMINO ACID ADSORPTION ON MINERAL AND METAL SURFACES

Thesis submitted in accordance with the requirements of the University of Liverpool for the degree of Doctor in Philosophy

by

María Leonor Támara

Department of Earth and Ocean Sciences

University of Liverpool

May 2009

ABSTRACT

Factors Controlling Enantiomer-Selective Amino Acid Adsorption on Mineral and Metal Surfaces

María L. Támara

This work examines the adsorption of racemic AAs (amino acids) on common-rock forming minerals (i.e. quartz, kaolinite and montmorillonite clays, pyrite, and gypsum) from aqueous solutions with the aim of evaluating the potential enantioselective adsorptive properties of these materials. It also addresses the possible catalytic role of clays in the polymerization of valine (Val) and the adsorption of Val on a single Cu(110) crystal in ultra-high vacuum by complementary spectroscopic techniques.

Although many adsorption experiments of chiral AAs on clays, quartz, and other relevant prebiotic materials have been conducted by researchers over the past 60 years, this research re-examines the problem by conducting experiments under more realistic conditions (i.e. lower initial concentrations of the AAs) and using high-performance liquid chromatography (HPLC) with chiral derivatisation to quantify chiral AAs down to the picomole range. Adsorption of AAs other than arginine (Arg) and histidine (Hist) on quartz is minimal. Arg adsorption on quartz sand is pH dependent implying an electrostatic mechanism. Enantiomers of Hist and Arg adsorb selectively on powdered synthetic quartz (unbuffered system) and quartz sand (pH= 8.5), respectively. In contrast to quartz, clays have affinity for AAs of different types (polar, nonpolar, acidic, basic). Montmorillonite K10 (K10) displays enantioselectivity towards serine (Ser), aspartic acid (Asp), Arg, and Val. The greatest effects take place in the Ser-K10 system with D-Ser adsorbed preferentially on K10 from 5 μM racemic DL-Ser solutions. It is speculated that the interlamellar region of the clay might discriminate against the enantiomers of Ser and that a three-point interaction is needed for this behaviour.

Cu-exchanged K10 (CuK10) promotes the formation of divaline dipeptide under simulated wet and dry cycles at 65°C. The yields of divaline from unbuffered 30 mM L-, D- and DL-Val solutions in contact with CuK10 (0.02 g/ml) after 8 days of reaction were 0.025%, 0.023%, and 0.019%. This is a novel result since clays other than K10 have not led to divaline formation. It is hypothesised that the acidic pH of

the clay might have facilitated the dimerization reaction and that an intermediate Cu-Val complex might have been involved.

Val enantiomers self-assemble on a Cu(110) single crystal at room temperature. Infrared spectra of the overlayer suggest that Val chemisorbs via its carboxyl and amino moieties, projecting a chiral triangular footprint on the surface. A structural model for the adlayers is proposed based on RAIRS, LEED, and STM. Moreover, Val molecules within the unit cell appear to adopt more than one adsorption geometry. Annealing of the room temperature adlayers to 400 K results in achiral $c(4\times2)$ overlayers. Room temperature adlayers from racemic *RS*-Val are generally achiral and annealing them produced distorted $c(4\times2)$ structures.

I certify that the work described in this thesis is my own except where otherwise stated and has not previously been submitted for any degree at this or any other University.

María Leonor Támara

CONTENTS

LIST OF TABLES

LIST OF FIGURES

LIST OF ABBREVIATIONS

a	Cell edge in the *x* direction
Å	Angstroms units (10^{-10} m)
AA	Amino Acid
ACN	Acetonitrile
Ala	Alanine
Arg	Arginine
Asp	Aspartic acid
b	Cell edge in the *y* direction
BET	Brunauer-Emmet-Teller
c	Cell edge in the *z* direction. Basal spacing of clays
Cu-K10	Copper-exchanged montmorillonite K10
Cyst	Cysteine
d-	Right-handed
DCM	Dichloromethane
DKP	Diketopiperazine
DFT	Density Functional Theory
ee	Enantiomeric Excess
ER	Enantiomeric Ratio
ESI	Electrospray Ionization
fcc	Face Centred Cubic
FT-IR	Fourier-Transformed Infrarred
GC-FID	Gas Chromatography Flame Ionization Detection
Glu	Glutamic acid
Gly	Glycine
Hist	Histidine
I	Ionic strength
IBLC	N-Isobutyryl-L-Cysteine
Ile	Isoleucine
K10	Montmorillonite K10
KSF	Montmorillonite KSF
l-	Left-handed
LC-MS	Liquid Chromatography Mass Spectrometry
LEED	Low Energy Electron Diffraction
Leu	Leucine
Lys	Lysine
MCT	Mercury Cadmium Telluride
Met	Methionine
OPA	*ortho*-phthaldialdehyde
Phe	Phenylalanine
pH_{pzc}	pH of the point of zero charge
pI	Isoelectric point
Pro	Proline
RAIRS	Reflection Absorption Infra-Red Spectroscopy
RP-HPLC	Reversed Phase High-Performance Liquid Chromatography
Ser	Serine
SFG	Sum Frequency Generation
SIPF	Salt-Induced Peptide Formation

SSA	Specific surface area
STM	Scanning Tunneling Microscopy
Thr	Threonine
TLC	Thin Layer Chromatography
UHV	Ultra High Vacuum
Val	Valine
XRD	X-Ray Diffraction
$\alpha\ \beta\ \gamma$	angles between the positive directions of the y and z, x and z, and x and y crystal axes

ACKNOWLEDGMENTS

I would like to acknowledge the support of the Dorothy Hodgkin Scholarship Award for funding my PhD. I would also like to sincerely thank my lead supervisor Dr. Martin Preston at the Department of Earth and Ocean Sciences for his continuous support and guidance through all the stages of this project. My special gratitude goes to Professor Rasmita Raval and her Group at the Surface Science Research Centre of the Univesity of Liverpool for their help, friendliness, and instruction during my three-month stay at the Centre. I am indebted to Dr. Sam Haq and Dr. Ning Liu for conducting the adsorption experiments of Valine on a Cu(110) single crystal under ultra high vacuum conditions and for their helpful discussions to interpret the results. The support and teaching of Dr. Nasser Moslemzadeh on the basics of LEED and sample preparation is greatly appreciated. Thanks also to Mr. Phil Donovan for providing pictures of STM equipment.

Thanks also to: Dr. Richard Holme for his diligent assistance with postgraduate matters, Prof. David Prior and Mr. John Kavanagh for helping with the Conoscopic Method to evaluate the handedness of a synthetic quartz specimen, Prof. Robert Hazen for kindly loaning and shipping to us two natural quartz crystals of opposite handedness, Prof. George Wolff and his Group for allowing use of their lab facilities and for their amicability, Dr. Anu Thompson for her advice and tutoring on the operation/troubleshooting of the High-Performance Liquid Chromatography System, Dr. Steve Crowley (Stable Isotope Laboratory) for kindly conducting X-ray diffraction analyses on Montmorillonite K10 samples, Prof. A.M. Glazer and Dr. Lucjan Pajdzik at the Department of Physics of the University of Oxford for analysing a synthetic quartz slab with their conoscopic method, Mrs Elena Kozhevnikov at the Department of Chemistry (University of Liverpool) for conducting surface area measurements of sand quartz and kaolinite.

I would like to acknowledge Mrs. Carmel Pinnington and Sabena Blackbird for their technical help, Dr. Conrad Chapman for providing UV-digested Open Pacific Ocean Seawater. Thanks to Mrs. Paula Houghton for support and administration of the Dorothy Hodgkin Award. I greatly appreciate the encouragement and friendliness

of my colleagues Mr. Syed Abid, Mrs. Jolomi Mordi, and Mr. Joe Wilkinson. I thank Mrs. Ines Pierce for giving me helpful advice on how to visualise situations from a positive perspective. Most importantly, I would like to express my gratitude to my husband Harry and my daughter Karen for their patience, encouragement, and love during this period of my life. My parents María and Néstor have undoubtedly made it possible for me to reach this far so I hope they feel delighted and share with me this accomplishment.

GLOSSARY

Cation exchange capacity: Neutralisation of the negative charge of clays by cations. It is expressed in units of meq/100g of clay.

Clays: Sheet aluminosilicates that are the main components of soils and sediments in temperate regions. Clay unit layers can be of two basic types: 1:1 clay-one tetrahedral sheet and one octahedral alumina sheet; and 2:1 clay-two tetrahedral sheets sandwiching one octahedral alumina sheet.

Designation of stereochemistry of α-carbon atom in α-amino acids: The absolute configuration of the α-carbon atom in α-amino acids is designated with the prefix D- or L- to indicate chemical correlation with D- or L-serine and thus with L-or D-glyceraldehyde. Using the Cahn-Ingold-Prelog rules (the 'RS system'), the common protein L-amino acids are *S*-amino alkanoic acids except for L-cysteine which is a member of the *R*-series. Traditionally, biologists have used the D and L notation whereas surface scientists have preferred the '*RS* system' notation. The prefixes DL- or (*RS*)- indicate an equimolar mixture of the two enantiomers of an amino acid possessing a chiral centre[1].

Kaolinite: 1:1 clay mineral. The unit layers are held together by hydrogen bonds between oxygen atoms on the tetrahedral face and hydroxyl groups on the adjacent octahedral face resulting in a low CEC, low surface area, and a fixed c spacing of 0.7 nm. pH-dependent charge on the clay edge is relatively more important in kaolinite than the other clays.

Mica: Sheet silicate formed by the sharing of three oxygens by each silica tetrahedron. The basic unit is $(Si_2O_5)^{2-}$. Muscovite $(KAl_2(Si_3Al)O_{10}(OH)_2$ is a mica.

Smectites: Group of 2:1 clay minerals with a low degree of isomorphic substitution and low layer charge. The most common smectite is montmorillonite in which substitution occurs in the octahedral layer. Interlayer bonding is weak, which allows expansion of the clay lattice and easy entrance of cations and water molecules into the interlayer space.

CHAPTER 1 INTRODUCTION

This chapter lays out the fundamentals of chirality in organic and mineral systems, reviews the existing literature on interactions of chiral molecules at mineral/metal surfaces as well as their relevance in life, environmental, and earth sciences and finally presents the main aim and objectives of this work.

Chiral selective adsorption at mineral surfaces is paramount to origins of life hypotheses that invoke minerals as symmetry breaking structures that might have led the homochirality of life. The question of why proteins are constituted of L-amino acids and sugars of D-units is still the subject of considerable interdisciplinary research effort with the mineral hypothesis being intensely investigated in the astrobiology field.

The fact that relevant biomolecules (e.g, pharmaceutical drugs, personal care products, pesticides) are chiral and generally produced as racemic mixtures has prompted interest in finding technologies/processes that can either separate the enantiomers to make enantioenriched/enantiopure products or lead to the asymmetric synthesis of enantiopure molecules. Natural and engineered materials (i.e., quartz, clays/clay composite material, and templated or intrinsically chiral metals) can interact selectively with chiral molecules, and therefore their potential can be harnessed in multiple applications. For example, the fate and transport of chiral pollutants in groundwater can be better assessed if the abiotic/biotic adsorption or transformation of the individual enantiomers in the subsurface is studied by using model mineral surfaces such as quartz and clays. Chiral sensors for the *in situ* detection of enantiomers of AAs in water and other planets as well as engineered drug delivery materials also constitute fields of research that benefit from understanding chiral processes at surfaces.

This research addressed three main topics; first, the interaction of AA enantiomers with model mineral surfaces under various experimental conditions, second the polimerization of Val on a clay by simulation of a prebiotic environment (wet and dry cycles), and third the chemisorption of Val on a single crystallographic plane of copper (i.e. Cu(110)) under ultra-high vacuum.

1.1. Definition of Chirality and Nomenclature

Pasteur's elegant experiment of separating mirror image crystals of sodium tartrate revealed that crystals of this organic compound can exist in different spatial configurations. The words chiral and chirality derive from the Greek χειρ (cheir, a hand) since hands easily illustrate this property[2]. Right- and left-hands possess no plane of symmetry and are non-superimposable mirror images of each other. Important molecules of life such as amino acids and sugars are chiral and their chirality originates from substitution of a central carbon atom by four different atoms or groups. The lack of a mirror symmetry plane as shown in Figure 1.1 for a pair of AA enantiomers, or optical isomers, is a key feature of chiral molecules.

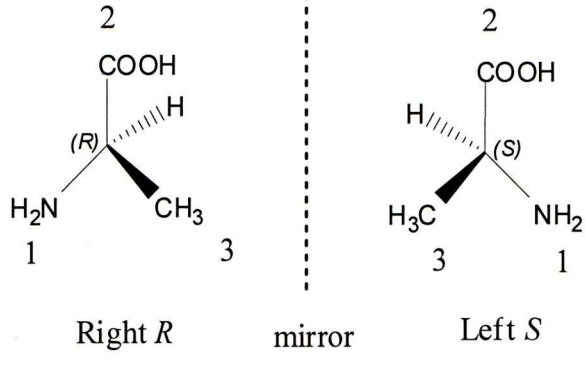

Figure 1.1. Enantiomers of alanine (Ala). Substituent priority numbers 1 to 3 are included to illustrate the Canh-Ingold-Prelog Rule

Later, the development of polarization microscopy revealed that chiral molecules have the same physical-chemical properties but differ in the way they rotate the plane of polarized light, thus giving rise to the term optical isomer [3]. Initially, enantiomers were labelled based on whether plane polarized light was rotated clockwise, equivalent to a positive rotation (+)-enantiomer (or the *dextrorotatory* enantiomer), or anti-clockwise implying a negative rotation (-)-enantiomer (or the *laevorotatory* enantiomer). However, the direction in which light is rotated is independent of the configuration of the stereogenic chiral centre. The Cahn-Ingold-Prelog rules were later developed for assigning the configuration *R* (Latin *rectus*, right) and *S* (Latin *sinister*, left) to the chiral centres of biomolecules. The rules can be summarized as: (1) assign a priority number to each substituent at the chiral centre. Atoms with higher atomic number get higher priority; (2) arrange the molecule so that the lowest priority substituent points into the plane of the paper;

(3) move from substituent priority 1 to 2 to 3. Assign the label *R* to the chiral stereocentre if direction of movement is clockwise and the *S* label if it is anticlockwise (Figure 1.1).

Note that it is important to clarify which nomenclature is used to refer to a chiral compound. For example, the natural Ala enantiomer has a chiral centre designated as *S*-Ala, which rotates plane polarized light to the right whereas *R*-ala, present in bacterial cell walls, rotates the light to the left. Amino acids are conventionally described with the labels D- (for dextro) and L- (for laevo). This nomenclature originated from using chiral glyceraldehyde as a standard. Before the advent of X-ray crystallography, chemists were able to resolve the configuration of enantiomerically pure compounds based on degradation to the L- or D-glyceraldehyde enantiomers.

There is other terminology pertinent to chiral systems that needs to be defined at this point. First, a *racemic mixture* contains a 1:1 ratio of each enantiomer. In the absence of chiral auxiliary compounds, the abiotic synthesis of biomolecules leads to a racemic mixture. Secondly, *enantiopure* systems are those consisting of just one enantiomer, whereas *enantio-enriched* systems contain a greater proportion of one of the enantiomers over the other. Finally, a reaction or separation is considered to be *enantioselective* if one enantiomer is produced or separated preferentially. Diastereomers are stereoisomers that are not mirror images of one another and therefore have different physical and chemical properties and they can arise when a compound has more than one stereogenic centre. Enantioselective separation of chiral compounds by using chiral auxiliary compounds and template surfaces occurs via diastereomeric association complexes [4] (Figure 1.2).

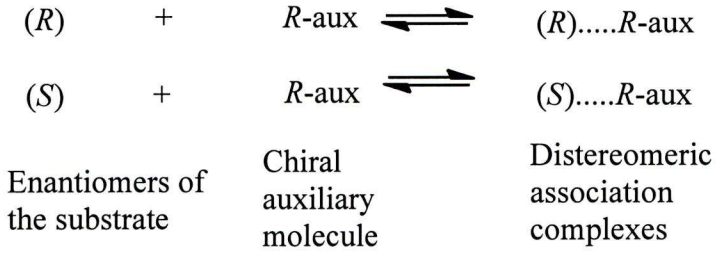

Figure 1.2. Illustration of the association of enantiomers of the analyte with a single enantiomer (R) of an auxiliary molecule

The association of enantiomers of a chiral compound with a chiral auxiliary compound can be visualized by using hands (Figure 1.3).

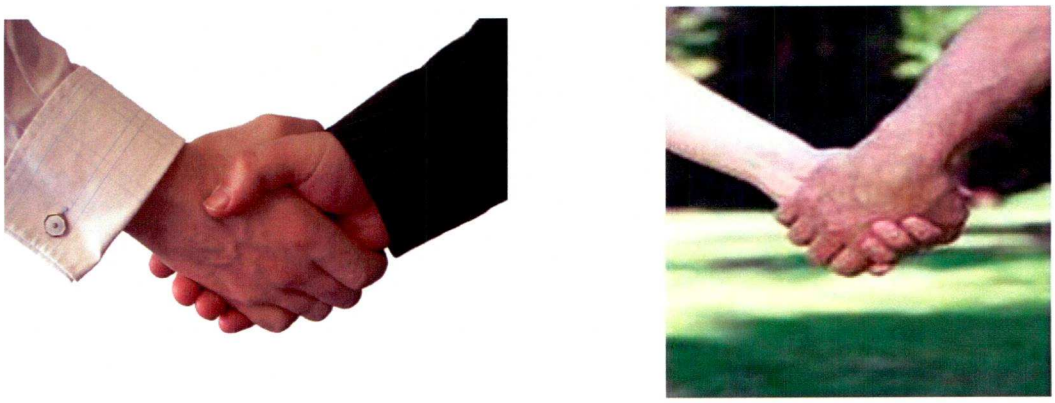

Figure 1.3. Schematic of a handshake(left) and holding hands (right)

The interaction of two right-hands differs from the interaction of a left-hand and a right-hand. Hence, a handshake represents an equal association whereas holding hands means unequal association. Holding hands is a diastereomer of shaking hands. Diastereomeric association complexes find application in the preparative separation of enantiomers via crystallization, an understanding of the biological activity of enantiomers, the separation of enantiomers by chromatography, and the reactivity of enantiomers in enzymatic resolutions. The interaction based recognition occurs through mechanisms such as hydrogen bonding, cation-anion attraction or π-π interactions as well as by inclusion (or partial inclusion) [4].

There are different ways to express the relative abundance of enantiomers in a mixture. The most common definitions are enantiomeric excess (*ee*), enantiomeric fraction (*EF*) and the ratio of the enantiomers (*ER*) according to the following equations:

$$ee = \frac{[S(R)] - [R(S)]}{[S] + [R]} \qquad \textit{(Equation 1.1)}$$

$$EF = \frac{[S(R)]}{[S] + [R]} \qquad \textit{(Equation 1.2)}$$

$$ER = \frac{[R]}{[S]} \qquad \textit{(Equation 1.3)}$$

Thus, *ee*=0, *EF*=0.5, and *ER*=1 mean that the enantiomers are equally abundant and therefore the mixture is racemic.

1.2. Chirality and Crystallography

Crystals of any material, whether organic or inorganic, reflect the order of the internal structure. All crystals in nature are made up by repeating a unit cell of a particular shape characterized by three distances a, b and c and three angles α, β, and γ (Figure 1.4) [5]. The unit cell is defined by lattice points which are arbitrary. Thus, lattice points represent equivalent positions and not atoms. In fact, a lattice point can be occupied by an atom, a complex ion, a molecule, or a group of molecules.

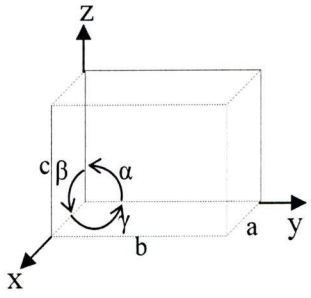

Figure 1.4. Definition of axes, unit cell dimensions and angles for a general unit cell

There are four types of three-dimensional unit cells (see Figure 1.5):

- Primitive (P): It has lattice point at each corner
- Body centred (I): It has a lattice point at each corner and at the centre of the cell
- Face centred (F): It has a lattice point at each corner and one in the centre of each face
- Face centred (A, B, or C): It has a lattice point at each corner, and one in the centre of one pair of opposite faces.

In addition there are seven classes of crystal systems from which a crystal can be generated (Table 1.1). The combination of the four types of lattice and seven classes of crystal systems leads to 14 permissible Bravais lattices (Table 1.1).

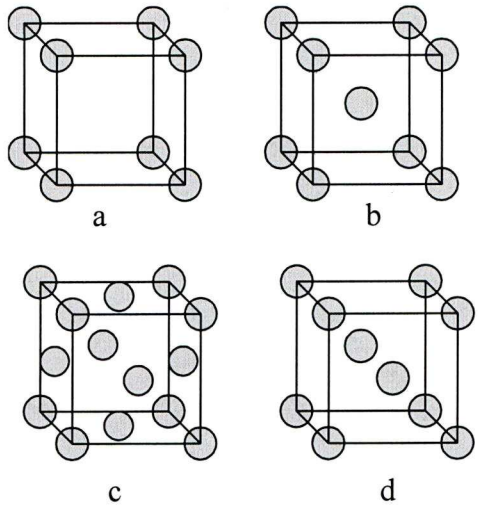

Figure 1.5. Types of unit cells. (a) primitive, (b) body-centred, (c) face centred, (d) face centred (A,B,or C). Blue circles represent lattice points

Table 1.1. The seven crystal systems and 14 Bravais lattices in three dimensions[5]

Crystal System	Unit Cell Dimensions	Symmetry	Bravais lattices
Triclinic	$a \neq b \neq c$; $\alpha \neq \beta \neq \gamma$	None	P
Monoclinic	$a \neq b \neq c$; $\alpha = \gamma = 90° \neq \beta$	One 2-fold axis or one symmetry plane	P, C
Orthorhombic	$a \neq b \neq c$; $\alpha = \beta = \gamma = 90°$	Any combination of three mutually perpendicular 2-fold axes or planes of symmetry	P,C,I,F
Trigonal/Rhombohedral	$a = b = c$; $\alpha = \beta = \gamma \neq 90°$	One three-fold axis	R
Tetragonal	$a = b \neq c$ $\alpha = \beta = \gamma = 90°$	A 4-fold axis	PI
Cubic	$a = b = c$ $\alpha = \beta = \gamma = 90°$	Four 3-fold axis	P,I,F
Hexagonal	$a = b \neq c$ $\alpha = \beta = 90°$ $\gamma = 120°C$	A 6-fold axis	P

Moreover, the combination of symmetry elements relating one atom to another in a crystal structure, independently of translational symmetry of the lattice, defines a point group. In three-dimensional systems symmetry elements are mirror planes (m), rotation axes about a line (1-, 2-,3-, 4-, and 6-fold), and inversion axes $\bar{1}$, $\bar{2}$, $\bar{3}$, $\bar{4}$, and $\bar{6}$, which involve a rotation followed by an inversion through a point lying in the axis. 32 point groups compatible with the symmetry of the seven crystal systems can

be derived by combining the above-mentioned symmetry elements. Glide planes and screw axes are translational symmetry elements. As illustrated in Figure 1.6, glide planes combine reflection through a plane of symmetry followed by a/2 translation, where *a* is the repeat distance between identical molecules. A screw axis, designated as n_i, represents a rotation of (360°/*n*) followed by a translation of *i*/*n*. Rotational and screw axes symmetry operations generate objects that are superimposable on each other. All other symmetry elements, mirror plane, glide plane, inversion axes, produce a mirror image of the object or an enantiomorph from the Greek *enantios*:opposite, and *morphosis*, form.

Finally, the combination of 32 point groups with the 14 Bravais lattices gives 230 three-dimensional space groups. All crystalline materials have structures that belong to one of these space groups. In the context of chiral systems, there are 65 possible space groups for chiral molecules. Furthermore, there are 11 pairs of enantiomorphic space groups that only accommodate optically active forms of chiral molecules [2].

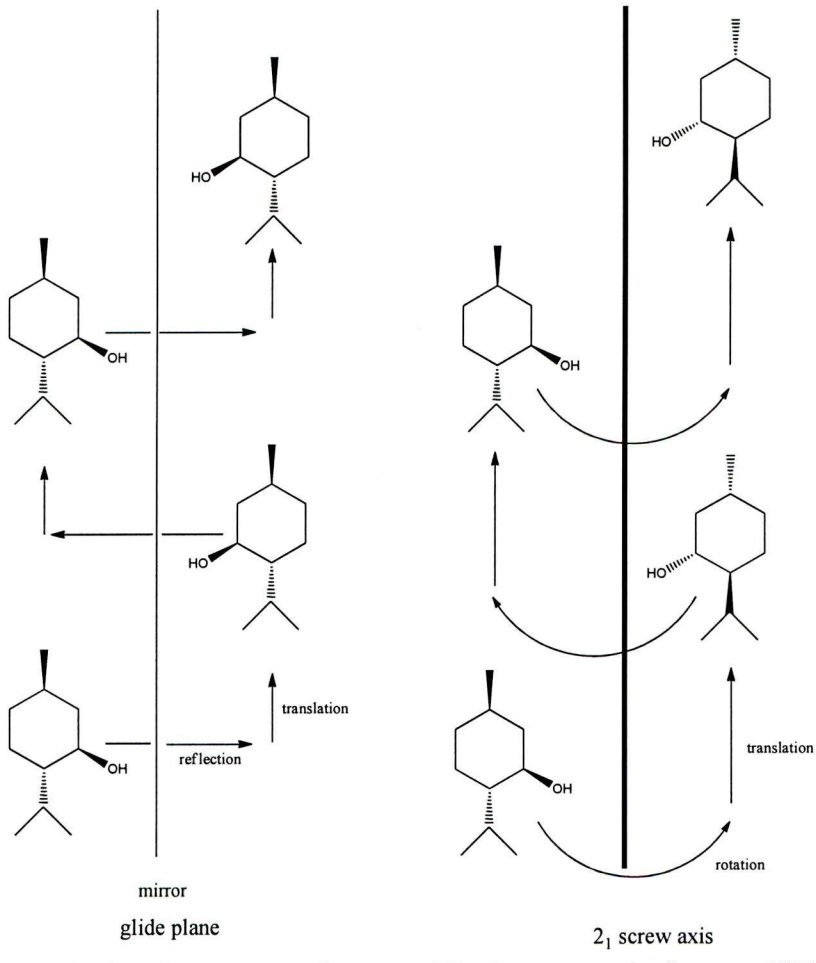

Figure 1.6. Translational symmetry elements. The 2_1 screw axis shows a 180° rotation and a/2 translation

1.3. Enantiomorphic Rock-Forming Minerals

The definition of chirality can also be extended to single crystals and surfaces. In mineralogy, a quartz crystal is intrinsically chiral because of its internal structure, which reflects on its morphological appearance. Thus, *l*- and *d*-quartz crystals exist in nature in almost equal proportion as will be discussed in Chapter 2. Surfaces of achiral single crystals of a variety of minerals can also exhibit chirality. This topic has recently been reviewed by Hazen [6, 7]. The following sections describe quartz enantiomorphism and the chiral properties of other minerals found on Earth.

1.3.1. Quartz

Silica (SiO_2) exists in several polymorphs, but quartz or low-quartz is the most common in the Earth's outer crust, being stable at temperatures below 573°C [8].

Quartz crystallizes in the trigonal trapezohedral class designated as (32) and is characterized by one axis of three-fold symmetry and three perpendicular polar axes of two-fold symmetry. Quartz lattice parameters are a=5.41 Å and c= 4.91 Å. It lacks both planar and centre symmetry and belongs to the spaces group $P3_12$ or $P3_22$ for structurally *d*- and *l*-quartz crystals, respectively. The morphological handedness of quartz is opposite to its structural handedness which is given by the arrangement of helical SiO_4 tetrahedra along the three-fold axis (Figure 1.7). Weiss' convention for the morphological hand of quartz has been adopted when describing its enantiomorphism. Thus, in *d*-quartz crystal the trigonal pyramidal and trapezohedral faces *s* and *x* slope to the right. Biot's optical convention agrees with the morphological convention of Weiss. Therefore, plane polarized light incident on a quartz slab perpendicular to the optical axis (*c*-axis) is rotated clockwise in a morphologically *d*-quartz specimen when the observer looks towards the source of the light.

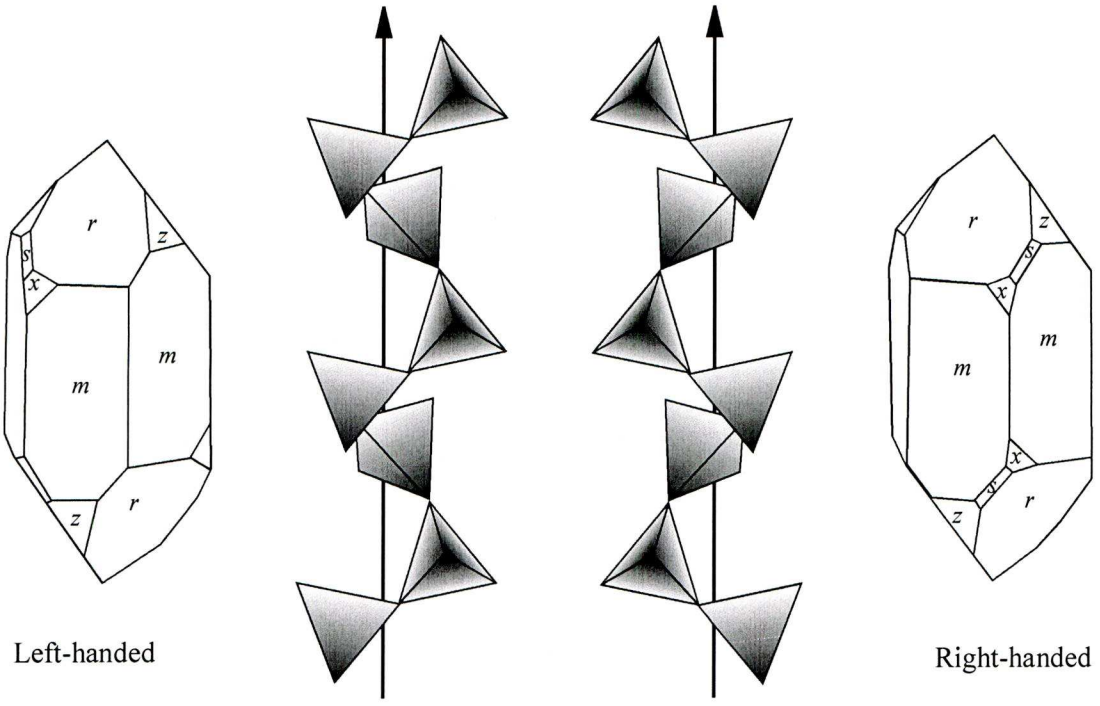

Figure 1.7. Enantiomorphic quartz single crystals. *l*-quartz (left) and *d*-quartz (right)

Table 1.2 summarizes the main crystallographic planes of *d*-quartz, their Miller index notation, common face development, and calculated reduced surface energy (RSE) which gives an indication of the cleavage tendency of a particular face. Interestingly, common growth faces tend to incorporate impurities such as Al and Fe which are responsible for the colouring of milky and rose quartz. In nature, quartz specimens can display twinning or the intergrowth of two crystals mainly along the positive rhombohedral direction $(10\bar{1}1)$ and along the $(11\bar{2}2)$ direction for the Brazil twin [9].

Table 1.2. Crystallographic planes of *d*-quartz[9]

Face	Notation	Miller Index	Common face development	RSE (kcal/m/ Å^2)
First-order hexagonal prism	*m*	$(10\bar{1}0)$	2	28.5
Positive rhombohedron	*r*	$(10\bar{1}1)$	1	24.7
Negative rhombohedron	*z*	$(01\bar{1}1)$	3	24.2
Right trigonal pyramid	*s*	$(11\bar{2}0)$	5	31.4
Positive right trapezohedron	*x*	$(51\bar{6}1)$	4	
Basal pinicoid	*c*	(0001)		32.7

1.3.2. Other Minerals (Calcite, Gypsum, Pyrite)

Hazen recently presented a comprehensive review of minerals that are ubiquitous on Earth and other terrestrial bodies that also exhibit enantiomorphic characteristics[6, 7]. As mentioned before, quartz is intrinsically enantiomorphic because it lacks any symmetry. Morphologically acentric minerals like calcite and gypsum having mirror symmetry planes possess chiral faces. The chirality of the faces originates from the orientation of the structural building units of the two-dimensional mineral surface that by definition cannot be superimposed on its reflection in a mirror perpendicular to the surface. Figure 1.8 better illustrates the concept of chiral faces for calcite ($CaCO_3$) and gypsum ($CaSO_4.2H_2O$). The dogtooth or scalenohedral calcite form displays faces designated as *v*(214) characterized for being mirror images of each other. Gypsum of the monoclinic space group shows pairs of *m*(110) and *l*(111) faces that have been found to interact selectively with enantiomers of AAs as evidenced by the growth of asymmetric crystal habits due to preferential attachment of one enantiomer on the *m* faces[10]. Pyrite is a symmetric mineral so it does not have morphological chirality, but as stated by others[7]: 'crystal surfaces possess etch pits, growth steps, twin boundaries and other nonperiodic features that provide numerous local chiral centers on an otherwise achiral surface environment.' Little is known on the role of these imperfections on chiral selective processes at mineral surfaces.

1.3.3. Clays

Clays are aluminosilicates made up of tetrahedral silica and octahedral alumina sheets (Figure 1.9). Kaolinite consists of a layer of alumina layer stacked on a tetrahedral silica layer to give a 1:1 layer clay with the general chemical formula $[Si_4]Al_4O_{10}(OH)_8$. Illite, vermiculite, and smectite are 2:1 layer type clays where the octahedral sheet is sandwiched between two tetrahedral sheets. Montmorillonite, which has been used extensively as a substrate in adsorption of organic compounds (pesticides, amino acids, proteins), is a typical smectite with formula $M_x[Si_8]Al_{3.2}Fe_{0.2}Mg_{0.6}O_{20}(OH)_4$. M represents cations residing on or in the cavities of the basal plane of the oxygen atoms of the tetrahedral sheet that balance the layer charge *x*.

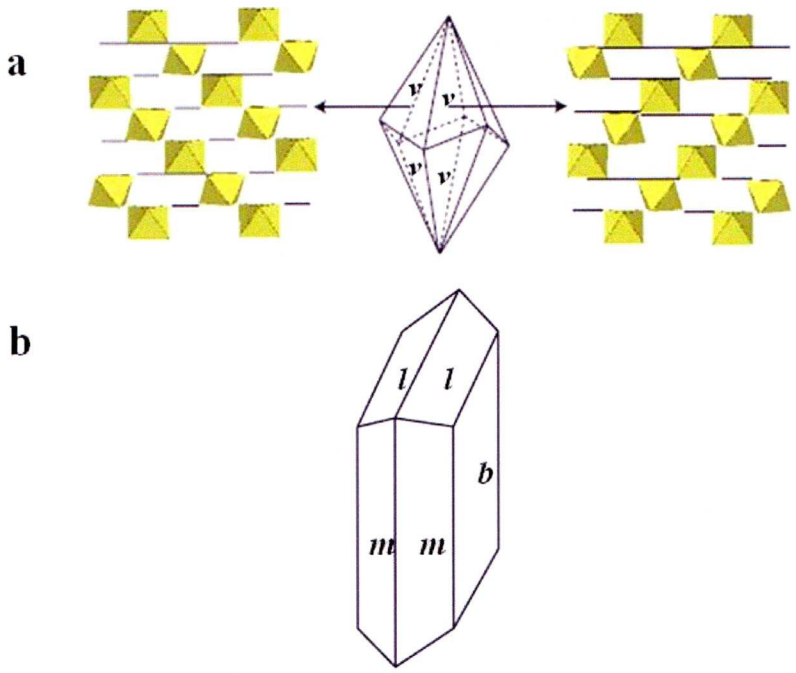

Figure 1.8. a. Trigonal calcite crystal. Enantiomorphic faces (*v*(211)) show corner linked CaO_6 octahedra (yellow) crosslinked by planar CO_3 groups. b. Monoclinic gypsum crystal showing the chiral *m*(110) and *l*(111) forms

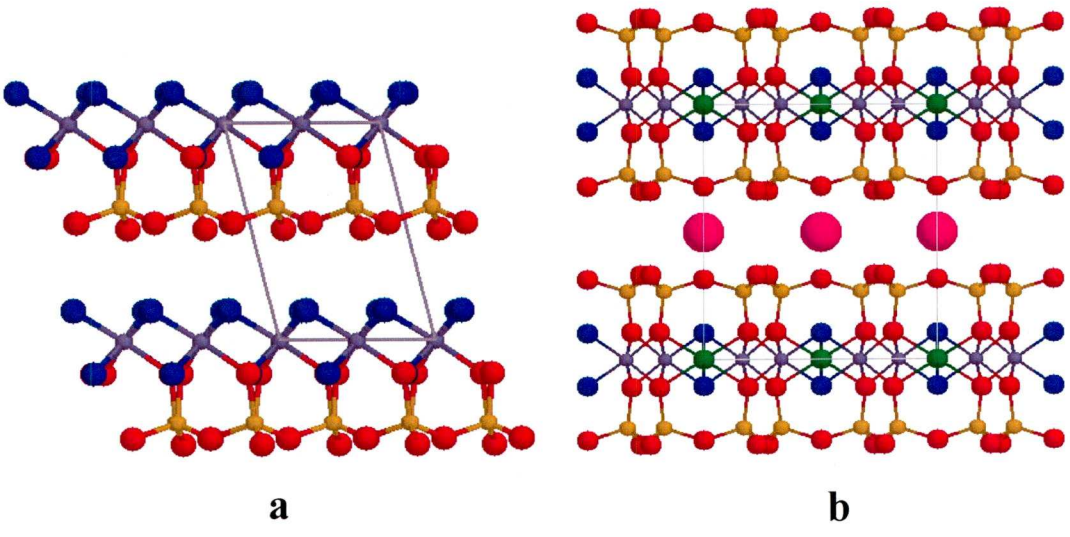

Figure 1.9. Schematic representation of aluminosilicate clays. a. Kaolinite 1:1 layer clay; Al:grey spheres, O:red spheres, Si: yellow spheres, OH groups: blue spheres. b. Montmorillonite 2:1 layer clay; Mg:green spheres, Al: grey spheres, OH groups: blue spheres, interlayer potassium:crimson spheres, O:red spheres, Si: yellow spheres. The unit cell is also shown in the pictures. Source: Mineral web (http://www.minweb.co.uk)

Many argue that clays do not have enantiomorphic properties[7]. However, the (*hk*) octahedral edges of kaolinite have been reported to be enantiomorphic owing to the arrangement of the O atoms, OH groups, Al atoms, and octahedral vacancies [11]. Later, Julg proposed that kaolinite could possibly have two opposite crystal forms known as the direct and inverse that can be mirror images of each other [12]. These, so called, enantiomorphic kaolinite forms were proposed to occur from the orientation of a trihedron $(\vec{a}, \vec{b}, \vec{c})$. It was estimated that the direct form is more stable and therefore Julg hypothesised that it could have been more abundant than the inverse one in a prebiotic scenario[13]. Unlike quartz, these enantiomorphic crystals have not been identified by any optical method, so their existence is based on a theory basis only.

1.4. Mechanisms of Adsorption of AAs on Minerals

Adsorption of AAs and proteins on silica surfaces is a common but difficult phenomenon since sorption is strongly dependent on numerous variables such as surface area, pH, matrix composition, and molecular structure of the adsorbate [14]. Negligible adsorption of acidic, non-polar, and hydrophobic AA onto crystalline and amorphous silica at neutral pH values has been reported [15-17]. In contrast, the basic AAs lysine (Lys), arginine (Arg) and histidine (His) readily adsorb on silica over a wide pH range [15, 16]. This stems from the presence of positively charged amino groups in their side chains (Figure 1.10) that interact electrostatically with the negatively charged silica surface. Therefore the lack of adsorption of alanine (Ala) enantiomers onto quartz in aqueous systems [18, 19] can be ascribed to the wrong choice of experimental conditions i.e., the model molecule and the pH of the solution.

Mineral surfaces display acid-base properties. The pH of the point of zero charge (pH_{pzc}) of a mineral, defined as the pH at which the mineral has no net charge, is used to illustrate the pH-dependent equilibrium of minerals. At $pH > pH_{pzc}$, mineral surfaces become negatively charged due deprotonation of hydroxyl groups, whereas at $pH < pH_{pzc}$ surfaces are positively charged according to:

$$SOH_2^+ \rightleftharpoons SOH + H^+$$

$$SOH \rightleftharpoons SO^- + H^+$$

Equations 1.4 and 1.5

where S stands for surface. Typically, S represents silicon (Si) or aluminum (Al) atoms. The pH_{pzc} of some soil minerals are listed in Table 1.3. For example, silanol groups (Si-OH) are the main sites present on the surface of clean hydroxylated silica surfaces and hence their interaction with water and other molecules determines the reactivity of the mineral in natural and technological applications. In general, water-oxide interactions are relevant in understanding physical, chemical, and biological processes such as weathering, corrosion, dissolution, catalysis, contaminant/ biomolecule sorption and bioavailability.

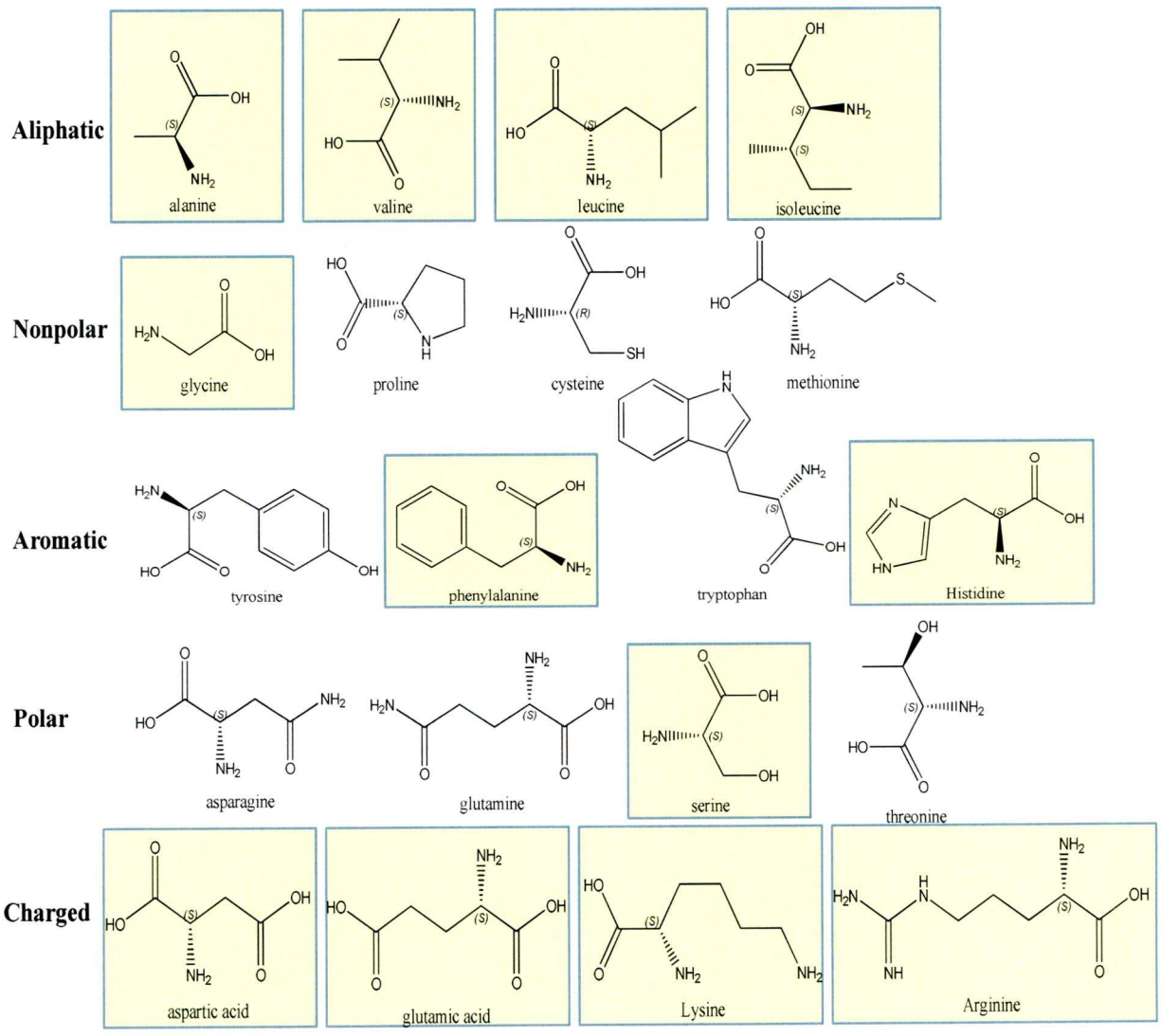

Figure 1.10. Amino acid classification according to their speciation at neutral pH. AAs used in this research are highlighted in yellow boxes. Carboxylic groups are deprotonated (COO^-) and amino groups are protonated (NH_3^+)[20]

Table 1.3. pH_{pzc} for Important Soil Minerals[21]

Soil Mineral	pH_{pzc}	Soil Mineral	pH_{pzc}
Quartz and silica	2.0-3.0	Pyrite	2.0-5.0[a]
Montmorillonite	4.0	Haematite	8.0-8.5
Kaolinite	4.0-5.0	Goethite	7.0-8.0

[a] pH_{pzc} depends on oxygen activity. Under anoxic conditions pH_{pzc} shifts to lower pH values.

Equation 1.5 illustrates that, at near neutral pH, silica and aluminosilicates surfaces bear net negative charge. Surface hydroxyl groups (SOH) are reactive moieties in the majority of mineral systems and their interaction with organic and inorganic compounds has been widely documented [22]. Therefore, any treatment, either chemical or physical, that reduces their density will result in a decrease in sorption capacity of the mineral. A good illustration of the rich chemistry offered by minerals in the natural environment is shown in Figure 1.11 [23].

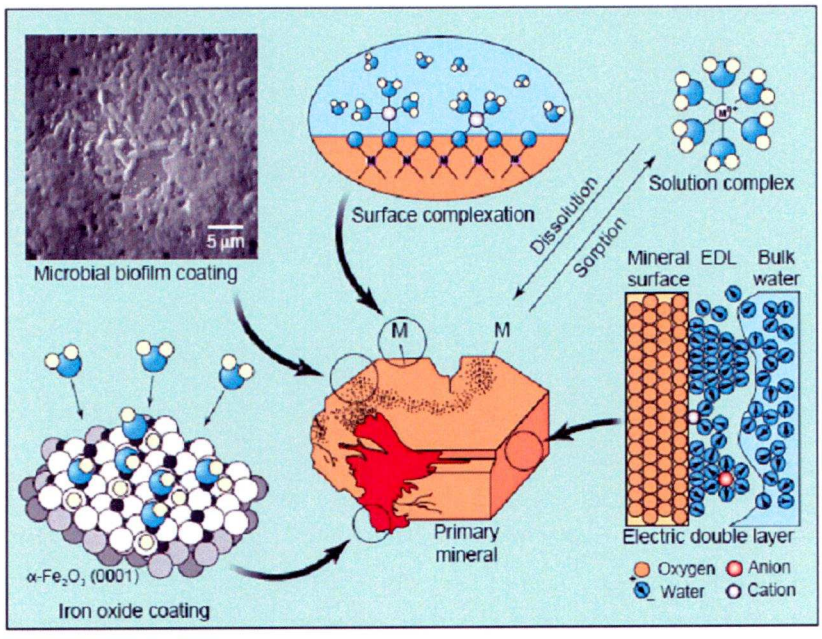

Figure 1.11. Illustration of the metal oxide-aqueous interface in a natural environment. Biofilm and iron oxide coating, interaction of surface with hydrated cations via inner-sphere and outer-sphere complex, and the electric double layer (EDL) are depicted [23]

It is clear that the properties of the interfacial water at minerals play a relevant role in the many physical-chemical processes occurring not only in the natural environment, but also in industrial processes such as catalysis [24]. Surface science techniques, in particular scanning probe microscopies, have been become a relevant tool for understanding complex mechanisms of molecular adsorption on single

crystals and bulk powder minerals. As will be discussed later, these techniques use well-defined systems; typically single crystals with flat surfaces are employed and the experiments are carried out under vacuum to eliminate potential interferences, including water [25].

Similarly to minerals, AAs exhibit acid-base equilibria as a function of pH:

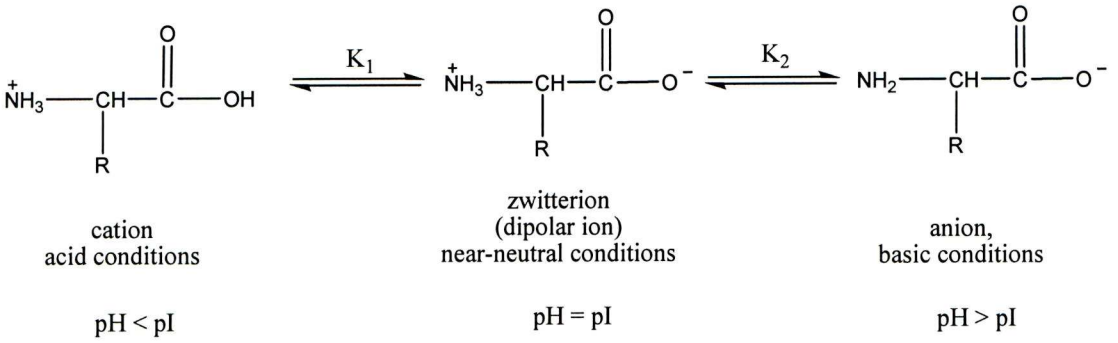

Equation 1.6

The zwitterionic species predominates at the isoelectric point (pI) of AAs whereas the cationic and anionic species prevail at acidic and basic conditions, respectively. A greater extent of adsorption of most protein AAs onto quartz is expected at acidic pH values due to the electrostatic interaction between the negatively charged mineral surface and the cationic AA. Arg due to its high pKa (12.48) has a positively charged guanidinium cation over a large pH range. Thus, Arg along with Lys and Hist have been reported to adsorb to a great extent onto silica, aluminosilicates and sediments [26-28].

Clays are good adsorbents due to their high surface areas reaching up to 600 m^2/g). The interaction of AAs and proteins with clays has been extensively addressed because of their widespread abundance in soils, sediments, and dust materials. The main mechanisms of adsorption of AA on clays in aqueous systems are cation exchange, proton exchange and physical adsorption. Langmuir-type (L) isotherms were obtained for acidic (glutamic acid (Glu), aspartic acid (Asp)) and neutral (phenylalanine (Phe)) adsorbed on hydrogen-montmorillonite[29]. Basic AAs (Arg, His, and Lys) also displayed L-type adsorption behaviour on sodium (Na-) and calcium (Ca)-montmorillonite. The cationic forms of the basic AAs are the species involved in the exchange processs which takes place via the NH_3^+ group. Evidence for this has been provided by infrared spectroscopy and the displacement of the cations originally present in the clay interlayer [29].

Proton exchange reactions of zwitterionic AA species ($RH^{\pm}$) at hydrogen-montmorillonite take the form:

$$RH^{\pm} + H_3O^+\text{-clay} \rightleftharpoons RH_2^+\text{-clay} + H_2O \qquad \textit{Equation 1.7}$$

Basicity of AAs and peptides plays an important role in the proton-exchange reactions. For instance, *p*-aminobenzoic acid intercalates with the aromatic ring parallel to the silicate surface as indicated by the extent of basal swelling ($d(001)$= 1.300 nm). In contrast, the orientation of the benzene ring of phenylalanine in the interlayer must be different given that the basal spacing of the intercalated complex is 1.385 nm[29]. Physical adsorption involves the partition of the zwitterionic AA species ($RH^{\pm}$) between the bulk water and the Stern-layer water (water adhering to the clay surface):

$$RH^{\pm}_{bulk} \rightleftharpoons RH^{\pm}_{Stern} \qquad \textit{Equation 1.8}$$

Adsorption isotherms of glycine (Gly) and its di-, tri- and tetra-peptides on Ca-montmorillonite and Ca-illite were linear over a wide concentration range (0.01-0.20M) at 298 K, pointing to a physical adsorption mechanism. Ala, serine (Ser), and leucine (Leu) also displayed linear isotherms on Ca-montmorillonite and Ca-illite over the 0.05-0.10 M concentration range[29].

The size and shape of the molecule are also relevant in clay-AA systems and influence the extent to which a particular AA is intercalated in the interlayer. Another variable to consider in clay aqueous systems is the low pH at the clay-water interface. The reactivity and catalytic potential of clays is strongly dependent on their interfacial acidity, which can be manipulated by exchanging the natural cations (i.e. Ca^{2+} and Na^+) with transition metal cations (i.e. Ni, Cu). In particular, Cu^{2+} is of interest since it is an abundant cation in natural waters where it can participate in exchange reactions with clays of natural sediment components. Additionally, Cu-clay-AA complexes find application in biochemistry because they can mimic enzymatic systems and catalyse the polymerization of glycine, alanine, aspartic acid and their mixtures by thermal activation [30-34].

Copper exchanged clays adsorb AAs to a greater extent than their natural counterparts because stable chelate compounds can be formed in the presence of copper. Jang and Condrate and [35] showed that monodentate and bidentate copper complexes of Val occur in the interlamellar spaces of Cu-exchanged montmorillonite at low and high pH, respectively (Figure 1.12). Similarly, the same authors reported

that Lys preferably formed a bidentate copper complex in the Cu-montmorillonite matrix.

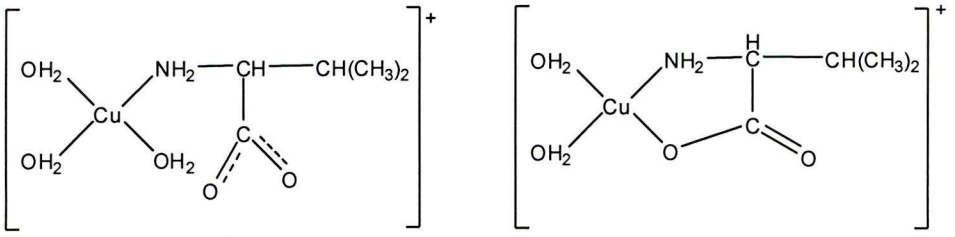

Figure 1.12. Cu-Val complexes in Cu-exchanged montmorillonite

Approximately 80% of the exchange capacity of smectite clays is due to substitution within the structure with the remaining 20% attributed to charges at the edge of the sheets, suggesting that the interaction of AAs with Cu-exchanged clays predominantly takes place in the interlayer region. Expansion of the basal distance of the clays *d*(001) as determined from X-ray diffraction analyses provides a measure of the intercalation of AAs in the clay structure. The structure of the AA is a key factor in the reversibility of adsorption on clays. For example, Brigatti et al. [36] reported that cysteine is more tightly bound to SAz-1 montmorillonite (a high layer charge montmorillonite originary from Cheto Apache County, Arizona, USA) than glycine. This might be a consequence of the specific interactions of the thiol group (-SH) of cysteine with the clay through covalent bonding. To support this, Benetoli *et al.* [37], in their recent work on the adsorption of AAs on bentonite and kaolinite in artificial seawater systems, reported that cysteine binds to the clays through both the amine and sulfhydryl group as concluded from infrared analyses. In addition, the interlayer expansion was greater in the cysteine-clay system in agreement with Brigatti *et al.* [36].

Protein and non-protein AAs can be intercalated in the interlamellar region as found for α- and β-Ala[38] (Figure 1.13). Ala chelation in the interlayer is more energetically favoured than that of Val as supported by the more negative energy of reaction for metal-AA complex formation for both 1:1 and 1:2 metal-AA complexes.

At near neutral pH, the reaction of protein AAs with cation-exchange sites has been demonstrated to occur via the zwiterrionic species. Thus, the zwitterion binds to the hexahydrated copper complex $(Cu)(H_2O)_6^{2+}$ through the amine and carboxylic group with release of a proton from the protonated amine group (NH_3^+) and the displacement of two water molecules.

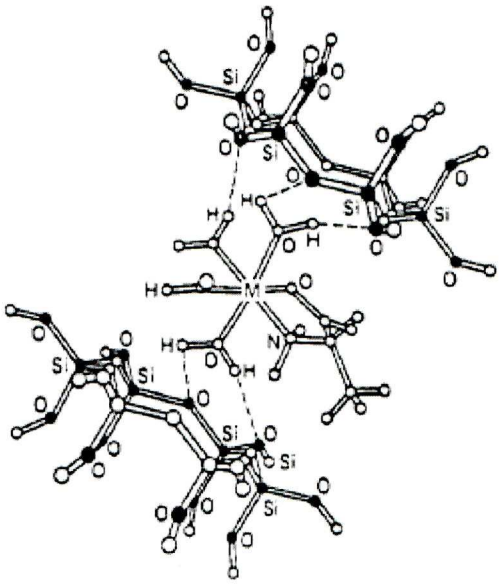

Figure 1.13. 1:1Cu^{2+}(Ala).4H_2O complex in the interlamellar spacing of an smectite clay. M represents Cu^{2+}. Dashed bonds show hydrogen bonding of coordination water to oxygen of the siloxane groups of the interlayer walls[38]

Five-membered chelate rings are therefore formed as a result of the chelation reaction in the interlayer. In contrast, the anionic AA species is the one involved in chelation in bulk water. The interaction of the chelate with the siloxane (Si-O-Si) functionalities of the clay through hydrogen bonding is another possible stabilising force. Steric factors also could influence the feasibility of intercalation considering that cation exchanged sites in smectites are estimated to be separated about 10 Å apart [38]. Complexes with van der Waals radii greater than this distance could be subject to repulsion forces and hinder intercalation.

Other soil components such as kaolinite and pyrite have also been investigated with regard to their interaction with AAs in aqueous media because of their high adsorptive capacity and abundance in extreme environments. For instance, kaolinite interaction with aspartic acid was recently studied with an extended constant-capacitance complexation model (ECCM)[39]. The extent of adsorption of Asp was practically constant (18%) from pH 3 to 11. The study concluded that a weak interaction of deprotonated Asp species with surface hydroxyl groups of the edge sites of the clay through formation of an outer-sphere complex was the main mechanism operating in this system.

Pyrite (FeS_2) has been invoked as a potential template and catalyst in the formation of organic species relevant to origins of life hypotheses since it is abundant in anoxic environments such as hydrothermal vents. Its surface exposes different

types of surface sites such as thiol(-SH) and hydroxylated iron groups (FeOH) that might participate in different interactions with AAs such as hydrogen bonding and chemical bonding. Adsorption of Ala, Cys, and Gly on pyrite took place under anoxic conditions although the surface of pyrite was negative over the pH range 2 to 8, suggesting that chemical reactions with Fe sites rather than electrostatic bonding was operating in the system. Moreover, Fe^{2+} and Cu^{2+} ions in solution affect the surface chemistry of pyrite and lead to increased adsorption of organic compounds via bridging or the formation of ternary complexes[40].

Summarising, AAs interact with minerals via specific and non–specific mechanisms. pH and ionic strength (I) are crucial variables when electrostatic bonding dominates, as in the case of adsorption of lysine on silica[15]. As recently stated by Lambert in his review on AA interactions with minerals, the chemistry of AA sorption on minerals is rich and more interesting than previously thought, thus opening opportunities of research[41]. In natural settings, the type of mineral and prevalent system conditions i.e, redox potential, presence of cations, multicomponent mixtures, etc. might result in AA interactions other than those observed in simplified systems. This is one of the reasons why descriptions of the degree and mode of adsorption of AAs, in particular those that are neutral and acidic, onto minerals may vary among different published studies. In addition, the methods used to calculate the amount of adsorbed AA vary. The majority of studies use the depletion method where the concentration of the AA in the mineral-solution system after equilibration is subtracted from the initial concentration of the AA to give the amount adsorbed. In other instances, the amount adsorbed is determined after washing off the residual AA solution at the mineral interface and extracting the surface. If physical adsorption predominates, then underestimation of the level of adsorption can occur when using the latter method. It would then be appropriate to use both approaches to conduct mass balances as undertaken by Fribiele *et al.* [42] in their study on the adsorption of AA enantiomers on Na-montmorillonite.

1.5. Selective Adsorption of AA Enantiomers on Minerals

Quartz, clays, and calcite have been found to adsorb selectively one of the enantiomers from a racemic mixture of different pairs of AAs[18, 19, 43-49].

Table 1.4 summarizes the main experimental and theoretical works that have reported selective adsorption of chiral amino acids on mineral surfaces and the conditions under which the experiments were conducted. Quartz has been studied the most because of its abundance, enantiomophism and intrinsic enantioselective potential. The asymmetric adsorption of dilute Ala enantiomers on powdered *l*- and *d*-synthetic quartz specimens has been reported to occur exclusively in non-aqueous systems[19, 48]. For example, at temperatures below 8°C, adsorption of Ala on quartz decreases to zero when the content of water in ethanol reaches 20%[19]. This is not surprising since water binds onto the quartz surface via hydrogen bonding forming structures that might even possess ice-like properties depending on pH[50]. These well-organized layers might hinder the adsorption of organic compounds directly on the substrate, but other physical interactions with the bound water are still likely to take place.

Kavasmaneck and Bonner concluded that NH_2 and NH_3^+ groups are responsible for the adsorption of Ala onto quartz in anhydrous solvents[44]. Nonetheless the influence of the crystallographic orientation of quartz faces on selective adsorption was only addressed later by Furuyama *et al.*[19]. Powdered quartz contains a mix of different crystallographic planes, in particular the low-energy ones resulting from cleavage such as the positive rhombohedron (*r*), the negative rhombohedron (*z*), and the first-order hexagonal prism (*m*). The uncommon basal pinicoid plane *c* (0001) has also been observed during cleavage and found more dominantly in fine particles[9]. Furuyama *et al.*[19] proposed that the enantioselective adsorption of neutral L-Ala on the $(10\bar{1}0)$ plane of *l*-quartz was due to favourable hydrogen bonding interactions of the carboxyl and amino groups of the L-enantiomer with the hydroxyl groups of the silanol groups. Placing L-Ala on the mirror image *d*-quartz plane would still result in the molecule interacting via the carboxyl group and the methyl group (Figure 1.14). They concluded that the more energetically favoured interaction of the NH_2 group and SiOH vs. that between CH_3 and SiOH was responsible for the preferential adsorption of L-Ala by *l*-quartz than that by the *d*-quartz. The previous model was hypothesized to work well for the adsorption of zwitterionic Ala ($CH_3(H)C(COO^-)NH_3^+$) from aqueous solutions onto hydroxylated quartz surfaces, but a reversal in the enantioselective adsorption was predicted taking into account the weaker strength of the NH_3^+-OH versus that of CH_3-OH bond.

Table 1.4. Compilation of selective adsorption behaviour of AAs in mineral systems

Mineral	Amino Acid enantiomers	Exp Conditions	Measuring method	Observed Selectivity	Reference
Kaolinite K6	L-Asp, D-Asp, DL-Asp	C_0=0.01 M. Room temperature. S/L= 0.1 g/mL.	AA analysis by automatic ion-exchange chromatography	L-Asp polymerized preferentially	[51]
Kaolinite K6	L-Asp, D-Asp, L-Phe, D-Phe	C_{0Asp}=0.01 M. T=90°C. S/L= 0.1 g/mL. pH= 3.2. Incubation of samples for 9 days. C_{0Phe}=0.001 M. T=90°C. S/L= 0.2 g/mL. Buffered system at pH 2, 6.	Extraction of clay with 2N NH_3. Analysis of Asp peptides by Biuret method. Phe supernatant analysis by UV-spectrometry.	L-Asp polymerized preferentially. L-Phe adsorbed preferentially at pH 6, but opposite behaviour at pH 2. Clay edges hypothesized to be enantioselective sites.	[52]
Kaolinite K6 Fisher Scientific	DL-phenylalanine	C_0=0.001 M. Room temperature. S/L= 0.2 g/mL. Buffered system at pH 2, 6	Optical rotatory dispersion and chiral gas chromatography analysis of supernatants. Thin-layer chromatography	None	[53]
Synthetic *l*- and *d*-quartz.	Individual L-Ala and D-Ala.	C_0=20μM in anhydrous dimethylformamide. Room temperature. S/L= 0.79 g/mL. SSA= 0.025m^2/g	Depletion. Supernatant concentration determined by radioactive counting.	L-Ala adsorbed preferentially on *l*-quartz and D-Ala on *d*-quartz	[18]
Synthetic *l*- and *d*-quartz.	Racemic DL-Ala	C_0=15μM in anhydrous dimethylformamide . Anhydrous system. Room temperature. S/L= 0.70 g/mL. SSA= 0.024m^2/g	Depletion. Supernatant concentration determined by radioactive counting.	L-Ala adsorbs preferentially on *l*-quartz and D-Ala on *d*-quartz	[43]
Synthetic *l*- and *d*-quartz.	Racemic (*R,S*) alanine isopropyl ester.	C_0=100μM in anhydrous chloroform. Room temperature. S/L= 1 g/mL. SSA= 0.11m^2/g	Depletion and extraction. Supernatant and enantiomeric extract concentrations determined by chiral gas chromatography.	(*R*)-Ala isopropyl ester adsorbed preferentially on *l*-quartz and (*S*)-Ala on *d*-quartz	[44]
Synthetic *l*- and *d*-quartz.	Racemic DL-Ala	C_0=10μM in anhydrous ethanol. T=-80°C, 8°C. S/L= 1 g/mL. SSA= 0.08 m^2/g	Depletion. Supernatant concentration determined by radioactive counting	L-Ala adsorbs preferentially on *l*-quartz and D-Ala on *d*-quartz	[19, 48]
$(10\bar{1}0)$ plane of quartz	L-, D-Ala	Crystal represented as finite point charges	*Ab* initio self-consistent field method	Cationic L-Ala is preferentially adsorbed on l-quartz. The energies of adsorption of the two enantiomers differ by 0.07 kcal/mole.	[54]

Mineral	Amino Acid enantiomers	Exp Conditions	Measuring method	Observed Selectivity	Reference
Na-Montmorillonite	Racemic DL-Valine, DL-Norvaline, DL-α aminobutyric acid, DL-alanine	C_0=100 μM. Room temperature. Buffered system at pH 3, 7, and 10	Depletion and extraction. Supernatant and extract D/L ratios determined by chiral gas chromatography and HPLC.	L-AAs adsorbed preferentially on montmorillonite in some experiments according to GC. LC data did not confirm the GC results.	[42]
Na-Montmorillonite (Magnia) (Algeria)	L-,D- and DL-glutamic acid L-,D- and DL-aspartic acid	C_0=0.02-0.4 M. Room temperature. Buffered system at pH 6. T= 20°C	Deamination kinetics of enantiomers and adsorption isotherms determined by the microKjedahl method	Stereoselective deamination of L-enantiomers	[55]
Allophanes with different Al/Si ratios	DL-Alanine and DL-alanyl-alanine	C_0=0.05M. T=20°C. Unbuffered system. S/L= 0.02 g/mL	Circular dichroism (CD) spectroscopy of supernatant	L-alanyl-alanine enantiomer adsorbs preferentially. No selectivity for alanine enantiomers	[56]
Calcite single crystal with terraced growth features	Racemic DL-Asp	C_0=0.05M. Room temperature. Unbuffered aqueous system.	Extraction. Extract concentration determined by chiral gas chromatography.	L-Asp adsorbs preferentially on the ($3\bar{1}\bar{2}1$) face whereas D-Asp adsorbs on the ($21\bar{3}1$) face.	[49]
Calcite ($21\bar{3}1$) face	L-, D-Ala		Density functional theory (DFT) calculations	Weak enantiospecificity. Negligible differences in adsorption energies (<1kcal/mol) for both enantiomers, attributed to disparity between Ala size and and O sites on calcite.	
($10\bar{1}0$) faces of quartz	D-carminic acid		Molecular modelling	*l*-quartz binds D-CA preferentially	[57]
Natural (100) *l*- and *d*-quartz faces	FMOC-L-Lys	Arrays of 3x8 150 μm FMOC-L-Lys spots on (100) surfaces followed by washing	Standard microarray technique with fluorescence tagging	Preferential retention of FMOC-tagged L-Lys on (100) face of *d*-quartz after washing	[58]
Silica gel 60 for TLC. Merck.	*S*-(+)-Ibuprofen, *S*-(+)-Naproxen	20 cmx20 cm glass plates covered with silica gel. 10 μL of each solute applied to plates at 2 cm intervals.	Elution of solutes with ACN-MeOH-H_2O. CD of silica gel.	Both *S*-(+)-Ibuprofen and *S*-(+)-Naproxen deviated from the vertical of the migration tracks after elution with mobile phase, suggesting asymmetry of microcrystalline silica gel possibly containing *l*- and *d*-quartz	[59]

Mineral	Amino Acid enantiomers	Exp Conditions	Measuring method	Observed Selectivity	Reference
				particles at a ratio different from 1.	
Serpentines	Racemic Ala,Val,Leu,Ile,Pro, Ser, Phe, Asp, Glu	C_0=0.005 M. Room temperature. S/L= 0.286 g/mL.	Depletion. Analysis of supernatant by HPLC with CD detection.	L-Asp, L-Glu, and L-Phe adsorbed more than D-Asp, D-Glu, and D-Phe.	[60]
Zeolites	L-, D-Hist	C_0=0.008 M. Room temperature. pH=7.	Isothermal titration calorimetry	Selectivity depended on type of zeolite	[61]

SSA: specific surface area.

In agreement with the previous discussion, chiral recognition appears to depend on a three-point interaction. This interaction can be visualized as a lock and key association which is common in enzymatic systems where the biological active ligand binds to a receptor in the membrane cell (Figure 1.15a). Unequal diastereomeric interactions of enantiomers of a ligand with a receptor are depicted in Figure 1.15b, showing that one of the enantiomers interacts with the receptor via three points[62, 63] and therefore binds preferentially.

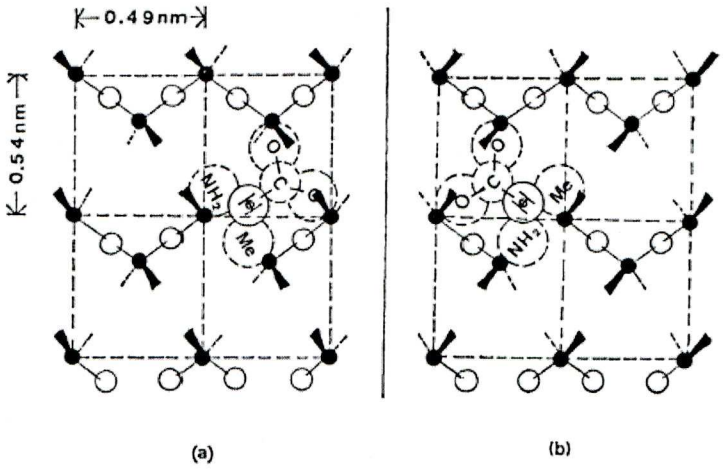

Figure 1.14. L-Ala adsorbed on the $(10\bar{1}0)$ plane of (a) *l*- and (b) *d*-quartz. •:silicon atom, ○: frame oxygen atom, ▬:surface hydroxyl group[19]

Selective influences of enantiomorphic quartz surfaces in other biological and chemical processes have also been documented. For instance, the chirality of quartz was found to influence the incidence of carcinogenic tumours in mice[64]. Thus, mice inoculated with powdered *l*-quartz had a higher number of tumours in comparison to their counterparts treated with *d*-quartz. The clearest example of the enantioselective potential of quartz, however, was reported by Soai *et al.* in their work on the asymmetric autocatalytic synthesis of pyrimidyl alkanol in the presence of diisopropyl zinc and handed quartz as the chiral initiator[65]. Initial low enantiomeric excesses of the alkanol were amplified to near enantiopure by a few catalytic steps.

Another example of enantioselective behaviour of quartz is the recent molecular modelling investigation of carminic acid (CA; a chiral dye) adsorption on the hydroxylated $(10\bar{1}0)$ planes of *l*- and *d*- quartz. In this study, the energies of adsorption of CA on the mirror image planes were found to differ by 5 kJ/mol with the *l*-quartz-CA system being more stable[57].

a

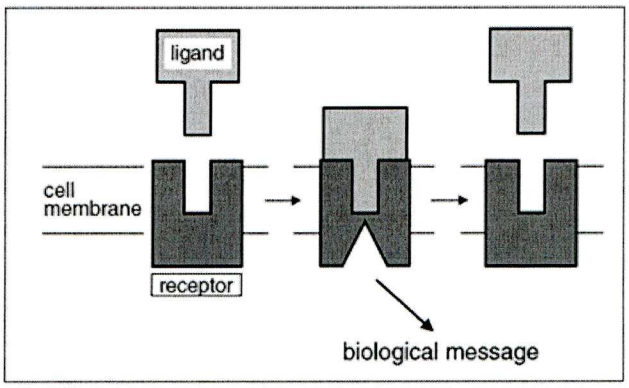

b

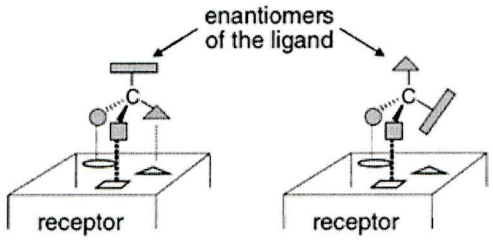

Figure 1.15. Illustration of a. ligand and receptor interaction in biological systems; and b. unequal interactions of enantiomers of a ligand with a receptor, showing three-point and two-point contacts as indicated by the dotted lines[62]

Note that technological advances have made it possible to observe the interactions of chiral molecules at mineral surfaces at the molecular level. For example, the use of a microarray technique with fluorescence tagging allowed the observation that FMOC-L-Lys sticks preferentially on *d*-quartz surfaces[58]. In conclusion, the existent literature reveals that quartz induces enantioselective processes at its surfaces although in some cases the observed enantiomeric excesses or interactions have been quite moderate and sometimes irreproducible [57].

Clays have also been extensively studied with regard to their enantioselective potential. Early studies showed that asymmetric adsorption of AAs on kaolinite took place [11, 51, 52], but later investigations found no selective behaviour at all[53, 66]. Selective interactions of Asp and Glu with Na-montmorillonite were reported by Siffert and Naidja[55]. Deamination of Glu and Asp acid enantiomers took place under the experimental conditions of this study. Moreover, L-Asp and L-Glu were preferentially transformed with respect to D-Asp and D-Glu, but the bulk adsorption results of the individual enantiomers showed that D-Glu adsorbed selectively on the clay. Stereoselective kinetic effects in the interaction of L-His and D-His with a

hydrotalcite have also been documented, with L-His exchanged preferentially for the Cl^- present in the interlayer[67].

A comprehensive analytical study on the adsorption of racemic mixtures of α-AAs Val, Ala, aminoisobutyric acid (ABA), and norvaline onto Na-montmorillonite at pH values of 3, 7, and 10 was conducted by Friebele *et al.*[42]. Gas and liquid chromatography were used to determine the concentrations of the AAs remaining in the supernatant (non-adsorbed fraction) after a 24-h adsorption period. In addition, the authors determined the amount of AAs strongly and weakly adsorbed onto the clay by extracting the mineral with HCl. They concluded that their direct method gives a better picture of the ratio of AAs enantiomers adsorbed onto the clay, since the recovery of the AAs was nearly 100%. Thus, bacterial contamination was ruled out. Their results showed that gross AA adsorption is pH dependent, with more AA adsorbed at acidic pH values. When using gas chromatography, selective adsorption of Val and norvaline onto the clay was observed at pH 3 and 7, whereas ABA was selectively adsorbed only at pH 10. On the contrary, only one instance of selective behaviour was observed by liquid chromatography for the adsorption of Ala on montmorillonite at pH 10[42]. These results can be interpreted in view of the precision of the methods used to quantify the enantiomers. Analysis of AA enantiomers by GC is reported to have an analytical error of the order of 0.01 to 0.8% while LC analyses have higher uncertainties of up to 5%. The inconsistencies in the results of selectivity given by the two chromatographic techniques led Friebele *et al.* to conclude that there is no significant selective adsorption of AA enantiomers on Na-montmorillonite[42]. Although rigorous, their study did not include other pairs of AA enantiomers such as the basic AAs Arg, Lys, and His, which have a greater affinity for the clay owing to the presence of nitrogenated groups in their side chains, and the hydrophilic AA serine.

Finally, molecular modelling of the interaction of D- and L-Ala dipeptides with a 2:1 nontronite clay has provided insight into the importance of the orientation of the molecules in the interlayer space[68]. The simulation found that the L-Ala dipeptide was orientated with the C(α)-C(β) bond directed away from one of the mineral basal planes toward the dioctahedral other cavity whereas the side group of D-Ala dipeptide was parallel to the mineral basal plane of the interlayer. This was interpreted in terms of the packing of the Ala dipeptides, with the L-Ala dipeptides being less sterically hindered and therefore more likely to undergo polymerization.

Other aluminosilicate materials that have been overlooked regarding their enantioselective potential are zeolites and serpentines. Recently, Dryzum *et al.* reported that chiral silicate zeolites exists in nature and more importantly that they were enantioselective in adsorbing L- and D-Hist enantiomers as determined from adsorption calorimetric studies [61]. For example, goosecreekite (GOO) $|Ca^{2+}_2 (H_2O)_{10}|$ $[Al_4Si_{12}O_{32}]$ adsorbed D-Hist preferentially over L-Hist with a high enthalpic enantioselectivity factor of ~7. Chrysotile and lizardite which belong to the serpentine group ($Mg_3Si_2O_5(OH)_4$) have a crystal structure similar to that of kaolinite ($Al_2Si_2O_5(OH)_4$). Hashizume treated these serpentines with acid to test the hypothesis that pits on the surface could be enantioselective and found a tendency for L-Asp and L-Glu to stick preferentially to acid-treated chrysotile[60].

All of the above findings point to the fact that clay-AA interactions can be complex since chemical reactions can take place and kinetic effects can be operating such as in the case of Asp, Glu, and His. Obviously the handling of the clays and whether they are synthetic or natural can introduce further complexity. As suggested by Theng[69], natural clays might possess chirality imprinted by bacteria or biofilms which could result in artifacts rather than in true selective adsorption.

Evidently, there are many variables that can be considered when studying the adsorption of AA enantiomers onto enantiomorphic mineral substrates in aqueous systems. Hence, the objectives pertinent to this part of this investigation were to study the adsorption of racemic mixtures of AAs onto:

- Powdered synthetic and natural sand quartz possessing a mix of crystallographic planes
- Single quartz crystals (i.e. synthetic quartz wafers and natural quartz) that expose well-defined crystallographic faces
- Commercial kaolinite and two types of montmorillonite (i.e. montmorillonite K10 and montmorillonite KSF) of different acidity
- Natural single crystals of pyrite and gypsum
- Natural sediments

The effect of pH and ionic strength (I) on a potential selective adsorption of chiral AAs on the minerals was also considered. This selectivity was evaluated by calculation of *ER* ratios and enantiomeric excesses (*ee*). These experiments were designed to get insight into the possible influence of chirality, impurities,

imperfections, and surface area of the minerals as well as multicomponent AA systems on any selective process. In addition, the optimum choice of the AAs to interact at a given mineral surface was undertaken based on the existent literature and preliminary experiments. Finally, to eliminate artifacts arising from bacterial contamination or dust, minerals were cleaned scrupulously by heat treatment where possible, except for the natural quartz crystals that shatter due the presence of fluid inclusions. Otherwise, removal of impurities was achieved by solvent extraction with ultrasonication or with a Soxhlet apparatus. Mass balances were carried out in some clay-AA systems to provide evidence of the validity of the data.

1.6. Separation of Chiral AAs by Chromatography

Separation and quantification of AA enantiomers is relevant for many disciplines. These include geochronological dating based on racemisation of amino acids, bioavailability and distribution in soil/water/air compartments and the purification of AA enantiomers used as drug precursors in the pharmaceutical industry. The methods for quantifying free and hydrolysable AAs in different matrices fall in two categories (1) indirect methods such as derivatization of AAs into fluorescent diasteromeric isoindole derivatives with the *ortho*-phthaldialdehyde/*N*-isobutyryl L-cysteine (OPA/IBLC) reagent and separation on a achiral column by reversed phase high-performance liquid chromatography (HPLC)[70, 71], and (2) direct methods involving the separation of AA enantiomers on a capillary column coated with a chiral stationary phase by gas chromatography (GC) [72].

A reaction scheme for the derivatization with OPA/IBLC is shown in Figure 1.16, where the amino group is the target moiety reacting with both OPA and IBLC to give two diastereomers, which have different physical properties and can thus be separated on a reversed-phase column.

The direct GC method relies on the selective interaction of one of the two enantiomers with the chiral phase due to differences in the energies of adsorption. Chirasil L-val capillary columns have been widely used for the resolution of AA enantiomers in complex matrices by gas chromatography [73-75]. Sample preparation for separation requires derivatization of the amino acids into volatile isopropyl esters with N-trifluoroacetic acid (N-TFA) and N-pentafluoropropionic acid (N-PFPA) in the presence of acetyl chloride. This is described in the experimental section (see Section 3.1).

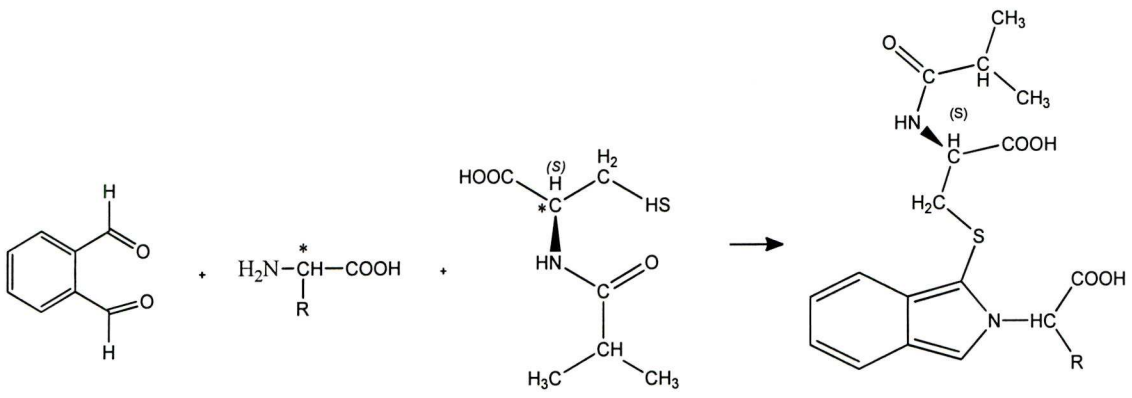

* Chiral centre

Figure 1.16. Derivatization of amino acids with OPA/IBLC

HPLC with chiral derivatization allows quantification of free AAs in the picomolar range when fluorescence detection is used, that is why it was used in this study to determine the enantiomeric distribution of AAs in supernatants and mineral extracts. The selectivity experiments conducted in this research aim to evaluate the adsorption of racemic mixtures of AAs on minerals by using HPLC-with OPA/IBLC derivatization because this technique is very robust and can resolve the 20 protein enantiomeric AAs in a single analysis. Chiral GC coupled with FID is characterized by higher detection limits, but a method was adapted from the literature as an alternative to HPLC for the determination of AAs enantiomers in our matrices and for comparison purposes.

1.7. Polymerization of AAs on Clays

Minerals can catalyze the formation of peptides in aqueous solution[31, 33, 76-81]. This is relevant for origins of life studies since peptides are the building blocks of proteins and minerals such as clays and silica were abundant in prebiotic times. Most published work has addressed the oligomerization reactions of glycine and alanine on silica, alumina, and 2:1 aluminosilicate clays, e.g. montmorillonite and hectorite, under fluctuating drying and wetting cycles which simulate episodes of evaporation from lagoons followed by rainfall or tidal events. Transition metal cations such as copper (Cu^{2+}) are widely present in Earth's aquatic systems. Thus, ion exchange reactions of Cu^{2+} with clays are likely to occur in natural environments. These Cu-exchanged clays have been reported to increase dipeptide yields in comparison to the alkaline earth-exchanged ones such as Na-clays[79]. Val, a chiral AA with a bulky

isopropyl side-chain, has been studied in the context of prebiotic reactions described above[77]. However, so far there is no evidence of divaline formation catalyzed by clays. Instead, Val has been dimerized in low yields in the salt-induced-peptide formation (SIPF) reaction which is hypothesized to occur via complexation of copper and chloride ions with the monomeric AAs[82]. The low reactivity of Val in the SIPF has been attributed to the steric hindrance posed by the hydrophobic side chain which in turns affects its electrophilicity in the highly polar aqueous media[83].

Complexation of AAs with Cu^{2+} in the interlamellar regions of ion-exchanged clays might activate peptide synthesis. Nevertheless, Collins *et al.*[84] and Rode [85] proposed that any peptide synthesis on clays is restricted to the clay edges where AA condensation can occur via anhydride formation with the participation $Si(OH)_4$ and $Al(OH)_4^-$ moieties under fluctuating dry and wet conditions. In this model, activation of the AA is hypothesized to occur when the anhydride forms (see Equation 1.9) rendering the carbonyl carbon more electrophilic and prone to nucleophilic attack by a neighbouring electron-rich amine group as depicted in Figure 1.17[84].

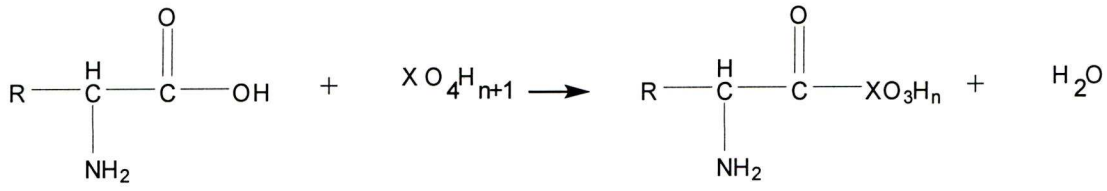

Equation 1.9

where X represents Si or Al.

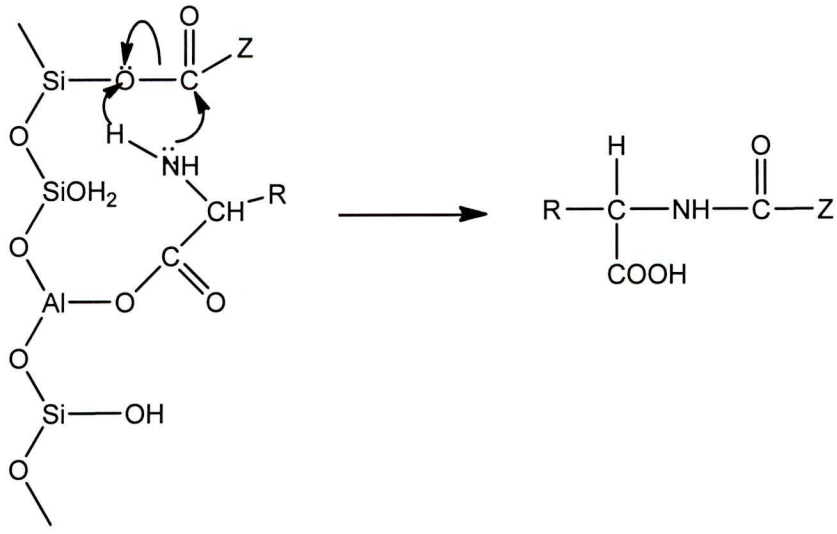

Figure 1.17. Collins' model for polypeptide formation on clay edges possessing tetrahedral Si and Al sites [84]. Z represents the α-carbon to which H, NH_2, and the side chain are attached to

Although the previous model seems very plausible, the surface chemistry of montmorillonite edges was shown to be unchanged by cation-exchange reactions[86]. In fact, the density of silanol and aluminol sites in Ca-, Cu-, Zn-montmorillonite was 2.72×10^{-4} and 2.32×10^{-4} mol/g, respectively as determined by potentiometric titration and a surface complexation model. The density of the same groups on the edges of H-montmorillonite was 2.72×10^{-5} and 2.32×10^{-5} mol/g, respectively. Therefore on a surface area basis, the number of edge sites is the same on the different montmorillonites considering that the ratio of surface areas of the divalent-cation exchanged montmorillonites and H-montmorillonite is about 10. The cation exchange capacity of all of the above clays owing to the layer charges (interlamellar region) is one order of magnitude higher than the density of silanol and aluminol at the edges. This suggests that the interlamellar zone of the clay might play a role in condensation of AAs as supported by the higher polimerization yields due to the presence of transition metal cations, in particular Ni^{2+} and Cu^{2+}. Defects such as cracks and steps on the surface of metal- exchanged clays have been also hypothesized to promote peptide formation because AAs can be concentrated at such defects where metals, otherwise inaccessible, are exposed at the surface [34, 76, 87].

Finally, Lambert has recently reviewed the adsorption and polymerization of AAs on mineral surfaces[41]. His review discusses the fundamentals of AA interaction and mechanism of peptide formation at mineral surfaces. Clearly, there are many gaps in knowledge in these systems. For example, is peptide formation on mineral surfaces chirally selective? What is the influence of solution variables (i.e. pH, ionic strength) and UV radiation on peptide yields? What is the effect of multicomponent mixtures of AAs on the adsorption of a given AA? Some of these questions will be addressed in this research. In particular, the influence of ionic strength and chirality of Val on the polymerization reaction of the monomers catalysed by montmorillonite K10, an acidic catalyst, under fluctuating wet and dry cycles will be examined.

1.8. Adsorption of AAs on Single Crystals in Ultra High Vacuum (UHV)

In order to understand how molecules bond and orientate on single crystals of metals such as Cu and Ni, UHV at pressures of 10^{-10} mbar and below are required[88]. This low pressure serves the purpose of creating a defined gas-solid system so that only interactions of the adsorbate and adsorbent are investigated, eliminating possible

interferences of other molecules such as oxygen. For example, it takes about 8 hours to adsorb a monolayer of oxygen on a clean surface in a vacuum system operated at 10^{-10} mbar and 300K, thus allowing for an adsorption experiment of a target molecule at a clean surface to be conducted[25]. In addition, many surface characterization techniques involving interaction of electrons with a material operate under vacuum conditions so that the trajectories of these particles remain undisturbed.

Typically, well-defined crystallographic planes of a single crystal of a face centre cubic metal (fcc) such as Cu can be cut with high-precision using the X-ray back-scattering technique. These single crystal surfaces may be either atomically flat (consisting solely of large terraces) or vicinal (consisting of short atomically flat terraces separated by atomic steps)[25]. The crystallographic (110) plane of fcc metals is illustrated in Figure 1.18. The Miller index, represented by the integer values in parentheses, is used to denote a given plane of a crystal. A fcc(110) plane intercepts the Cartesian axes in the x and y directions in multiples of the unit cell dimension a. Note that the intercept of the plane with the z-axis is at infinity since the plane runs parallel to it. Thus, for a (110) plane, the intercepts, in multiples of the unit cell dimension, are 1, 1 and ∞ with x,y, and z. The reciprocal values of the intercepts define the Miller index (110).

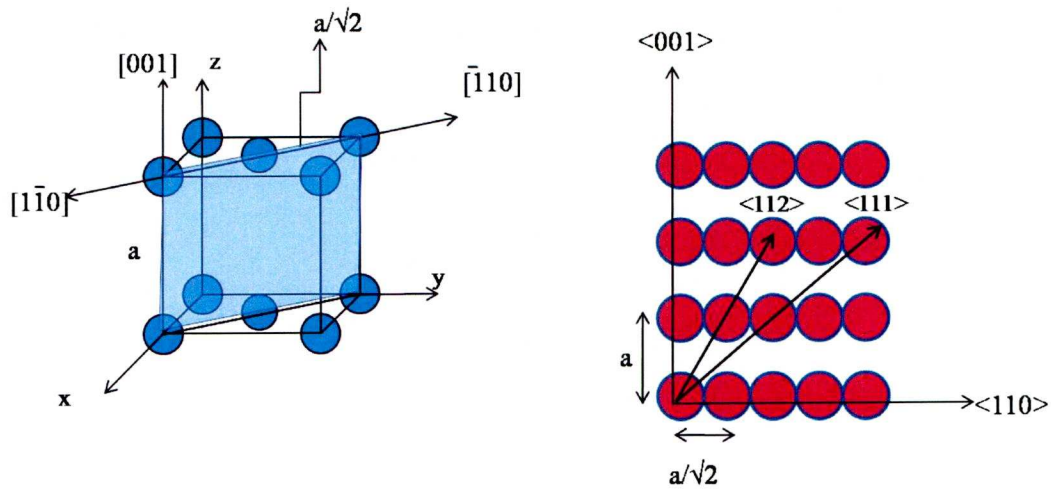

Figure 1.18. (110) plane of fcc crystals. Square brackets [] represent crystallographic directions. < > brackets mean set of directions, which are equivalent in a cubic system. e.g. <001> represents a family of directions such as the [001, [100], [010], [00$\bar{1}$], [$\bar{1}$ 00], [0$\bar{1}$ 0]. For simplicity, atoms in the centre of the cube faces have been left out unless contained within the cut plane

Understanding how biomolecules interact with metallic surfaces is relevant in enantioselective catalysis, corrosion control, origins of life, and biocompatibility of metal implants. Barlow and Raval[89] have shown that the adsorption of chiral AAs on Cu(110) bestows chirality to the otherwise achiral metallic surface due the supramolecular assembly of AAs in well-defined chiral domains which can be mirror images of another depending on the chirality of the adsorbed AA. To illustrate this, Figure 1.19 displays the low energy electron diffraction (LEED) and scanning tunnelling microscopy (STM) images of *R*- and *S*-Ala on Cu(110) at annealing temperatures of about 400K[90]. This figure shows that Ala enantiomers self-assemble into chiral overlayers that are made up of unit cells consisting of 8 or 6 molecules (hexamer vs. octamer clusters) as indicated in Figure 1.19 b and c. The use of multiple techniques such as reflection-absorption infrared spectroscopy (RAIRS), LEED, and STM as well as molecular modelling has allowed a better understanding of how the molecules bond, orientate, and assemble at metallic surfaces. In the case of Ala, different phases have been observed depending on coverage (θ) and temperature (Figure 1.20a), resulting in a highly complex polymorphic system. Moreover, the orientation of Ala on Cu(110) as a function of coverage has been worked out based on interpretation of infrared spectra. For example, the μ_3 species shown in Figure 1.20a binds to the surface via its carboxylate and amino groups. Thus the carboxylic group of neutral Ala is deprotonated upon adsorption onto adjacent copper atoms in the <110> direction whereas the electron pair of the NH_2 moiety interacts with a copper atom located in the <001> direction to give a triangular chiral footprint (Figure 1.20b) where the molecule essentially lies nearly flat on the surface. It is been suggested that the nanochannels generated by the supramolecular assembly of these chiral AAs on metallic surfaces may be suited for enantioselective processes and hence the interest in pursuing adsorption of biomolecules of different characteristics (size, polarity) on metal substrates as summarized by Barlow and Raval [89].

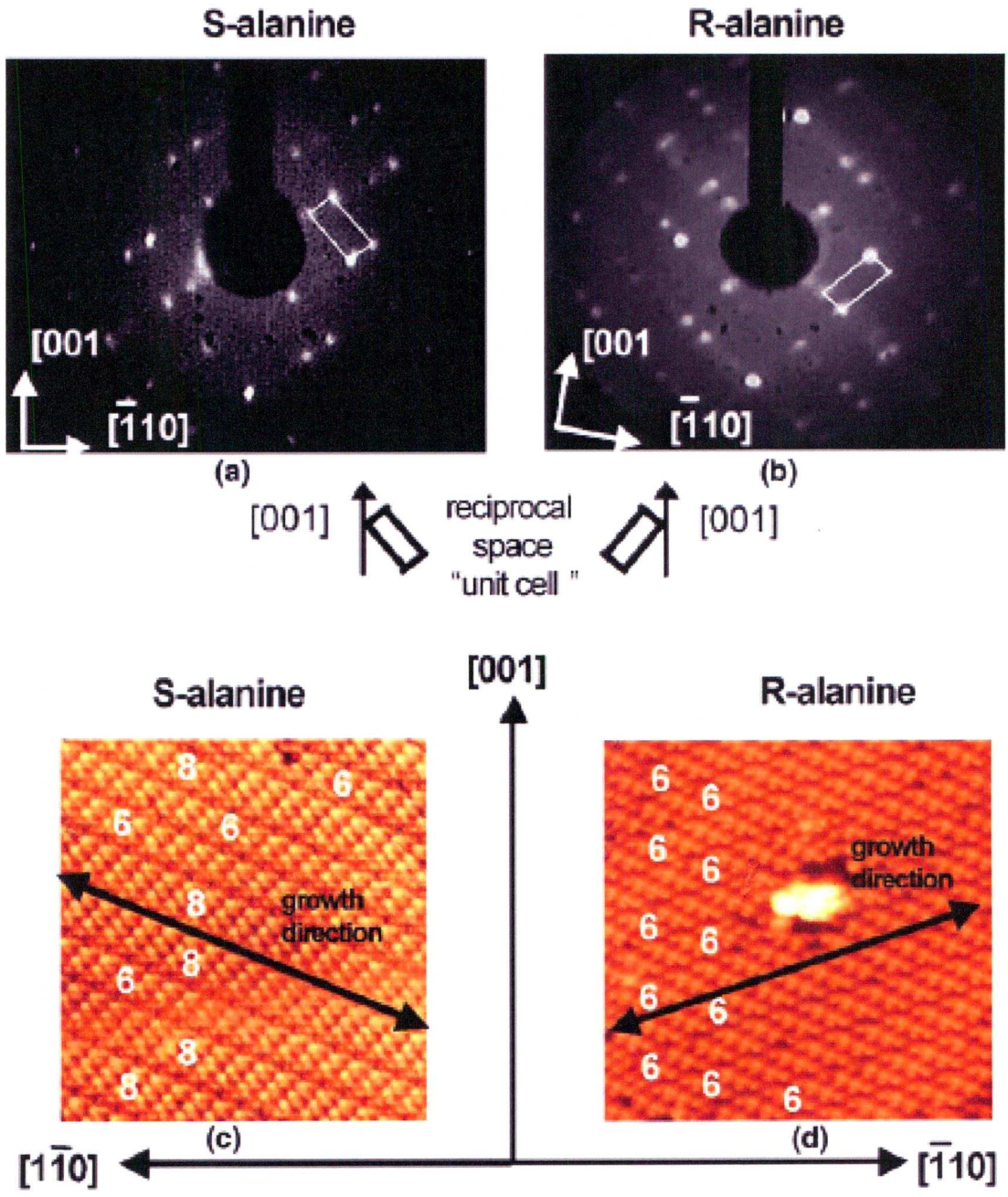

Figure 1.19. LEED patterns and STM images of the chiral phase III of the *S*- and *R*-Alaninate. a. *S*-Alaninate LEED (LEED energy=52 eV, annealing temperature 395 K); b. *R*-Alaninate LEED (LEED energy=54 eV, annealing temperature 423 K); c. *S*-Alaninate STM (165 ×160 , V_t=-2.08 V, I_t= 1.97 nA, annealing temperature 403K); d. *R*-Alaninate STM (165 × 160 , V_t=-2.08 V, I_t= 1.04 nA, annealing temperature 413K). Rows of hexamer and octamer clusters are marked with 6 or 8, repectively[90]

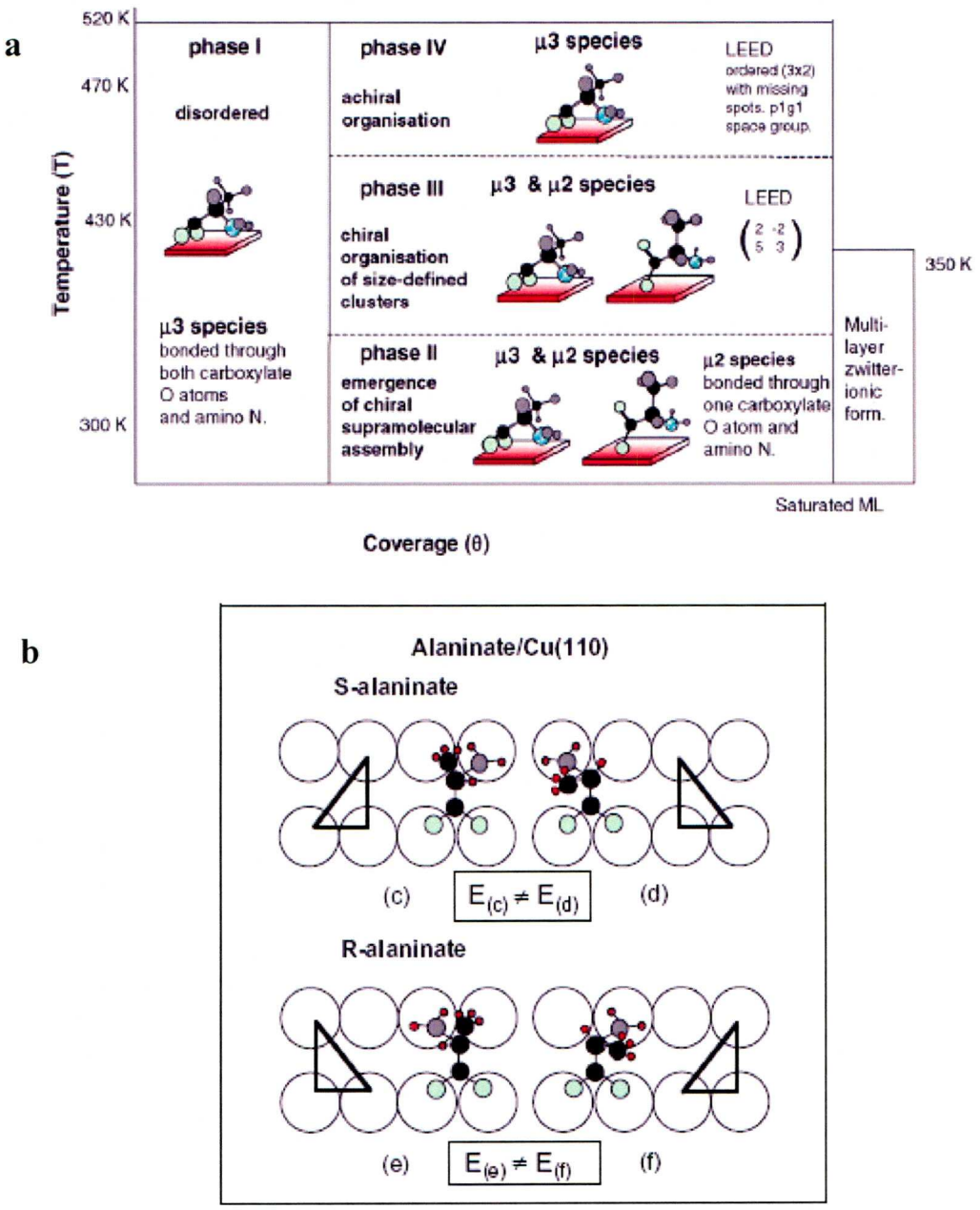

Figure 1.20. (a). *S*-Alaninate/Cu(110) adsorption phase diagram showing four different phases of alaninate as a function of coverage in the temperature range of 300-520K ; (b). Adsorption footprint of the *S*- and *R*-Alaninate on Cu(110). DFT calculations showed that the energetically equivalent and preferred footprints are for (d) *S*-Alaninate and (f) *R*-Alaninate, respectively[90, 91]

The specific objective of the surface science part of the work was to study the adsorption of Val, an isopropyl substituted AA, on Cu(110) under UHV conditions by a multi-technique approach with the final aim of proposing a structural model for the adlayer. We chose Val as a model molecule because it has a branched side chain as opposed to Ala and norvaline, which have been investigated already and have linear side chains in the homologous aliphatic series. Val exists in the gas phase mainly as

the conformer illustrated in Figure 1.21, because of hydrogen bonding between the hydrogens of the amino group and the carbonyl oxygen. Adsorption of *S*-Val and *R*-penicillamine, a Val derivative, onto metallic surfaces has been examined by in-situ electrochemical STM and attenuated total reflection infrared spectroscopy (ATR) in solvent systems[92, 93]. Both of these molecules interact with the surface via the carboxylate and amine functionalities. From the origins of life perspective, this type of investigation is important since it provides a mechanistic understanding of the interaction of AA at solid surfaces in a system resembling outer space (i.e. interstellar medium), which many believe was involved in enantioselective processes leading to the handedness of life on Earth. Other important applications of studying the interaction of AAs on metallic surfaces are in the fields of corrosion, chiral sensors, and biocompatibility of metallic implants. In order to keep consistency with the literature in the surface science field, the '*RS* system' will be used to refer to Val enantiomers when discussing their adsorption on Cu(110) (see Glossary).

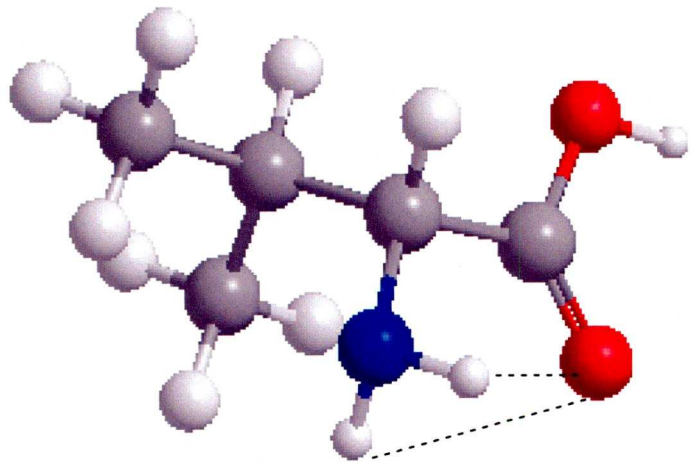

Figure 1.21. Most stable Val conformer in the gas phase. Dotted lines indicate hydrogen bonds[94]

1.8. Surface Science Techniques to Study Surface Chirality

As highlighted in the previous section, two-dimensional chirality at surfaces can be investigated by a combination of surface-sensitive techniques. The fundamentals of RAIRS, LEED, and STM are presented Appendix 1, indicating what a typical experiment involves and the information to be obtained. The theory pertinent to these surface science techniques largely derives from textbooks and lectures on surface analysis[25, 88, 95].

1.9. Objectives of the Study

Some of the research needs concerning studies of chiral molecules at mineral surfaces were mentioned in the previous sections. The main objectives of this investigation were:

1. To understand the influence of environmental variables (i.e., pH and ionic strength) on the adsorption of AA enantiomers onto powdered and crystalline mineral surfaces from multicomponent and single component systems, looking at any potential selective adsorption of one AA enantiomer over the other.

2. To evaluate the role of surface crystallinity and purity of minerals on the adsorption of AAs on single crystal faces of minerals and polycrystalline materials.

3. To investigate the possibility of peptide formation on mineral surfaces subjected to fluctuating environmental conditions (i.e. wet-dry cycles).

4. To investigate the self-assembly of Val enantiomers onto Cu(110) in ultrahigh-vacuum by using RAIRS, LEED, and STM.

Chapter 2 presents a statistical review of the distribution of quartz enantiomorphs on Earth. This topic although not experimental was addressed because of the relevance of quartz as an intrinsically asymmetric material. Chapter 3 presents the experimental methods used in this research. Chapter 4 is a comprehensive chapter that presents the results and discussion of all the questions addressed in this research. Finally Chapter 5 compiles the main conclusions of the work and outlines recommendations for future work.

CHAPTER 2 STATISTICAL REVIEW ON THE RACEMIC DISTRIBUTION OF QUARTZ ENANTIOMORPHS

(Paper submitted to American Mineralogist, May 2009)

There has been conflicting evidence about the global distribution of quartz enantiomorphs on Earth. On a global scale, *l*- and *d*-quartz are presumably equally abundant or racemic. Local deviations from the racemic state at certain locations may occur so that either *l*- or *d*-quartz may predominate. Thus the hypothesis that the homochirality of life may have come about through interactions with a dominant quartz enantiomorph at a particular location has been proposed[18]. This short section reviews the problem of the distribution of quartz (racemic vs. nonracemic) by subjecting published data on number of crystals at different places on Earth to a comprehensive statistical analysis.

As mentioned in the introductory chapter, quartz (SiO_2), the most abundant silica mineral on the surface of Earth, is an enantiomorphic mineral because it can exist as *l*- and *d*-quartz single crystals and fibers. Origins of life hypotheses have sometimes invoked quartz as a plausible prebiotic inorganic substrate which might have initiated the homochirality of life, by either breaking the symmetry of the initial racemic organic biomolecules or by amplifying small enantiomeric excesses. There have been numerous reports on the symmetry breaking properties of enantiomorphic quartz in catalytic syntheses of enantioenriched organic mixtures as well as in the enantioselective separation of amino acid enantiomers [18, 19, 43, 45, 47, 48, 58, 65, 96, 97]. Therefore, the debate centres on whether quartz enantiomorphs are equally abundant on the surface of the Earth. This has particular significance because an imbalance in their abundance might imply a possible symmetry breaking mechanism.

Early studies on the distribution of quartz suggested an equal proportion of *l*- and *d*-quartz [98]. Palache, on the contrary, reported an *l*-quartz percentage of 50.5 % in a total of 16807 samples[99]. More recently Evgenii and Wolfram summarized and analysed data on quartz distribution based on a wide range of results from different sources[98]. They concluded that *l*-quartz and *d*-quartz are equally abundant as inferred from the ratio of excess enantiomorphic quartz (%*d* - %*l*, or %*l*- %*d*) to the total number of samples in each data set. This ratio tended to zero for the two data sets

analysed, one where *l*-quartz was in excess of *d*-quartz and vice versa. Many authors have pointed out that excesses of either quartz enantiomorph in a given location are most likely due to seeding effects [98].

However there appear to be some inaccuracies in the paper by the previous authors in that they reported the unweighted rather than the weighted averages of the sample sets they examined. The weighted averages were calculated taking into account the total number of *l*- and *d*-quartz in each dataset. We have recalculated the data and find that the weighted average percentages are 51.06% *l*-quartz and 50.4% *d*-quartz, respectively, for the *l*-quartz and *d*-quartz dominated data sets reported in Table 2.1. The question then arises: is the *d*/*l* value statistically different from 1?

Table 2.2 presents detailed data on the distribution of *l*- and *d*-quartz in Samshvildo, Georgia of the former USSR [100]. This dataset correspond to 40 subsets, each one composed of 100 crystals, to give a total of 4000 crystals (Table 2.1, entry 9). Statistical analysis of the data shows that they follow a normal distribution as supported by the histogram, boxplot of the quartiles, and the normality plot (Figure 2.1). The mean percentage of *l*-quartz is 50.88 ± 1.42 at the 95% confidence interval, suggesting an equal distribution of *l*- and *d*-quartz at this particular location. We have further examined these data using the 'coin-flipping' procedure described below and the probability data provides some indication of the variability of enantiomorph ratios in small data sets which leads us to emphasise the importance of collecting statistically robust numbers of observations for the purposes of determining enantiomorph excesses.

Tables 2.1 summarises the % of *l*-quartz in locations around the globe. This Table shows that that there is considerable geographical variation in the relative abundance of the two quartz enantiomorphs. For example samples originating from Greece display the greatest reported percentages of % *l*-quartz, 58.6% and 60.6% respectively (entries 13 and 14 in Table 2.1).

Two hypotheses can be constructed from these data (1) *that the global abundance of d- and l-quartz is indistinguishable from a 50:50 ratio* and (2) *that local variations from a 50:50 ratio are significant.* We test these hypotheses in the treatment below

Hypothesis (1)

A common way of evaluating the significance of differences between data sets is the Student's *t*-test. However in this case the data sets making up the total

information available to us are of very different size and it is therefore necessary to take proper account of this factor when evaluating the data. The easiest way to do this is simply weight the data by the number of crystals.

Table 2.1. Distribution of *d*- and *l*-quartz crystals in different locations on Earth

Entry	Region, localities of quartz (authors)	Number of Crystals examined in given location	% *l*- quartz in given location	% difference between *l*- and *d*- quartz	No. of *l*-quartz crystals
	l- quartz dominated samples				
1	Brazil, Tromsdorff, 1932[a]	4442	50.05	0.1	2223
2	Dauphine quartz, Alaska, Gault[a]	383	50.1	0.2	192
3	Switzerland, Friedländer, 1951[a]	1811	50.6	1.2	916
4	Russia, Lemmlein, Vistelius[b,c]	6404	50.61	1.22	3241
5	Brazil, Colombia, Hurlbut, 1946[a]	2415	50.68	1.36	1224
6	Dauphine quartz, Austria, 1951[a]	840	50.7	1.4	426
7	Alaska, Gault, 1949[a]	298	50.7	1.4	151
8	Volyn, Ukraine[b]	122	50.8	1.6	62
9	Samshvildo, Georgia, USSR[b,c]	4000	50.87	1.74	2035
10	Austria, Brandenstein, 1951[a]	214	52.3	4.6	112
11	Samples examined by Muegge, 1892[b]	137	52.6	4.66	72
12	Neroika, Russia[c]	204	53.9	7.8	110
13	Plakas, Greece[c]	568	58.6	17.2	333
14	Plakas,Greece, Kokkoroes, 1935[b,c]	549	60.6	21.2	333
	d- quartz dominated samples				
15	Hurlbut[d]	3100	49.99	-0.02	1550
16	Frondel, 1978[d]	23652	49.82	-0.36	11783
17	Suraiz, Ural, Russia[b]	627	49.8	-0.4	312
18	Bussiere, 1971[d]	301	49.5	-1	149
19	Parnuk, Ural, Russia[b]	1518	49.32	-1.36	749
20	Samples from granite rock, Kokkoroes[b]	122	45.1	-9.8	55
21	Samshvildo, Georgia, USSR[b]	300	44	-12	132
22	Lemmlein[b]	400	43	-1.6	172
23	Lemmlein[b]	200	40	-20	80
24	Samples examined by Thompson 1937[b]	37	35.1	-29.8	13
Total		52644			26425

[a] Palache (1962) (cited in [8])

b [101]

c [102]

d [103]

Table 2.2. Number of *l*-quartz crystals in Samshvildo, Georgia, USSR including probabilities of the occurrence of the observed distributions

Number of 100 crystals	1	2	3	4	5	6	7	8	9	10	Σ	p^*
100	56	51	53	55	48	48	56	52	51	51	521	0.01
200	45	54	48	53	49	47	43	51	51	48	489	0.02
300	55	53	60	56	50	49	60	51	52	56	542	0.0007
400	52	49	41	51	53	56	44	47	42	48	483	0.014
Total											2035	

Source: [100]

* p calculated from 'coin-tossing' statistics (see text for method)

Simply multiplying the total number of crystals examined by the reported percentage of *l*-quartz generates non-integer values for the number of *l*-quartz crystals in each data set which is unrealistic, so the weighted products were rounded to the nearest integer value. A histogram and normal quantile plot of this are shown in Figure 2.2. The mean abundance of *l*- quartz in the full data set is straightforward to calculate by simply totalling all of the crystals of each type from all the data sets and taking the percentage. This value is 50.195% which indicates a very slight excess of *l*-quartz. The key question is therefore whether this value is significantly different from 50%. Each data set generates a single value of the *l*-quartz abundance but, because of the different sizes of the data sets account needs to be taken of this factor in generating the summary statistics. This can be done by summing the weighted contribution of each data set to the total variance of the complete crystal assembly. This calculation produces a total variance of 3.38, a weighted standard deviation of the mean of 1.84 and a standard error of 0.38. This is consistent with a global mean value of a 50:50 *l*-:*d*-quartz distribution.

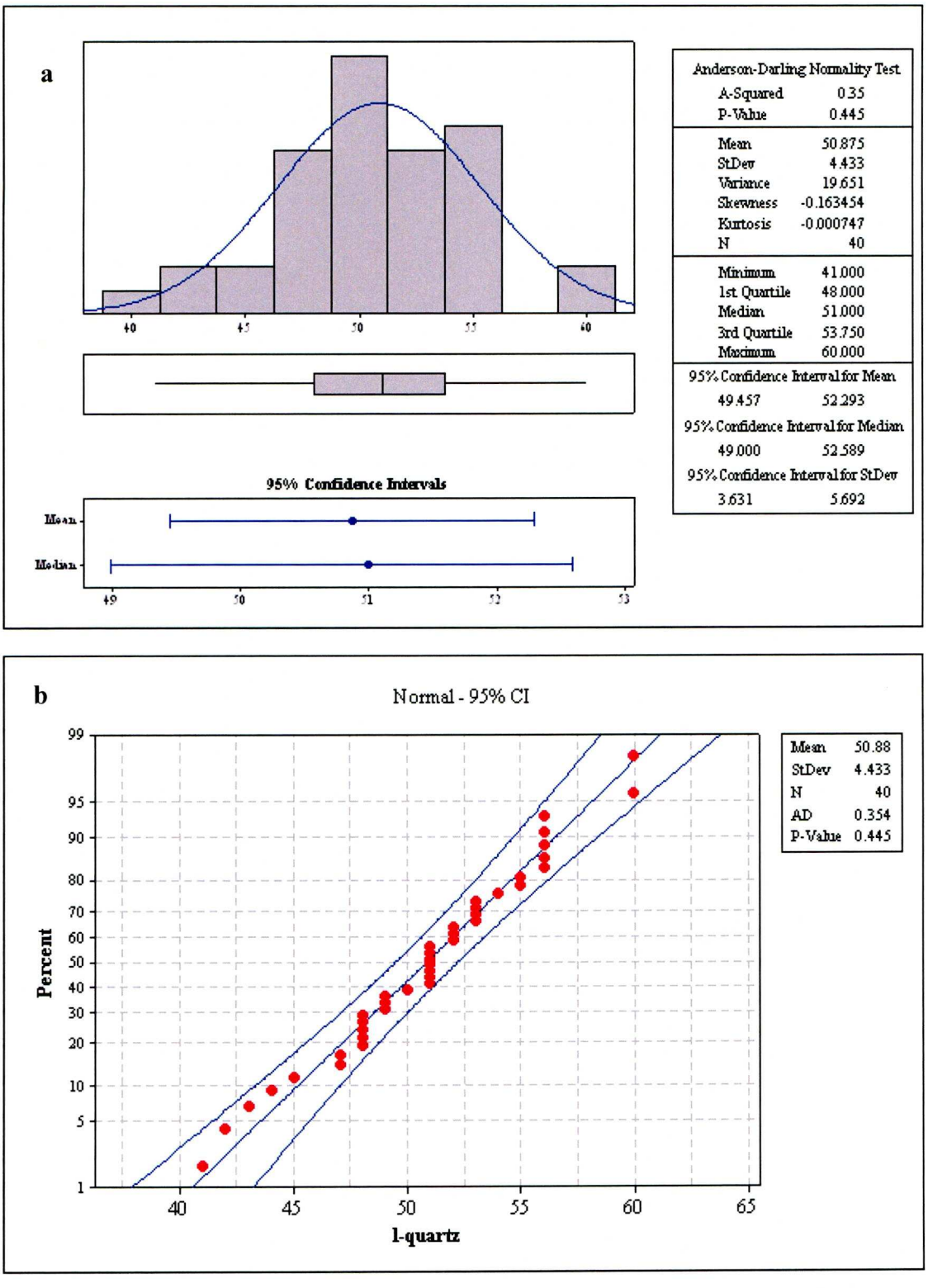

Figure 2.1. a. Statistical summary of the data in Table 2.2 b. Probability normality plot abundance

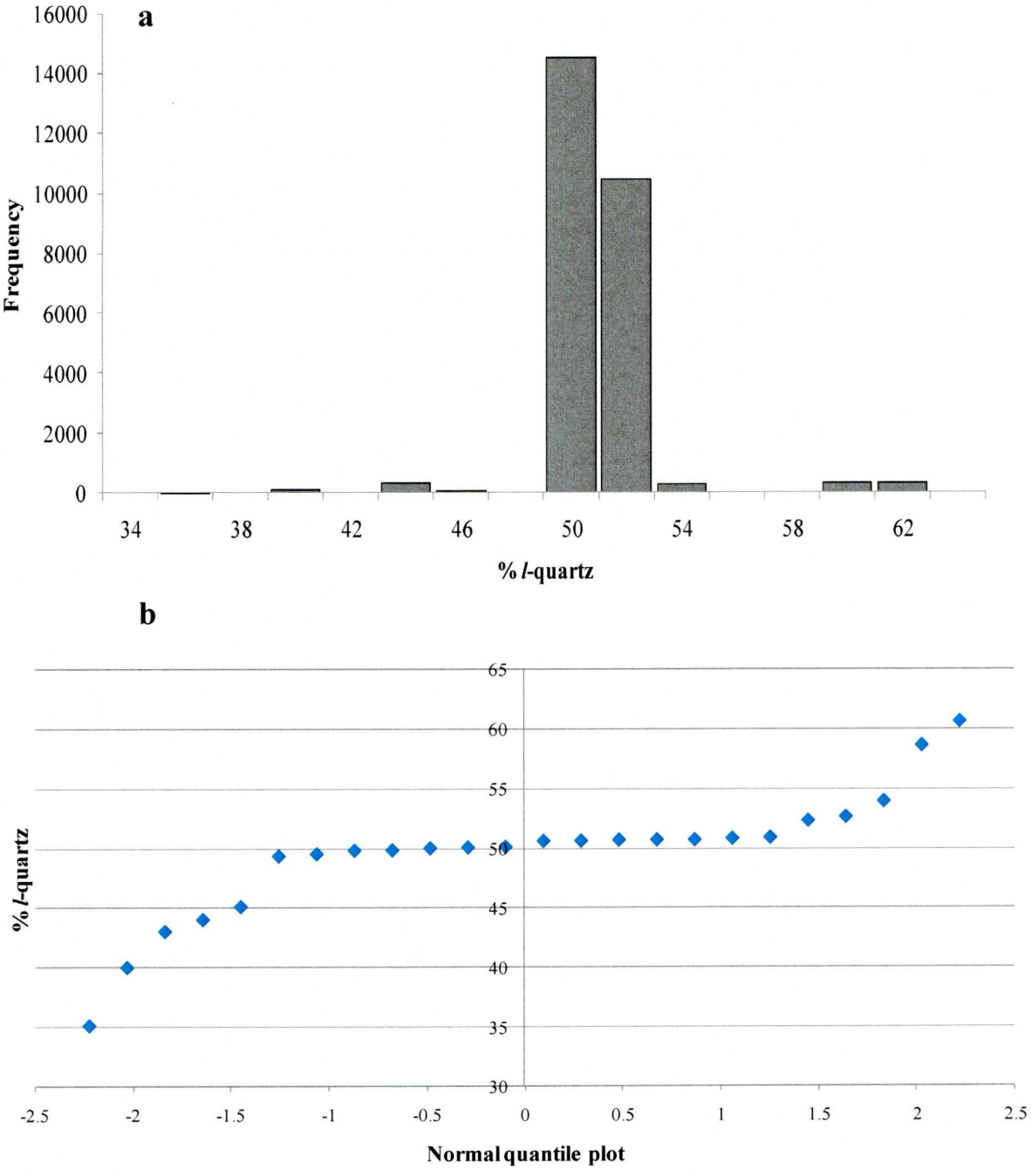

Figure 2.2. A (a) histogram and (b) normal quantile distribution of *l*-quartz abundance (Table 2.1)

Hypothesis (2)

Resolving whether the local deviations from the global distribution are statistically significant is more difficult to test and the authors are indebted to Don Rimstidt for his helpful and perceptive remarks that have helped us to improve the statistical treatment presented in this paper. The suggestion is that the orientation of each crystal be treated as a random event analogous to the flipping of a coin. Analysis of the current problem can then be cast in determining the probability of the observed

distribution. To analyse this it is necessary to assume that there are sufficient 'flips' that the probability distribution approaches the bell curve of a normal distribution[104]. Using this approach the probability of obtaining x (i.e. % *l*-quartz) in n 'coin flips' (i.e. total number of crystals in each data set) is given by

$$\frac{1}{\sigma\sqrt{2\pi}} e^{-\left(\frac{(x-\mu)^2}{2\sigma^2}\right)}$$

Where

$$\sigma = \sqrt{\frac{\mu}{2}} = \sqrt{\frac{n}{4}}$$

σ is the standard deviation of a population, μ is the mean of a population, x the number of *l*-quartz crystals, and n the total number of crystals for each data set. The results of this calculation are shown in Figure 2.3 from which it can be seen that most (16 out of 24) outcomes (including some of the outliers) fall at probabilities of <0.01, 5 fall in the range 0.01-0.001, one result lies between 0.001 and 0.0001 and with the final two results having values of 7.7×10^{-6} and 1.47×10^{-7}.

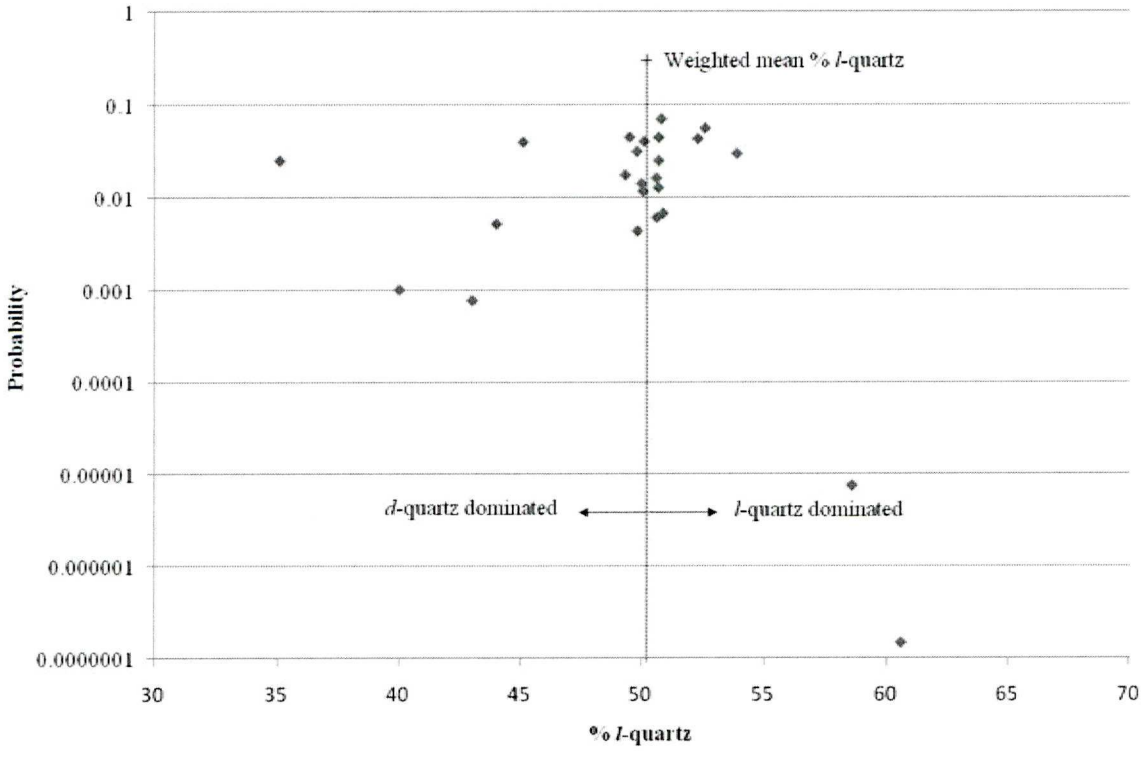

Figure 2.3. The probability of observing the reported *l*- quartz distributions in the 24 data sets calculated on the basis of 'coin-flipping' statistics

Both of these last two values relate to sample collections with a major excess of *l*-quartz (58.6 and 60.6%, respectively: entries 13 and 14 in Table 2.1). Two other outlier sample sets lie at the probability of 0.001 or less. In all 4 cases we feel that the conclusion that local populations of quartz crystals may show significant differences from a 50:50 ratio is valid. The fact that significant deviations occur in both directions i.e. *d*- or *l*-quartz dominance in different locations is interesting as is the fact the most extreme outliers show *l*-quartz dominance. Evidence from the manufacture of synthetic quartz crystals (Janet M. Radwanski, Sawyer Technical Materials, LLC pers. comm.) indicates that *d*-quartz is easier to produce than *l*-quartz. Why this should be the case is unclear but appears to depend on differences in the behaviour of *l*- and *d*-quartz seed crystals. Whether the difficulty of preparing synthetic *l*-quartz is reflected in our measured improbabilities of the extreme *l*-quartz dominated sample sets is an intriguing speculation.

The assumption that the determination of the orientation of each crystal is a random event is a conservative one. As noted previously, during crystallisation processes involving chiral or enantiomorphic materials, the orientation of the crystals is influenced by the orientation of the first crystal (or the seed crystal). Therefore the discovery that crystal distributions are non-racemic is not surprising and is perfectly logical.

In conclusion, our statistical analysis strengthens the point that there are local excesses of *l*- and *d*-quartz but that these excesses are probably counterbalanced when considered on the global scale. Therefore we conclude that the hypothesis that the homochirality of life could have arisen from interactions with locally enriched quartz enantiomers cannot be discounted on the basis of the evidence we have evaluated.

CHAPTER 3 MATERIALS AND METHODS

Introduction

This chapter summarises the materials and experimental methods used to study the adsorptive behaviour of amino acid enantiomers onto minerals and metals in both liquid and gas phase systems. First, a description of the materials and reagents is given. Second, operating conditions and method reproducibility for the separation of amino acid enantiomers by HPLC and GC are presented. Although, both methods were adapted and tested in the execution of this project, adsorption data were collected by using HPLC because this technique allows high-throughput and data reproducibility as well as low detection limits. After this, there is a section on the statistical approach used to assess enantioselective adsorption. Finally, there is a summary of experimental conditions for the study of the interaction of Val enantiomers on Cu(110) surface under ultra-high vacuum using RAIRS, STM, and LEED.

3.1. Chemicals and Materials

A list of the reagents used as received is presented in Table 3.1. Milli-Q water (18.2 μΩ-cm resistivity; Milli-Q Gradient, Millipore) was used for the preparation of aqueous solutions. Filtered sea water from the open Pacific Ocean was kindly supplied by Dr. Conrad Chapman from Prof. Van der Berg's electrochemistry laboratory at the Department of Earth and Ocean Sciences, University of Liverpool.

Derivatization Reagents. OPA/IBLC and acylation reagents were prepared according to the following recipes:

OPA/IBLC Reagent: Weigh 0.00285 g of OPA and 0.00621 g of IBLC. Then add 375 μL Milli-Q water and 125 μL of 1M borate buffer (pH = 10.4). The reagent can be stored in a freezer for up to a week. Note that the ratio of IBLC to OPA is 2.18. Therefore the amounts of OPA and IBLC can be adjusted accordingly if more of volume of the reagent needs to be prepared.

Acylation Reagent: Mix 2-propanol and acetyl chloride in a 4:1v/v ratio. Add acetyl chloride slowly to 2-propanol.

Table 3.1. List of reagents used in the experimental work

Reagent	Chemical Formula	Purity	Supplier
L- and D- protein AA		>98%	Sigma Aldrich (Gillingham, UK)
L- homoarginine	$H_2NC(=NH)NH(CH_2)_4CH(NH_2)CO_2H \cdot HCl$	>98%	Sigma Aldrich (Gillingham, UK)
1-hexanesulfonic acid sodium salt	$CH_3(CH_2)_5SO_3Na$	>98%	Sigma Aldrich (Gillingham, UK)
Calcium chloride dihydrate	$CaCl_2.H_2O$	>98%	Sigma Aldrich (Gillingham, UK)
ortho-phthaldialdehyde (OPA)	$C_8H_6O_2$	>99% (HPLC)	Fluka (Buchs, Switzerland)
N-isobutyryl-L- cysteine (IBLC),	$C_7H_{13}NO_3S$	ChiraSelect, ≥97.0% (RT)	Fluka (Buchs, Switzerland)
Potassium phosphate monobasic	KH_2PO_4	>99.5%	Fluka (Buchs, Switzerland)
ortho-phosphoric acid	H_3PO_4	Puriss. P.a., for HPLC.85-90%	Fluka (Buchs, Switzerland)
Pentafluoropropionic acid	CF_3CF_2COOH	97%	Sigma Aldrich (Gillingham, UK)
Trifluoroacetic anhydride	$(CF_3COO)_2O$	Puriss. p.a., derivatization grade (for GC), 99%	Fluka (Buchs, Switzerland)
Acetyl chloride	CH_3COCl	Puriss. p.a., 99%	Fluka (Buchs, Switzerland)
Sodium acetate trihydrate salt	$CH_3COONa.3H_2O$	Hypersolv	BDH (Poole, England)
Methanol	CH_3OH	HPLC-grade	Fisher Scientific (Loughborough, Leicestershire, UK)
Acetonitrile	CH_3CN	HPLC-grade	Fisher Scientific (Loughborough, Leicestershire, UK)
Dichloromethane	CH_2Cl_2	HPLC-grade	Fisher Scientific (Loughborough, Leicestershire, UK)
2-propanol	$(CH_3)_2CHOH$	HPLC-grade	Fisher Scientific (Loughborough, Leicestershire, UK)
Potassium hydroxide	KOH	AnalaR grade	BDH (Poole, England)
Boric acid	H_3BO_3	AnalaR grade	BDH (Poole, England)
Hydrochloric acid (35.4%v/v)	HCl	AnalaR grade	BDH (Poole, England)
Cupric sulphate 5-hydrate	$CuSO_4.5H_2O$	AnalaR grade	BDH (Poole, England)
Sodium chloride	NaCl	HPLC-grade Bioreagent	Fisher Scientific (Loughborough, Leicestershire, UK)
Sodium hydroxide	NaOH	HPLC-grade Bioreagent	Fisher Scientific (Loughborough, Leicestershire, UK)
Valine dipeptide	H-val-val-OH. LL configuration	>99%	Bachem (Bubendorff, Switzerland)

Powdered Minerals and Single Crystals. Silica and aluminosilicate minerals were from Sigma-Aldrich (Table 3.2).

Table 3.2. Physical chemical characteristics of powdered minerals

Mineral	Structural Formula	Surface Area (m^2/g)	Other Properties
Kaolinite	$Al_2Si_2O_5(OH)_4$	14.3 [a]	Off-white powder pH=3.5-5 (20% in water) 0.1-4μm particle size
Montmorillonite K10	$M_{0.33}^{+}(AlMg)Si_4O_{10}(OH)_2.nH_2O$ [b]	220-270	Off-white powder pH=2.5-3.5
Montmorillonite KSF (K-catalyst)	Contains 5% sulphuric acid	20-40	Off-white to beige powder. pH=1-2
Quartz Sand [c]	SiO_2	0.0563 [a]	Off-white to beige granules. ~ 50-70 mesh particle size. >6 μm

[a] Surface area determined by BET analysis on a Micromeritics ASAP 2000 analyzer.
[b] M^+ in the natural material includes one or more cations such as Na^+, K^+, Mg^{2+}, and Ca^{2+}
[c] This is a natural sand washed with virgin spring water free of additives, then dried.

Montmorillonite K10 is an acidic clay catalyst prepared by calcination of natural montmorillonite. It is considered a strong Brönsted and Lewis acidic catalyst that can be modified by exchanging the interlayer cation present in the clay with other cations such as Fe, Zn, Pd, Cu, Ru, Rh, Ce, or by increasing the interlamellar space by pillaring [105]. Montmorillonite KSF is also an acidic catalyst made up of 53% montmorillonite, 10% illite, 6% kaolinite, 10% quartz, 5% plagioclase, 1% gypsum, 4% anhydrite, 7% amorphous material, and 6% unknown material[86]. Natural enantiomorphic quartz crystals (Ron Coleman Mining, Hot Springs, Arkansas) were kindly supplied by Prof. Robert Hazen at the Carnegie Institution of Washington's Geophysical Laboratory. These specimens are approximately 6-to 8-cm in length and 3- to 4-cm in diameter. Their terminal faces tend to be small, maximum 1 cm^2. More crucially, they are 90%+ electronic grade specimens that were used extensively during the Second World War (Personal Communication with Prof. Hazen). Purity of the *l*- and *d*-quartz crystals is relevant since natural quartz crystals can exhibit twinning of the two enantiomorphs and one of the main objectives of this work is to address the effect of quartz intrinsical enantiomorphism on enantioselective adsorption of AA enantiomers. Cubic pyrite (Navajun, Spain), 3×3×3 cm, and gypsum single crystals (unknown origin) were purchased from Manchester Minerals (Stockport, Cheshire, UK). Synthetic quartz specimens of unknown enantiomorphism and source were

provided by Prof. David Prior at the Department of Earth and Ocean Sciences, University of Liverpool. Synthetic *l*- and *d*-AT-cut polished quartz wafers (1 inch diameter and 0.01" thickness) were purchased from Sawyer Technical Materials, LLC. USA. AT-cut is a commercial designation for a specifically oriented resonator plate, having desirable and repeatable operating characteristics. Figure 3.1 illustrates the single crystals.

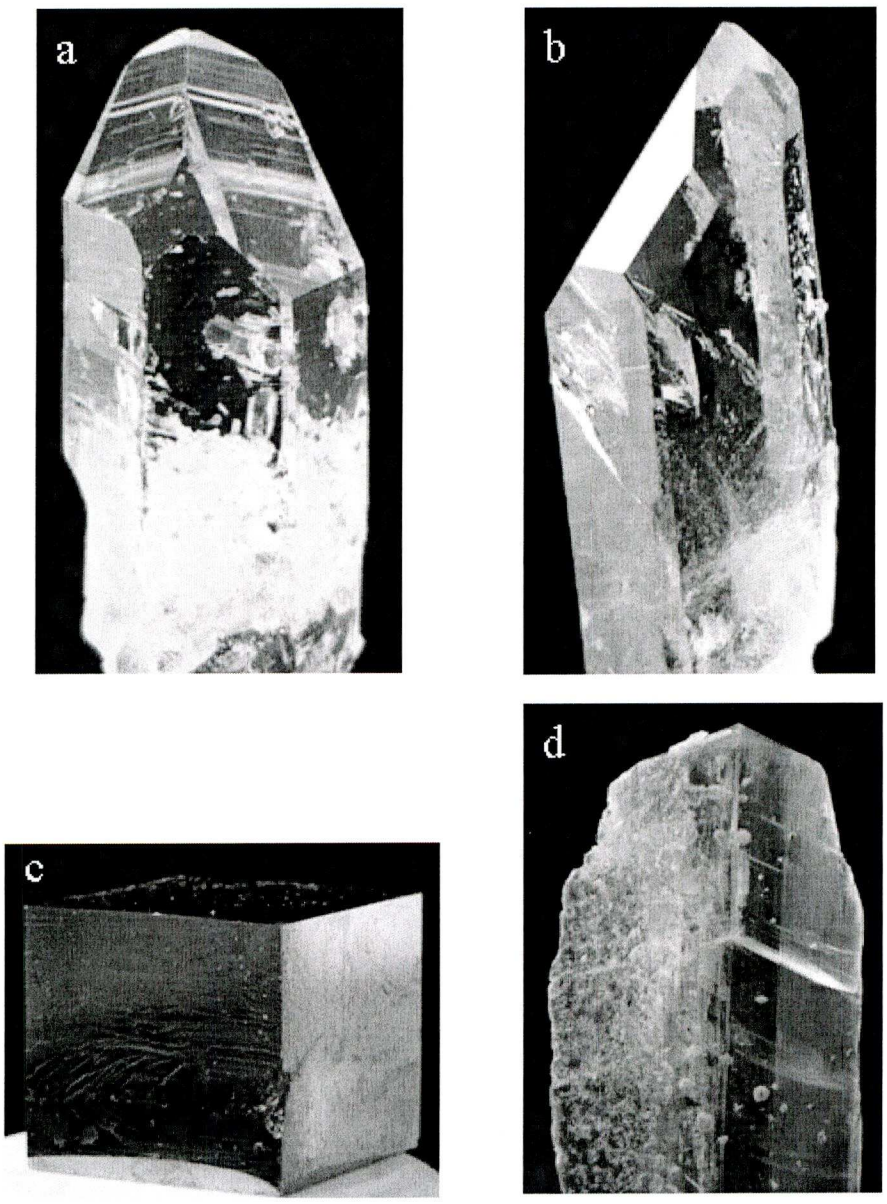

Figure 3.1. Natural single crystals of a. *l*- quartz, b. *d*-quartz, c. pyrite, d. gypsum

3.2. Glassware Cleaning Protocol

Glassware was soaked in Decon 90 (Decon Laboratories, Sussex, UK), a surface active cleaning agent, and then thoroughly rinsed with tap water. Following this, glassware was acid-washed in a 10% v/v nitric acid solution, copiously rinsed with water, and finally rinsed with Milli-Q water before use. Aluminum foil, glass pipettes, and 7 mL capacity glass vials were heated at 400°C to eliminate organic impurities. 1.5 mL Eppendorf plastic centrifuge tubes and pipettes tips were cleaned by immersion in methanol for 30 s, and subsequent air drying for at least one hour. Handling of glassware was carried out under aseptic conditions and nitrile gloves were worn throughout the experiments.

3.3. Preparation of Minerals and Single Crystals

Sand Quartz and Kaolinite. Sand quartz and kaolinite were washed in 2 M HCl solution for 1 hour and then rinsed repeatedly with HPLC-grade water until the pH of the water wash was 6 or above. Wet minerals were dried overnight at 120°C and then heated overnight at 500°C to remove organic contaminants.

Montmorillonite K10 and KSF. These minerals were heated overnight at 400°C to remove organic contamination.

River Mersey Sediments. Sampling of River Mersey sediments was conducted in September 2005. The sampling location was an intertidal area at Hale Point on the River Mersey Estuary, UK. The sediment at this point is a very fine mud consisting largely of clay, organic fragments of biological origin, and pyrite occasionally framboids [97]. Triplicate sediment cores were taken to the lab and immediately frozen. After defrosting, one core was cut into nine slices of about 2 cm each. Slices one and seven, corresponding to surface and anoxic sediment respectively, were dried at 120°C, and then homogenized on an agate mortar and pestle. The uniform dry material was finally pyrolysed at 500°C to give a red powdered material.

Powdered Synthetic Quartz. Synthetic quartz crystals were milled in two stages. First, a jaw crusher was used to break the material into smaller pieces. After this, the material was pulverized on a TEMA mill to produce a greyish powder of 20-100 μm particle size. Synthetic quartz wafers were powdered by milling in the TEMA device only. Powdered quartz was cleaned as reported above for sand quartz and kaolinite.

Synthetic Quartz Wafers. Wafers were rinsed with distilled water, methanol, distilled water and then dried at 100°C and heated overnight at 500°C.

Single Crystals of Quartz, Gypsum, and Pyrite.

Quartz. Synthetic and natural quartz single crystals were washed successively with distilled water, dichloromethane, hexane, dichloromethane, and distilled water. Afterwards, quartz crystals were dried at low temperature. Dried synthetic crystals were heated overnight at 500°C whereas the natural ones could not be subjected to this treatment because of the presence of fluid inclusions which would lead to rupture of the crystal.

Pyrite and Gypsum. These two crystals were washed with water, dichloromethane, methanol, and distilled water before use.

Copper-Exchanged Clays. Copper-exchanged montmorillonite (CuK10) and kaolinite (CuKao) were prepared by adding 1M $CuSO_4.5H_2O$ to 25 g of raw montmorillonite K10 and kaolinite with constant stirring for two days. Then, the clay suspensions were centrifuged, the supernatants discarded and the minerals washed with Milli-Q water. At least 15 water washes were carried out to remove sulfate anions from the minerals. Once clean, the copper-exchanged clays were dried overnight at 70°C and subsequently pyrolysed at 400°C to eliminate organic material.

3.4. Preparation of AA Standards and Aqueous Solutions

Typically, 0.01 M AA stock solutions were made up in freshly collected distilled or Milli-Q water, and diluted to the desired initial AA concentration. AA standards contained L-homo arginine as an internal standard (IS) for quantification purposes and were made up in the same matrix as the sample. Low and high solution pH adjustment was performed with 0.1M HCl and NaOH. 0.05 M acetate buffer

(pH=4) was prepared by mixing 41 mL of 0.1 M acetic acid and 9 ml of 0.1M sodium acetate and adjusting the final volume to 100 mL. 0.05 M phosphate buffer (pH 7) was prepared by adding 4.83 g of NaH_2PO_4 and 2.71 g of Na_2HPO_4 to a 1L-volumetric flask and filling up with water to the mark. 23 mM acetate buffer solution (pH=6) was prepared by dissolving 3.13 g of sodium acetate trihydrate in 1L of water and adjusting pH with 10% v/v acetic acid. 1 M potassium borate buffer (pH=10.4) was made up by mixing 6.18 g of boric acid and 8.4 mL of 10M potassium hydroxide in a 100 mL volumetric flask. Aqueous buffers for liquid chromatography applications were filtrated through a 0.45 μm cellulose nitrate filter paper using a vacuum filtration apparatus.

3.5. Experimental Apparatus

3.5.1. Batch Adsorption

3.5.1.1. Powdered Minerals

Adsorption of racemic mixtures of AAs onto powdered minerals was conducted in batch experiments at room temperature. Mineral to solution loads ranged from 0.01 to 0.7 g/ml. Initial concentrations of AAs were 2 to 10 μM. In general, vials were shaken for a 24 h, followed by centrifugation at 3000 rpm for 20 minutes. Aliquots of the supernatants were taken for AA analysis. For RP-HPLC analyses, aliquots were spiked with L-homo arginine to give an IS concentration of 5 μM; i.e. 20 μL of 50 μM IS were added to 180 μL of sample.

3.5.1.2. Single Crystals

Clean quartz, pyrite, and gypsum specimens were immersed in racemic aqueous solutions of different AA pairs at acidic pH values. After 24 h, the supernatants were sampled and prepared for AA analysis.

3.5.2. Extraction

3.5.2.1. Powdered Material

Mineral samples from selected adsorption experiments were extracted to quantify weakly and strongly adsorbed AAs on mineral surfaces, so that mass balances could be conducted. Briefly, the AA solution remaining after sampling was removed from the mineral. Then, 500 μL Milli-Q water or solution of the same pH of the racemic mixture was added to the vials containing the minerals, followed by manual shaking and 10-min centrifugation. At least three of these cycles were

performed and the supernatants combined. A final wash with 500 μL 1M HCl was carried out to extract strongly adsorbed AAs[42].

3.5.2.2. Single Crystals

Faceted minerals were rinsed with solution of the same pH of immersion and then extracted with 0.1 M HCl (quartz) and 0.02M HCl (pyrite and gypsum). HCl was added dropwise with a Pasteur pipette to the face to be extracted and collected back in the pipette after 40 s contact time[26]. The extract was subjected to LC or GC analysis. For chiral GC analyses, samples were spiked with L-norleucine (Nle) as the internal standard.

3.5.3. Wet-dry Cycle Experiments

Open ocean seawater was UV-digested by irradiation with a high-pressure mercury lamp (125 W) for 45 minutes. 30 mM aqueous solutions of L-Val, D-Val and racemic DL-Val were made up in freshly prepared Milli-Q water (pH=5.0) and UV-digested seawater (pH=7.7). 20 mg of CuK10 was weighed out in 7 mL glass vials and 1 mL of 30 mM L-, D, DL-Val solutions were added to them. Five vials were prepared for L-, D-, and DL-val-clay systems. Blanks containing aqueous solution but no CuK10 were also set up identically. To start the wet-dry cycle experiments, vials were manually shaken, loosely covered with punctured clean aluminium foil and heated for 24 h at 65°C to allow water evaporation. After this period, vials were replenished with 1 mL of Milli-Q water or 0.5 M NaCl solution for the seawater system, shaken and heated again for 24 h. After 1, 3, 5, 6, and 8 days, 1 mL of 0.1M $CaCl_2$ was added to the dry CuK10 in the vials to extract material adsorbed on the surface. Extracts were filtered through 0.45 μm Durapore membrane filter (Millipore, UK) and analysed immediately on the LC or frozen if awaiting analysis. Duplicate reacti-vials containing 30 mM L- D- and DL-Val solutions were capped with Teflon lined caps to avoid evaporation and thus test the effect of heating on the possible formation of divaline.

3.6. Chromatographic Methods

3.6.1. RP-HPLC with Chiral Thiol Derivatisation.

Analysis of free AAs and divaline was conducted on Agilent 1100 and 1200 liquid chromatographs equipped with reversed phase C-18 Hyperclone BDS columns (250 mm × 4 mm, 5 μm particle size) from Phenomenex (Macclesfield, Cheshire). The column compartment was kept at 25°C. Chiral derivatisation of AAs and divaline with the OPA/IBLC reagent was automated as in previous methods[70, 71].

Fluorescence detection parameters were 330 nm excitation and 445 nm emission. AAs of different polarity were separated according to a gradient program run at 0.5 mL/min with the mobile phase delivered by a quaternary pump. Eluents were methanol, acetonitrile, and 23 mM sodium acetate buffer adjusted to pH 6.00 (Table 3.3).

Table 3.3. HPLC gradient elution program

Time (min)	Methanol (%)	ACN (%)	Sodium Acetate Buffer
0	5	0	95
2	5	0	95
31	23	0.4	76.6
75	50	2	48
85	95	5	0
95	95	5	0
105	5	0	95
120	5	0	95

Figure 3.2 shows a chromatogram of a 10 μM equimolar AA mix containing eleven pairs of AA enantiomers, L-threonine, glycine, and L-homoarginine. The detection limit was 2.5 pmole on-column for most of the AAs except for lysine, which has been reported to form unstable OPA derivatives[70], and 15 pmole for divaline, respectively. Moreover, the detector response was linear in the concentration ranges illustrated in Figures 3.3 for a wide array of AAs and in Figure 3.4 for divaline.

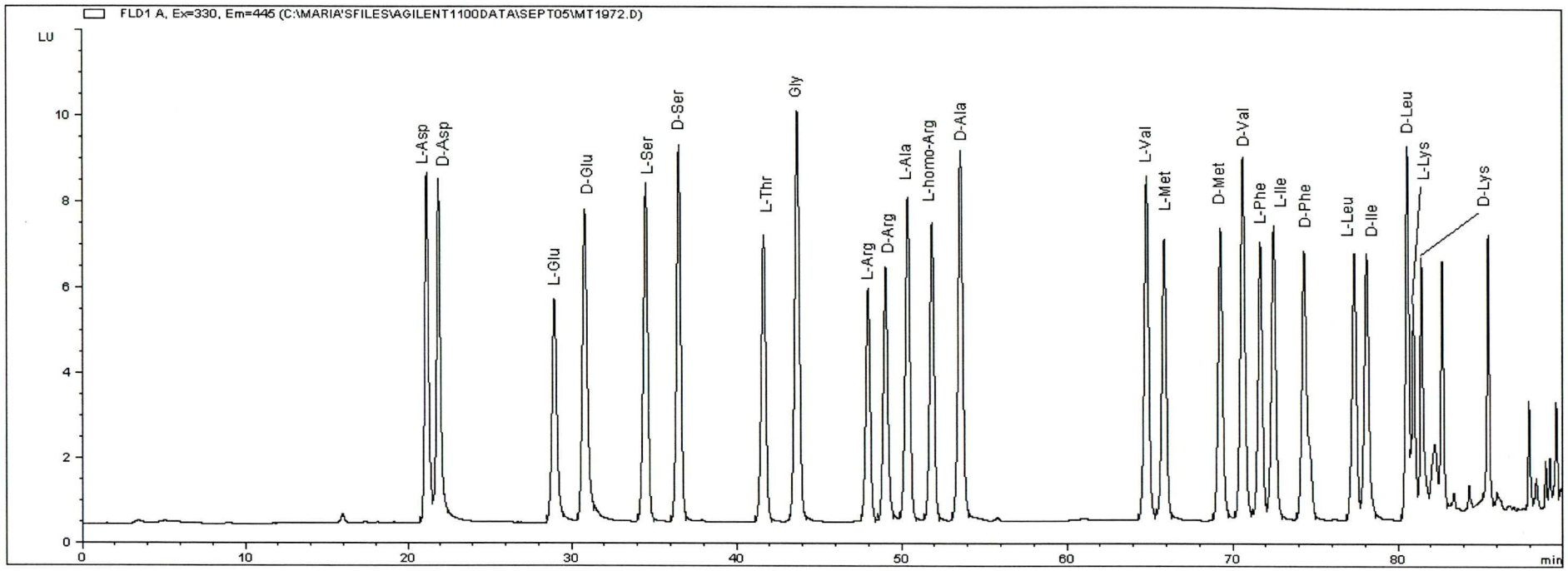

Figure 3.2. Chromatogram of a 10 µM standard AA mix showing eleven pairs of AA enantiomers, L-Thr, Gly, and L-homoarginine. Unlabelled peaks eluting after D-Lys correspond to reagents

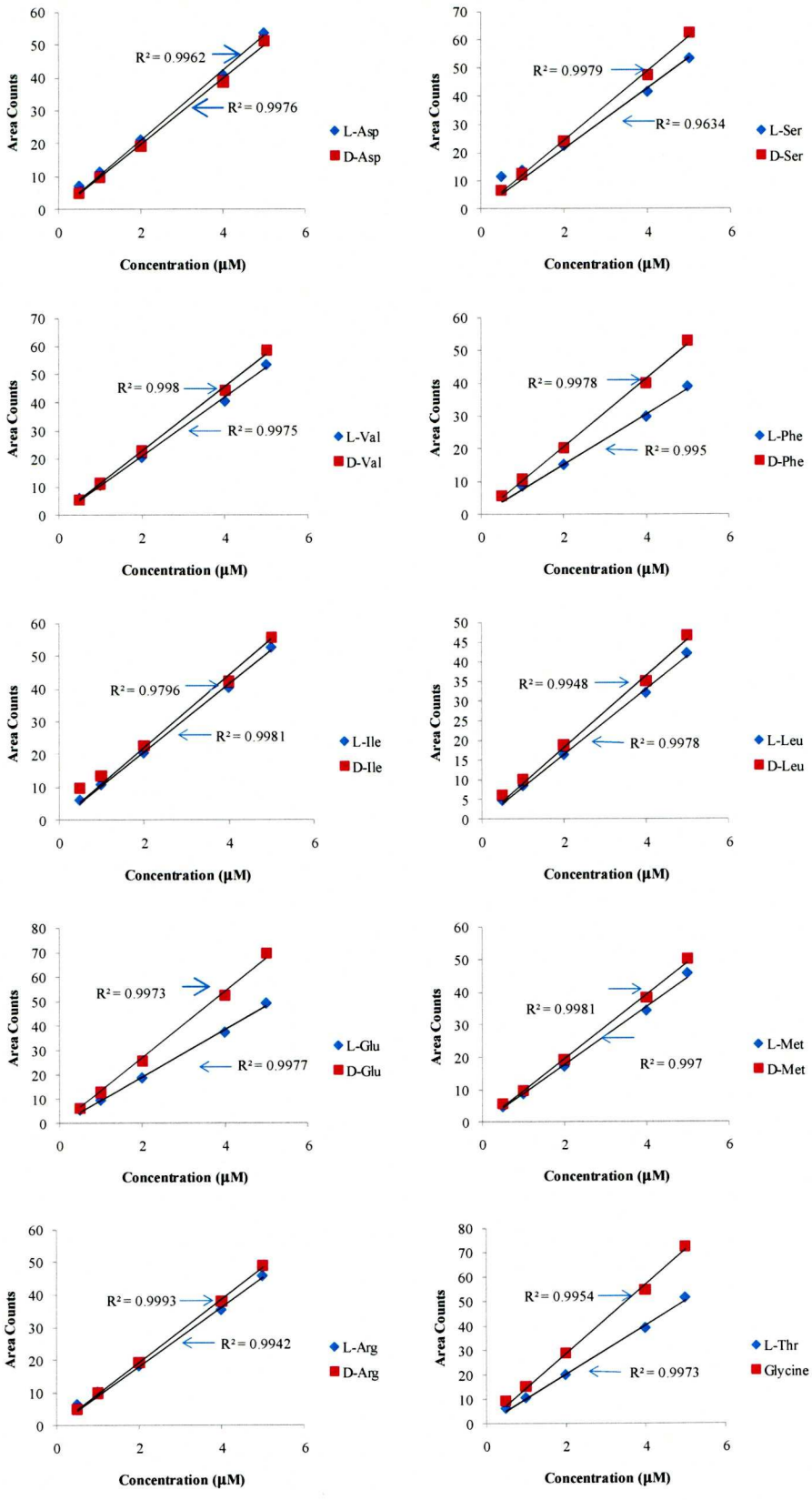

Figure 3.3. Amino acid linearities by FLD on RP Hyperclone BDS C-18, 250 mm × 4 mm, 5 µm column using an Agilent 1100 System. DL-Asp, DL-Glu, DL-Ser, L-Thr, Gly, DL-Arg, DL-Val, DL-Met, DL-Phe, DL-Ile, DL-Leu

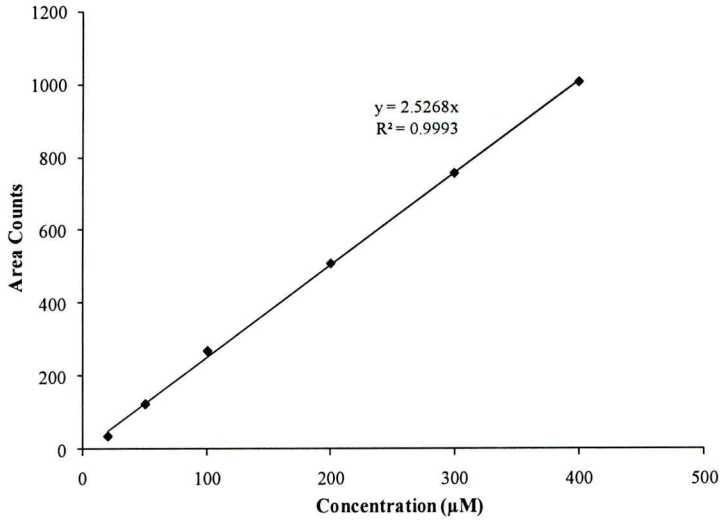

Figure 3.4. Divaline response vs. concentration. FLD detection

The reproducibility of the method was tested by multiple injections of a 5 µM AA standard (Table 3.4).

Table 3.4. Peak area reproducibility of AAs resolved on a RP Hyperclone C-18, 250 mm × 4 mm, 5 µm Column Using an Agilent 1100 System

AA	RSD (%) (n=4)	AA	RSD (%) (n=4)
L-Asp	0.52	D-Asp	0.99
L-Glu	0.67	D-Glu	0.66
L-Ser	0.71	D-Ser	0.93
L-Arg	0.44	D-Arg	0.30
L-Ala	1.96	D-Ala	1.71
L-Val	1.16	D-Val	1.20
L-Met	0.93	D-Met	0.93
L-Phe	1.30	D-Phe	0.79
L-Ile	0.93	D-Ile	0.54
L-Leu	0.95	D-Leu	0.20
L-Thr	0.82	Gly	0.93
L-homoarginine	1.00		

3.6.2. Ion-pair RP-HPLC

Ion-pair RP-HPLC with UV-detection at 200 nm allows the detection of short peptides down to the picomole limit with high throughput[82]. Analysis of divaline was carried out on an Agilent 1100 equipped with a diode array detector (DAD). Solvent A was a mixture of 50 mM KH_2PO_4 and 7.2 mM 1-hexane sulfonic acid. Solvent B was ACN. The mobile phase flow rate was set at 0.35 mL/min with a binary gradient program summarized in Table 3.5. Separation was conducted on a C-18 BDS 250 mm × 4.6 mm, 5μm column (Phenomenex, Cheshire) kept at 40°C. The injection volume was 5 μL. UV-detector settings were 200nm, 4 nm bandwidth; reference wavelength 550nm, 100nm bandwidth. The UV-response of divaline was linear in the 10-200 μM range as determined from a five-point calibration curve of standards made up in 0.1 M $CaCl_2$ (see Figure 3.5). The relative standard deviation of four consecutive injections of a 50 μM divaline standard was 13% whereas the detection limit was about 6 μM.

Table 3.5. Gradient program for divaline analysis by RP-HPLC with UV-detection

Time (min)	Solvent A (%)	Solvent B (%)
0	95	5
0.5	92.5	7.5
4	70	30
6	95	5
25	95	5

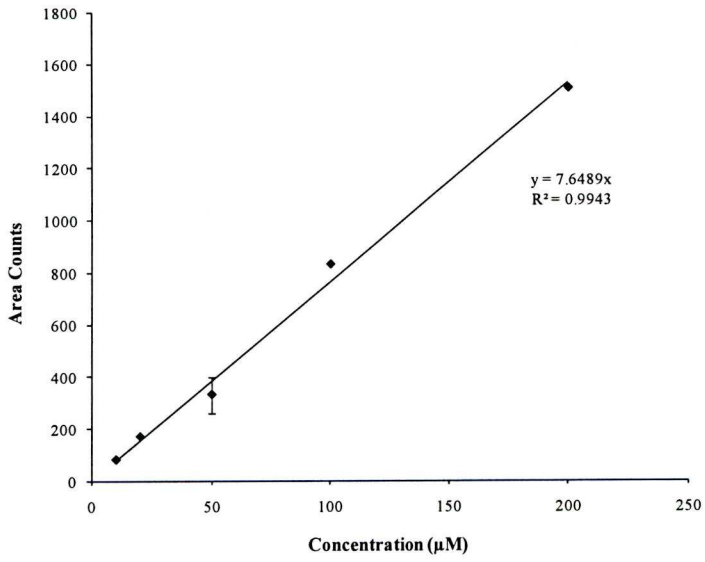

Figure 3.5. Divaline response vs. concentration. UV detection

3.6.3. Chiral Gas Chromatography

This method allows the separation and quantification of AAs by using a column coated with a chiral stationary phase. First, free AAs were derivatised to produce *N*-pentafluoropropionyl or *N*-trifluoroacetyl-isopropyl ester derivatives (*N*-PFP-ip or *N*-TFA-ip, respectively) according to the procedure by Erbe and Brückner [106]. The steps involved in the derivatisation are summarized below:

- Liquid samples were gently evaporated at 70°C in a 0.3 mL Reacti-vial.
- Dry residues were then dissolved in 0.1 M HCl and samples evaporated to dryness in a stream of N_2.
- 200 µL of the acylation reagent was added the dry residue and the vial capped with a Teflon-lined screw top.
- Samples were heated at 110°C for one hour and then cooled to 40°C, before excess reagent was removed under N_2 with slight heating.
- 100 µL of PFPA or TFA and 100 µL of dichloromethane (DCM) were added to the dry residue and the mixture heated at 100°C for 20 minutes.
- The reacti-vial was cooled and reagents removed under a stream of N_2.
- The residue was finally re-dissolved in 100 µL of DCM and 1-2 µL was injected into the column.

Separation of PFP- and TFA-isopropyl esters was conducted on a Hewlett-Packard 5980 gas chromatograph equipped with a capillary Chirasil L-Val column, 25 m × 0.25 mm, 0.16 µm film thickness, (Alltech, USA) and an FID detector. On this column, D-AAs eluted before the L-AAs as illustrated in Figures 3.6 and 3.7. The carrier gas was helium at 1 mL/min. Injector mode was splitless. The injector and detector temperatures were set at 200°C and 220°C, respectively. Column temperature was programmed as follows: 3 min hold at 40 °C, 40°C to 90°C at 45°C/min, 90°C to 190°C at 2°C/min, and 10 min final hold at 190°C. The limit of quantitative determination of AAs with GC-FID was about 10 µM, which is in agreement with values reported previously for quantification of AAs in other matrices [73]. These values are considerably higher than the quantification limits attained by RP-HPLC with chiral thiol derivatisation. The relative standard deviation of manual triplicate injections of 100 µM TFA-ip esters of L-Asp acid standard was around 7%. TFA-ip esters of Asp acid were better resolved on Chirasil L-Val than their PFA-ip counterparts as seen in Figure 3.7.

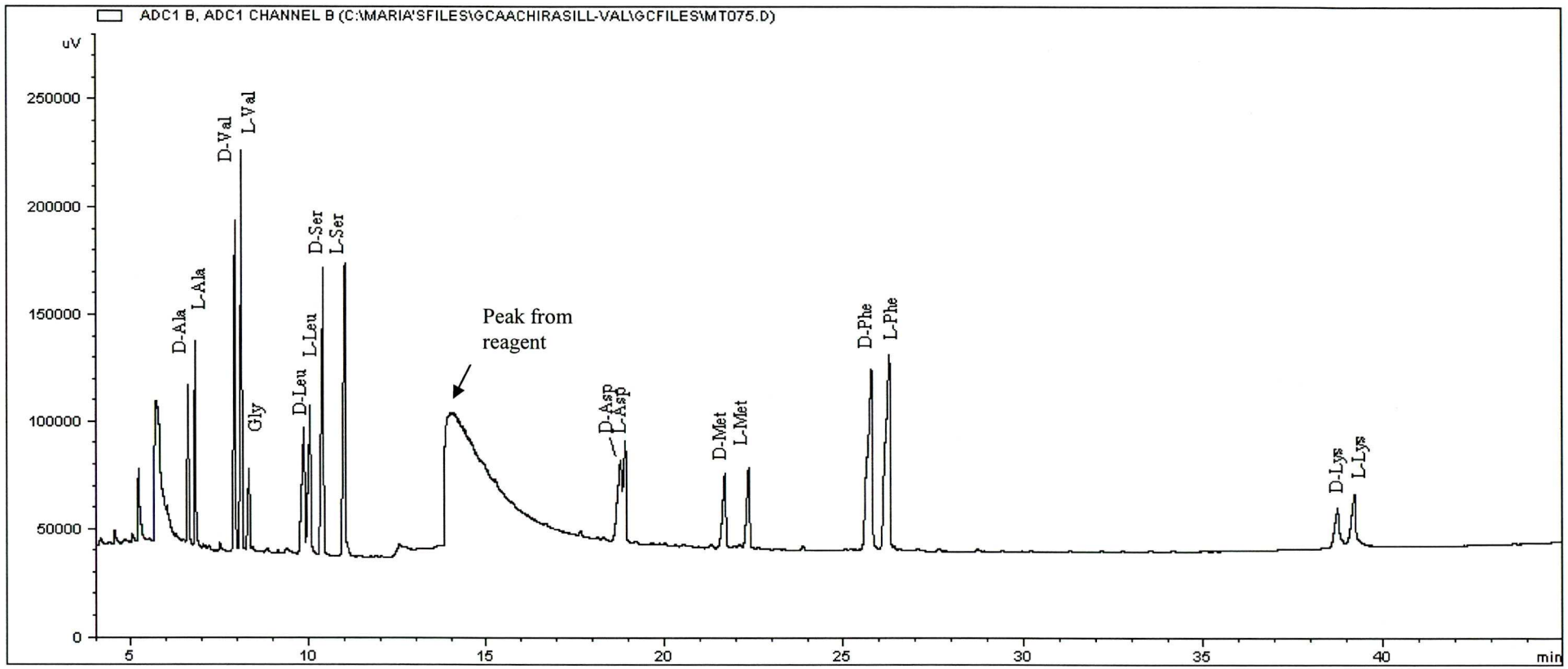

Figure 3.6. Gas chromatogram of AA enantiomers (*N*-PFP-ip ester derivatives) of a standard mixture. Each AA 50 µM

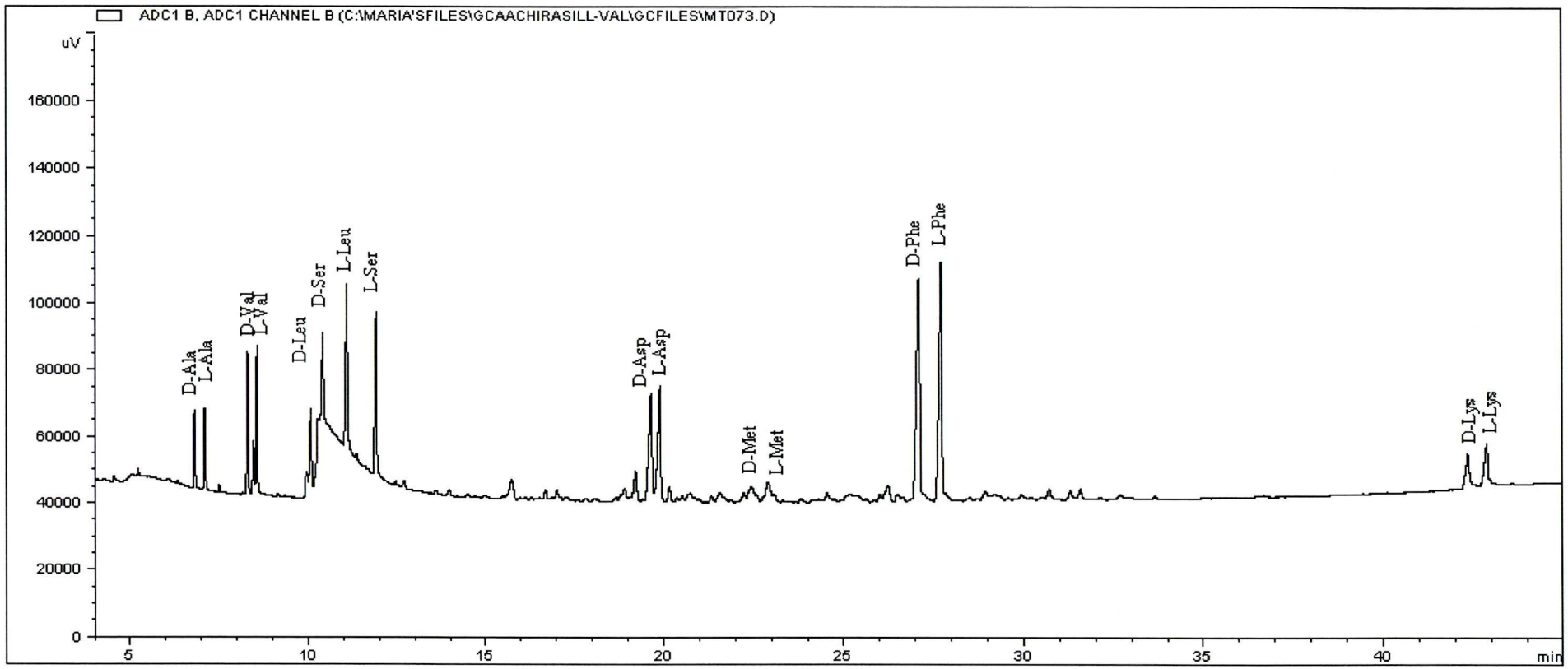

Figure 3.7. Gas chromatogram of AA enantiomers (*N*-TFA-ip ester derivatives) of a standard mixture. Each AA 100 μM

3.6.4. Liquid Chromatography-Mass Spectrometry (LC-MS)

Samples were analysed using a Spectra-Physics HPLC system connected to a TSQ-7000 triple quad mass spectrometer via an electrospray interface. Electrospray ionization (ESI) was used to ionize the sample. ESI parameters were capillary temperature of 350°C and spray voltage of 4.5 kV. Sample extracts (5-10µl) were injected using a TSP AS1000 auto sampler and separated on a reversed-phase Hyperclone C18 column (Phenomenex, 250 × 4.6mm × 5µm column). Solvent A was methanol (0.5% acetic acid v/v) and solvent B was water (0.5% acetic acid v/v). Solvents were degassed by ultrasonication. Samples were eluted at 0.25 mL/min according to the following gradient program: (0-5 min) 30%A:70%B, (5-30 min) 30%A:70%B to 95%A:5%B, (30-40 min) 95%A:5%B, (40-50 min) 95%A:5%B to 30%A:70%B, (50-60 min) 30%A:70%B. Full scan spectra in positive mode were recorded over an m/z range from 60 to 500 amu with a scan time of 1s, the auxiliary gas set at 20 (arbitrary units) and sheath gas at 80 p.s.i. The capillary was set at 250 °C, and the tube lens at 132 V. The data was collected using Xcalibur software.

3.6.5. Quantification of Analytes

AAs and divaline were quantified by two approaches outlined below.

3.6.5.1. The Internal-Standard Method

The response factors (*RF*) of AAs were determined in relation to L-homoarginine and calculated according to the equation

$$RF = \frac{A_{AAstd} \times C_{is}}{A_{is} \times C_{AAstd}} \qquad \textit{Equation 3.1}^{[107]}$$

where A_{AAstd} is the peak area of AA in standard, A_{is} the peak area of IS, C_{is} the concentration of IS, and C_{AAstd} the concentration of the AA of interest.

Samples to be analysed were spiked with IS to give a concentration equal to that in the standard AA mixture. The concentration of AAs in samples, C_{AAs}, was calculated with the following equation

$$C_{AAs} = \frac{A_{AAs} \times C_{is}}{A_{is} \times RF} \qquad \textit{Equation 3.2}$$

3.6.5.2. Calibration with Standards

Standards of known concentrations of the analyte of interest were analysed on the chromatographic system. Concentration of the analyte was determined from calibration curves of peak area vs. concentration.

3.7. Statistical Data Analyses

Chromatograms were processed with the ChemStation software (Agilent, UK), which allowed manual and automatic peak area integration as well as subtraction of blank runs. Analysis of statistical data was conducted using the Data Analysis option of MSOffice Excel. Error bars of reported data represent 95% confidence intervals calculated assuming that the data follow a Student's *t* distribution for small data sets according to

$$CL = \bar{x} \pm \frac{ts}{\sqrt{N}} \qquad \textit{Equation 3.3}^{[108]}$$

where $\bar{x}$ is the mean value of the set, *t* is a statistical parameter defined as

$$t = \frac{\bar{x} - \mu}{s/\sqrt{N}} \qquad \textit{Equation 3.4}$$

t-values depend on the number of degrees of freedom in the calculation of the standard deviation *s*, and *N* is the number of replicate measurements. Mean values of different data sets were compared to assess whether there was a statistically significant difference between two systems. These comparisons assume that the null hypothesis is valid ($\bar{x}_1 - \bar{x}_2 = 0$). To test this hypothesis, the following equation was employed:

$$\bar{x}_1 - \bar{x}_2 = \pm t s_{pooled} \sqrt{\frac{N_1 + N_2}{N_1 N_2}} \qquad \textit{Equation 3.5}$$

Where s_{pooled} is the pooled sample standard deviation

$$s_{pooled} = \sqrt{\frac{\sum_{i=1}^{N_1}(x_i - x_1)^2 + \sum_{j=1}^{N_2}(x_j - x_2)^2 + ...}{N_1 + N_2 + ... - N_s}} \qquad \textit{Equation 3.6}$$

where N_1 is the number of data in set 1, N_2 is the number of data in set 2. N_s are the number of data sets that are pooled. The number of degrees of freedom is given by N_1+N_2-2. If the hypothesized difference of the means ($\overline{x_1} - \overline{x_2}$) is smaller than the calculated value obtained with Equation 3.5, then the null hypothesis is not rejected and there is no significant difference between the means.

3.8. Experimental Setup for Surface Science Experiments

This section provides a brief description of the equipment and procedures employed for conducting adsorption enantiomers of Val onto Cu(110) under UHV conditions. This experimental description is largely derived from the work by Humblot[109], which succinctly presents the necessary information to understand the experiments.

3.8.1. RAIRS, LEED, and TPD Ultra High Vacuum Chamber

RAIRS and LEED experiments were carried out in an UHV chamber equipped with a mass spectrometer, an argon (Ar) sputter gun, and ion gauge. Figure 3.8 illustrates the main components of the chamber which operates at a pressure of 10^{-10} mbar. This low pressure is achieved by using a diffusion pump and a titanium sublimation pump (TSP) in sequence. Other components include: two KBr windows, which are transparent to IR radiation, and a gate valve that isolates the main chamber from the sublimation doser.

For RAIRS experiments, an FT-IR spectrometer (Mattson Galaxy 7020) is interfaced to the chamber. As discussed in detail in Appendix 1, the IR radiation is focused at the sample at near grazing incidence (~ 85° to the surface normal) and the reflected light detected by a mercury-cadmium-telluride (MCT) detector. Spectral resolution is 4 cm^{-1}.

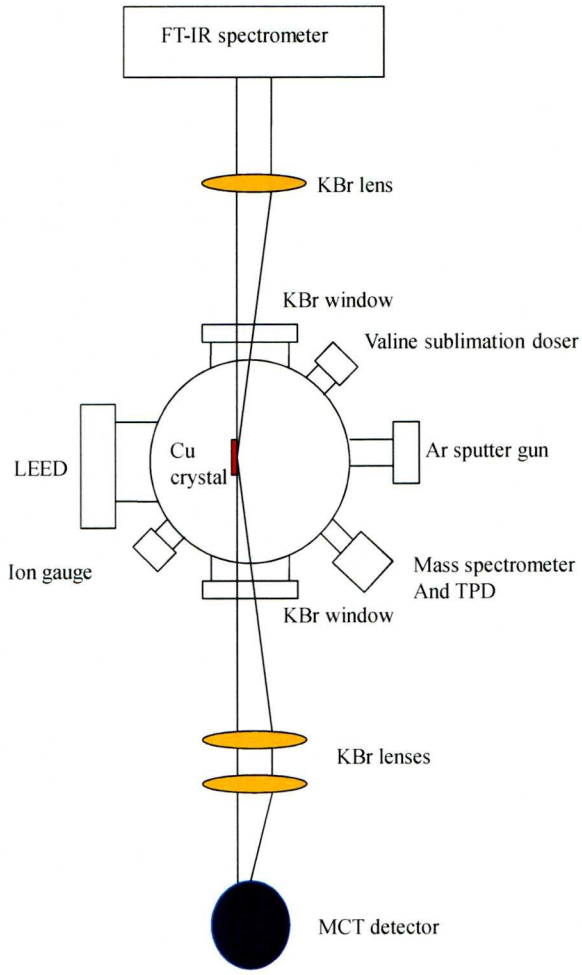

Figure 3.8. Schematic representation of the UHV chamber and optical set-up to perform RAIRS and LEED experiments

The LEED optics is composed of the electron gun and a mesh assembly consisting of three concentrical spherical sector meshes and a phosphor covered glass screen. The sample is earthed and positioned in the centre of curvature of the meshes and the screen. A graphic description of the LEED components and their role is provided in detail in Appendix 1, along with the information that can be obtained from a typical LEED experiment. A LEED experiment is usually conducted to check the cleanliness and surface order of the crystal before depositing any material onto it and after formation of the adlayer to check if the surface possesses an ordered structure.

The energy range of the electron beam is generally 50-200 V, but low electron energies are preferred to avoid potential damage to the adlayer.

Finally, the crystal temperature can be adjusted by resistive heating using a DC source that delivers a 10A current, which translates into a heating rate of 2 Ks^{-1}.

3.8.2. STM and LEED UHV Chamber

The STM system used to conduct the experiments was an Aarhus 150 chamber depicted in Figure 3.9. Both the STM and RAIRS chambers were baked at 423 K to eliminate residual gases that could interfere with the experiments. The scanner head and chamber design from the manufacturer are shown in Figure 3.10. Vacuum was achieved by pumping the system with a 240 $L.s^{-1}$ turbomolecular pump (Balzers TPU300) and a Varian ion pump (270 $L.s^{-1}$). Heating of the crystal was done by firing a 1 keV Ar^+ ion gun at the surface (e-beam heating), which results in a current of 7 μA at the surface sufficient to heat the crystal up to 823-873 K.

Calibration of the STM was undertaken before conducting adsorption experiments. The calibration procedure involved adsorbing O_2 onto the Cu(110) surface giving the typical (2×1) reconstruction. Four calibration ranges were employed to take into account different sizes of the acquired images i.e. 150 Å × 150 Å, 300 Å × 300Å, 500 Å × 500 Å, and 700 Å × 700 Å. Imaging was conducted in the constant current mode.

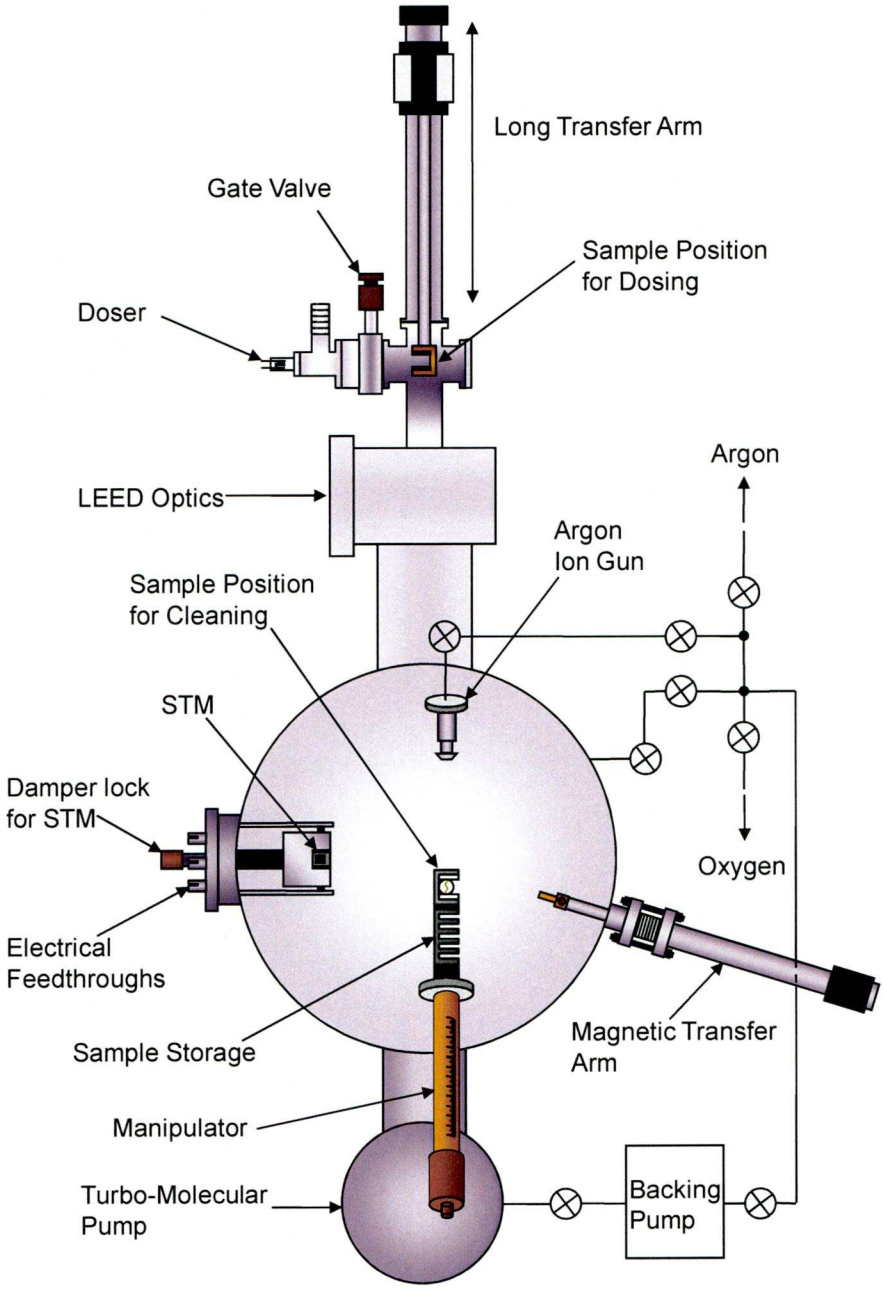

Figure 3.9. Illustration of principal components of the SPECS Aarhus 150 chamber

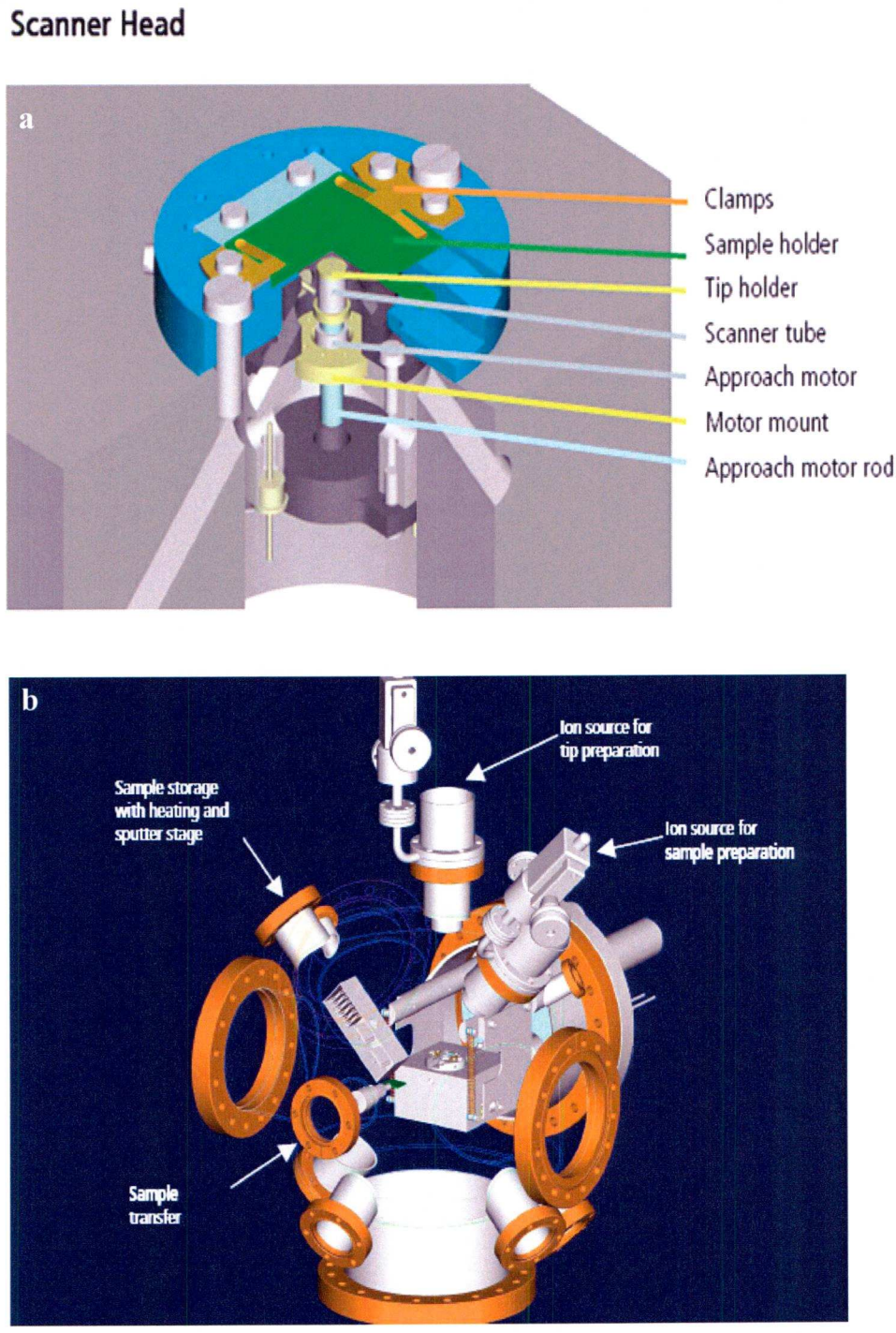

Figure 3.10. a. Scanner head of Aarhus150 STM. b. Chamber layout of Aarhus 150. Technical information from SPECS website. http://www.specs.de/cms[110]

3.8.3. Crystals and Samples

3.8.3.1. Crystals

The Cu(110) crystal is mounted on the *xyzθ* manipulator by using two 0.25 mm Tantalum (Ta) wires attached to the sample via two grooves sparked-eroded as illustrated in Figure 3.11. The crystal can be resistively heated with a DC power supply and cooled, if needed, with liquid nitrogen. The range of operating temperatures obtained with this method is 80-1000 K, as measured with a chromel-alumel thermocouple located at one side of the crystal. Cu(110) crystals (99.99% purity) were purchased from Surface Preparation Laboratory and were certified to have alignment accuracies of 0.2°, thus guaranteeing that the majority of the surface is made up of terraces in relationship to steps edges or other defects.

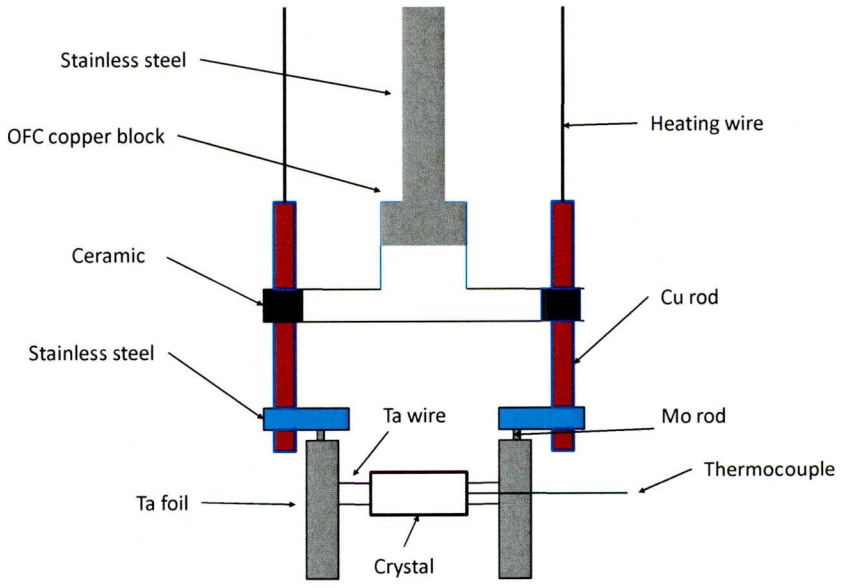

Figure 3.11. Illustration of the attachment of the Cu(110) crystal to the manipulator of the RAIRS UHV chamber

For the RAIRS experiment, the dimensions of the rectangular Cu(110) crystal were 15 mm ×10 mm × 1.2 mm. For the STM experiment, the Cu(110) crystal was a disk of 6 mm diameter. The STM crystal was mounted on a holder by a magnetic arm and then the holder was moved upside down for the tip to scan the crystal.

3.8.3.2. Cleaning of crystals

Removal of unreactive material was conducted by cycles of sputtering and annealing at 800 K for 15 minutes each. During sputtering, the surface was bombarded with an ionized argon beam (Ar^+) of diameter 2-10 mm. The crystal was then manipulated into different positions so that the entire surface of the crystal could be cleaned. The structure and cleanliness of the surface was subsequently checked with LEED.

3.8.3.3. Dosing procedure

R-Val, *S*-Val, and *RS*-Val (>99% purity) were obtained from Sigma-Aldrich and used as received. The powders were packed into a thin glass tube (*ca* 2 mm diameter) and wrapped with a coiled wire to make a device known as a doser. The doser-flange assembly is shown schematically in Figure 3.12. The doser tube was resistively heated via Ta wires that make a circuit with two copper rods. Generally, a current of 0.75 A was enough to raise the temperature to 370 K. The powder was degassed at 330 K and then heated at 350 K due to its low vapour pressure. Once the material started subliming, the gate valve between the doser and the main chamber (Figure 3.14) was opened to expose the Cu(110) crystal to gaseous Val and the resulting chamber pressure was about 2×10^{-9} mbar. A quadrupole mass spectrometer fitted in the main chamber allowed decomposition of the dosed molecules to be determined as inferred from the mass fragments. The doser flange assembly was bolted to the main chamber at a port containing a gate valve, resulting in a four-way cross that can reach pressures of 5×10^{-9} mbar by means of a Varian turbo molecular pump (see Figure 3.13).

RAIRS spectra were collected continuously after starting to dose Val at a rate of 256 scans per 90 s. The single beam spectra were corrected against a background spectrum of the clean copper surface. Dosing time for RAIRS experiments was approximately 12-15 min. In contrast, dosing times for STM experiments varied from 30 s to 2 minutes because the experiment objective was to image the adlayer at low and high coverage rather than monitoring the growing adlayer as a function of time as in the case of the RAIRS experiment. In addition, the STM doser is closer to the sample so that the flux of sublimed Val reaches the Cu(110) crystal faster.

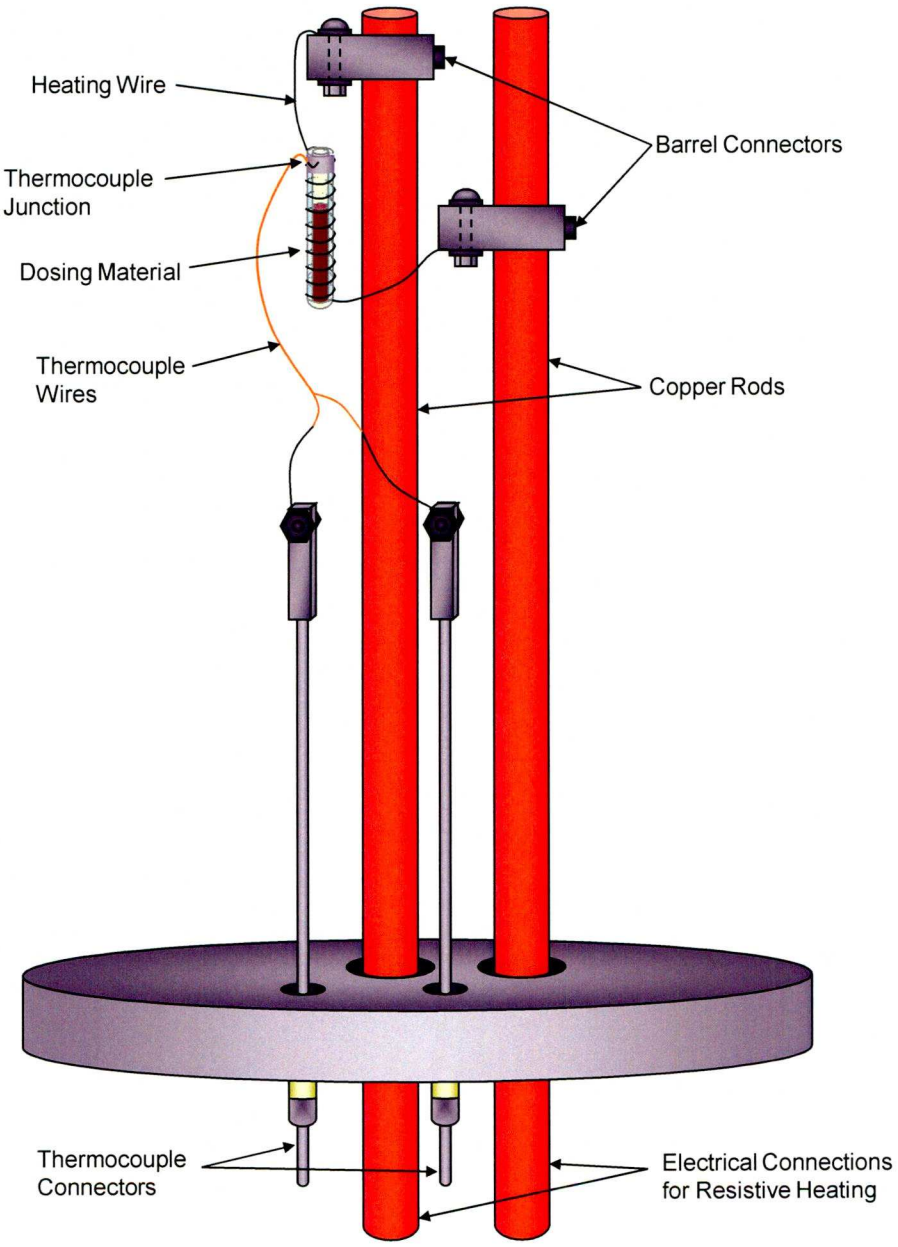

Figure 3.12. Schematic illustration of the doser assembly

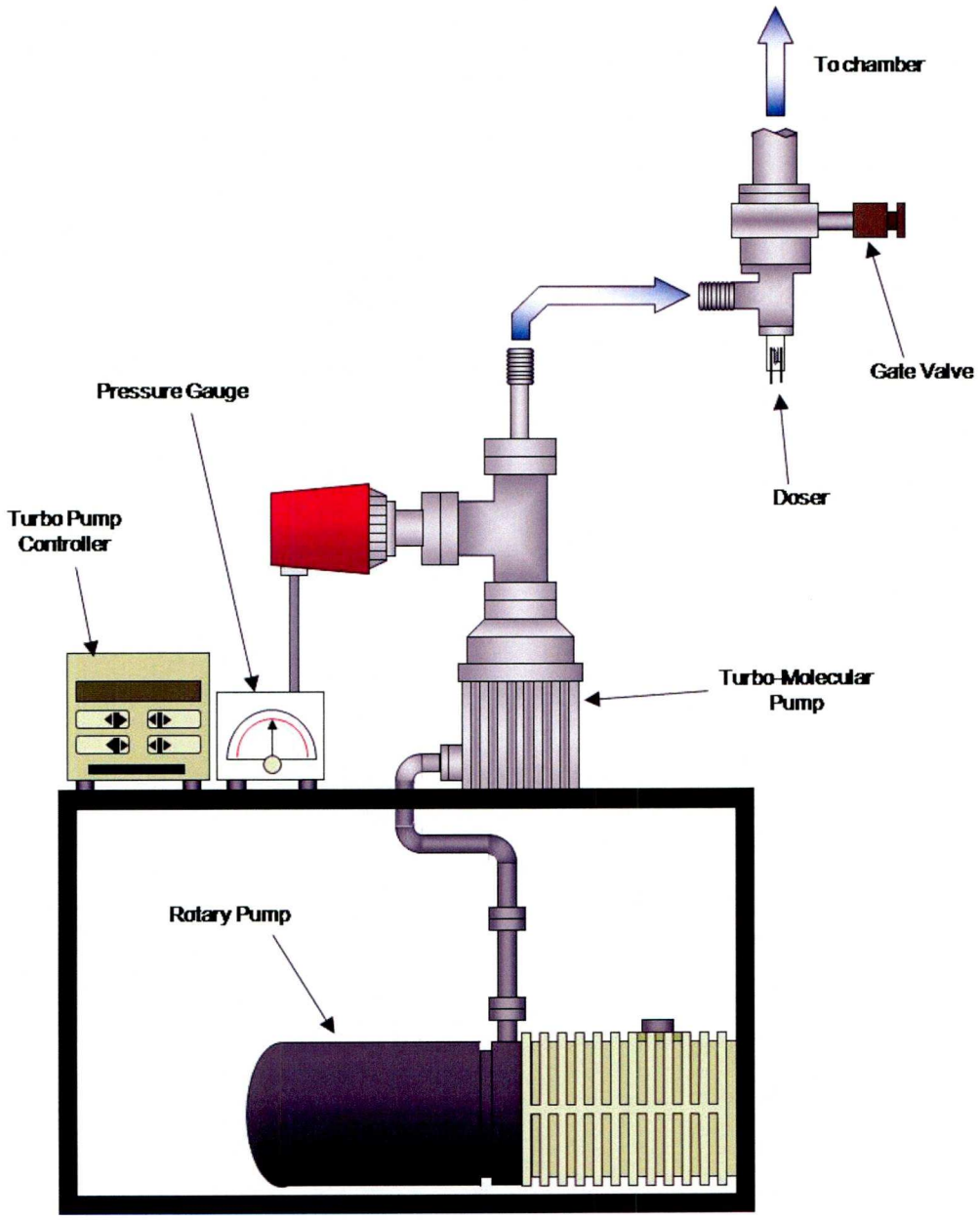

Figure 3.13. Dosing line vacuum system

CHAPTER 4 RESULTS AND DISCUSSION

4.1. Adsorption of Racemic AAs onto Common Rock-Forming Minerals

The adsorption of racemic mixtures of AAs on naturally occurring minerals that are constituents of the Earth crust and sediments was studied under different environmental conditions. The variables tested included: pH, ionic strength (I), type of amino acid, single component systems with only one pair of enantiomers in aqueous solution, multicomponent systems with more than one pair of AAs in aqueous solution, and mineral loading. Previous research has addressed adsorption of AA enantiomers on quartz and clays, but few have reported selective adsorption of one of the enantiomers over the other on the mineral (see Table 1.4). Furthermore, most of the preceding experiments were conducted at relatively high initial AA concentration or in non-aqueous solutions such in the case of quartz. In this work, the initial concentration of AAs was in the 2-30 μM range, with a few exceptions such as the case of Arg and His adsorption on quartz substrates. More importantly, the indirect HPLC method with chiral derivatization for quantifying free AA enantiomers was particularly suited for these analyses because it provides excellent resolution for all the 20 pairs of protein AAs with low detection limits, making it more robust than the methods used in the past. In view of the dissimilar systems investigated, a matrix was constructed to show all the experiments carried out on the minerals and those systems where statistically significant enantioselective adsorption was observed (see Section 3.7) are indicated next to the variable(s) by an asterisk (see Table 4.1). Note that all the minerals used in the adsorption experiments were free of AA impurities that might bias the results since HPLC analysis of the control samples (mineral + aqueous solutions) showed no peaks other than that of the internal standard. Unless otherwise stated, adsorption experiments were conducted over a 24-h period during which equilibrium conditions were attained. The D- and L-AA notation is used when describing the adsorption of AAs on mineral surfaces to be consistent with the previous literature addressing the enantioselective potential of mineral surfaces (Table 1.4).

Table 4.1. Matrix of adsorption experiments of racemic AAs on minerals in aqueous solutions

	Amino Acid										
	Asp	**Glu**	**Ser**	**Val**	**Arg**	**Hist**	**Ala**	**Met**	**Phe**	**Leu**	**Lys**
Mineral Type/Form											
Sand Quartz	1,6*				1,3,5*,6		1,3,5				
Powdered synthetic *d*-quartz	6	6	6	6	1,4,5,6	5	5,6	6	6	6	
Powdered synthetic *d*-quartz wafer						5					
Powdered synthetic *l*-quartz wafer						5					
Racemic mixture of powdered *l*- and *d*-quartz wafers	6	6	6	6	6						
Natural *l*- and *d*-quartz single crystals	5				5						
Calcined K10		2,6	1*,2,3*,4,5*,6*	1,2,5*,6	1,3,5*						
Calcined CuK10				1,2,5,6							
Calcined Kaolinite	1,2,6	1,2,6	2,6	1,2,5,6	1,2,6		1,2,6				1,2,6
Calcined CuKao				1*,2,5*,6							
Calcined KSF				5							
River Mersey Sediments	1,6	1,6			1,6		1,6				
Pyrite single crystal	1,6	1,6			1,6		1,6				1,6
Gypsum single crsytal	1,6	1,6			1,6		1,6				1,6

Variables

1 pH
2 Ionic strength (I)
3 Mineral loading
4 Initial AA concentration
5 Single component
6 Multicomponent
* Statistically significant at 95% confidence

4.1.1. Adsorption of Racemic AAs on Quartz

In Section 1.3.1 it was established that quartz exists in a variety of forms on Earth and it has been the subject of much interest owing to its enantioselective properties in a variety of reactions. Despite this, the adsorption of racemic mixtures of biomolecules, particularly AAs, on quartz under aqueous conditions has not previously been examined in detail because of the poor adsorbing capacity of this mineral in unbuffered systems [18]. For example, the quartz sand used in this research is characterised by coarse particles and consequently low surface area (SSA=0.0563m^2/g). As reported by Vlasova [15], basic AAs such as Arg, Lys, and His adsorb the most on silica since these AAs are in the cationic form in a wide pH range as indicated by the high pK_a values of their side chains (pK side chain Arg= 12.84, pK side chain Lys= 10.53). Several types of quartz were used as adsorbents with the purpose of evaluating the effect of purity and adsorption capacity of crystallographic faces of natural and synthetic specimens in powdered and single crystal form. Natural materials such as quartz sand and single quartz crystals probably also contain impurities and defects that can affect their adsorptive and catalytic properties[111]. Thus, comparing sorption of AAs on different sorbents might provide insight into the mechanism of enantioselective adsorption.

In this research, Arg was chosen as the adsorbate to investigate selective adsorption in all of the quartz systems because of its basicity. The adsorption extent depended on the mineral load and therefore on the surface area of the quartz. As expected, AA adsorption was very limited on single quartz and synthetic quartz wafers and batch experiments highlight the relevance of the surface area. For instance, adsorption of Arg on synthetic single crystal quartz wafers was only detectable with ten one-inch wafers immersed in solution and mineral loads of 1 g/mL of quartz sand were needed for measurable amounts of acidic and neutral AAs to bind to the surface at acidic pH.

Adsorption of racemic mixtures of AAs onto powdered synthetic *d*-quartz was investigated in single (DL-Arg, DL-His, DL-Asp, DL-Ala) and multicomponent (Asp, Glu, Ser, Arg, Ala, Val, Met, Phe, Leu) systems. The influence of pH and solvent in the Arg-powdered *d*-quartz and Arg-quartz sand systems was addressed. A set of experiments with a 5 μM solution of DL-Arg in methanol was aimed at understanding the effect of AA solvation on adsorption and possibly on selectivity at the mineral surface. The following discussion focuses on the generalities of individual

quartz systems such as adsorption capacity and, where applicable, any selective effect is noted.

4.1.1.1 Adsorption of Racemic AAs on Quartz Sand

Quartz sand, a mineral component of soil and sediments, was used as an adsorbent of racemic AAs in aqueous solutions. It is a coarse material with low surface area (0.0563 m^2/g) as determined from the Brunauer, Emmet, and Teller (BET) adsorption isotherm method with nitrogen as the adsorbing gas. Batch experiments were setup in vials with various solid/liquid ratios of quartz to AA solution at room temperature and constant mixing on a rotary shaker. After 24 h adsorption, vials were centrifuged and aliquots of the supernatant taken for HPLC analysis.

Negligible adsorption of AA enantiomers (except Arg) from racemic mixtures took place in quartz systems at a 0.1g/mL mineral load under no pH control. This agrees quite well with the results by Vlasova[15] and Zaia *et al.*[111], who reported no detectable adsorption of neutral, acidic, and polar AAs on highly dispersed amorphous silica in unbuffered aqueous systems, but significant adsorption of basic AAs such as His, Arg, and Orn. Further support for the lack of affinity of AAs other than Arg for hydroxylated silica was recently published by Rimola *et al.*[112], who correlated the adsorption energy of AAs on silica with a hydropathy index. Thus, the nonpolar (Gly, Ala, Met, Phe) and basic (Arg, Lys, His) AAs are the least prone and more prone to be adsorbed on silica, respectively[112]. Dissolved AAs in aqueous solutions attain a pH close to their isoelectric points, which is about 6 for Ala, Ser, Val, Leu, and Phe and 10.8 and 9.8 for Arg and Lys, respectively. Since the pH of point of zero charge of silica is about 3, silica is therefore negatively charged at neutral pH and the predominant AA species are the zwitterions. This results in diminished adsorption due to repulsive interactions of the carboxylate group of the AA with the deprotonated silanol groups of quartz. The protonated amino group is essential for adsorption of AAs on quartz surfaces even in non-aqueous systems [44]. Consequently, cationic AAs such as Arg and Lys have more affinity for silica over a wide pH range. The minimum mineral load for significant adsorption of AAs other than Arg on quartz sand was 1 g/mL.

Figure 4.1a shows an isotherm for the adsorption of a racemic Arg solution on 0.1 g/mL sand quartz. The adsorbed AAs (Q=nmol/m^2) were calculated according to

$$Q = \frac{C_0 - C_e}{ML \times SSA} \qquad \textit{(Equation 4.1)}$$

where C_0 is the initial concentration of AA (nmol/mL), C_e is the concentration of AA in the supernatant after adsorption (nmol/mL), ML is the mineral load (g/mL) and SSA is the specific surface area (m^2/g).

D-Arg appeared to be adsorbed more than L-Arg over the whole concentration range in particular at low equilibrium concentrations. Nevertheless, this interpretation is rather qualitative and experiments discussed in the following paragraphs were conducted at least in triplicate to assess the statistical significance of the data. The Langmuir isotherm fitted the data (Figure 4.1b); L-Arg saturated quartz adsorption sites at concentrations greater than 5 μM reaching a maximum coverage of 104 nmol/m^2. D-Arg behaved similarly to L-Arg, but due to uncertainty of the data at high concentrations the maximum calculated coverage was 73 nmol/m^2.

In multiple later experiments, the adsorption of racemic Arg solutions on quartz sand was studied as a function of pH (Figure 4.2). The amounts of adsorbed Arg in Figure 4.2 are reported as the surface area normalized values. Where possible, surface area normalized adsorption values were calculated for adsorption of AAs on different minerals so that comparison of their sorptive capacity could be carried out. As expected from the model proposed by Vlasova[15], the amount of Arg adsorbed increased with pH owing to a higher density of deprotonated silanol groups (SiO^-) on the surface of quartz that can interact with the cationic Arg species (AAH_2^+) according to:

$$SiO^- + AAH_2^+ \leftrightarrow SiO^- - AAH_2^+ \qquad \textit{(Equation 4.2)}$$

In this model, the interaction between the AA and SiO^- is electrostatic and therefore characterised by the formation of an outer sphere complex. Further evidence for this is the decreased adsorption of AAs with increasing ionic strengths. Fluctuations in the extents of adsorption of AAs among multiple experiments indicated that average adsorption values were subject to high variability. Hence, the average supernatant enantiomeric ratios (ER=D/L) are a better indicator of selectivity and were used to interpret enantioselective effects.

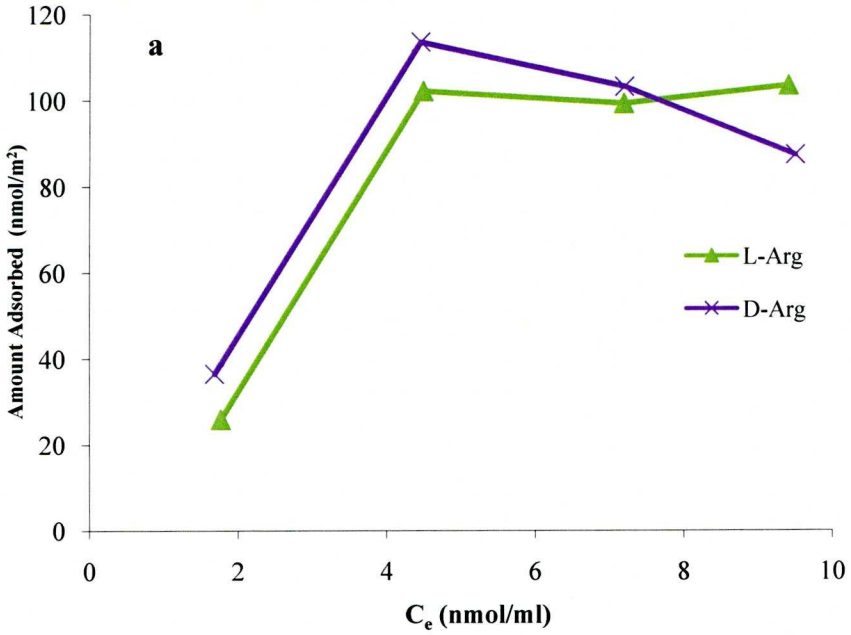

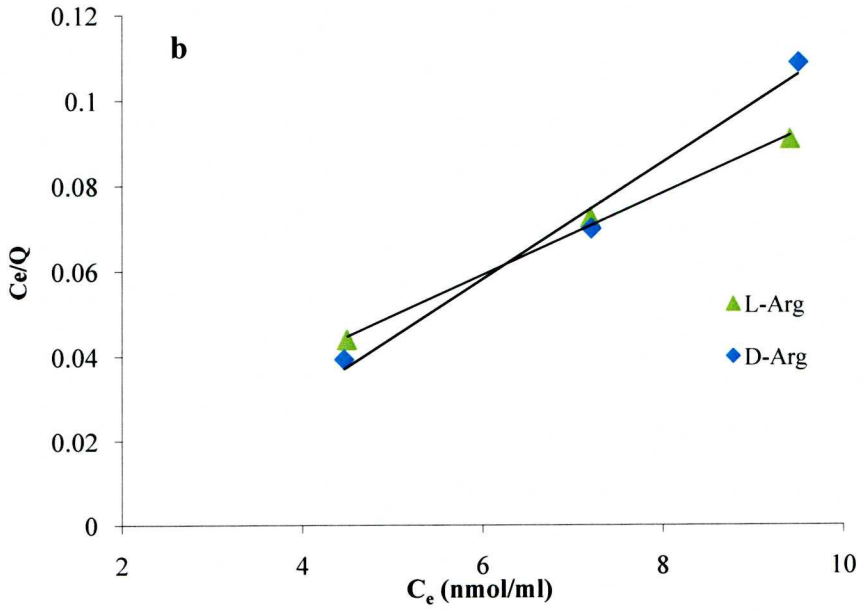

Figure 4.1. a.Adsorption isotherm of DL-Arg on quartz sand in an unbuffered system . Initial C_0 Arg = 2, 5, 8 and 10 µM. Mineral load=0.1 g/mL. pH Initial Arg solutions= 4.2. Ambient temperature. b. Data fit to the Langmuir isotherm. Q represents amount adsorbed and C_e is the equilibrium concentration after adsorption

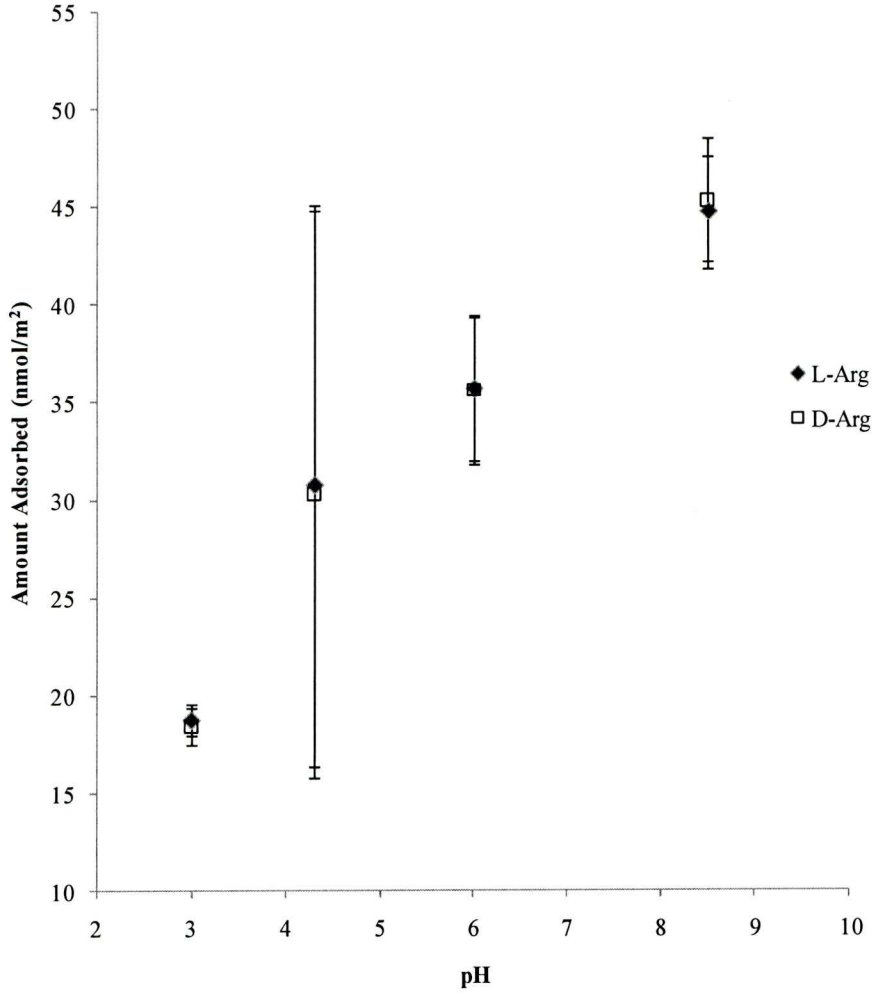

Figure 4.2. Influence of pH on the adsorption of DL-Arg on quartz sand. C_0 Arg = 5 μM. Mineral load=1 g/mL. Ambient temperature. Error bars correspond to 95% confidence intervals

Tests of hypothesis of equality of the means indicated that the null hypothesis could not be rejected for the quartz sand systems at pHs 3 and 6, but at pH 8.5 the mean *ER*s appeared to be different at the 95% significance level. At pH 8.5, D-Arg adsorbed preferentially over L-Arg on quartz sand (1 g/mL) as supported by an *ER* =0.985 ± 0.011 which is statistically different from the ER of the starting racemic solution of 1.000 ± 0.004 (Table 4.2, entry 1). The relevant statistical parameters suggesting a selective effect for Arg enantiomers on quartz sand are presented in Table 4.2, which also contains the information for other AA-mineral systems where selective effects were probable.

Table 4.2. Statistical parameters of mineral-AA systems displaying selective behaviour

	System[a]	AA	$t_{critical}$	T	P(T<=t) two-tail [b]	*ER* = D/L[c]	
						Initial solution	Mineral
1	Quartz Sand, (1g/mL), SC, pH 8.5	5 μM DL-Arg	2.262	-3.8586	<1%	1.000 ± 0.004(6)	0.985 ± 0.011(5)
2	Quartz Sand, (1g/mL), MC, pH 3	5 μM DL-Asp	2.776	-5.1446	<1%	1.000 ± 0.012(3)	0.953 ± 0.037(3)
3	Powdered *l*-quartz wafers, 0.4 g/mL, unbuffered	500 μM DL-Hist	2.776	-5.5244	<1%	1.000 ± 0.003(3)	1.007 ± 0.004(3)
4	Powdered *d*-quartz wafer, 0.4 g/mL, unbuffered	500 μM DL-Hist	2.776	-3.1004	3.6%	1.000 ± 0.003 (3)	1.010 ± 0.013 (3)
5	Powdered *d*-quartz synthetic, 0.4 g/mL, unbuffered	500 μM DL-Hist	2.776	-3.5822	2.3%	1.000 ± 0.003 (3)	1.004 ± 0.004 (3)
6	K10, 0.1 g/mL, MC, pH 3	5 μM DL-Asp	2.776	-2.6744	5.5%	1.004 ± 0.021 (3)	0.946 ± 0.091 (3)
7	K10, 0.1 g/mL, MC, pH 3	5 μM DL-Ser	2.776	2.1674	9.6%	0.995 ± 0.008 (3)	0.976 ± 0.036 (3)
8	K10, 0.3 g/mL, MC, pH 3	5 μM DL-Ser	2.776	-7.220	2.0%	0.995 ± 0.008 (3)	0.953 ± 0.024 (3)
9	K10, 0.3 g/mL, SC, pH 3	5 μM DL-Ser	2.571	-10.96	<1%	1.000 ± 0.006 (4)	0.933 ± 0.030 (3)
10	K10, 0.1 g/mL, SC, pH 3	500 μM DL-Arg	2.306	2.632	3%	1.000 ± 0.006 (5)	1.063 ± 0.066 (5)
11	Cu-K10, 0.3 g/mL,SC, pH 9	5 μM DL-Val	2.570	2.423	6%	0.999 ± 0.018 (2)	1.031 ± 0.018 (5)
12	Cu-Kao, 0.3 g/mL, SC, pH 9	5 μM DL-Val	2.4469	2.6272	3.9%	0.999 ± 0.016 (3)	0.964 ± 0.043 (5)

[a] SC: single component system, MC: multicomponent system. [b] P(T<=t) two-tail is the minimum probability value at which the null hypothesis can be rejected. The null hypothesis can be rejected if the probability of the observed difference occurring by chance is less than 5%. Thus, values below 1% are indicative of a high degree of confidence in the observed selective behaviour. [c] *ER* is the enantiomeric ratio of the D-enantiomer to the L-enantiomer in the supernatant after adsorption has taken place. Hence, D/L values greater than 1 indicate preferential adsorption of the L-enantiomer and D/L values below 1 indicate selective adsorption of the D- enantiomer. Values in parentheses indicate the number of replicates.

Finally, adsorption of a 5 μM multicomponent racemic mixture of Asp, Glu, Ser, Arg, and Val was conducted at pH 3 and 1 g/mL mineral load. By lowering the pH, the speciation of AAs changes with the cationic species being predominant. The silica surface is likely to have fewer deprotonated silanol functionalities, resulting in electrostatic forces of attraction. The gross percentage adsorption values of L-Asp, and D-Asp were 16.5 and 20.4%, respectively, and were statistically different at the 95% significance level (Table 4.2, entry 2). In contrast, L-Arg and D-Arg were both equally adsorbed at 21%. Ser and Val did not adsorb above 1%, which is within the uncertainties of the measurement, so selective adsorption could not be assessed for these AAs.

It is not clear why D-Asp and D-Arg tended to interact preferentially at quartz sand at pH 8.5 and 3, respectively (Table 4.2, entries 1 and 2). One speculation is that this polycrystalline mineral might possess an intrinsic asymmetry. Sajewicz *et al.*[59] hypothesized that unmodified silica gel, a synthetic highly porous material used for chromatographic applications, might be crystalline and chiral (i.e., made up of *l*- and *d*-quartz particles at a ratio different from 50:50) in order to explain the deviation of *S*-ibuprofen and *S*-naproxen vertical migration tracks during thin layer chromatography experiments. This possibility cannot be discounted in our natural quartz sand system and may add to the influence of defects and minor impurities on the observed tendencies as previously suggested by Wedyan and Preston[97]. Scanning electron micrographs of the samples showed that the sand is a coarse material with average particle size of 330 μm. SEM with energy dispersive X-ray analysis (EDX) of random untreated sand particles allowed the identification of a Zr inclusion, a pyrite (FeS_2) framboid and a potassium feldspar ($KAlSi_3O_8$) overgrowth along with sodium chloride salts, corroborating the presence of impurities in the natural sand.

In summary, the systems Asp- and Arg-quartz sand combinations appear promising for further studies of preferential adsorption at acidic and basic pH values and also to look at potential oligomerization reactions driven by wet-dry cycles. The question of whether selective adsorption of one AA enantiomer over its counterpart on a mineral influences the chirality of the resulting peptides is very relevant. Recently, Ota *et al.* [113] reported oligomerization of Gly on montmorillonite and silica at acidic pH. The highest yields of di-, tri-, and tetra-Gly peptides occurred in the silica system at pH 2.6, suggesting that silica is an even a better catalyst than montmorillonite under appropriate reaction conditions.

4.1.1.2 Adsorption of Racemic AAs on Powdered Synthetic Quartz

The powdered synthetic quartz used in these experiments was found to be right-handed (*d*-quartz) as determined by the conoscopic method summarised in Appendix 2. Batch experiments were setup similarly to the quartz sand system. Although the material was considerably finer than the quartz sand there was no measurable adsorption of DL-Asp, DL-Glu, DL-Ser, DL-Arg, DL-Ala, DL-Val, DL-Met, DL-Phe, DL-Ile, DL-Leu, or Gly onto this material (0.1g/mL) from 10 μM unbuffered aqueous solutions during a 24-h equilibration period. L- and D-Hist adsorbed to the extent of 8.8 and 8.5%, respectively, from 500 μM racemic aqueous solution with a mineral load of 0.4 g/mL (see Figure 4.3). The D/L ratios of the equilibrium supernatant concentrations are plotted on a secondary axis in Figure 4.3. Statistically, the mean *ER*s of supernatant and initial Hist solution were significantly different at the 95% confidence interval (Table 4.2, entry 5). Thus, L-Hist adsorbed preferentially over D-Hist on *d*-quartz.

The influence of pH on the adsorption of 5 μM Arg on synthetic powdered quartz was also examined. At a solid-liquid ratio of 1 g/mL, Arg enantiomers were 20% and 33% adsorbed at pH 6 and 8, respectively, which contrasts with 40% and 50% gross adsorption values on quartz sand at the same pHs and initial concentration. Statistically there were no significant differences in the mean values of the adsorbed amounts of L- and D-Arg or the average supernatant *ER* compared to the initial *ER* of the initial racemic solution (*ER*=1) at pH 3 and 6. A possible explanation for the variation of gross adsorption of Arg between powdered synthetic quartz and quartz sand could be that the former has a slightly higher pH_{pzc}, and therefore the density of deprotonated silanol groups is smaller in comparison to that of the natural material at the same pH values.

To illustrate this better, the speciation of mineral hydroxyl groups (MOH^{2+} and MO^-) vs. pH at low and high ionic strengths for oxides and oxy-hydroxides in aqueous solutions is displayed in Figure 4.4.

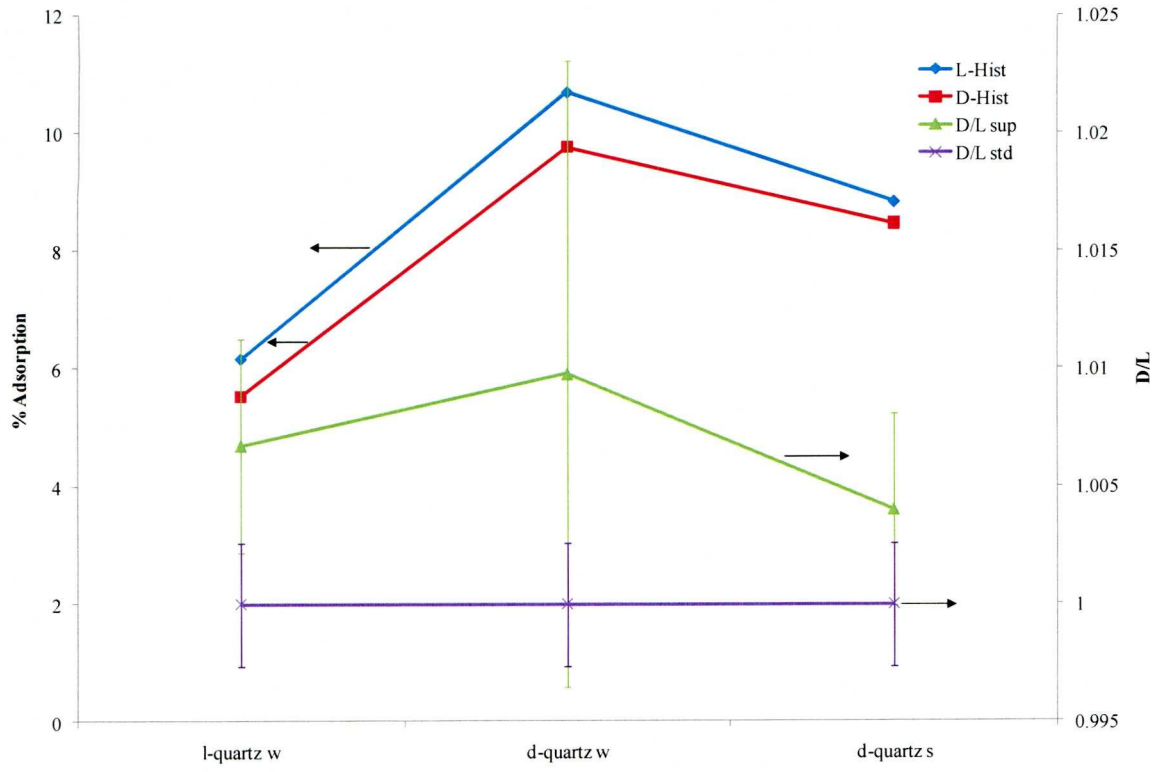

Figure 4.3. % Adsorption of racemic 500 µM DL-Hist from unbuffered aqueous solutions onto powdered *d*-synthetic quartz (*d*-quartz s), and powdered *d*- and *l*-synthetic quartz wafers (*d*-quartz w, and *l*-quartz w, respectively). Initial pH of DL-Hist = 5.45. Mineral load=0.4 g/mL. Triplicate experiments. Error bars represent 95% confidence intervals

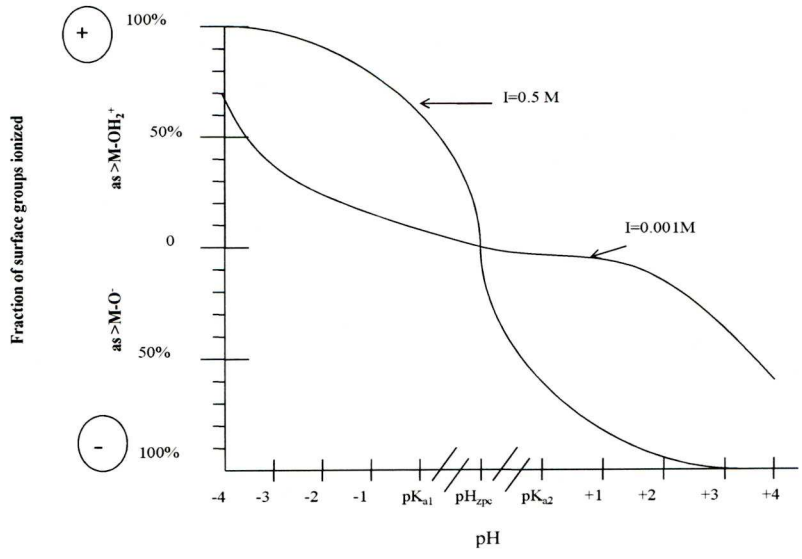

Figure 4.4. Variation of surface charge on a solid oxide as a function of pH and I [114]

The pH_{pzc} of a mineral depicted in Figure 4.4 is halfway between the intrinsic acidic constants pK_{a1}^{int} and pK_{a2}^{int} of the solid determined using different methods, which for silica are equal to -3 and 7[114]. Nevertheless, these intrinsic constants can vary slightly for different silica materials [115]. Figure 4.4 clearly shows that the cation exchange capacity (CEC) of silica in mol/m^2 is highly dependent on pH. Note that the estimated CEC of quartz and amorphous silica is 8×10^{-8} mol/m^2 (80 $nmol/m^2$) at pH 7, I=0.01M, and T= 293 K, assuming a total concentration of MOH=2×10^{-6} mol/m^2 [114], a value that compares quite well with the adsorptive capacity of quartz sand (Figures 4.1 and 4.2).

Another possible explanation for the dissimilar extents of Arg adsorption on quartz sand and synthetic quartz could be a decrease in the surface area for adsorption owing to agglomeration of fine particles of the synthetic material, given that the ratio of mineral to aqueous solution was quite high.

Percentages of L-and D-Arg adsorption on *d*-quartz in MeOH (1 g/mL) exceeded 90% highlighting the relevance of surface and biomolecule charge on physisorption of ionized molecules at silica in aqueous systems. However in this case concentrations were near the detection limit, hindering identification of selective effects. The mechanism of Arg adsorption on quartz from methanol probably involves hydrogen bonding with the surface in a way similar to that of neutral Ala adsorption on quartz depicted in Figure 1.14 [19]. Molecular modelling of the interaction of methanol and methylamine (compounds that have some of the functional groups of AAs) at a hydroxylated quartz surface has shown that a hydrogen bond on the bare silica surface is broken and two hydrogen bonds between the surface and the adsorbed molecules are formed[116]. Han *et al.* suggested that understanding how methanol and methylamine interact at a hydroxylated chiral crystalline quartz surface is a preliminary step towards understanding the adsorption of chiral AAs on such surfaces[116].

Finally, L-Glu, L-Arg, L-Val, and L-Ser consistently adsorbed more than the D-enantiomers at pH 3 from an aqueous 5μM multicomponent mixture and 0.7g/mL *d*-quartz load, giving D-enriched supernatants (Figure 4.5).

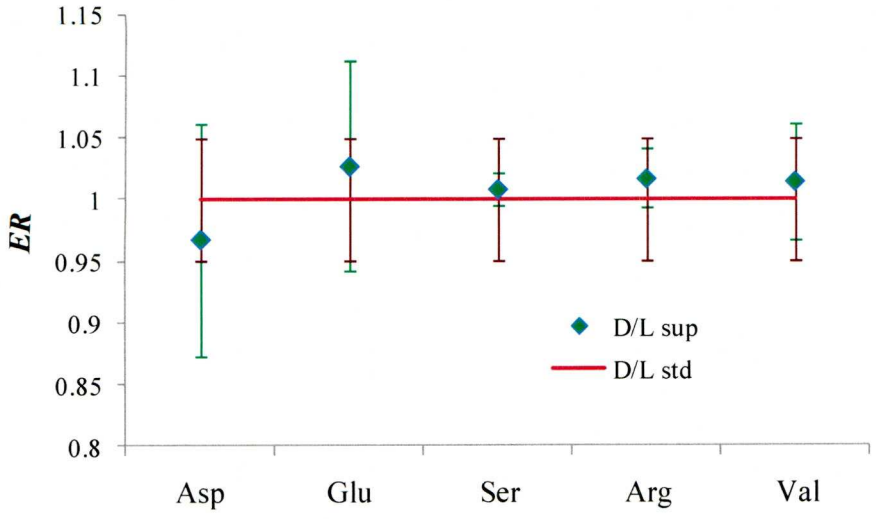

Figure 4.5. *ER* of supernatants after 24 h adsorption of 5 μM racemic mixtures of Asp, Glu, Ser, Arg, and Val on synthetic *d*-quartz. pH=3. Mineral load=0.7 g/mL

4.1.1.3 Adsorption of DL*-Arg and* DL*-Asp on Synthetic Single Quartz Wafers*

Multiple parallel adsorption experiments were conducted with thoroughly cleaned *l*- and *d*-single quartz wafer crystals (Section 3.3). The heat-sterilized wafers were arranged inside a clean Teflon beaker containing racemic aqueous solutions of Arg and Asp at different concentrations (Table 4.3) and the system was allowed to equilibrate for 24 h. Immersion of *l*- and *d*-quartz wafers in acidic 2×10^{-3} M DL-Asp, which is a rather concentrated solution, was conducted in order to measure the amount of adsorbed AAs on the surface directly by extraction with 0.1 M HCl according to the procedure by Hazen[26] (Section 3.5.2.2). Chromatographic analysis of the extracts showed that the concentrations of D- and L-Asp were below the quantification limit, indicating that either no adsorption occurred or that adsorption was so weak that water desorbed the AAs. Adsorption was undetectable in the remaining systems (Table 4.2, entries 2-4) except for the Arg-quartz wafer systems at pH 8.50 (Table 4.2, entry 5). In this high pH system, 4.7% of L-Arg and 3.7% D-Arg adsorbed on *l*-quartz wafer surfaces whereas 6% L-Arg and 5.9% D-Arg adsorbed on *d*-quartz wafer surfaces as determined from the change in supernatant concentrations. The null hypothesis $(D/L)_{Arg\text{-}l\text{- or }d\text{-quartz}} = (D/L)_{ArgInitialSolution}$ could not be rejected at the 95% significance meaning that there is no evidence to suggest that the mean enantiomeric ratios differ

between the *l*-or *d*-quartz systems and the initial AA solution and therefore selective effects are unlikely.

Table 4.3. Supernatant *ER* ratios for adsorption of DL-Arg and DL-Asp acid on synthetic quartz wafers

Entry	No. Wafers	Immersion System	*ER* = D/L ratio [a]		
			Standard	*l*-quartz wafer	*d*-quartz wafer
1	4	2000 μM DL-Asp pH 2.80	1.000 ± 0.009 (9)	1.031 ± 0.016 (4)	1.014 ± 0.005 (4)
2	2	5 μM DL-Asp pH 2.80	1.000 ± 0.007 (5)	0.999 ± 0.005 (4)	0.997 ± 0.008 (4)
3	2	5 μM DL-Arg pH 2.80	0.999 ± 0.012 (5)	1.021 ± 0.008 (4)	0.996 ± 0.009 (5)
4	4	5 μM DL-Arg in MeOH	1.000 ± 0.012 (9)	1.001 ± 0.012 (5)	1.004 ± 0.003 (5)
5	10	5 μM DL-Arg pH 8.50	1.007 ± 0.031 (3)	1.001 ± 0.026 (3)	1.010 ± 0.039 (3)

[a] Uncertainties correspond to 95 % confidence intervals. The number of replicates is given in parentheses.

4.1.1.4 Adsorption of racemic AAs on powdered synthetic quartz wafers

As discussed before, the adsorption of Asp and Arg on the single crystal wafers was small owing to the low combined surface area of the wafers. To circumvent this difficulty, thin synthetic quartz wafers were milled and cleaned according to the procedure outlined in Section 3.3 to obtain a powdered material of higher surface area.

Adsorption of 5 μM multicomponent racemic mixtures of Asp, Glu, Ser, Arg, and Val on powdered synthetic *l*- and *d*-quartz wafers (0.7g/mL load) at pH 3 resulted in highly irreproducible data. Results from duplicate experiments with a powdered 1:1 mix of *l*- and *d*-synthetic quartz wafers, each at 0.3 g/mL to give a total load of 0.6 g/mL, immersed in the above racemic solution are presented in Figure 4.6. Although the system contained equal amounts of the powdered single crystals, D-AAs, excluding D-Arg, had a tendency to exhibit a higher affinity for the 1:1 *l*- to *d*-quartz mix. Undoubtedly, more research is needed to assess any selective effective on powdered *l*- and *d*-quartz wafers which were used as sorbents in parallel experiments to test for possible reversal in preferential adsorption, i.e. L-AA adsorbing preferentially on *d*-quartz against D-AA interacting preferentially at *l*-quartz. Enantioselective adsorption of Hist enantiomers on *l*- and *d*-quartz wafers cannot be ruled out since the statistical test for *ER*s means for both substrates resulted in rejection of the null hypothesis (Table 4.2, entries 3 and 4). Despite their intrinsic chirality, *l*- and *d*-surfaces displayed higher affinity for L-Hist as seen in Figure 4.3.

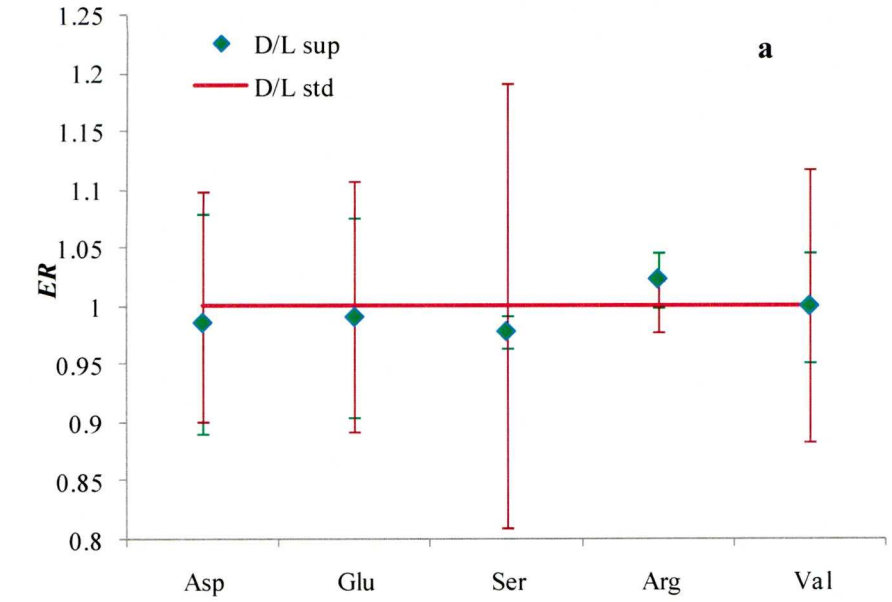

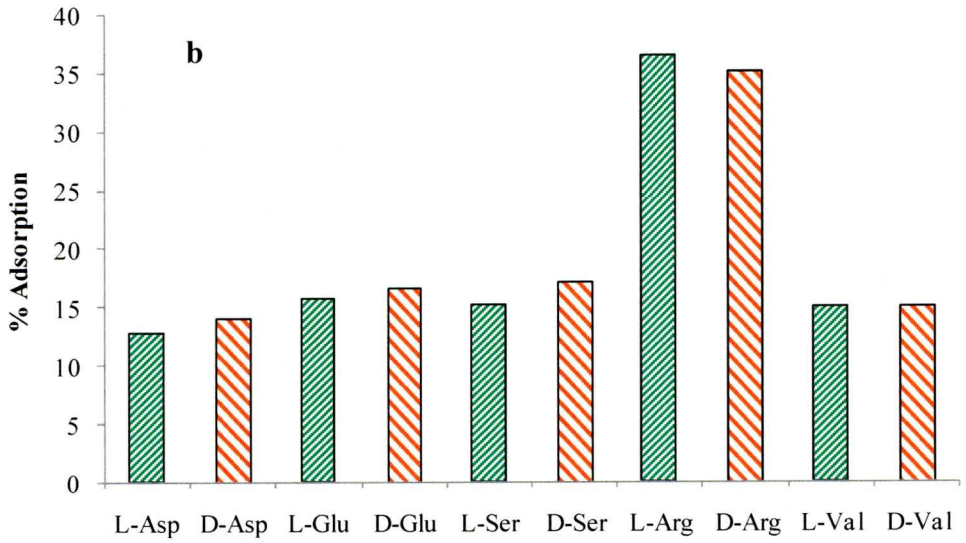

Figure 4.6. a. *ER* of supernatants after 24 h adsorption of 5 μM racemic mixtures of Asp, Glu, Ser, Arg, and Val on 1:1 mix of powdered *d*- and *l*-quartz wafers. b. % adsorption of AA enantiomers on 1:1 mix of powdered *d*- and *l*-quartz wafers. pH=3. Combined mineral load=0.6 g/mL

One important outcome of these experiments is that under controlled experimental conditions (Figure 4.6b), AAs other than Lys and Arg are adsorbed onto quartz surfaces. Molecular level techniques such as microarray analysis coupled with time of flight secondary ion mass spectroscopy (ToF-SIMS) can then be used to examine the adsorption of a variety of AAs on enantiomorphic quartz surfaces[58].

Clearly, AA chemical structure, concentration and solution pH play an important role in determining the relative abundance of AAs on quartz (Figure 4.6b). Ongoing experiments by Stievano *et al.*[117] are focusing on the effect that markedly different extents of adsorption of AAs from aqueous multicomponent mixtures might have on the polymerization of adsorbed AAs on silica driven by heating and wet-dry cycles.

4.1.1.5 Adsorption of DL-Asp and DL-Arg on Natural Single Quartz Crystals

The interaction of racemic Asp (2×10^{-3}M) with natural *l*- and *d*-quartz crystals in acidic pH aqueous solutions was also studied. These experiments were designed in accordance with the procedure outlined by Churchill *et al.*[26] for investigating adsorption at crystallographic faces of a single mineral by extracting the adsorbed material with 0.1 M HCl and analysing the extract for the enantiomeric ratio. In the case of quartz, electrostatic interactions between positively charged AA and negatively charged silica predominate and adsorbed material is held only weakly at the surface. Therefore, rinsing the crystal repeatedly with acidic aqueous solution resulted in removal of the weakly adsorbed AA. Analysis of the extracts supported this speculation. For example, this effect was shown in the adsorption of 0.002 M racemic DL-Asp (pH 2.8) on *l*- and *d*-quartz natural crystals at room temperature. After 24 h the crystals were treated as described in Section 3.5.2. The HCl extracts of the crystallographic faces of the two crystals, eight faces per crystal, were analysed for Asp. Only one prismatic face of *d*-quartz, Area = 7.0 cm^2, had measurable amounts of the Asp enantiomers (Figure 4.7). The enantiomeric ratio of adsorbed D-Asp to L-Asp for this face was 1.01 (*ee*=0.5% D-Asp), which is within the uncertainty of the analytical method.

The supernatant D/L ratios for *l*- and *d*-quartz systems were 1.008 and 1.005, respectively. Thus, any minor adsorption behaviour on the surface of the crystals is probably not reflected in the D/L ratios of the supernatants because of the high initial concentration of racemic Asp. The negligible adsorption of Asp onto quartz at low pH suggests that rinsing the crystal at the pH of immersion was sufficient to remove any weakly adsorbed material. Moreover, the small surface area of the quartz faces was another limiting condition when conducting adsorption of AAs onto single crystals with either the depletion or direct extraction method. To circumvent this problem, the

selective adsorption of Lys enantiomers on faceted quartz was successfully demonstrated by using a standard microarray technique with fluorescence tagging[58]. L-Lys was found to bind preferentially on the (100) face of *d*-quartz. Carminic acid (right-handed molecule) also was stabilised on a prismatic $(10\bar{1}0)$ *l*-quartz surface by 5 kJ/mol with respect to its counterpart *d*-quartz surface[57]. This suggests that selective interactions of biomolecules at quartz are possible, albeit weak as documented in the literature and reported in this research.

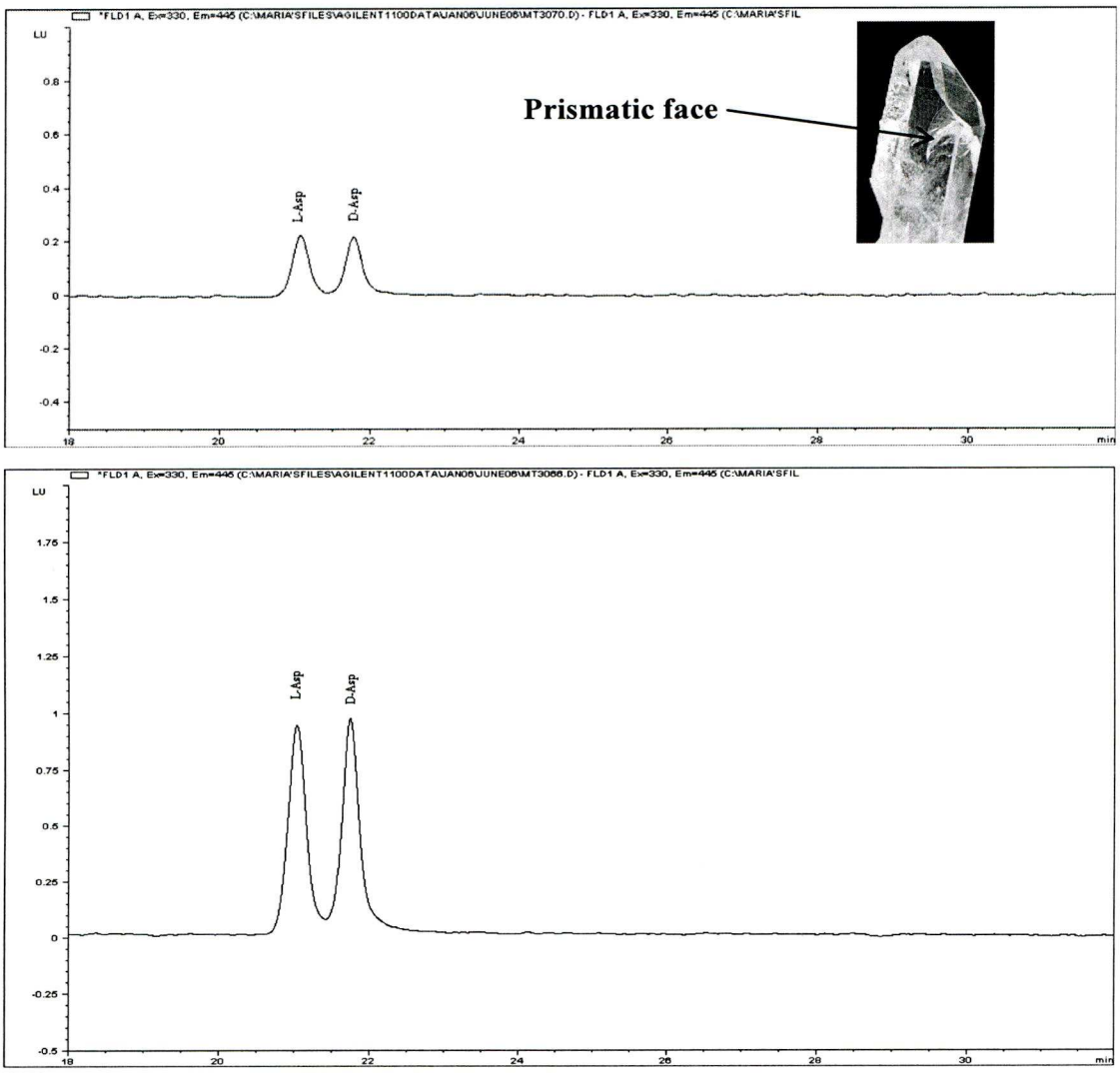

Figure 4.7. Chromatogram of a. DL-Asp acid adsorbed on *d*-quartz and b. 2 μM DL-Asp standard

Starting from the knowledge that Arg binds to quartz surfaces to a greater extent than other protein AAs, *l*- and *d*-natural quartz crystals were immersed for 24 h in a 5 μM DL-Arg buffered solution at pH 8.5. Analysis of the supernatants showed that approximately 1.77% D-Arg and 1.76% L-Arg adsorbed on *l*-quartz whereas no

adsorption took place on *d*-quartz. The enantiomeric D/L ratios of the initial racemic solution and the *l*-quartz supernatant were 1.002 ± 0.002 and 0.9999 ± 0.004, but these values are not statistically different at the 95% confidence interval. Adsorption of 5 μM DL-Arg, prepared in methanol, on the handed crystals was also conducted, but there was no adsorption under these conditions as determined by the depletion method.

4.1.2. Adsorption of Racemic AAs on Clays

4.1.2.1. Adsorption of Racemic AAs on Montmorillonite K10 (K10)

The adsorption of racemic AA mixtures on montmorillonite K10, hereafter referred to as K10, was conducted initially at acidic pH (*ca* 3) to screen potential combinations leading to selective adsorption. To set up the experiments, 500 μL of a 5 μM multicomponent mixture of Asp, Glu, Ser, and Val was added to pre-weighed amounts of K10 (0.001g, 0.05, 0.15, and 0.25 g) in clean microcentrifuge vials. Vials were wrapped in foil and shaken at room temperature for a 24 h period after which the solid pellet was settled by centrifugation.

Figure 4.8 illustrates that the acidic AAs Asp and Glu had the highest affinities for K10 whereas the hydrophilic Ser adsorbed the least. DL-Arg, also present in the mixture, was completely adsorbed on the surface as evidenced by non-measurable concentrations of the enantiomers in the supernatant after 24 h.

Regardless of the initial pH of the AA solutions, the measured pH of the K10-water suspension was 3 due to the inherent acidity of this clay. Therefore, AAs exist in the cationic form in the vicinity of the clay. Isomorphic substitution of Al^{3+} for Mg^{2+} in the octahedral layer of montmorillonites results in excess negative charge that is balanced by hydrated exchangeable cations in the interlayer (mostly Ca^{2+}, Mg^{2+}, and Na^{+}) (Figure 1.9). In addition the edges possess variable charge as a function of pH due to due to the presence of hydroxyl groups that participate in acid-base reactions. Consequently, when addressing the interaction of AAs with montmorillonite, three sorption scenarios are possible: (1) ion-exchange reactions between the cationic form of the AA and the natural cations in the interlayer (Na^{+}, K^{+}, Mg^{2+} or Ca^{2+}), (2) complex formation between AA and interlayer cations with possible stabilisation of the complex via hydrogen bonding interactions of amino groups with siloxane (Si-O-Si) of the tetrahedral sheet, and (3) AA reaction with silanol and aluminol groups on the edges depicted in Figure 4.9.

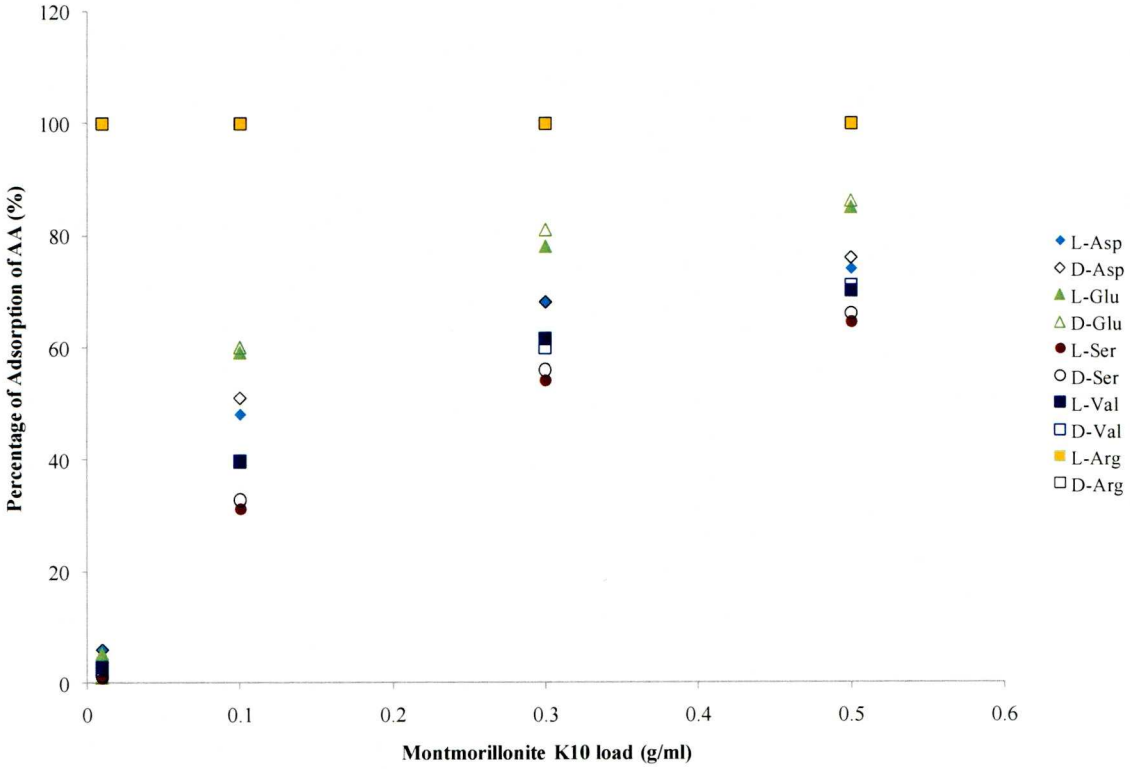

Figure 4.8. Percentage of adsorption of AA vs. mineral load. Solution pH= 3, C_{0AA}=5μM

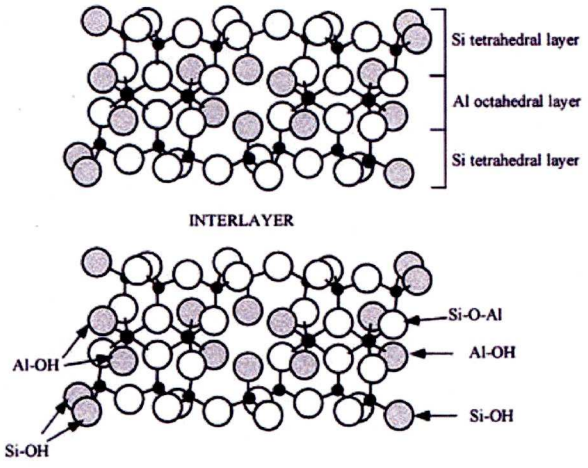

Figure 4.9. The structure of montmorillonite clay showing the possible functional groups where AA adsorption might take place at the edge sites. The shaded circles represent hydroxyl groups, the unshaded circles represent oxygen atoms and the dark circles represent the central atoms in the tetrahedral layer (Si or isomorphically substituted metals) or octahedral layer (Al or isomorphically substituted metals). Image after Morton *et al.*[118]

K10 is an acidic clay prepared by calcination and washing with mineral acid (Sigma-Aldrich proprietary process). The cation exchange capacity (CEC) of the raw

K10 and the calcined K10 (T=400°C), used in the adsorption experiments, was determined by the copper ethylenediamine method with atomic absorption spectroscopy[119] In this technique, CEC is measured by exchanging the natural inorganic cations for bis(ethylenediamino) Cu cations [$Cu(en)_2^{2+}$]. The values obtained were 84 and 71 milliequivalents (meq) per 100 g of clay for the raw and calcined material respectively, indicating that heating had just a minor effect on the exchange capacity. Heating of the clay to high temperatures can lead to collapse of the interlayer as the water is driven out[120]; nullifying the Brønsted acidity (proton donor) which is associated with the interlayer and catalytic activity of acid-treated clays, but the amorphous solid retains Lewis acidity (edge sites, electron acceptor). In fact, the Lewis:Brønsted acidity ratio of metal-doped K10 is greatly affected by calcination (T > 500°C)[121]. Calcination eliminated the Brønsted acidity of the clay. Moreover, silanization of calcined Cu(II)-K10 and Fe(III)-K10 led to end-capped substrates with even lower acidity, which was explained by a decrease in the number of Lewis acid sites such as hydroxyl groups whose Lewis acid properties are associated with the formation of hydrogen bonds[122].

A recent study reported that the peak d_{001} of raw Sigma-Aldrich K10, determined from XRD analysis, was absent, suggesting layered structure collapse in agreement with previous analyses [120]. Therefore, it cannot be ruled out that K10 employed in this research has a disarranged framework despite the measured values of CEC. XRD patterns of a K10 sample indicated the presence of clay mineral of both the smectite and mica groups, albeit the smectite reflection peak at 2θ =6° (d_{001}=14.7 Å) was weak and broad, and a minor quartz phase[123]. In another study, K10 was characterized by XRD and two main phases crystalline phases were identified: (1) muscovite (primary phase with structural formula $KAl_2(Si_3Al)O_{10}(OH,F)_2$ and (2) montmorillonite A15 ($Ca_{0.2}(AlMg)_2Si_4O_{10}$ $(OH)_2.xH20$)[124]. Muscovite belongs to the mica mineral group and it is non-swelling clay because of the strong electrostatic attraction between successive crystalline layers (d_{002} = 9.942 Å). On the contrary, montmorillonite A15 is a 2:1 swelling clay with d_{001} = 14.458 Å.

In this research, raw K10 was size-fractioned in order to separate fractions with different particle sizes to identify their main mineral phases by X-ray diffraction analysis. For details regarding the size fractioning procedure and XRD experimental conditions the reader is referred to Appendix 3. XRD diffractograms were collected

on randomly oriented samples. The bulk material is made up of several crystalline phases, mainly mica (M), quartz (Q) and smectite (S) as seen in Figure 4.10a.

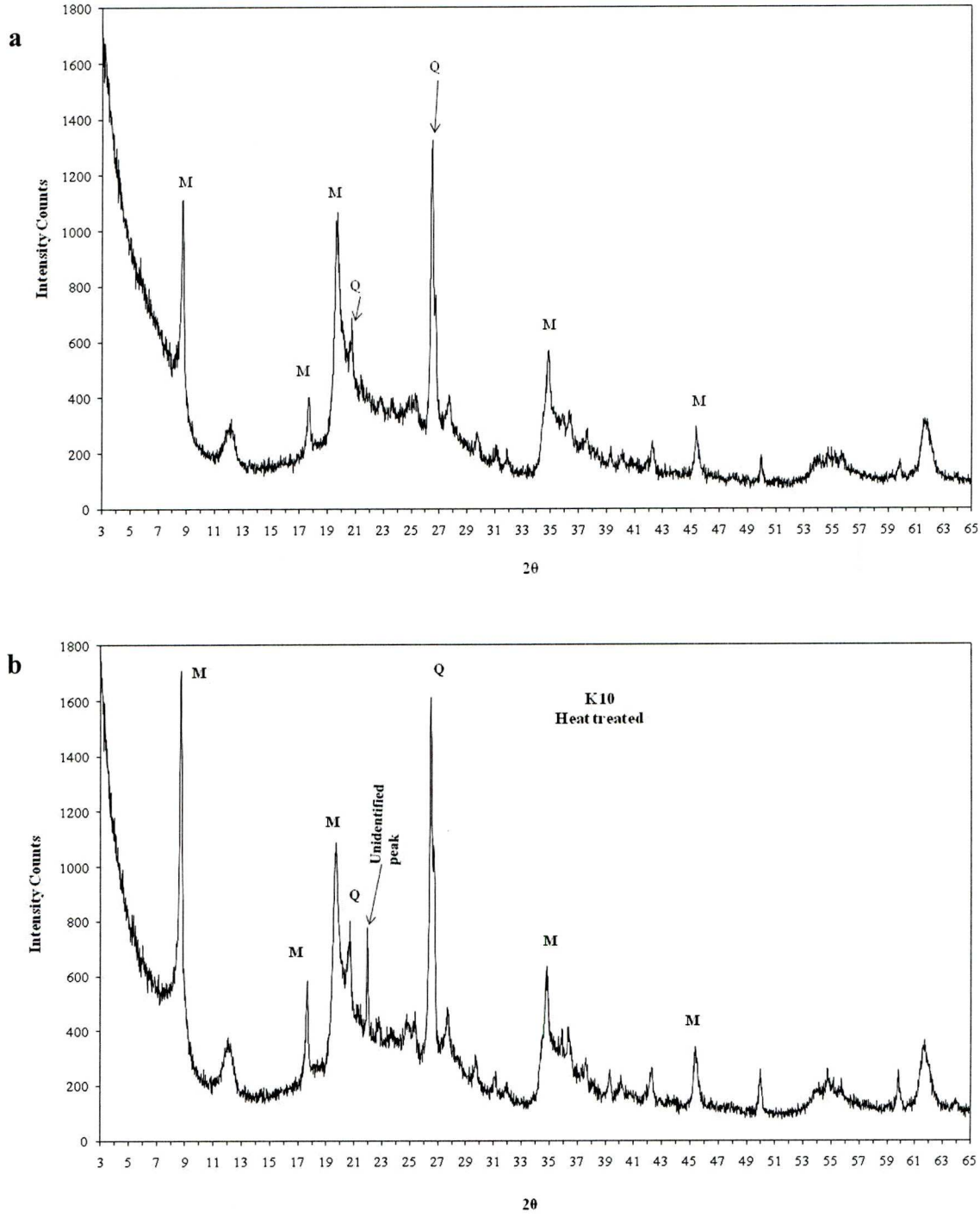

Figure 4.10. XRD pattern of a. bulk K10 and b. heat-treated K10 (Q= quartz; M= mica)

The less than 2 μm fraction contained smectite although the basal plane (001) reflection at $2\theta = 6°$ was very broad possibly because the clay crystallite contains just a few stacked layers giving very weak reflection at that plane orientation. However,

the reflection at 2θ = 19.8° which is characteristic of a (020) plane of a smectite clay suggests that this fraction is mostly smectite (Figure 4.11a). Moving progressively towards the coarser fractions such in the case of the 2-20 μm and >20 μm (Figures 4.11b and 4.11c), it can be seen that quartz and mica minerals are present in these fractions.

An estimate of the composition of K10 was made based on the chemical analysis of K10 reported by Jiang and Zeng[124] (see Appendix 3). The assumptions made in the estimation of the percentages of mica (muscovite), smectite (montmorillonite) and quartz are also compiled in Appendix 3. Thus, K10 can be assumed to be composed of 56.5% montmorillonite, 28.5% quartz, and 15% muscovite. This calculation contradicts the conclusion of Jiang and Zang about montmorillonite being a secondary phase of the commercial K10 material. Finally, the K10 used in the adsorption experiments was heated to 400°C to remove organic contamination. Therefore the XRD pattern of this heat treated K10 was also acquired (Figure 4.10b). The same diffraction lines as for the untreated material appeared in the diffractogram. However, the heat-treated sample had an extra diffraction line at 2θ = 22° suggesting that heating had an effect on one the existing crystalline phases most likely muscovite, but this just an speculation. Based on the above characteristics of K10, it seems plausible that AA adsorption takes place by different mechanisms: intercalation of AAs in the interlamellar space of montmorillonite, interaction at acid-base sites on the broken edges of the smectite/muscovite, and interaction at quartz surfaces.

Statistically, there was no evidence of enantioselective adsorption at the 95% confidence level for DL-Asp, DL-Glu, and DL-Val in the multicomponent system. The only exception was for DL-Ser at 0.3 g/mL which showed an *ER* of 0.953 (equivalent to an *ee* of 2.5%) in supernatant solution (L-excess), thus indicating the preferential adsorption of D-Ser (Table 4.2, entry 8). It is not clear why Ser selectivity was observed only at 0.3 g/mL in the multicomponent mixture. Note that the enantiomeric ratios of D-Ser to L-Ser between the standard and the 0.1 g/mL K10 sample were significantly different at approximately the 90% confidence level (Table 4.2, entry 7). Moreover, about 51% of D-Asp adsorbed vs. 48% L-Asp at 0.1 g/mL, the values being significantly different at a probability (*P*) of 0.055, pointing to a selective effect (Table 4.2, entry 6). Stereoselective deamination of the L-Asp and L-Glu enantiomers by Na-montmorillonite at pH 6 was reported by Siffert and Naidja[55].

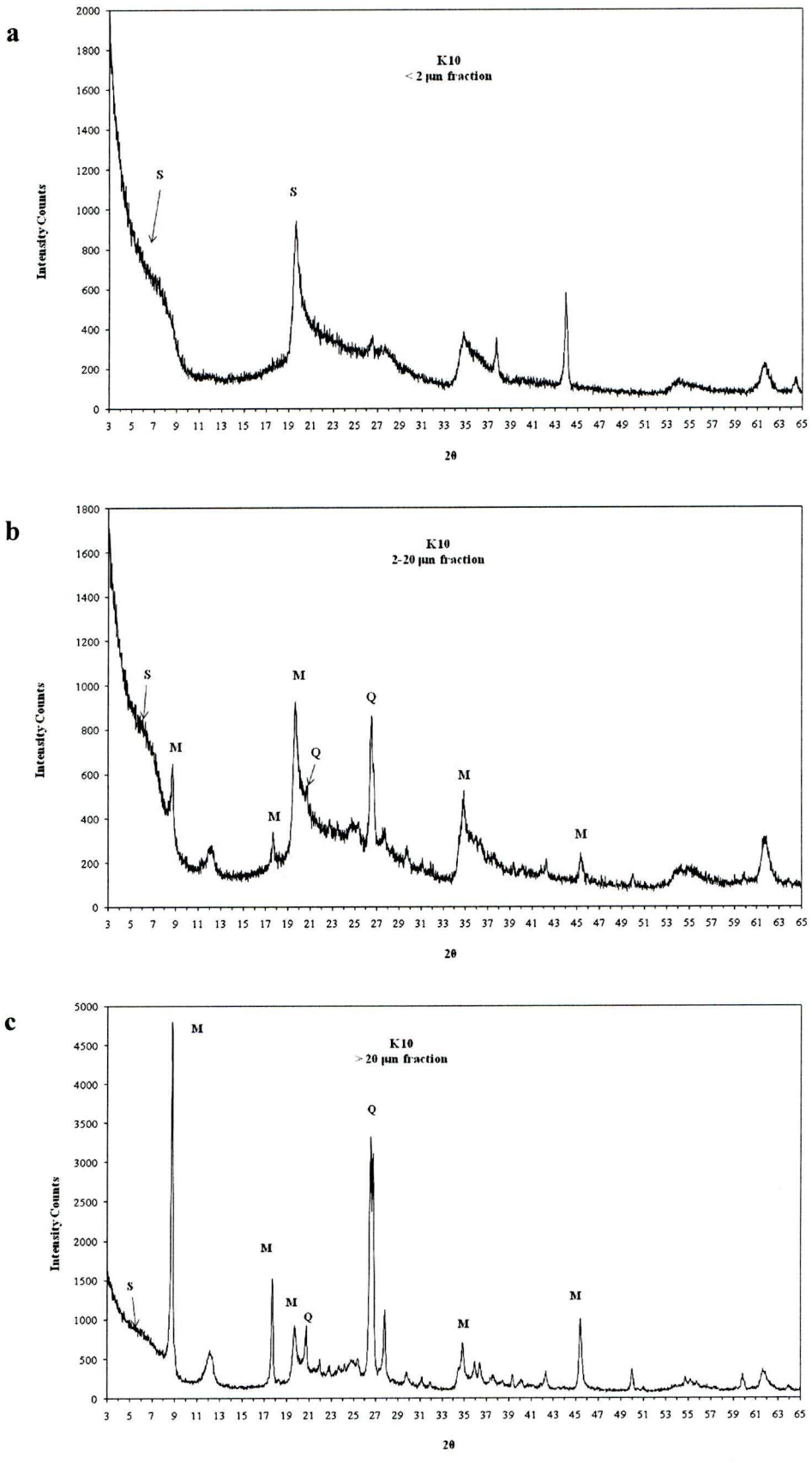

Figure 4.11. XRD pattern of a. < 2 µM K10 fraction, b. 2-20 µM K10 fraction, and c. > 20 µM K10 fraction (Q= quartz; M= mica; S= smectite)

The main product of Glu deamination is α-hydroxyglutaric acid. It is highly unlikely that L-Glu and L-Asp underwent decomposition by K10 due to the short duration of the adsorption experiment. Besides, the supernatant *ER*s of Asp and Glu were below 1, also indicating a slight abundance of L-Asp and L-Glu rather than their depletion by chemical transformation.

The system Ser-K10 was investigated in further detail by conducting multiple adsorption experiments of 5 μM racemic DL-Ser on this clay at pH 3. Interestingly, the selective effect was reproducible for a single component system at pH 3 (*L*-supernatant *ee* = 3.5%, *ER*=0.933) (Table 4.2, entry 9). To test the influence of Ser concentration on its probable selective interaction at K10, adsorption experiments were conducted with racemic mixtures of DL-Ser at higher concentrations (10, 30 and 50 μM) and the same K10 load of 0.3 g/mL at room temperature (see Figure 4.10). At a low initial concentration, D-ser clearly adsorbed preferentially on K10. Conversely, a reversal in selectivity was observed at higher initial concentrations of Ser, but it is unclear why this occurs. The *ER* values of strongly adsorbed fractions of 0.3 g/mL K10 equilibrated with 30 μM racemic Ser were consistently below 1 (0.92 ± 0.007, average of three clay pellets extracted with 1M HCl) indicating that L-Ser bonded preferentially on the surface, lending support to the observed change in selectivity with concentration.

In contrast to the experiments with quartz that exhibited saturation of reactive sites at low concentrations of Arg, the isotherm of Ser on K10 was linear at least in the 5-25 μM region (Figure 4.12). Physical adsorption, or partition of the solute between the bulk water and the water adhering to the clay surface (Stern-layer water) was the main mechanism responsible for Ser adsorption on calcium-montmorillonite and calcium-illite up to 0.2 M[29].

Presumably, Ser behaves in a similar way on K10, suggesting that the observed selectivity might be limited to the external or edge adsorption sites rather than to the interlayer. To get insight into the mechanism of bonding, a mass balance was carried out to quantify non-adsorbed, weakly and strongly adsorbed fractions of Ser on K10 in accordance with the procedure tested by Friebele *et al.* [42]. To accomplish this, the K10 pellet of a 24 h adsorption experiment in 5 μM racemic Ser was subjected to repeated washes with pH 3 solution to remove the weakly adsorbed material and the remaining pellet was extracted with 1 M HCl to recover the strongly adsorbed solute.

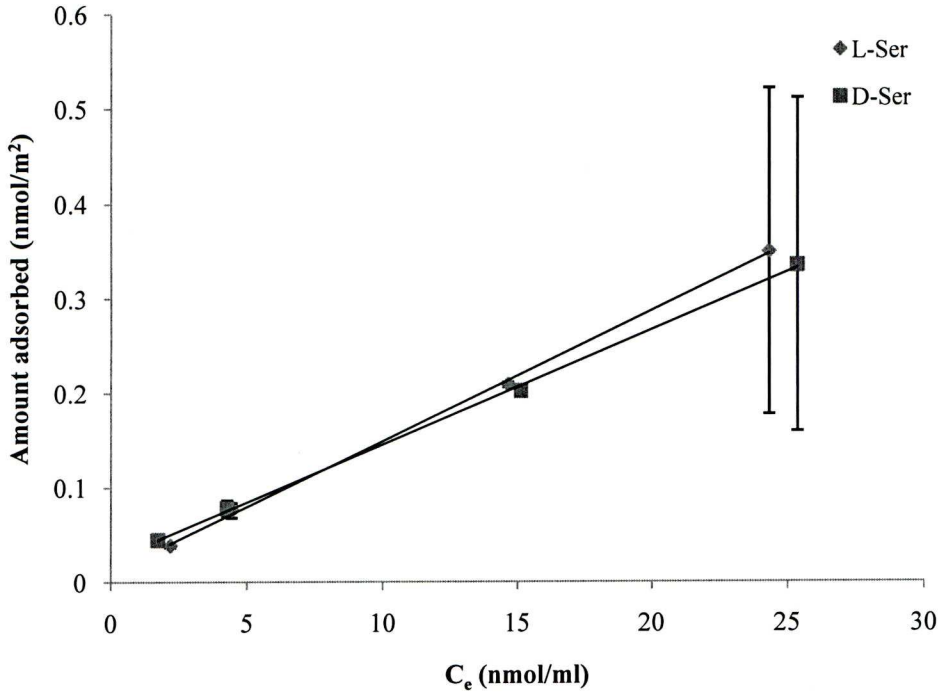

Figure 4.12. Adsorption isotherms of L- and D-Ser on K10 (0.3 g/mL). Solution pH= 3, C_{0AA}=5μM. Error bars represent 95% confidence intervals

The total recovery values were 111% and 103% for L-Ser and D-Ser, respectively, so initial material was accounted for by the measured weakly and non-adsorbed fractions. The slightly high recovery value for L-Ser might be due to contamination during the washing and extracting procedures. Approximately 48% L-Ser and 49.6% D-Ser were recovered in the weakly adsorbed fraction, whereas the non-adsorbed fraction values were 52% L-Ser and 41% D-Ser, but 9% D-Ser was strongly adsorbed whereas no L-Ser was found to be strongly adsobed. These results confirm, first that weak adsorption predominated in the adsorption of Ser on K10 at acidic pH and, second that a specific adsorption mechanism (i.e. covalent bond formation, coordinative bond) might be influencing the observed selectivity since a fraction of D-Ser was strongly adsorbed on the clay.

IR and XRD studies of Ser on K10 might help to clarify the nature of bonding and orientation of Ser on this substrate as a function of pH and concentration. A similar study on the adsorption of Asp on a Ca-montmorillonite concluded that this AA bonded weakly to hydrated Ca through a water bridge (outer sphere complex) and also by hydrogen bonding of the protonated amino group to the structural oxygen of the siloxane surfaces[125]. It could be speculated that Ser adsorbs on K10 akin to Asp on Ca-montmorillonite as depicted in Figure 4.13, where the hydroxyl group is shown

interacting with the siloxane basal plane. Cysteine which is analogous to Ser, but has a thiol group (-SH) instead of a hydroxyl, can theoretically bond to K10 via the –SH group and therefore may interact selectively with smectites. Indeed, IR spectra of bentonite-cysteine samples provided evidence that cysteine interacted with bentonites via both the amino (NH_3^+) and –SH groups [37].

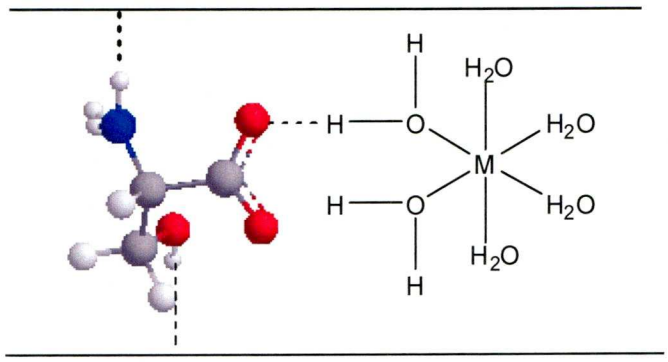

Figure 4.13. Schematic of potential Ser interaction in the interlayer of K10. Dashed lines depict hydrogen bonds. M is a cationic metal such as Ca^{2+} or Cu^{2+}. C atoms in grey, N is blue, O atoms are red, and H atoms are white

Arg and Val, which are characterized by basic and hydrophobic side chains, respectively, were chosen for further adsorption experiments with K10. 500 μM DL-Arg was adsorbed on 0.1 g/mL K10 at pH 3. In this case, the supernatant concentrations could be measured and gave an average solution enantiomeric excess of 3.7% in D-Arg (i.e. equivalent to L-Arg adsorbed preferentially on the surface). A statistically significant difference between *ER*s of sample supernatants and the standard was found with the *t*-test (Table 4.2, entry 10). The *ER* of the sample supernatant was 1.063 ± 0.066 whereas the *ER* of the standard was 1.000 ± 0.006.

The interaction of K10 and CuK10 with Val, an aliphatic AA whose side chain is a bulky isopropyl group, was addressed in detail at 0.3 g/mL mineral load. In the past, adsorption of Val enantiomers (C_0=100 μM) on a Na-montmorillonite was carefully investigated by GC and HPLC analysis of the adsorbed and non-adsorbed fractions with inconclusive results as to the enantioselectivity of this natural clay[42]. The recovery of Val enantiomers was stoichiometric, which prompted us to re-examine the issue of clay selectivity with diluted racemic DL-Val mixtures under different aqueous conditions.

First, Table 4.4 summarises the amounts of Val adsorbed on K10, Cu-K10, and montmorillonite KSF after 24 h adsorption. The measured pH values of the initial L, D- and DL-racemic Val solutions ranged between 5.5 and 5.7 which are close to the isoelectric pH of 5.96 where Val is in the zwitterionic form. The pH values of the K10 and KSF suspensions in water were about 3 and 2, and were unchanged after adsorption of Val. Therefore, cationic Val or the protonated amino species were the most likely species sorbed on the clay, either in the interlayer or on aluminol/silanol sites at the edges.

The extent of adsorption of L- and D-Val on K10 was independent of pH and the presence of other AAs, i.e, about 60% grosss adsorption of each enantiomer in single and multicomponent mixtures (Table 4.2, entries 1-4). This is consistent with data reported by Nagy and Konya who found only a slight effect of pH on the adsorption of Val on cation-exchanged montmorillonites [86]. Parallel experiments with L- and D-Val adsorbing on the clays were conducted to check for other processes (e.g. hydrolysis and racemisation)[126] that might bias the results when enantiomers of Val adsorbed from racemic mixtures. L- and D-Val adsorbed to the same extent on K10, CuK10 and KSF within the uncertainty of the measurements (entries 1 and 2 for K10, entries 7 and 8 for CuK10, and entries 12 and 13 for KSF).

The amounts of Val adsorbed decreased two-fold at high ionic strength (Table 4.2, entries 3 and 5) suggesting that electrostatic interactions are relevant in the K10-Val system. This is probably due to inorganic seawater cations such as Na^+ competing with cationic Val for sites at the clay surface. The abundance of AAs on the surface of K10 in seawater clearly depended on the type of AA. Affinity for the surface followed the order Arg>Glu>Val> Ser (Figure 4.14) in accord with the results by Benetoli *et al.* [37].

Cu-exchanged K10 was also used as an adsorbent of racemic mixtures of DL-Val to test the influence of Cu possibly intercalated in the interlamellar space of the clay on the adsorption of enantiomers of Val. Previous studies have shown that the extent of adsorption of AAs on homoionic natural clays decreases in the following order: Cu^{2+}>Ni^{2+}>Zn^{2+}>Na^+ because the stability constants of Cu^{2+}-AA complexes are higher than those of the other metal-AA complexes.

Table 4.4. Amounts of Val enantiomers adsorbed on K10, CuK10, and KSF at different experimental conditions. Errors are reported as 95% confidence intervals

Entry	Type of Montmorillonite	SC or MC[a]	pH[b]	I(M)[c]	Amount adsorbed (nmol/m^2)		ER_{ads}[d]
					L	D	
1	K10	SC (L)	unbuffered		0.0402 ±0.0005		
2	K10	SC(D)	unbuffered	0		0.0405±0.0012	1.007
3	K10	SC(DL)	unbuffered	0	0.0393 ± 0.0009	0.0411±0.0012	1.046 (1.039 - 1.054)
4	K10	MC(DL)	3	0	0.042 ± 0.008	0.041±0.011	0.969 (0.88 -1.02)
5	K10	SC(DL)	unbuffered	0.5	0.026 ± 0.0028	0.027±0.002	1.038 (1.033 - 1.054)
6	K10	MC(DL)	unbuffered	0.5	0.0067 ± 0.007	0.0068±0.007	1.007 (0.9416 - 1.143)
7	Cu-K10	SC(L)	unbuffered	0	0.0442 ± 0.0004		
8	Cu-K10	SC(D)	unbuffered	0		0.0444 ±0.0008	1.005
9	Cu-K10	SC(DL)	unbuffered	0	0.0438 ± 0.001	0.0436 ± 0.0012	1.009 (0.988 - 1.005)
10	Cu-K10	SC(DL)	3	0	0.0417 ± 0.0011	0.0418 ± 0.002	1.003 (0.9842-1.028)
11	Cu-K10	SC(DL)	9	0	0.0417 ± 0.0016	0.041 ± 0.0017	0.9803 (0.973 - 0.993)
12	KSF	SC(L)	unbuffered	0	0.306 ± 0.022		
13	KSF	SC(D)	unbuffered	0		0.305 ± 0.014	0.997
14	KSF	SC(DL)	unbuffered	0	0.289 ± 0.016	0.308 ± 0.018	1.065 (1.043 - 1.087)

[a] SC means single component system containing either L- or D-Val or racemic DL-Val. MC means multicomponent system containing racemic mixtures of DL-Val, DL-Asp, DL-Glu, DL-Arg, and DL-Ser. C_{0Val} = 5μM. [b] Unbuffered means that pH was not controlled, but the pH of the 0.3 g/mL K10 and Cu-K10 suspensions was acidic before and after adsorption (pH=3). [c] Ionic strength (I)=0.5 M assumed for Open Pacific Ocean Seawater (pH =7.7). [d] Values in parentheses refer to the range of *ER*s in the adsorbed state.

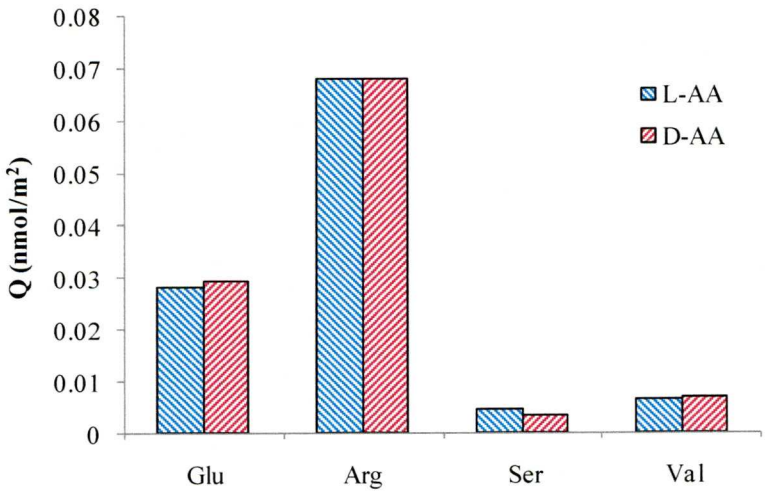

Figure 4.14. Adsorption of racemic DL-Asp, Glu, Ser, Arg, and Val on K10 from seawater. The adsorption values represent the mean of at least two experiments. Mineral load = 0.3 g/mL. C_0=5 μM

The observed adsorption trend might also be correlated with the acidity of the clay since high surface acidity might be achieved if strongly polarisable cations (e.g. Al^{3+}, Cu^{2+}) are present in the interlayer [126]. For example, hydrated Al can yield protons in the interlamellar zone according to:

$$[Al(OH_2)_6]^{3+} \rightarrow [Al(OH_2)_5]^{2+} + H^+$$

The gross extent of adsorption of enantiomers of Val on CuK10 was about 4% higher than in the K10 system. This marginal difference in Val adsorption between K10 and CuK10 suggests that the original adsorption sites in K10 remained unaffected by Cu exchange. Migration of intercalated Cu to hexagonal cavities in the montmorillonite structure due to high temperature treatment can make Cu unavailable for exchange/complexation reactions[127], which might explain the nearly invariable adsorption extent despite the Cu treatment.

No significant selective adsorption (α=0.05) was observed for enantiomers of Val interacting with K10 and CuK10 under various experimental conditions, contrasting with the earlier finding that Asp and Ser enantiomers displayed significant selectivity on K10 at acidic pH in single and multicomponent solutions. Note that the amount of L-Val adsorbed on CuK10 at pH 9 was significantly different from adsorbed D-Val at 94% confidence (Table 4.2, entry 11). In agreement with this, a slight preference of L-Val adsorption on a Cu-exchanged montmorillonite was reported at pH 11[128]. Nevertheless, the reproducibility of the supernatant *ee* (2%, D-Val excess) was not assessed statistically, but L-Leu and L-Glu adsorbed selectively too[128]. Interestingly, Tsvetkov and Mingelgrin[128] speculated that the observed selectivity stemmed from the presence of optically active complexes of Cu such as bi- or polynuclear hydroxides $[Cu_2(OH)_2(H_2O)_4]^{2+}$ on the clay surface; an hypothesis that might be worth further investigation. Preferential complexation of one AA enantiomer with adsorbed Cu^{2+} or Cu-complex on clays seems plausible. Plankensteiner *et al.* [129] recently reported that the stability constants of aqueous Cu-L-Ala complexes (1:1 and 1:2 Cu^{2+}:Ala) were consistently higher than their Cu-D-Ala counterparts, which might explain enantioselective effects in systems where Cu is used as a chelating agent (e.g. the salt-induced peptide formation) or as a solid catalyst[130, 131].

4.1.2.3. Adsorption of Racemic DL-Val on Montmorillonite KSF (KSF)

Batch adsorption experiments were conducted with montmorillonite KSF and 5 μM DL-Val at a solid/liquid ratio of 0.3 g/mL. KSF is a commercial acidic solid catalyst with a smaller surface area of about 20 m^2/g and CEC of 30.4 meq/100g. It

has been reported that acidic treatment of the natural clay with sulphuric acid destroys its interlamellar structure. Analysis of KSF by XRD has shown that is made up of 53% montmorillonite, 10% illite, 6% kaolinite, 10% quartz, 5% plagioclase, 1% gypsum, 4% anhydrite, and 4% amorphous material[86], indicating that part of the original montmorillonite structure is preserved. A more detailed characterization of raw KSF was performed by Jiang and Zeng[124], who reported that KSF is comprised of main crystalline phases: muscovite (d_{002} = 9.924Å) and montmorillonite ($AlSi_2O_6(OH)_2$, d_{001} = 12.183 Å).

The amounts of L- and D-Val adsorbed were about 7.5 times the values in the K10 system (Table 4.4, entry 3 vs. entry 14) highlighting the effect of surface area. Since the pH of the KSF-water suspension was always acidic, it is reasonable to assume that the mechanism of adsorption may have involved exchange of cationic Val for H^+ in the interlayer or complexation reactions with silanol and aluminol sites on the edges. Individual enantiomers were adsorbed to the same extent (Table 4.4, entries 12 and 13). In the racemic mixture, however, D-Val appeared to be adsorbed preferentially, observation that also applies to the Val-K10 system. So far, it is unknown whether enantiomers from a racemic mixture self-assemble at mineral surfaces in aqueous systems. However the intermolecular interactions of enantiomers of opposite chirality (LD and DL) are possibly weaker than the homochiral LL and DD associations as found for the adsorption of racemic cysteine on a gold single crystal Au(110) observed by scanning tunnelling microscopy[132]. A study on the adsorption of enantiomeric (L- and D-) and racemic DL-cysteine on a silver electrode by surface-enhanced raman scattering spectroscopy (SERS) gave evidence of the formation of cyclic cysteine dimers at the electrode surface via bonding of the carboxylic acid groups of the enantiomers at acidic pH values[133]. Slight differences in the dimerization of enantiomers of Val in the acidic interfacial region of the clays, originating from the intrinsic structural asymmetry of the enantiomers (parity-violating energy difference) as proposed by Deamer *et al.* [134], could possibly explain the preferential adsorption of D-Val, if the formation of cyclic L-Val dimers in aqueous solution is minutely favoured.

4.1.2.4. Adsorption of Racemic AAs on Kaolinite

Flat hexagonal kaolinite crystals consist of octahedral alumina sheets stacked on silica tetrahedral sheets (Figure 4.15). The silica faces possess permanent negative

charge caused by isomorphic substitution of Al^{3+} for Si^{4+} within the crystal whereas the edges of the crystals display variable charge with pH owing to hydroxyl groups that display acid-base behaviour. Acidic AAs adsorb readily on kaolinite from distilled water, but neutral AAs such as Ala and Val are adsorbed the least[27]. Asp, for example, adsorbs onto kaolinite edges via monodentate outer sphere complexes stabilised by electrostatic interaction of deprotonated carboxyl group with protonated surface hydroxyl groups, but there was no evidence for Asp adsorption to permanently charged sites [39].

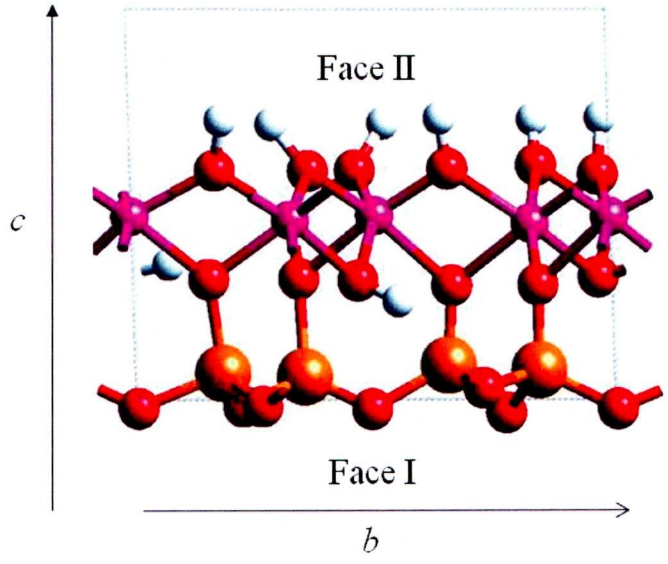

Figure 4.15. Structure of kaolinite: O atoms are red, the tetrahedral Si atoms are yellow, octahedrally coordinated Al are pink, and H atoms are white. The Al surface is the top layer and the Si surface is the bottom layer. Image after Warne *et al.*[135]

Figure 4.16 illustrates the adsorption pattern of different AAs on kaolinite from buffered aqueous solutions (Figure 4.16 a) and from seawater (Figure 4.16 b). The basic AAs, Arg and Lys, adsorbed to a greater extent on kaolinite at acidic and neutral pH values. In contrast, acidic AAs were not adsorbed onto the mineral at pH 6.8 whereas AAs of different polarities were bound by kaolinite in seawater. This can be explained by the different mineral loads used in the two separate experiments. No selective adsorption could be ascertained for the adsorption of selected AA enantiomers from multicomponent systems as seen in Figure 4.16. Note that there has been conflicting evidence on the discrimination of AA enantiomers, specifically Asp and Phe, by kaolinite[11, 51-53]. Bonner and Flores[53] rigorously demonstrated that there was no evidence for the preferential adsorption of D- vs. L-Phe by kaolinite from either pH 6 or

pH 2 solutions, contrasting with the earlier finding of Jackson who hypothesized that the edges of kaolinite were enantioselective towards L-Phe as a function of pH[52].

Similarly to K10, adsorption of racemic 5 μM Val onto calcined kaolinite and Cu-treated kaolinite was conducted in aqueous solutions to examine the potential enantioselectivity of this mineral. On a surface area basis, the amount of Val adsorbed on calcined kaolinite exceeded that of K10 by a factor of 5 (Tables 4.4 and 4.5, entry 3). Adsorption of Val was affected by the ionic strength of the system as evidenced by reduction of the amount of Val adsorbed in the presence of seawater by over half (Table 4.4, entry 3 vs. entry 4), again signalling an electrostatic interaction between Val and the clay. pH_{pzc} of kaolinite fluctuates between 4 and 5. In the non-buffered system, zwiterrionic Val was the predominant species adsorbed onto kaolinite as supported by the measured pH of the DL-Val-clay suspension of 5.7 after 24 h adsorption. Adsorption of Val on kaolinite is expected to be maximal close to the pH_{pzc} of the mineral because the surface bears no net charge and repulsive interactions are minimized. Interestingly, the adsorption of Val on Cu-treated kaolinite was significantly lower than in the untreated clay, pointing to reduction of the reactive sites by the copper treatment. In this respect, adsorption of Cu^{2+} on kaolinite resembles the adsorption of other cationic species such as AAs and it is thought to occur at the edges (variable charge surface sites) given that the amount of adsorbed Cu^{2+} is strongly dependent on ionic strength, pH, activation/deactivation of the clay [136]. Figure 4.17 shows the pH-dependence of adsorption of Val enantiomers on Cu-treated kaolinite.

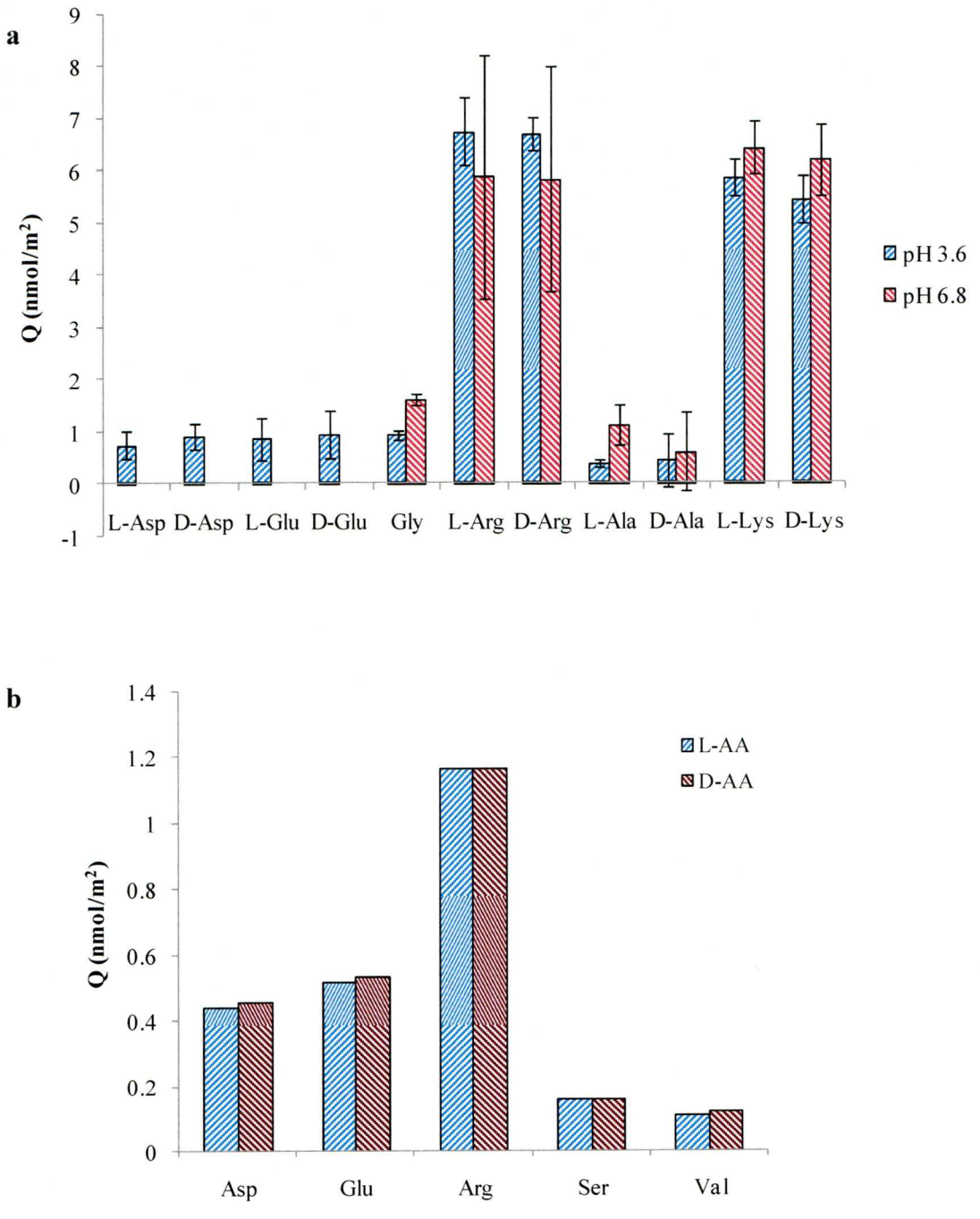

Figure 4.16. a. Adsorption of racemic DL-Asp, Glu, Gly, Arg, Ala, and Lys on kaolinite at pH 3.6 and 6.8. Mineral load = 0.1 g/mL. C_0 = 10 µM, error bars correspond to 95% confidence intervals (duplicate experiments). b. Adsorption of racemic DL-Asp (*N*=5), Glu (*N*=5), Ser (*N*=3), Arg (*N*=5), and Val (*N*=3) on kaolinite from seawater. Mineral load = 0.3 g/mL. C_0= 5 µM. *N* refers to the number of experiments

Table 4.5. Amounts of Val enantiomers adsorbed on Kaolinite, Cu-Kaolinite at different experimental conditions. Errors are reported as 95% confidence intervals

Entry	Type of kaolinite	SC or MC[a]	pH[b]	I(M)[c]	Amount adsorbed (nmol/m^2)		ER_{ads}[d]
					L	D	
1	Kaolinite	SC (L)	unbuffered	0	0.209 ±0.017		
2	Kaolinite	SC(D)	unbuffered	0		0.212 ± 0.023	1.014
3	Kaolinite	SC(DL)	unbuffered	0	0.2223 ± 0.010	0.2275 ± 0.008	1.023 (0.965-1.078)
4	Kaolinite	SC(DL)	unbuffered	0.5	0.0964 ± 0.0155	0.0936±0.0146	0.976 (0.850-1.106)
5	Cu-Kaolinite	SC(L)	unbuffered	0	0.110± 0.020		
6	Cu-Kaolinite	SC(D)	unbuffered	0		0.100± 0.030	0.909
7	Cu-Kaolinite	SC(DL)	unbuffered	0	0.093± 0.020	0.130± 0.050	1.406 (1.039-1.885)
8	Cu-Kaolinite	SC(DL)	3	0	0.078± 0.022	0.066± 0.010	0.87 (0.676-1.042)
9	Cu-Kaolinite	SC(DL)	9	0	0.134± 0.071	0.171± 0.064	1.33 (1.090-1.743)

[a] SC means single component system containing either L- or D-Val or racemic DL-Val. MC means multicomponent system containing racemic mixtures of DL-Val, DL-Asp, DL-Glu, DL-Arg, and DL-Ser. C_{0Val} = 5μM. [b] Unbuffered means that pH was not controlled. The pH values of the unbuffered calcined kaolinite and Cu-Kaolinite suspensions (0.3 g/mL) were 5.6 and 3.3. [c] Ionic strength (I) = 0.5 M assumed for Open Pacific Ocean Seawater (pH = 7.7). [d] Values in parentheses refer to the range of *ER*s in the adsorbed state.

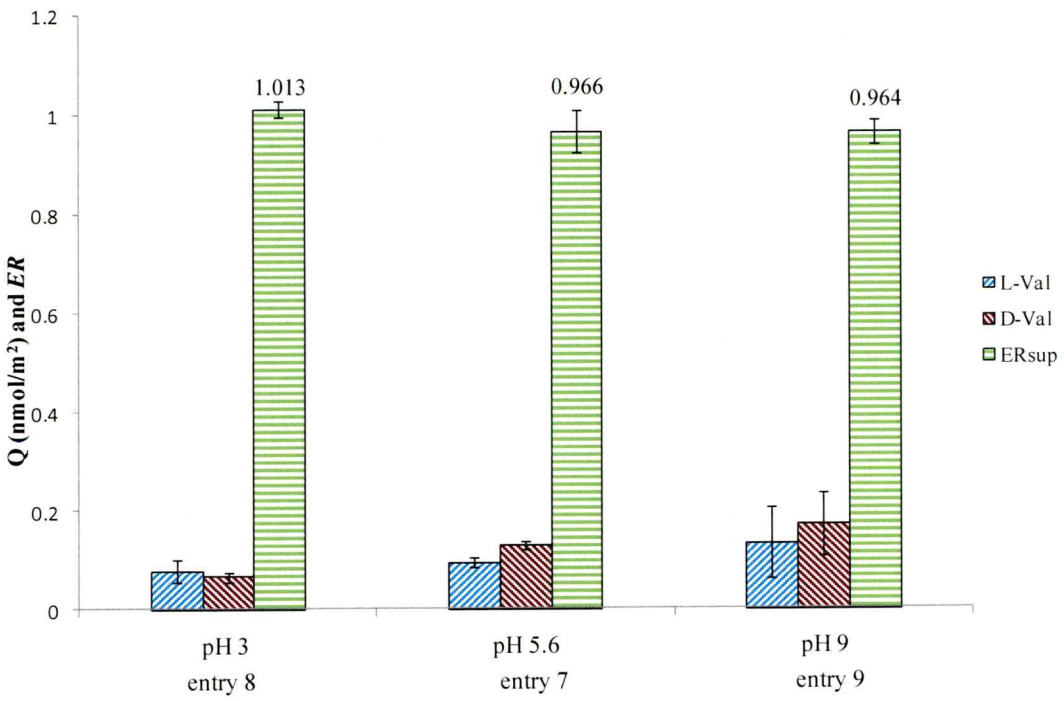

Figure 4.17. pH dependence of of L- and D-Val adsorption on Cu-Kaolinite. Mineral load = 0.3 g/mL. C_0= 5 μM. The *x*-axis shows displays pH and respective entry from Table 4.5

Maximum uptake of Val took place at pH 9. The dissociation constant of the NH_3^+ group of Val is 9.62 (pK NH_3^+ = 9.62), hence above pH 9.62 Val is present in solution as the anionic species, so it is likely that bonding of anionic Val to positively

charged copper complexes is more favourable at high pH. Statistically, the mean values of *ER*s were not significantly different at pH 3 and 5.6, but the D/L ratios of the supernatant (24 h adsorption) and initial DL-Val solution were significantly different at pH 9, hinting at selective adsorption of D-Val (Table 4.2, entry 12). It is unknown why Cu-Kaolinite discriminates towards D- Val at high pH. Existing evidence has pointed to the opposite effect such in the case of a theoretical work on the adsorption of Ala enantiomers on kaolinite. This study proposed that cationic and zwitterionic Ala can adopt two adsorption geometries: upright and bridge configurations on the basal faces of kaolinite (see Figure 4.16). The average energy differences between L-Ala and D-Ala adsorbed on a variety of sites of faces I and II (See Figure 4.18) were estimated to be 0.14 kJ/mol and 0.04 kJ/mol for the positive ion and the zwitterion, respectively, indicating that the L-forms are more easily adsorbed than the D-forms.

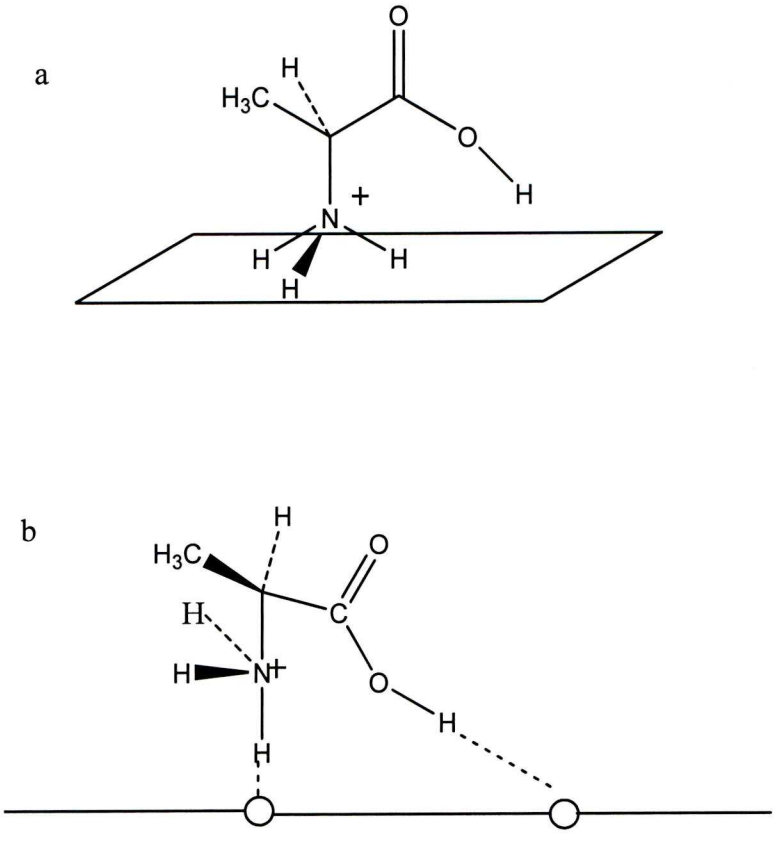

Figure 4.18. Adsorption geometries of Ala on the basal faces of kaolinite. a. Upright or tripod position, each N-H bond of the NH_3 group pointing to an oxygen atom; both the zwiterion and the cation can adopt this configuration. b. Bridge position, only one N-H bond pointing to an oxygen atom of the face and the O-H of the COOH to another oxygen[137]

4.1.3. Adsorption of Racemic AAs on River Mersey Sediments

Previous work has shown that calcined sediment from the River Mersey selectively adsorbed one enantiomer over the other, and the effect was more pronounced at low pH [97]. The River Mersey sediment was predominantly comprised of coarse particles, mainly sand, and possibly contained a significant proportion of metals such as Al, Fe, and Mn, presumably present in the sample as their corresponding oxides[138]. Adsorption of multicomponent mixtures of racemic AAs on calcined River Mersey sediments was conducted at different pH values under experimental conditions similar to those employed for adsorption of AAs on the model mineral surfaces discussed in the preceding sections. Figure 4.19 summarises the results corresponding to the adsorption of 10 μM racemic DL-Asp, DL-Glu, Gly, DL-Arg, and DL-Ala onto calcined slice 6 of the sediment core prepared by Wedyan and Preston[97].

In agreement with Wang and Lee [139], the basic AA, Arg, adsorbed the most in the pH range 3.6-6.8. Notice, however, that adsorption of Arg dropped remarkably at pH 12.8 reflecting the role of the electrostatic mechanism in the Arg-sediment interactions. Asp and Ala adsorption were minimal at neutral pH. Interestingly, Ala was nearly equally adsorbed at both acidic and alkaline pH which suggests that a mechanism, other than electrostatic bonding, such as specific adsorption of the Ala anion via covalent or coordinative bonds to surface atoms (Fe, Mn, Si) of the sediment could have occurred as reported by Lambert in his review on the adsorption of AAs on mineral surfaces[41]. Specific bonding of molecules onto surfaces via covalent or hydrogen bond formation has a higher discriminatory potential[41]. Evidence of enantioselectivity was not clear from the data owing to the high uncertainty of the duplicate experiments as can be seen from the enantiomeric ratios of Asp, Glu, Arg, and Ala displayed in Figure 4.17b. *ERs* for Asp and Ala appeared to switch from less than 1 at acidic and neutral pH (preferential adsorption of D-AA) to greater than 1 at pH 12.8 (preferential adsorption of L-AA). The differences between the degree of selectivity reported in this study and the earlier might be attributed to aging of the material and possibly to recalcination which was carried out to ensure an organic-free material before the adsorption experiments.

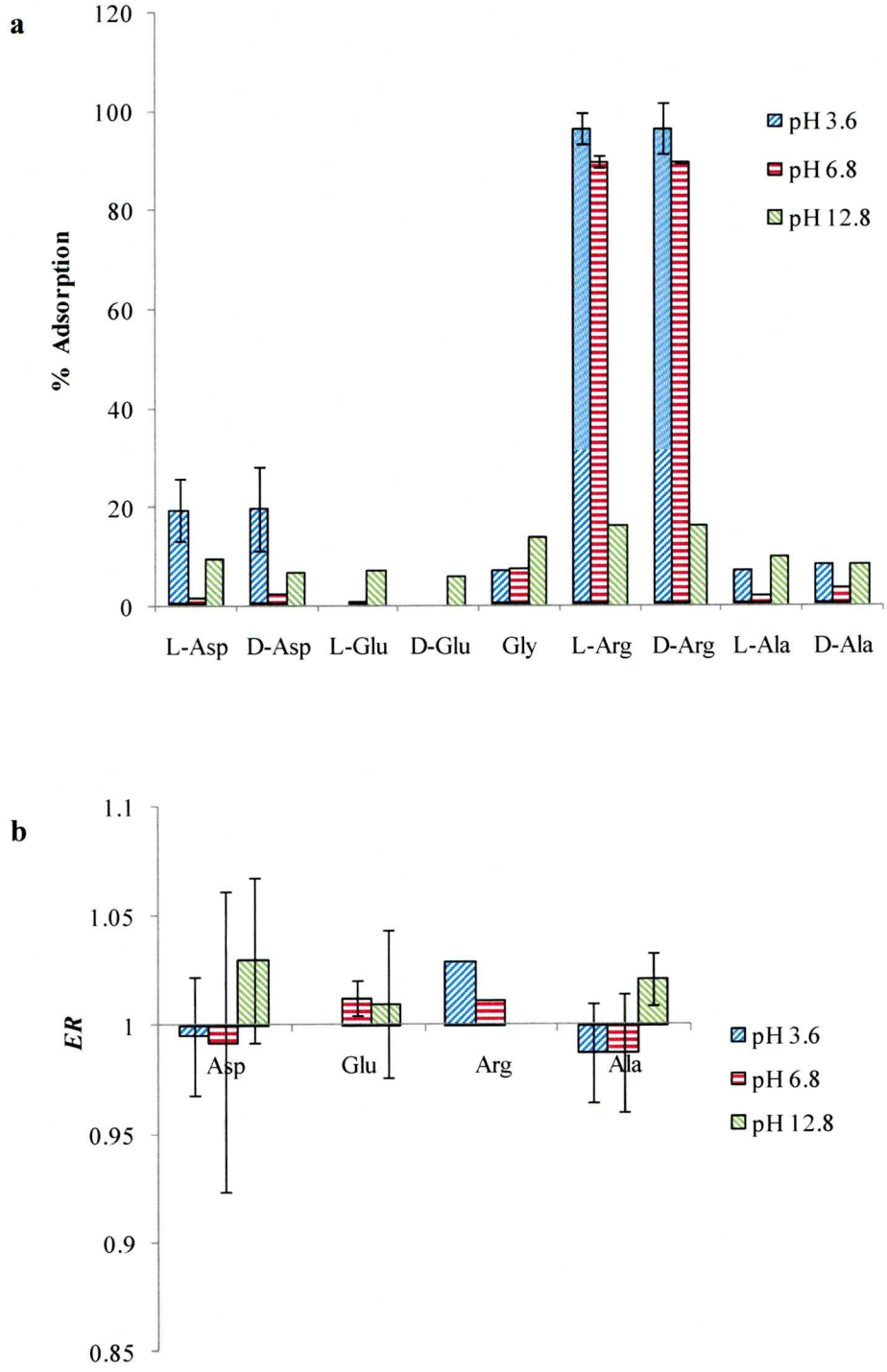

Figure 4.19. a. Adsorption of racemic DL-Asp, Glu, Gly, Arg, and Ala on River Mersey sediment as a function of pH. Mineral load = 0.1 g/mL. C_0= 10 μM, error bars correspond to 95% confidence intervals (duplicate experiments); b. Supernatant enantiomeric ratios of Asp, Glu, Arg, and Ala

An anoxic sediment fraction, denominated slice 7, was treated as described in Section 3.3. The calcined material was used without particle size fractionation for

adsorption of 10 μM racemic DL-Asp, DL-Glu, DL-Ser, Gly, DL-Arg, DL-Ala, DL-Val, DL-Met, DL-Phe, DL-Ile, and DL-Leu under no pH-control (Figure 4.20). Asp, Glu, and Arg were noticeably adsorbed, but Ser, Ala, Val, Met, Phe, Ile, and Leu were not bound to the surface. Discrimination of one enantiomer over the other was uncertain for this mineral sample.

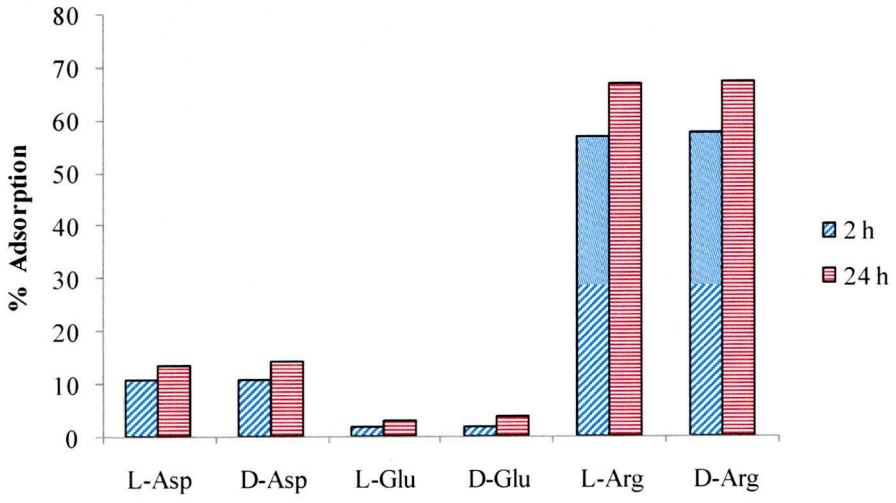

Figure 4.20. Adsorption of racemic DL-Asp, Glu, Gly, Ser, Arg, Ala, and Val on anoxic slice of River Mersey sediment as a function of time. Mineral load =0.1 g/mL. C_0=10 μM. The adsorption values represent the mean of at least two experiments

4.1.4. Adsorption of Racemic AAs on Pyrite Single Crystal

Pyrite was chosen as a model mineral surface because it has been invoked to be a relevant prebiotic material for primitive bidimensional metabolism and chiral discrimination [140]. Opposing this view, Pontes-Buarque *et al.*[141] argue that the pyrite-water interface in a primitive seawater system is a complex one that it is modulated by the adsorption of cations and anions, thus challenging the chiral discrimination characteristics of the pyrite substrate.

A natural single crystal of pyrite was cleaned as described in Section 3.3 of the Materials and Methods chapter. The cubic crystal (3.1×3.1×3.1 cm) was then immersed in a 2.5×10^{-3} M multicomponent racemic mixture of DL-Asp, Glu, Arg, Ala, Lys and Gly (pH 3.2) for a 24-h period after which it was rinsed repeatedly with water to remove residual AA solution. Each face was extracted with 0.02 M HCl, and the extracts were analysed by HPLC to quantify any adsorbed material. No adsorbed AAs could be measured under these experimental conditions perhaps due to surface area limitations. Moreover, the crystal probably was passivated by an iron oxide or

oxy-hydroxide layer since pyrite surfaces are highly reactive in air [40]. The isoelectric pH of untreated pyrite surfaces is about 5.5, which is close to that of iron oxides [141]. Therefore, at pH 3.2, the cationic AA species were predominant and the pyrite surface was positively charged, indicating that electrostatic interactions play a role in pyrite-AA systems. Bebié and Schoonen [40] studied the adsorption of Ala, Ser, Gly, and Cys on acid-washed powdered pyrite over the pH 2-8 range in the absence and presence of potential determining ions such as Fe^{2+} and Cu^{2+} and under anoxic conditions. Notwithstanding that pyrite was negatively charged over the entire pH range, L-Ala interacted with the surface up to pH 5 with and without the influence of Fe^{2+}. Gly only interacted in the presence of Fe^{2+} whereas L-Ser displayed no affinity for pyrite surfaces. Cys showed a very strong interaction, hypothesized to occur via its thiol group with sulphur deficient (iron rich) surface sites (specific covalent bonding). Considering this, it seems worthy to study the adsorption of racemic mixtures of selected AAs, for example Ala and Cys on well-characterized powdered pyrite or single crystals under anoxic conditions. Interestingly pyrite not only exists in the achiral cubic space group *P*a3, but also in the enantiomorphic triclinic space group *P*1 that is characteristic of low temperature formation in sedimentary rocks or hydrothermal ore deposits [142]. Hence, both cubic and triclinic specimens are good candidates for future research. Molecular modelling of the adsorption of Gly at the pyrite-water interface has suggested that sulphur vacancies (sites with non-coordinated iron) increase the retention time of Gly on the surface in comparison to the ideal surface[143]. Gly was anchored on these defects by chemisorption of the carboxylate oxygen. Attenuated total reflection IR spectroscopy [144] and sum frequency generation vibrational spectroscopy[145] might help to clarify the mechanism of adsorption of chiral AAs at the pyrite-water interface.

4.1.5. Adsorption of Racemic AAs on Gypsum Single Crystal

Gypsum, a natural sulphate evaporite on Earth and Mars[146], belongs to the monoclinic space group and it has been documented that its *m* and *l* faces interact selectively with chiral Ala, Asp, Glu, Lys, Hist[10]. Enantiomers of opposite handedness inhibited the growth of mirror image crystallographic faces (*m* and *l*, see Figure 1.8 b) of the mineral giving distorted minerals[10]. Adsorption of chiral molecules on gypsum has not been conducted because of the mineral's high solubility[7]. Note however that the amino acids Asp, Ser, Glu, Ala, Gly, and Val have been detected in ancient

terrestrial sulphate deposits[146]. Therefore, it was concluded that AAs appeared to be preserved for geologically long periods in sulphate mineral matrices. Extrapolation of these results to extraterrestrial clues for life suggests that sulphate minerals should be targets in the search for organic compounds[146].

A 18.5-cm long gypsum specimen (see Figure 4.21) was treated in the same way as pyrite. After a 24 h immersion period in the multicomponent racemic mixture, the crystal was rinsed and its crystallographic faces extracted with 0.02 M HCl. The *m* faces can be related by a mirror symmetry plane whereas the *b* plane is a perfect cleavage plane.

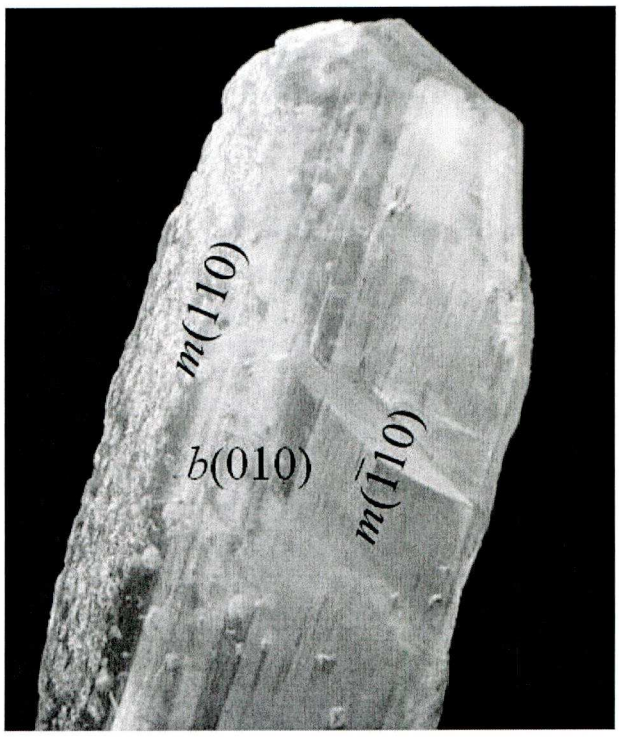

Figure 4.21. Gypsum single crystal specimen used in adsorption experiments

In comparison to pyrite, there were measurable amounts of AAs in the 0.02 M HCl extracts as shown in the chromatograms (Figure 4.22) for faces *b*(010) and *m*($\bar{1}$10) along with the standard mixture. Figure 4.23 shows the extents of adsorption of the AAs on the three faces as a percentage of the AA adsorbed with respect to the initial concentration of AA (2.5×10^{-3} M, except for Arg with initial concentration of 1×10^{-3} M). It can been seen that AAs of different nature have comparable affinities for the gypsum surfaces, which agrees with the findings by Aubrey *et al.* [146] on the preservation of ancient AAs in sulphate minerals.

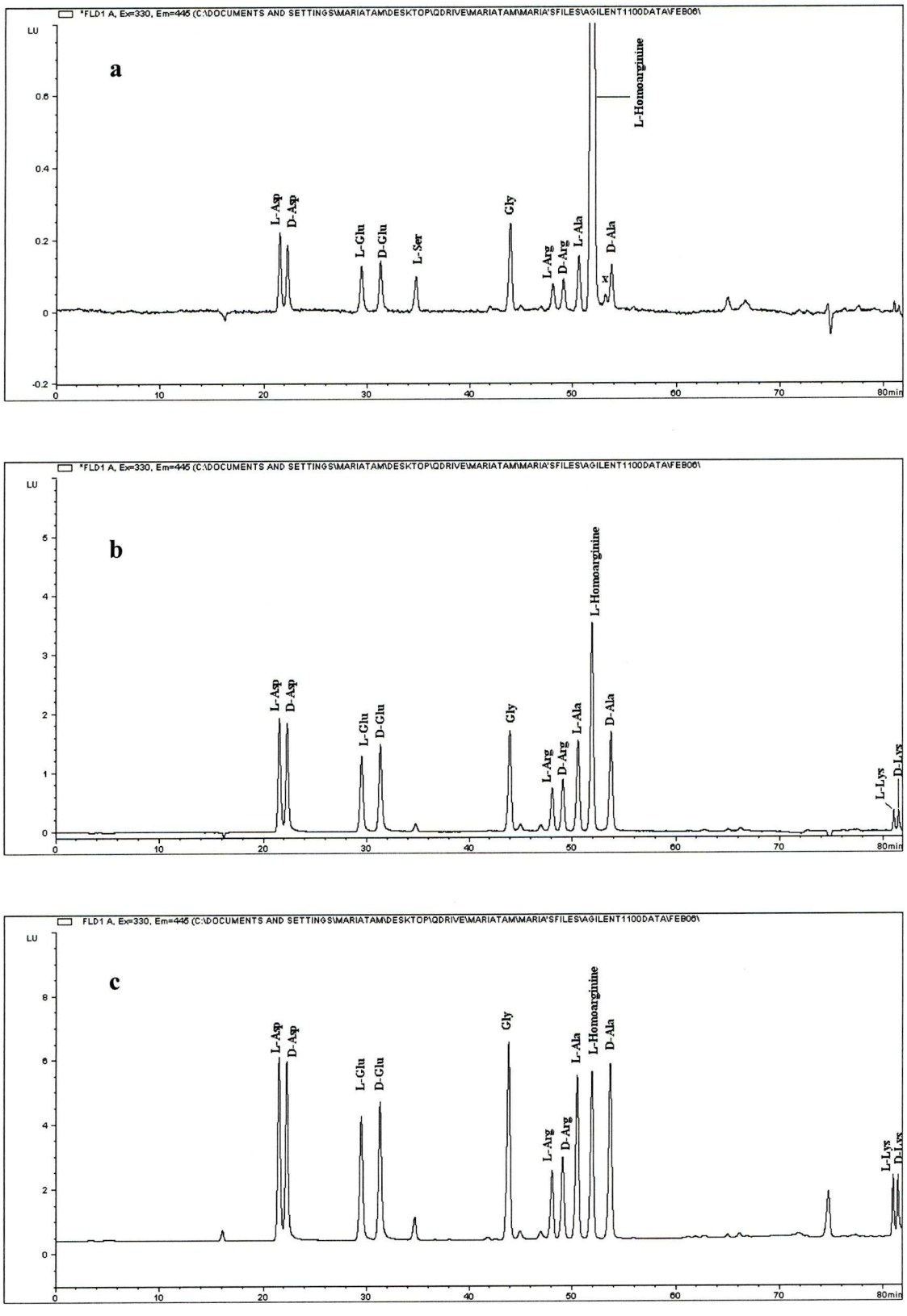

Figure 4.22. Adsorption of racemic multicomponent mixture on gypsum faces. a. AAs extracted from *b*(010) face, b. AAs extracted from *m*(-110) face, and c. Standard multicomponent AA mixture, 10 μM each AA, except Arg enantiomers (4μM each), x designates an unknown compound

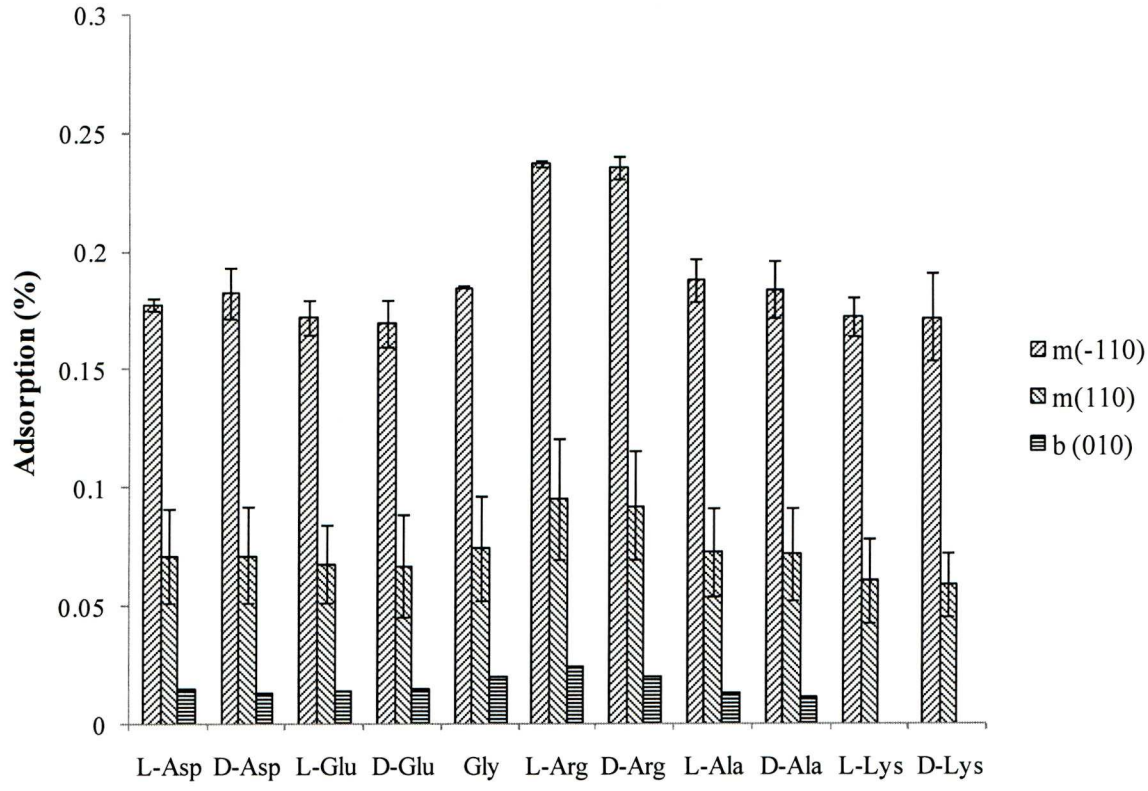

Figure 4.23. Percentage of AAs adsorbed on crystallographic faces of gypsum single crystal from a multicomponent racemic mixture of DL-Asp, Glu, Arg, Ala, Lys and achiral Gly (pH 3.2). C_0= 2.5×10^{-3}M each AA except Arg. Error bars correspond to the standard deviation of three separate extractions on the same face

For illustrative purposes, the *ER* values of the extracted amounts are presented in Table 4.6 where it is observed that *m* faces follow the same *ER* tendencies whilst the *b*(010) plane displays much lower values of enantiomeric ratios for Asp, Arg, and Ala, hinting at preferential adsorption of the L-enantiomers. This plane was used as a control surface because it lacks symmetry operators, therefore it should not present chiral discriminating properties as opposed to the *m* planes, so it is unclear why *b*(010) appeared to be selective. Further investigation with various gypsum cleaved planes and selected racemic AA pairs might clarify the aforementioned preliminary results.

Table 4.6. Enantiomeric ratios (*ER*=D/L) of adsorbed samples on gypsum single crystal

AA	Crystallographic planes			
	$\bar{m}$(1 10)	*m*(110)	*b*(010)	*Standard*
Asp	1.03	1.00	0.87	0.98
Glu	0.98	0.99	1.02	0.98
Arg	0.99	0.97	0.84	1.01
Ala	0.98	0.99	0.85	0.99
Lys	1.00	0.98	*nd*[a]	0.99

[a] *nd*: not detected

4.1.6. Relevance of the Enantioselective Adsorption of Racemic AAs on Minerals

According to the results presented in the preceding sections, it can be stated that stereoselective adsorption of AAs at quartz surfaces in aqueous conditions was limited to a few cases for all the types of crystalline quartz studied (Table 4.1). Experimental conditions where selective adsorption occurred spanned a wide pH range and AAs with different side chain functionalities i.e. Asp, Arg, and His (see Table 4.2). The issue remains of whether AAs could have self-assembled on quartz surfaces under prebiotic conditions. Experimental evidence suggests that the interaction of AAs at quartz is weak. For example, SFG spectra of the AA-solution-fused silica interface showed the lack of formation of ordered adsorbate layers for Asp and Phe[145]. Altogether, the quartz system clearly does not manifest its enantioselective potential in aqueous solutions in a systematic way.

Clays possess affinity for various AA types, but lack the structural chirality displayed by single quartz crystals. For this reason, the enantioselective potential of clays is still questioned. A closer look at Table 4.1 reveals that most of the instances of chiral discrimination, as evaluated by the statistical significance of the data at the 95% confidence interval, took place in the K10-Ser aqueous system at low pH. K10 seems to display selectivity towards the D-AAs at low concentration and acidic conditions. These results contrast with those of earlier studies where clays invariably adsorbed the L-enantiomer preferentially [55] leading to the hypothesis that clays might have started` the homochirality of life by concentrating the L-enantiomer, so that complex reactions such as polymerization might have taken place at the surface. A recent study on the adsorption of L- and D-Asp on rutile (TiO_2) indicated that D-Asp adsorbed more than L-Asp at higher Asp concentrations at acidic pH values, suggesting that there might be cases where the D-enantiomer adsorbs enantioselectively at a mineral surface. The authors however made it clear that further

experiments need to be conducted to verify this important finding because it raises the question of mineral selectivity dependence on aqueous experimental conditions[147]. Little is known about the mechanism of AA interaction at mineral surfaces due to the complexity of the mineral-water interface. However progress in this area is underway by the coupling of spectroscopic data and surface complexation models. A good example of the recent advance on this subject is the work by Sverjensky *et al.* [148] who studied the adsorption of glutamate on hydrous ferric oxide in aqueous solution and proposed a phase diagram for the attachment of glutamate as a function of pH and concentration.

Recently, Deamer *et al.*[134] suggested an alternative scenario where chiral selective adsorption of the D-enantiomer might have taken place at chiral grains or mineral phases of parent bodies of meteorites, leading to an L-enantiomeric excess at the surface. Collision processes might have then broken the meteorite surface so that fragments transported to Earth would have been characterised by an L-excess, which could have been amplified by many possible environmental conditions. Interpretation of the selective adsorption trend of D-AAs on clays lends support to this astrobiological hypothesis of the homochirality of life.

Certainly, the main outcome of the results on selective adsorption of AAs on clays is that both the structural characteristics of AAs and their concentrations could be the most relevant factors determining enantioselectivity. In this respect, it appears that AA polarity might be an important characteristic influencing selective behaviour at K10, since the highest preferential adsorption signal took place in the Ser-K10 system. It is likely that the hydroxyl group at the end of the side chain provides an extra point of interaction with the mineral surface that leads to selective adsorption of one enantiomer over the other. Support for this hypothesis is given by the three-point interaction model where the enantiomer must contact the target surface/receptor at three points for enantioselective discrimination to occur (Figure 1.15). Moreover, Ser is a special AA because homochiral Ser octamers, consisting of four hydrogen bonded dimers, can form in aqueous solution and their abundance is a function of the enantiomeric composition of the system[149]. Interestingly, the homochiral L- and D-Ser protonated octamers were not observed in significant amounts from the racemic Ser solution[149].

It appears also that the concentration of AA might cause a change in the mechanism of selectivity, at least on clay minerals. Therefore, unexplained conflicting

evidence on selective adsorption could be attributed to dissimilar systems, some of which might have used unrealistically high concentrations that offer no real insight into the phenomena being studied. For example, Parbhakar *et al.*[150] recently proposed that L-Lys sorbs in the montmorillonite interlayer at >45-90° to the plane of the siloxane O atoms depending on concentration, with the lowest concentration (0.02M) favouring a tilted orientation of L-Lys (45°) that might give clues as to the preferred orientation of Lys in diluted solutions, but one could argue that 0.02 M is still within the high concentration range.

In the prebiotic context, the conditions employed in this study are more realistic of the early Earth since the experiments were conducted at low concentrations (2 - 500 μM). Moreover, in the case of clays, low pH might have aided stereoselective reactions such as the condensation of nucleotides into RNA[151]. Environments such as hydrothermal vents and hotsprings, set in muddy pools lined with clays characterised by low pH have been suggested as possible scenarios for self-assembly in the prebiotic environment [152]. Collectively, the results of adsorption on K10 open the possibility for molecular modelling of Asp and Ser interaction with this clay in order to understand the mechanism of selectivity. Hypotheses as to why selective behaviour occurs on clays include AAs conferring structural chirality to the clay by an unknown mechanism that is most likely autocatalytic in nature [55], differences in the rate of intercalation of the enantiomers into the structure [67] and very small differences in energy between D- and L-enantiomers that could affect the hydration shells surrounding the AAs, thus in turn influencing other macroscopic properties (e.g. adsorption, nucleation, crystallization, and polymerization rates)[134].

Finally, pyrite did not display any selective behaviour towards AAs in the present work. Clean and well-characterized pyrite e.g. (100) surfaces have been prepared by using a sputter/annealing procedure in an ultra high vacuum (UHV) chamber[153]. This opens the possibility of studying the interaction of chiral molecules at defect-free pyrite surfaces in order to identify self-assembly processes.

4.2. Formation of Divaline in CuK10 Systems

This section presents and discusses results pertinent to the polymerization of enantiomers of Val caused by subjecting the CuK10-Val system to repeated cycles of wetting and drying. These cycles simulate episodes of periodic wetting and drying that were likely to occur in prebiotic times on mineral surfaces and that might have

driven the condensation of AAs into peptides which are the building blocks of proteins. The driving force for peptide formation is the drying step or thermal activation because the condensation reaction is thermodynamically unfavourable in water solution[41]. The wetting cycle desorbs any peptides formed on the surface so that further condensation of AAs can take place in the next drying step. Peptides can be also formed by wetting-drying cycles in the salt-induced peptide formation reaction in the presence of Cu and/or NaCl and chloride ions seem to be relevant in the dry state condensation reaction[154]. In view of this, it was hypothesized that CuK10 could possibly catalyse the formation of Val peptides in wet-dry cycle experiments which were started by mixing 0.02 g of CuK10 with 1 mL of 0.03 M L-, D- and DL-Val as described in Section 3.5.3. Following this, the vials were shaken and placed in an oven kept at 65°C for 24h. After this period, one vial per experiment was removed, allowed to cool, and the dry residue extracted with $CaCl_2$. The remaining vials were replenished with water or 0.5 M NaCl solution, shaken and heated for 24 h to complete another cycle. The enantiomeric and racemic Val aqueous solutions were prepared in Milli-Q water and in Open Pacific Ocean seawater. Thus, parallel experiments were conducted with CuK10 in contact with low and high ionic strength Val solutions as well as the corresponding blank systems i.e. aqueous solutions in the absence of clay. High initial concentrations of Val were used to ensure that any peptide formation could be measured with the analytical methods available.

4.2.1. Results

The yields of divaline reported in this paper correspond to the percentage of dipeptide formed from the initial amount of Val before the reaction. The extent of Val dimerization in unbuffered suspensions of CuK10, obtained from the RP-HPLC ion-pair method with UV detection at 200nm (Method I) and RP-HPLC with chiral thiol derivatization (Method II) is presented in Table 4.7. In general, measurable quantities of the product were observed after five days of reaction (Method I), but there is no clear trend of the effect of the chirality of the starting Val solution on the yields of divaline. This in contrast to previous studies where preferential formation of L-Val and L-methionine dipeptides after long reaction times was observed in the salt-induced peptide formation which is catalysed by aqueous complexes of Cu and chloride [130, 155]. There was no detectable divaline production in the cycled unbuffered low ionic strength blank systems. Therefore, it can be hypothesized that CuK10

catalysed the dimerization reaction in the low ionic strength system. Interestingly, unidentified peaks were present in the chromatograms of the $CaCl_2$-extracted CuK10 clays that cannot be ascribed to the extracting solution. Figure 4.24 presents the separation of the analytes extracted from the clay residue of the last reaction cycle of the CuK10-L-Val system.

Table 4.7. Divaline yields (%) from wet-dry cycles in the CuK10-Val system. Initial concentration of Val = 30 mM

Reaction time (days)	Divaline Yield (%)			
	Method I			Method II
	L-	D-	DL-	L-
1	*nd*	*nd*	*nd*	*nd*
3	*nd*	*nd*	*nd*	0.012
5	0.0259 ± 0.0035[b]	0.0295 ± 0.0040	0.0306 ± 0.0041	0.0213
6	0.0118	0.0077	0.0092	0.0246
8	0.0238	0.0224	0.0194	0.0264 ± 0.0005

[a] L-, D- and DL- refer to the yields of divaline obtained from the starting enantiomeric and racemic Val solutions. [b] Error reported as the standard deviation of the analytical method.

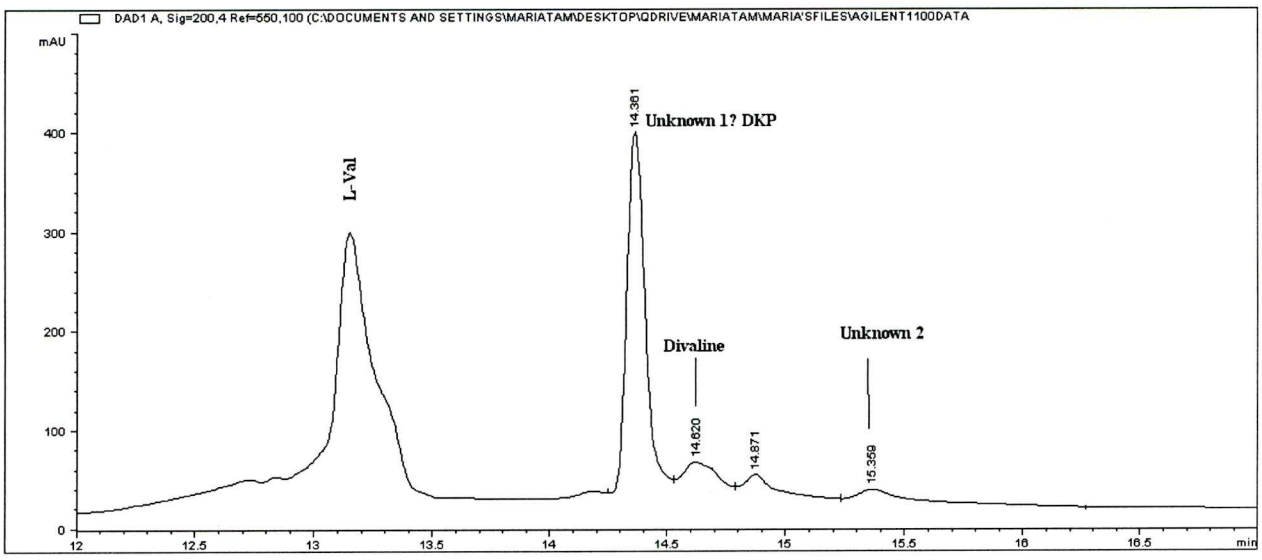

Figure 4.24. Chromatogram showing the separation of L-Val, divaline and the unknown compounds 1 and 2 by reversed phase ion pair chromatography. For conditions see Section 3.6.2

The peaks at retention times of 14.36 and 15.36 minutes exhibited a time dependency as shown in Figure 4.25.

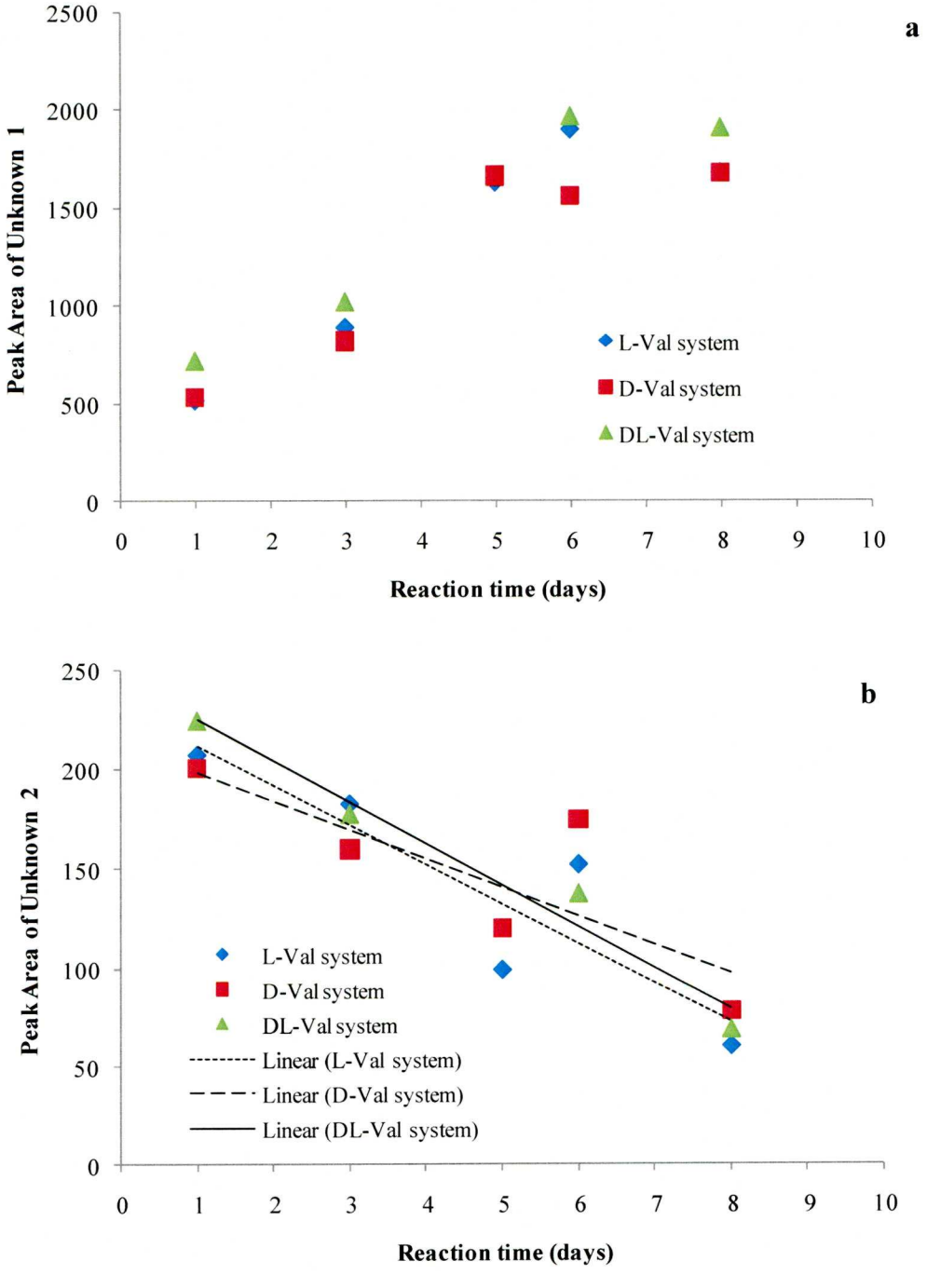

Figure 4.25. Peak area vs. reaction time for unidentified compounds formed in CuK10-L-, D- and DL-systems at retention times of a. 14.36 min and b. 15.36 min

Whilst the peak area for the unidentified compound eluting at 14.36 min increased with time in all the CuK10-Val systems, the peak areas for the unknown at

elution time of 15.36 min decreased linearly with time. It can be speculated that the unknown at 15.36 min retention time might be a Cu or a Cu-Val complex that catalyses the formation of the compound at RT= 14.36 min. LC-MS- ESI analysis of the $CaCl_2$ extract of the CuK10-L-Val sample after 8 days of reaction allowed conclusive identification of linear divaline as a reaction product by comparison of the retention times and mass spectra of the experimental sample and an authentic sample of divaline dipeptide standard. Figures 4.26a and 4.26b show the chromatograms and mass spectra of authentic divaline and a sample, respectively. The retention times and m/z = 216.9 of divaline$^+$ H^+ (Val_2H^+) in the sample matched the values of the authentic standard, indicating the presence of the dipeptide.

Moreover, divaline could not be detected in the unbuffered Blank-LVal sample cycled for 8 days, which agrees with the results described previously for divaline detection by ion-pair RP-HPLC. Based on the single area value of the standard, the concentration of LL-Val in the sample was approximately 8 μM resulting in a calculated yield of 0.027% which agrees with the values reported in Table 4.7. As with the RP-HPLC ion-pair chromatography and chiral thiol derivatization methods, peaks other than divaline appeared on the chromatogram, suggesting that other reactions such as the formation of cyclic divaline or substituted diketopiperazines (DKP) might have occurred according to the following reaction that shows the condensation of two AAs to give a cyclic dimer (DKP) [41]:

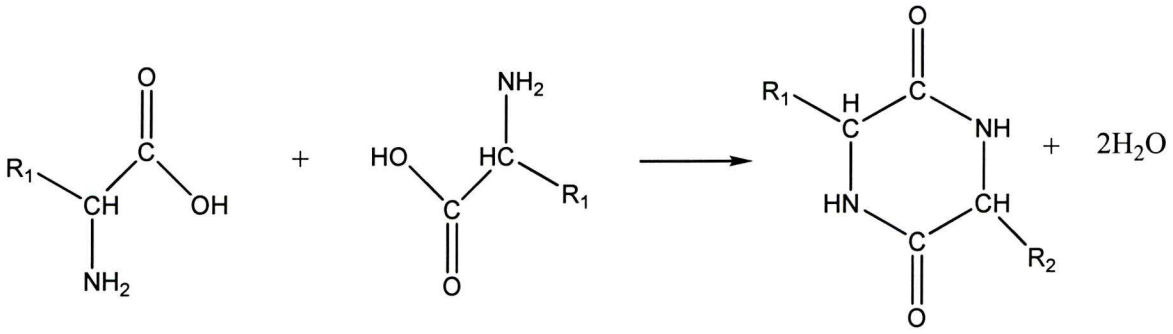

For divaline DKP R_1=R_2= 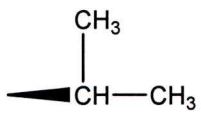

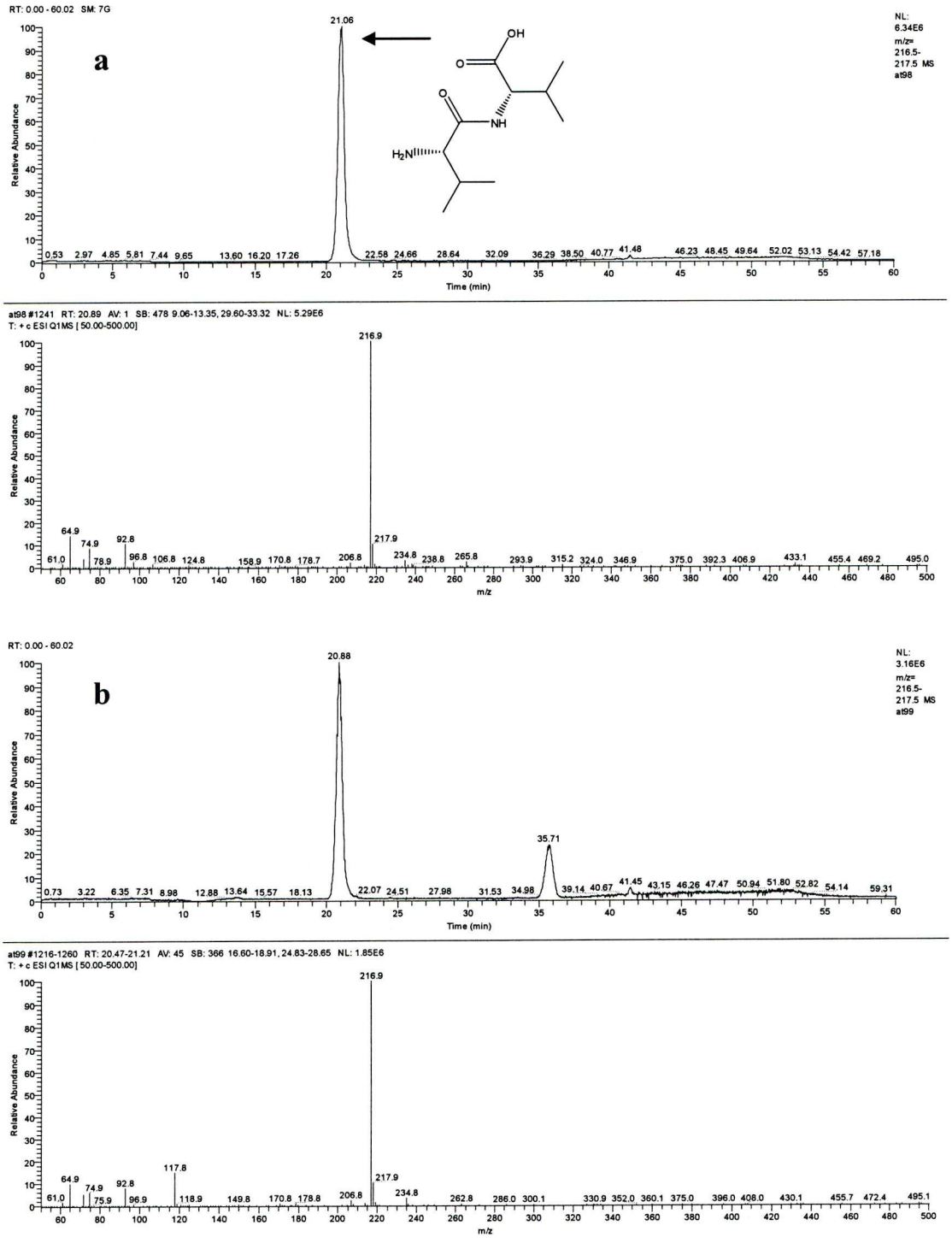

Figure 4.26. Chromatograms and mass spectra of a. 10 μM solution of authentic divaline and b. CuK10-L-Val sample after 8 days of reaction. Experimental conditions as in section 3.6.4

Knowing that the *m/z* value for cyclic divaline H^+ (*c*-Val_2H^+) is 199, the chromatogram of the sample was searched for peaks possessing a mass range of 198.5-199.5. A compound eluting at 26.30 min possessed a mass spectrum characterised by a high relative abundance of *m/z* = 198.8 (Figure 4.27), which most likely corresponds to *c*-Val_2H^+, but the concentration of the cyclic dimer could not be calculated due to the lack of a calibration standard. Cyclization of linear dipeptides has also been postulated to account for the formation of cyclic dipeptides of Gly and Ala in mineral systems [77]. Therefore, partial conversion of divaline to the cyclic anhydride might have taken place in the CuK10-Val system:

$$Val \leftrightarrow Val_2 \leftrightarrow cyc-Val_2$$

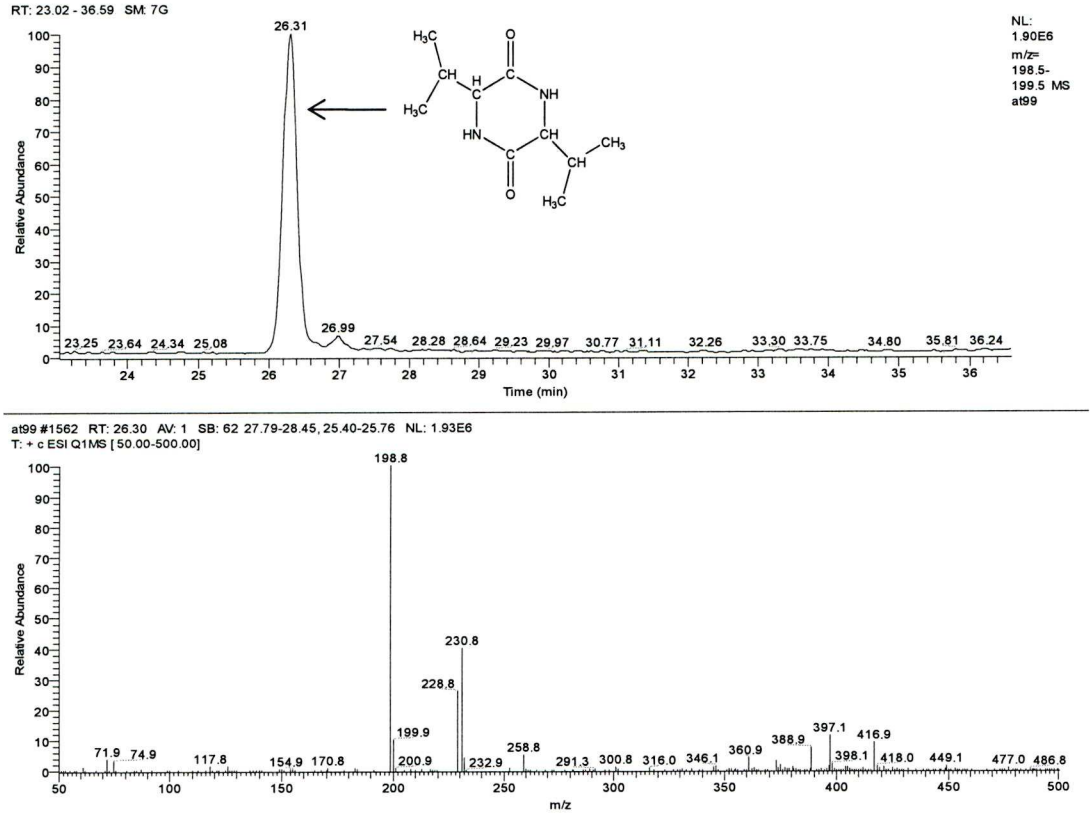

Figure 4.27. Chromatogram of CuK10-L-Val sample after 8 days of reaction showing the mass spectrum of the compound eluting at 26.3 min. Experimental conditions as in Section 3.6.4

Wet-dry cycle experiments of CuK10-Val seawater suspensions were also carried out to examine the combined role of Cu in the clay with the dehydration potential of sodium in solution on possible divaline formation. No divaline could be detected in these experiments with either Method I or II. However, the unknown compounds were detected in this high ionic strength system with Method I. The peak areas of unknown 1 increased with reaction time whereas unknown 2 appeared to be formed rather than depleted, which contrasts with the findings for the low ionic strength system. Further experiments are needed to clarify these results.

The production of divaline vs. time in the low ionic strength CuK10-L-val system was also measured by RP-HPLC with chiral derivatization (Table 4.7, Method II). This method was used to confirm the formation of linear divaline and is sensitive only for compounds containing NH_2 groups. Consequently, reaction by-products formed by oxidation and deamination as wells as the cyclic anhydride could not be analysed with Method II. The condensation reaction started after 24 h, increasing steadily to reach a yield of 0.026% divaline at the end of the last cycle. There was no measurable divaline in the unbuffered blank-L-Val samples, suggesting that dimerization was catalysed by the clay. CuK10-D-val and CuK10-DL-val samples were also analysed by RP-HPLC and chiral derivatisation. Quantification of DD-Valine was not carried out since only the LL-valine standard was available for calibration purposes. Note that all the stereoisomers of divaline, four in total (LL, LD, DL, and DD), are expected to elute at different retention times when performing chiral chromatography. Co-elution of D-Val and LL-Val hindered detection of the latter in the CuK10-DL-Val samples.

4.2.2. Discussion

It can be concluded that divaline was synthesized in low ionic strength CuK10 systems under fluctuating wet-dry cycle conditions at a mild temperature of 65°C. Synthesis of dipeptides other than divaline, has been found to take place under similar conditions in the presence of clays [31, 33, 77]. However, this is the first instance where divaline production catalysed by a Cu-exchanged montmorillonite (CuK10) has been thoroughly investigated by using complementary liquid chromatographic techniques. Bujdak and Rode [77] reported that neither divaline nor cyclic divaline formed in wet-dry cycle experiments using Ca-hectorite, a 2:1 clay of the smectite group where Mg^{2+} is the cation in the octahedral layer, as a possible catalyst. Note that the pH values of

the Ca-hectorite-AA suspensions varied from 5.8 to 6.5, and more importantly stayed in the same interval after reaction. Divaline, however, has been shown to form in the salt-induced-peptide-formation reaction, with a maximum yield of 0.088% after seven days of fluctuating wetting and evaporation cycles at 85°C [130]. The highest yield of 0.027% obtained in our CuK10-L-val system is of the same order of magnitude as the above reported yield for the SIPF at comparable reaction times. Thus, clay catalysed dipeptide synthesis could be as efficient as the SIPF. Despite divaline being formed in enantiopure and racemic systems in the presence of CuK10, there is insufficient data to conclude that the linear dipeptide was formed preferentially in a particular system. This is in contrast with the SIPF reaction where L-Val dimerized preferentially over its D-counterpart due to kinetic effects in the complexation of Cu^{2+} and D-Val. All atoms possess inherent chirality, proportional to Z^5 or Z^6 (Z is the atomic number), due to parity violating energy differences at the nuclear level. It has been proposed that the inherent chirality of the Cu ion (Z=29) and the chirality of the two L- or D-AA ligands in the SIPF complex overlap resulting in diastereomer structures with different physical and chemical properties and reactivities. This in turn could explain the observed differences in dimerization[155].

The role of pH on the formation of dipeptides other than diglycine has not been systematically addressed in the literature. The optimum pH range for the formation of diglycine during the SIPF reaction was 2-3, with higher yields at pH values near 3 [156]. It is expected that variations in temperature and pH could influence the initial adsorption of the monomeric Val onto the clay before the dimerization reaction. The acidic pH in the vicinity of the CuK10 surface most likely provides a buffered environment that facilitates the adsorption of Val in the clay interlayer via complexation with Cu^{2+} or on clay edges silanol sites [86]. Expansion of the clay interlayer due to acidic pH might have possibly contributed to accommodate the sterically constrained Val monomers in the intergallery region of the clay [157].

There is controversial evidence on the effect of Cu^{2+} in catalysing peptide bond formation. An early study demonstrated that exchangeable cations in homoionic bentonite greatly influenced the yields of diglycine and dialanine, with Cu-bentonite displaying the utmost catalytic influence [79]. In contrast, another work reported that calcium-montmorillonite (CaM) and a Cu-exchanged montmorillonite prepared from CaM gave similar yields of diglycine from glycine, suggesting that the cation did not have any influence on the mechanism of dipeptide formation[33], implying that peptide

formation is mostly associated with catalysis by edge sites (Figure 1.17). It is also possible that these discrepancies originated from different types of clays used in the experiments, handling of the mineral, as well as pH effects. It is clear from the results of this research that aluminosilicate minerals can catalyse divaline formation. Nevertheless, the catalytic role of Cu on peptide bond catalysis by minerals is debatable, at least in our systems. Wet-dry cycle experiments with the raw K10 will help understand this issue. The fact that K10 is composed of an assemblage of crystalline materials might imply that the observed catalytic effect can be the result of a synergistic effect of montmorillonite, quartz, and muscovite. There is evidence that silica can catalyse divaline formation, but to the best of our knowledge the smectite clay hectorite has not catalysed the formation of divaline dipeptide [77].

In a possible prebiotic scenario the SIPF reaction and catalysis by clays may be coupled. Our data, however, suggest that high ionic strength is unfavourable to divaline formation in the presence of clays. This could be explained by decreased adsorption of Val monomers due to the disruption of outer sphere complexes between AA and surface sites by the high I of the media. Salts decrease the activity of water, so that the dimerization reaction in homogeneous aqueous solution can be thermodynamically favoured [41], but in heterogeneous systems high salt content can hinder adsorption of AAs at reactive sites of the mineral surface as reported for Val on K10 in Section 4.1.2.1.

4.2.3. Summary

Divaline was synthesized in CuK10 systems by repeated wet-dry cycles which simulate prebiotic earth environmental conditions. The acidity of the clay catalyst and therefore the pH of the clay-solution interface seem to be relevant factors in the activation of the Val monomers for peptide bond formation. Considering that the mechanism of Val adsorption onto the clay is affected by I and pH, we propose that conditions than enhance Val adsorption on the clay can result in higher yields of the dipeptide. Although the dipeptide yields in the CuK10 system are smaller than in the homogeneous SIPF reaction, clays are good templates because they provide a stable matrix that prevents decomposition of products by side reactions (i.e. hydrolysis, oxidation) and also promote the elongation of peptide chains [31, 158]. These results have implications for prebiotic chemistry since ancient organisms such as archae contain Val-Val linkages in their membrane proteins [130]. The results also underscore

the relevance of the interplay of environmental variables in assisting the catalyzed formation of dipeptides by minerals.

4.3. Adsorption of *R*- and *S*-Val on Cu(110) under Ultra High Vacuum Conditions

The following sections present the results and interpretation of the IR, LEED and STM images of enantiomers of Val adsorbed on Cu(110) under UHV conditions. Monomeric Val exists in the gas phase mainly as the conformers Ia and IIa shown in Figure 4.28 where the intramolecular N-H····O=C and N····H-O hydrogen bonds stabilize their structures[94]. In both conformers the isopropyl chain possesses the same orientation, possibly to minimize the steric strains in the molecule[159]. The infrared spectrum of gaseous Val is characterized by vibrations in the high frequency region attributed to OH and NH_2 stretching, in the medium frequency 1800-1700 cm^{-1} due the carbonyl (C=O) stretch, and below 1500 cm^{-1} for NH_2 and OH bending modes. Table 4.8 provides a comparison of the main vibrational modes of conformers Ia and IIa. The downshifted OH vibration for the conformer IIa results from the intramolecular N····H-O bond. Similarly, the downshifted C=O stretch mode in conformer Ia results from N-H····O=C hydrogen bond.

Table 4.8. Vibrational modes for gaseous Val conformers [159]

Frequency (cm^{-1})	Assignment	Conformer
3561	OH stretch	Ia
3183	OH stretch	IIa
1784	C=O stretch	IIa
1761	C=O stretch	Ia
1388, 1382	OH bending	Ia
975	NH_2 bending	Ia
877,825	OH torsion	Ia
783	C-C backbone stretch	Ia

4.3.1. Reflection-Absorption Infrared Spectroscopy of Val on Cu(110)

The infrared spectra of *S*-Val and *R*-Val on Cu(110) as a function of coverage and temperature are shown in Figures 4.29 and 4.30, respectively. Note that infrared is a characterization technique that does not allow the differentiation of the enantiomers of a chiral compound[142]. One important observation from these figures

is the absence of the OH and C=O stretching vibrations of the gaseous Val summarized in Table 4.8, suggesting that the carboxyl group changes upon adsorption onto the surface. In addition, the spectra of *S*-Val and *R*-Val were quite similar in the types of bands observed implying that both enantiomers might bond to the surface via the same mechanism. At 313 K, all of the bands increased in intensity as coverage was increased. Interestingly, the adlayer was stable to heating to 373 K since the spectral features remained unchanged (Figures 4.29 and 4.30). This suggests that Val formed a stable structure on Cu(110) since bonding was independent of coverage regime from room temperature to 373K, which contrasts with the behaviour of Ala that displays a complex polymorphism[90].

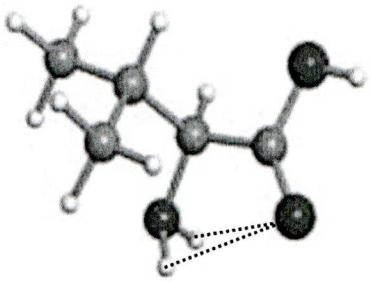

0

Ia

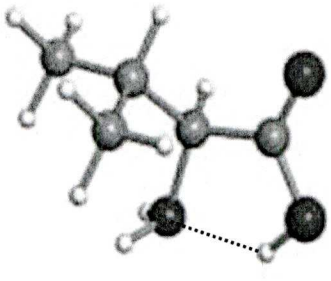

77

IIa

Figure 4.28. Conformers of Val Ia and IIa. The dashed lines indicate hydrogen bonds[94]

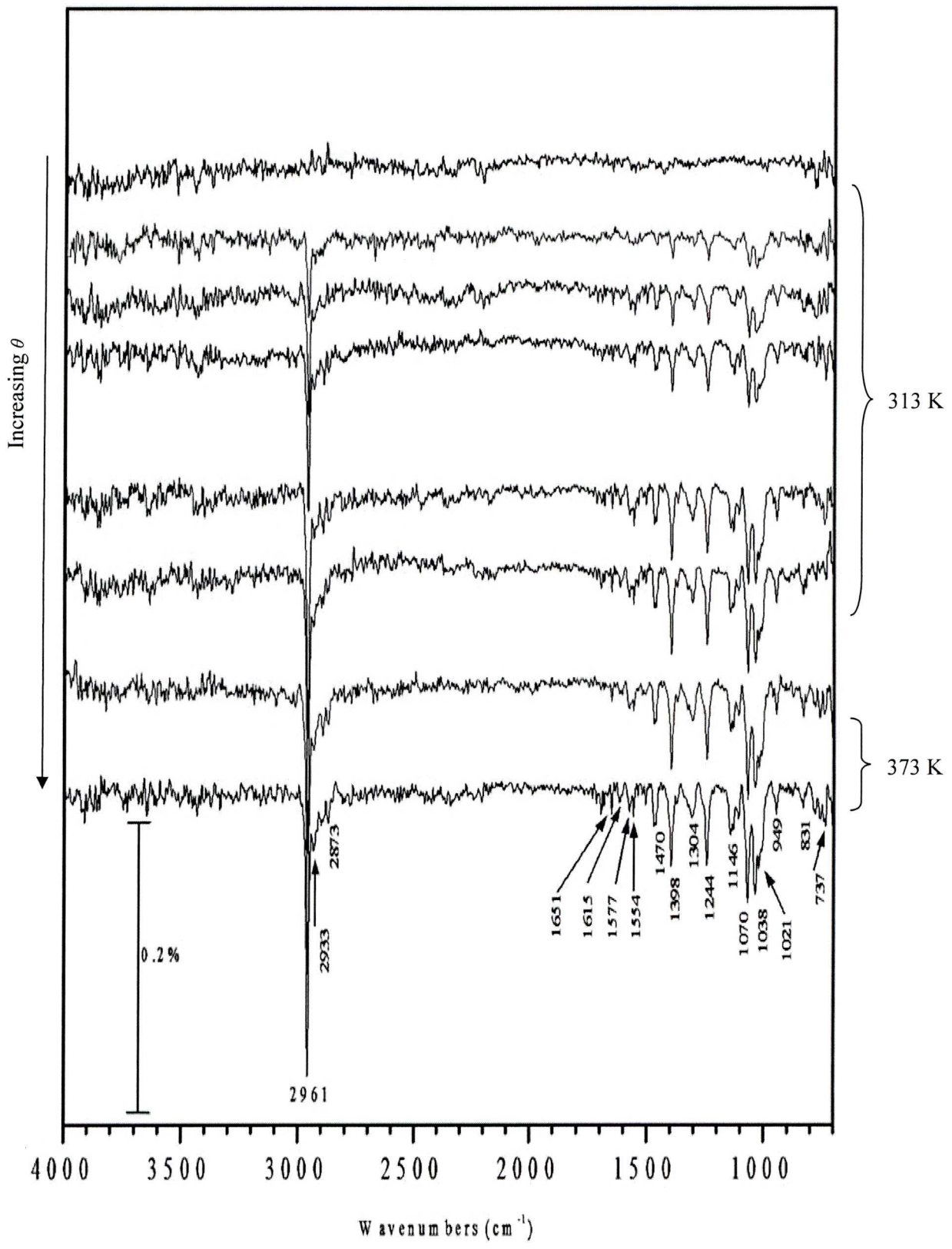

Figure 4.29. Infrared spectra of *S*-Val adsorbed on Cu(110) showing the influence of coverage (θ) and temperature

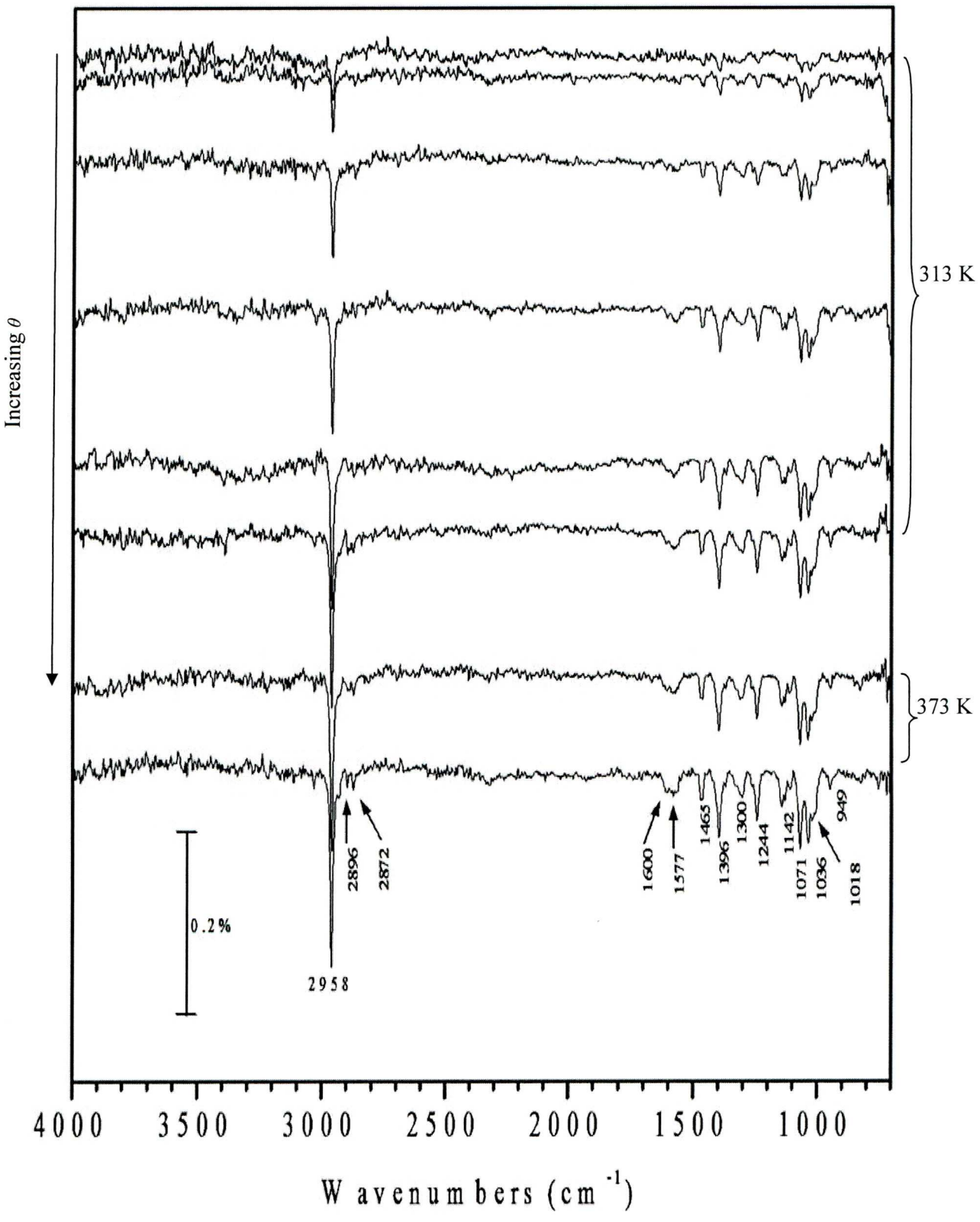

Figure 4.30. Infrared spectra of *R*-Val adsorbed on Cu(110) showing the influence of coverage (θ) and temperature

Table 4.9 summarises the main vibrational modes of Val adsorbed on Cu(110) along with the reference frequency values of Cu and Ni-Valine complexes

prepared from aqueous solutions. These 2:1 bidentate complexes form due to the coordination of the AA to the metal via its NH_2 and carboxylate groups forming five-membered chelates that adopt the *trans* configuration with respect to the metal since only vibrations antisymmetric to the centre of symmetry are infrared active[160].

Table 4.9. Vibrational frequencies, cm^{-1}, of *S*-Val and *R*-Val on Cu(110) and metal-$(Val)_2$ complexes[160]

Assignment	Low/High Coverage		Cu-(*S*-Val)$_2$	Ni-(*S*-Val) $_2.2H_2O$
	R-Val	*S*-Val		
ν_{as} (CH_3)	2961s	2958s	2960s	2965s
ν (CH)	2933sh	2931sh	2932m	2931m
ν_s (CH_3)	2873w	2872w	2876m	2876w
ν_{as}(COO-)	1615w	1600w,b	1610s	1591sh
$\delta(NH_2)$	1577w,b	1580w,b	1572s	1578s,b
$\delta_{as}(CH_3)$	1470m	1465m	1466m	1461m
ν_s(COO-)	1398s	1396s	1381s	1405s
$\delta_s(CH_3)$	1370sh	1370sh	1370sh	1368sh
δ(CH) + $\omega(NH_2)$ for Cu	1304m,b	1300m,b	1309m	1310w
	1244s	1244s	1277m	1250w
$\omega(NH_2)$	1146m	1142m	1122s,b	1153w
ν_{as}(CCN)	1070s	1071s	1080w	1113m
ν(CN) + ν_s(COO-) +	1038m	1036m	1049w	1070m
ρCH_3+ ν(CC)+ $\omega(NH_2)$	1021sh	1021sh		1015m
	949w	949w	939vw	951w
δ(COO-)	737w		737m,b	790m,b

s:strong, m:medium, sh:shoulder, w:weak, b:broad, vw:very weak. ν_{as}: asymmetric stretch, ν_s: symmetric stretch, δ_s: symmetric bending mode, ω:wagging mode, ρ:rocking mode.

The most prominent absorption band in the spectra of enantiomers of Val adsorbed on Cu(110) is seen at 2961 cm^{-1} and corresponds to the asymmetric stretching mode of the methyl group, $\nu_{as}(CH_3)$. In contrast, the symmetric stretching of the methyl group $\nu_s(CH_3)$ is weak. In order to better understand the significance of the vibrational modes of the functional groups and bonds of Val adsorbed on Cu(110), the reader is refered to the study of Gly adsorption on Cu(110) using RAIRS[161]. Figure 4.31 has been adapted from Barlow *et al.*[161] and displays the local dipole moments associated with vibrations of CH_2 (NH_2) and CO_2 groups of Gly.

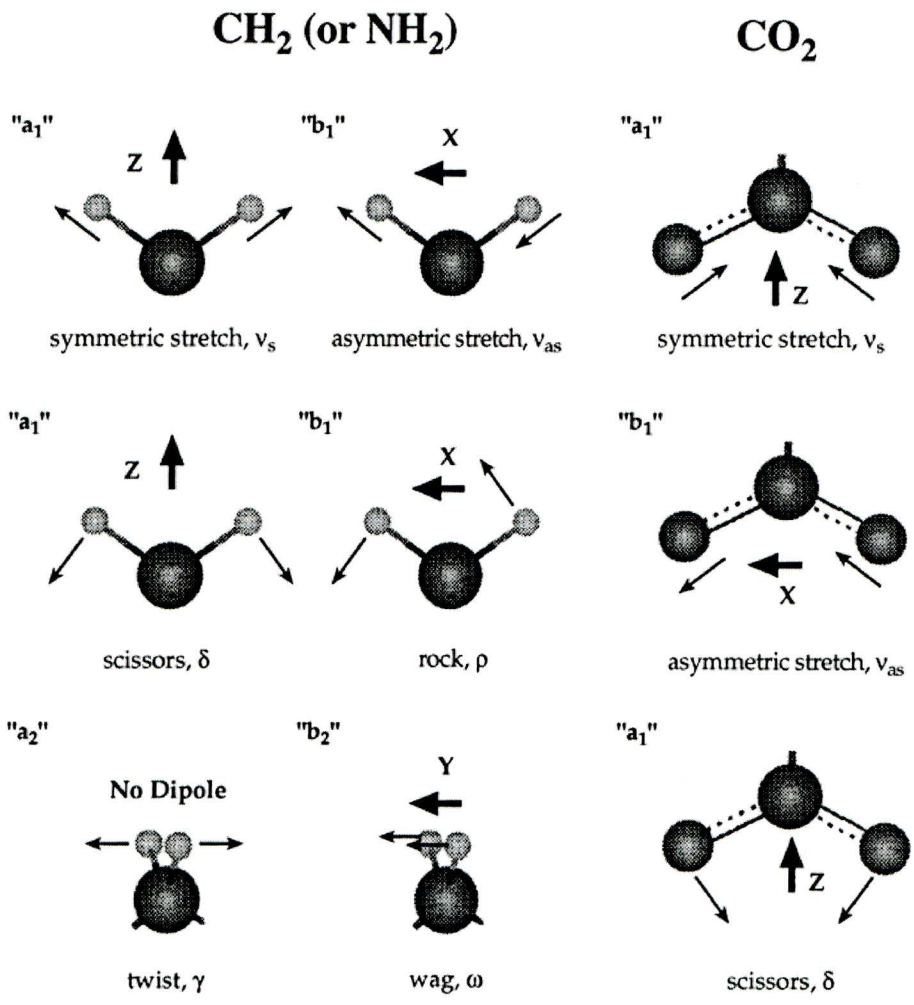

Figure 4.31. The principal localized vibrations associated with the CH_2 (or NH_2) and CO_2 groups of Gly showing the local dipole moments and symmetry with respect to a local symmetry elements. Source: Barlow *et al.*[161]

According to the RAIRS selection rule described in Appendix 1, only vibrations with a dipole moment perpendicular to the surface are infrared active, thus providing insight into the bonding of the molecule at the surface. The strong IR absorption band for the asymmetric stretching of the methyl groups of Val can be explained by a total dipole moment nearly perpendicular to the surface as shown in Figure 4.32. The asymmetric stretching vibration of the molecule's methyl group involves extension of two of the carbon-hydrogen bonds whilst the third undergoes contraction.

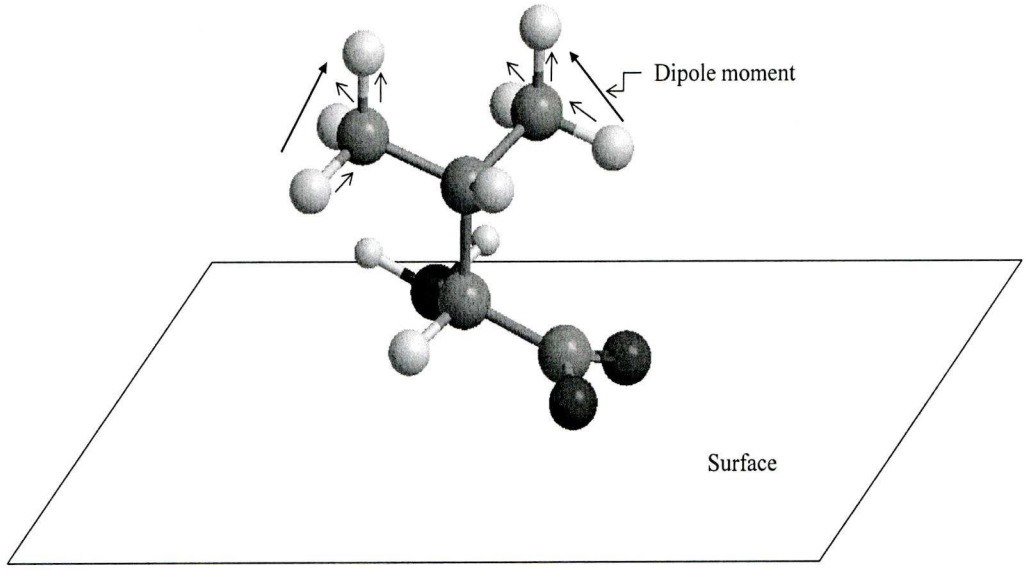

Figure 4.32. Illustration of the dipole moment of the asymmetric stretch of the methyl groups of Val and possible orientation of Val on Cu(110) based on RAIRS

The NH_2 scissoring and wagging bands at 1577 and 1146 cm^{-1}, respectively, were also present in the spectra and compared well with the bands of the metal-Val complexes in the solid state, suggesting coordination of nitrogen to the metal via an electron pair as reported previously for the adsorption of other AAs on Cu(110). DFT modelling of Ala on Cu(110)[162] has shown that the plane of NH_2 is aligned relatively to being parallel to the surface since it is oriented 23° from the surface plane, but whether this is the case for Val cannot be ascertained from the RAIRS data. Note that the antisymmetric vibrational range of the protonated amino group NH_3^+ (1560-1597 cm^{-1})[163] overlaps with the NH_2 scissoring band, but X-ray photoelectron studies of Ala on Cu(110) have ruled out NH_3^+ as a possible species in Cu(110)-Ala systems [90]. It is likely that the amino group in Val bonds onto Cu(110) in a similar manner, given that the NH_2 vibrational frequencies are in close agreement with the values for the metal-Val complexes (Table 4.9). The symmetric mode of the carboxylate group, $\nu_s(COO^-)$ at 1398 cm^{-1} was more intense than the asymmetric vibration $\nu_{as}(COO^-)$ at 1615 cm^{-1}, hinting at the molecule bonding symmetrically to the surface via both oxygen atoms of the carboxylate moiety as a result of the deprotonation of the carboxyl group (COOH). Figure 4.33 shows that the symmetric stretching mode of the resonant carboxylate has a total dipole moment perpendicular to a surface plane which enhances the IR signal. In contrast, the dipole moment of the asymmetric stretch is parallel to the surface and hence is infrared inactive according to the surface selection rule explained in Appendix 1. Taking this into account, the resonant carboxylate of

Val most likely anchored to two adjacent copper atoms of the Cu(110) surface, as depicted in Figure 4.30a, along the closed-packed row in the [$\bar{1}$10] direction as found for Ala on Cu(110).

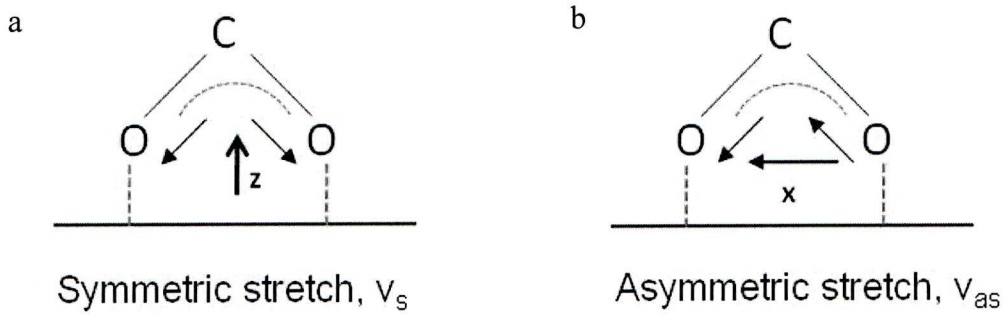

Figure 4.33. Dipole moments of a. symmetric and b. asymmetric stretch vibrations of carboxylate group on a surface

C-H bending vibrations can be seen at 1470 cm^{-1} and 1304 cm^{-1} for the C-CH_3 degenerate deformation and the isopropyl C-H, respectively, providing insight into the orientation of the bulky isopropyl group. In this respect, the C-H bond must be greatly directed parallel to the surface allowing also the $\nu_{as}(CH_3)$ stretch to give a strong absorption band. The band at 1244 cm^{-1} in the spectra of both enantiomers matches quite well with the bending modes of the CH_3 groups at 1247 cm^{-1} for the conformer Ia of neutral Val which are coupled with the CH bending mode of the isopropyl carbon at 1307 cm^{-1}[159]. Finally, the vibrational modes for the asymmetric CCN and symmetric CN stretches intermixed with carboxylate stretching and scissoring deformations were observed at 1070, 1038, 1021, and 949 cm^{-1}. The ν_{as}(CCN) stretch hints at a CCN bond at an angle with respect to the surface, supporting the conclusion that Val lies tilted on the surface rather than in an upright position. In brief, the infrared data provide evidence for Val interacting with the Cu(110) surface via three points with the OON triangular plane nearly flat on the surface. Figure 4.33 also depicts a possible model for Val bonding onto Cu(110) based on RAIRS data only. Interestingly, the orientation of Val on the surface remained unchanged with coverage and temperature as opposed to alanine and norvaline [89], highlighting the simplicity of the Cu(110)-Val system. The invariable orientation can possibly be attributed to the branched isopropyl group that restricts the rotational freedom of the molecule since

the molecular rotational freedom decreases with the increasing complexity of the side chain functional groups[164].

4.3.2 Low Energy Electron Diffraction of Val Adsorbed on Cu(110)

LEED images of the chemisorbed Val adlayers on Cu(110) at room temperature indicated long-range order of the enantiomers on the surface (Figures 4.32 and 4.33). Increasing the energy of the electrons resulted in a greater number of LEED spots as observed from the figures 4.34a-e and 4.35a-e. A_s and B_s in Figure 4.34d and 4.35d are the reciprocal unit cell vectors for Cu(110) that permit the calculation of the dimensions of the adlayer unit cell in real space. Note that the centre of the unit cell (00) in the images is located in the position of the ion gun and the coordinates of the unit cell of the Cu(110) substrate are designated as (01) and (-10) (Figures 4.34e and 4.35e). The extra spots correspond to Val. The repeat unit cells for *S*-Val and *R*-Val on Cu(110) are sketched in Figures 4.34d and 4.35d that correspond to the 44 and 46 *eV* electron energies, respectively. The overlayer vectors A_0 and B_0 of *S*-Val on Cu(110) were derived geometrically from the LEED patterns. To better illustrate this, the reciprocal space LEED pattern of *S*-Val on Cu(110) is reproduced as shown in Figure 4.34f. Recalling this figure, A_0 and B_0 are related to the vectors A_s and B_s of the substrate by

$$A_0 = (-1/14)A_s + (1/7)B_s$$
$$B_0 = (-1/2)A_s + (0)B_s$$

which in matrix notation is equivalent to

$$\begin{pmatrix} A_0 \\ B_0 \end{pmatrix} = \begin{pmatrix} -\frac{1}{14} & \frac{1}{7} \\ -\frac{1}{2} & 0 \end{pmatrix} \begin{pmatrix} A_s \\ B_s \end{pmatrix}$$

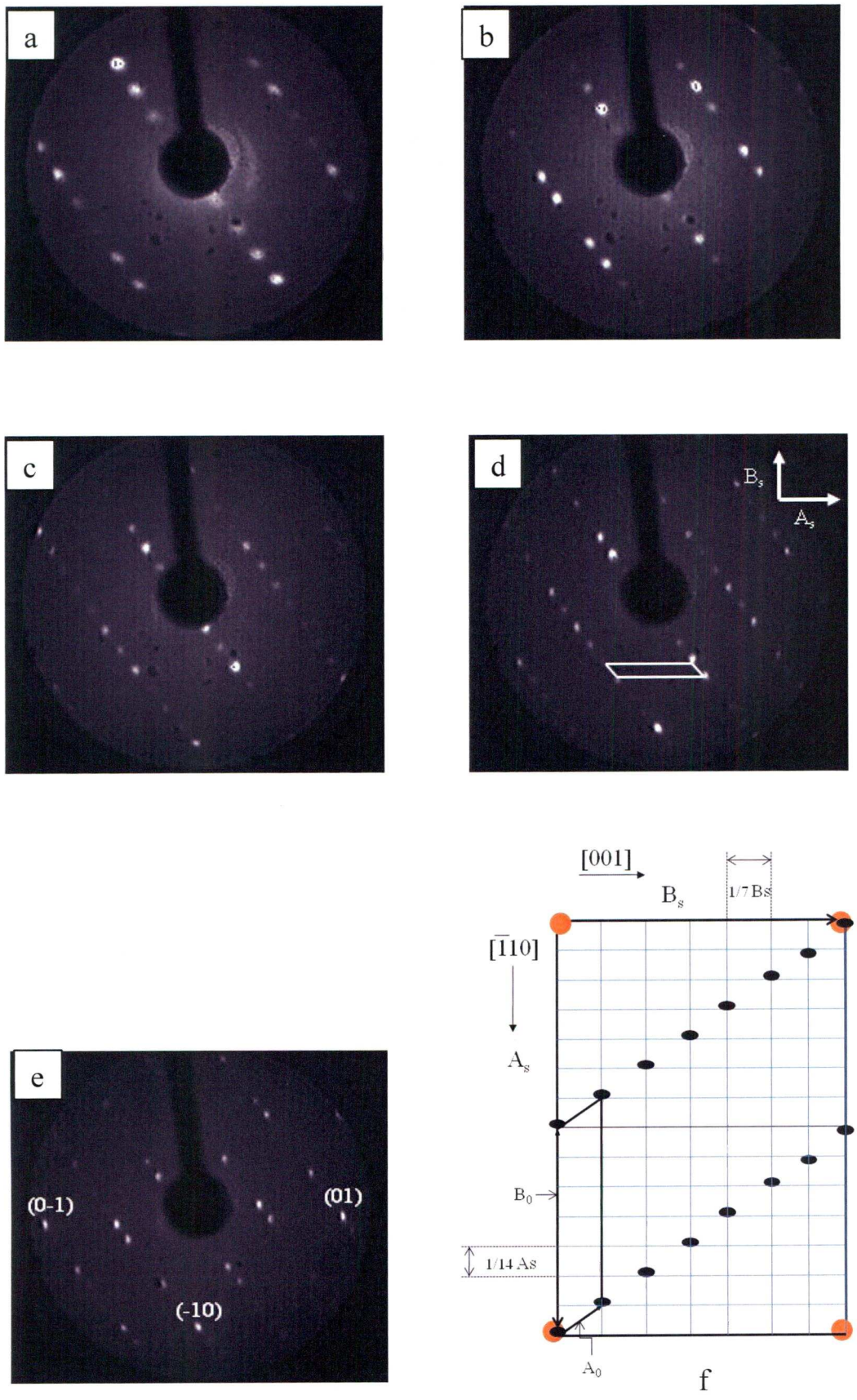

Figure 4.34. LEED images of *S*-Val dosed on Cu(110) at room temperature. a. 19 *eV*. b. 29 *eV*. c.35 *eV*. d.44 *eV*. e.56 *eV*. f. Schematic representation of LEED pattern of *S*-Val adlayer on Cu(110) in reciprocal space. Ovals:Val; Circles: Cu(110) substrate

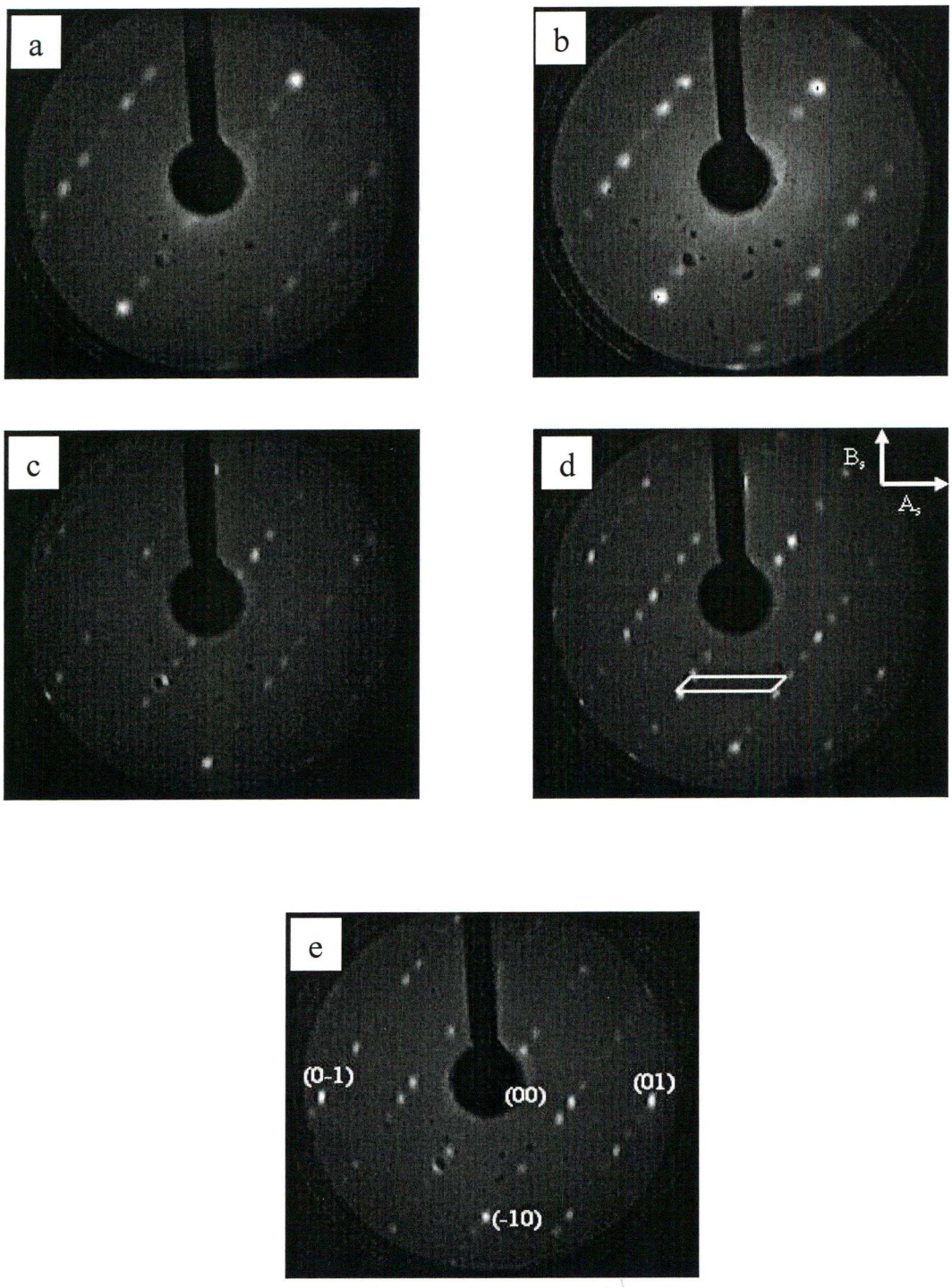

Figure 4.35. LEED images of *R*-Val dosed on Cu(110) at room temperature. a. 20 *eV*. b. 25 *eV*. c.37*eV*. d.46 *eV*. e.57 *eV*

Applying equation 14 of Appendix 1 for calculating the real space vectors a_0, b_0, we have:

$$\begin{pmatrix} a_0 \\ b_0 \end{pmatrix} = \begin{pmatrix} 0 & 7 \\ -2 & -1 \end{pmatrix} \begin{pmatrix} a_s \\ b_s \end{pmatrix}$$

Analogously, the adlayer matrix notation for *R*-Val on Cu(110) is represented by

$$\begin{pmatrix} a_0 \\ b_0 \end{pmatrix} = \begin{pmatrix} 2 & -1 \\ 0 & 7 \end{pmatrix} \begin{pmatrix} a_s \\ b_s \end{pmatrix}$$

The notations for the overlayer and substrate vectors follow the conventions by Barlow and Raval[89]. Since the dimensions a_s and b_s of the Cu(110) unit cell are 2.56 Å and 3.61 Å (Figure 1.18), respectively, then the dimension of the adlayer unit cell are a_0= 25.27 Å and b_0=6.26 Å. The angle between the vectors a_0 and b_0 is *ca* 125°. The LEED patterns indicate that the adlayers of enantiomers of Val on Cu(110) have long-range two-dimensional periodicity and self-assemble as chiral structures of opposite handedness.

Annealing of the *S*- and *R*-Val adlayers to temperatures above 473 K resulted in faint, undistinguishable disordered achiral adlayer structures (Figure 4.36) (due to the high background noise. These achiral adlayers were found to be arranged as centred, *c*(4×2) structures from STM images as it will be discussed in Section 4.3.3. High temperature disrupted the room temperature chiral arrangement because the molecules rearranged to acquire a thermodynamically stable orientation. The molecular size of Val is greater than that of Gly and Ala, thus explaining the bigger size of the Val unit cell in comparison to that of Ala (*c*(3×2)). The reciprocal and real space representations of $c(4\times 2)$ adsorbate overlayers are sketched in Figure 4.37. Figure 4.37b displays the $c(4\times 2)$ unit cell defined by four adsorbate molecules positioned at the corners of the rectangle and one adsorbate molecule in the centre. In the unit cell depicted there are two adsorbate molecules (one in the middle plus one obtained by the contribution of the four corners) per eight copper atoms to give a coverage $\theta = 2/8 = 1/4$ monolayer (ML). The smallest repeat primitive unit cell with matrix notation as shown below is also depicted in Figure 4.37 b.

$$\begin{pmatrix} a_0 \\ b_0 \end{pmatrix} = \begin{pmatrix} 2 & 1 \\ -2 & 1 \end{pmatrix} \begin{pmatrix} a_s \\ b_s \end{pmatrix}$$

In the real space representation the adsorbate molecules have been positioned on top of the Cu atoms, but LEED alone cannot give the adsorption sites. That is why to understand how molecules self-assemble at surfaces other complementary techniques such as RAIRS and STM are used to get more insight into the type of bonding, number of molecules per unit cell, and to find out if there is any disorder.

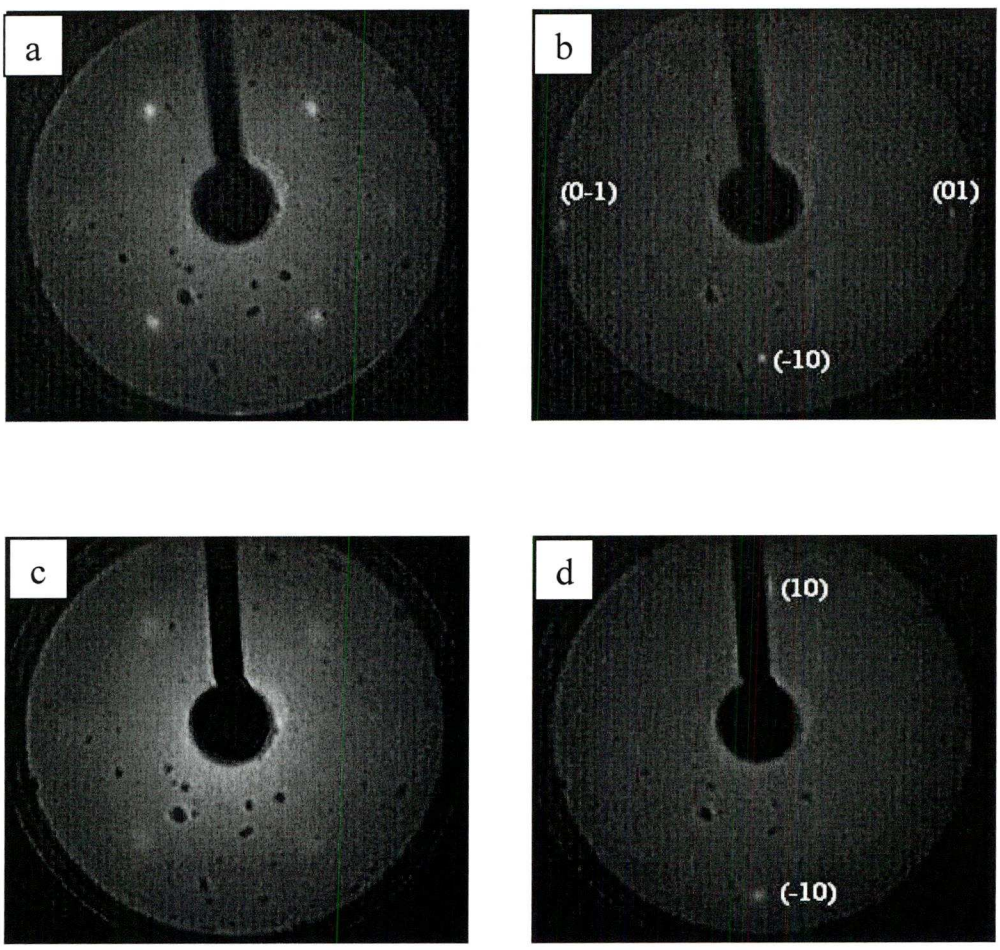

Figure 4.36. LEED patterns of adlayers of *S*-Val on Cu(110) annealed to 473 K for electron beam energies of a. 24 *eV* and b. 50 *eV*, and of *R*-Val on Cu(110) for electron beam energies of c.23 *eV* and d. 41 *eV*

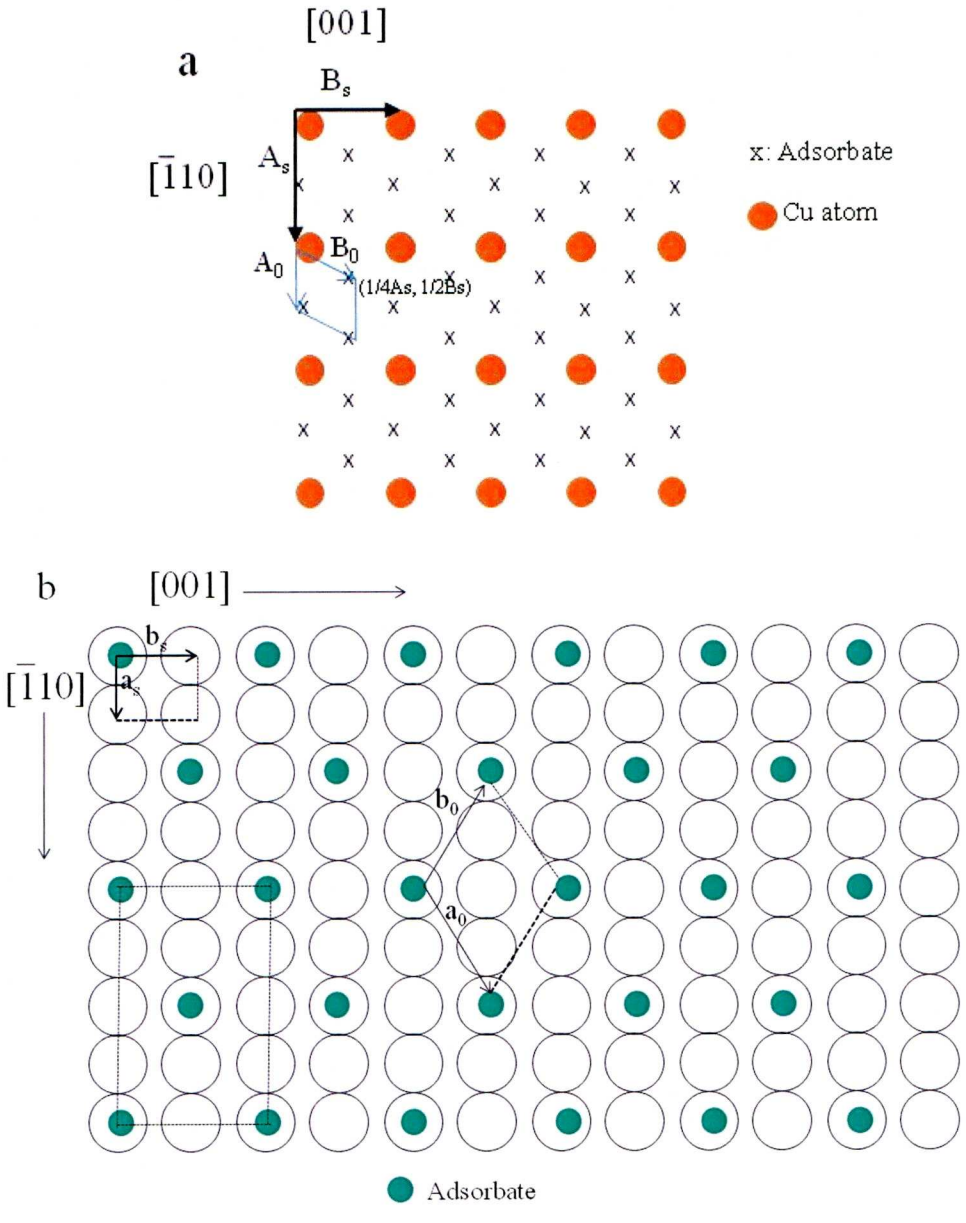

Figure 4.37. Representation of a *c*(4 × 2) adsorbate overlayer on a Cu(110) plane in a. reciprocal space and b. real space

4.3.3 Scanning Tunnelling Microscopy of Val Adsorbed on Cu(110)

STM imaging of enantiopure and racemic Val overlayers was undertaken in order to observe any possible chiral arrangement of the molecules on Cu(110) at the molecular level. In contrast to LEED, STM images give a real space representation of adsorbates at surfaces. It is important to mention that the observed contrasts in the images result from different density of states of adsorbates/substrate atoms rather than a strict geometrical representation of them. This technique in particular allowed observation of how the molecules oriented with respect to each other within the unit

cell, which ultimately permitted the proposal of a structural model for the Val overlayers on Cu(110).

4.3.3.1. STM of Enantiomers of Val Adsorbed on Cu(110)

Figures 4.38 and 4.39 display STM images of *S*- and *R*-Val overlayers on Cu(110) at different magnifications at room temperature. The big size images (Figures 4.38a and 4.39a) show islands of Val scattered on the flat Cu(110) surfaces. Clearly, Val self-assembled in well-defined domains characterized by uninterrupted long chains of four Val molecules as represented by brighter spots in the middle of the chains and less bright ones towards the edges. This particular arrangement of the chains resulted in nanochannels or dark areas in the images (Figures 4.38c and 4.39c). The chains are orientated along the $[\bar{1}\,11]$ and $[1\bar{1}1]$ directions for *S*- and *R*-Val, respectively. In these images, colour-contrasted protrusions represent Val molecules against a streaky background (Figures 4.38a,b and 4.39a,b). The bright protrusions in the middle of the chains appeared to adopt adsorption geometries different from the ones at the edges. In addition, topographic scans along the $[\bar{1}11]$ direction showed that the height of the bright spots is approximately 1.5 times the height of the other protrusions (scans not shown). The repeat STM unit cell of *S*-Val on Cu(110) sketched in Figure 4.40 and has the same dimensions as the LEED unit cell (25.2 Å $\times$ 6.2 Å). The ovals on this image are intended to illustrate that *S*-Val molecules appear to project mirror image chiral triangular footprints within the unit cell, possibly as a result of rotation of the amino group. This speculation can only be confirmed by molecular modelling studies such as density functional theory (DFT). If this were the case, the energies of adsorption of the molecules adopting different chiral footprints would be different and the adlayers would be characterized by molecular homochirality and footprint heterochirality[91]. As previously reported for enantiomers of Ala, the *S*- and *R*-Val adlayers are mirror images of each other (Figure 4.41) signalling that molecular chirality is transferred from the nanoscale (molecule) to the macroscale (organization into chiral domains), which override any underlying symmetry elements of the substrate. The coverage of this phase is 2/7 ML and there are 4 molecules per unit cell. A possible structural model for *S*- and *R*-Val on Cu(110) based on STM, RAIRS, and LEED information is depicted in Figure 4.42.

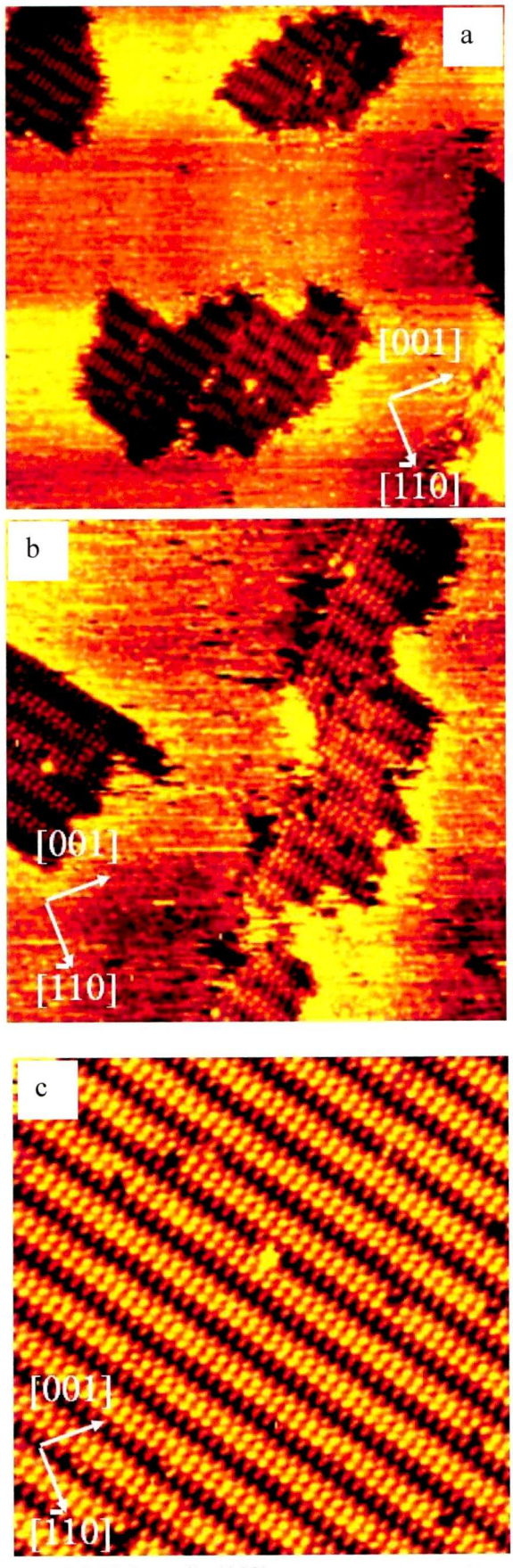

Figure 4.38. STM images of *S*-Val on Cu(110) at room temperature. a. 448 Å × 448 Å [V_t=-0.88V; I_t=-0.46 nA], b. 314 Å × 312 Å [V_t=-0.88V; I_t=-0.44 nA], and c. 217 Å × 217 Å [V_t=-0.88V; I_t=-0.35 nA]

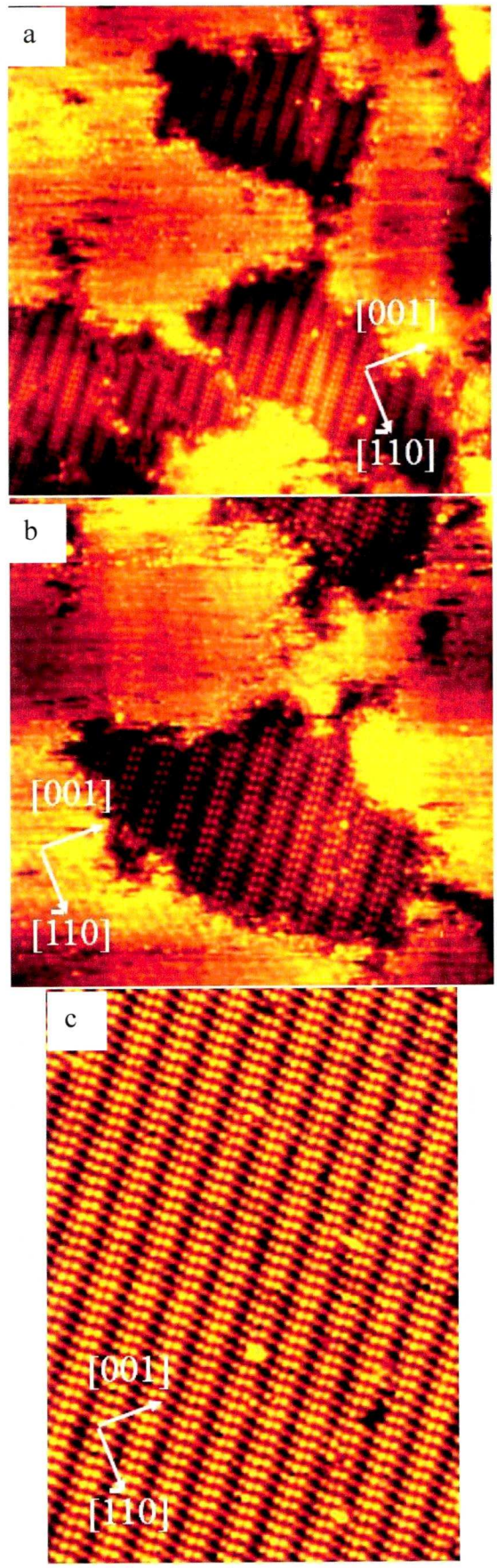

Figure 4.39. STM images of *R*-Val on Cu(110) at room temperature. a. 448 Å × 448 Å [V_t=-0.88V; I_t=-0.57 nA], b.314 Å × 312 Å [V_t=-0.88V; I_t=-0.53 nA], and c.208 Å × 288 Å [V_t=-0.88V; I_t=-0.45 nA]

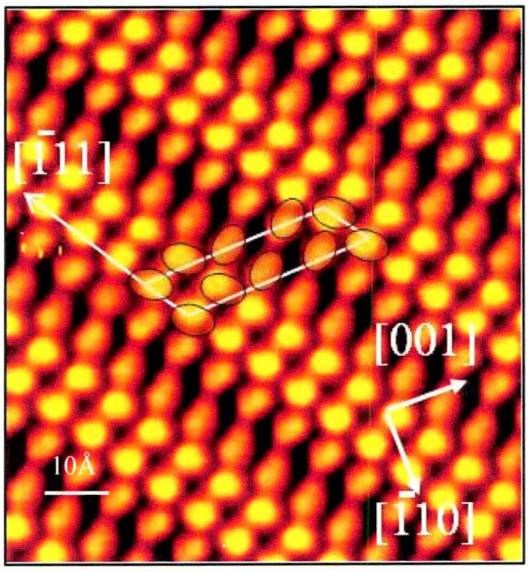

Figure 4.40. Schematic of the STM unit cell of *S*-Val on Cu(110) at room temperature. Image 69 Å × 73 Å. [V_t=-0.88V; I_t=-0.4 nA]

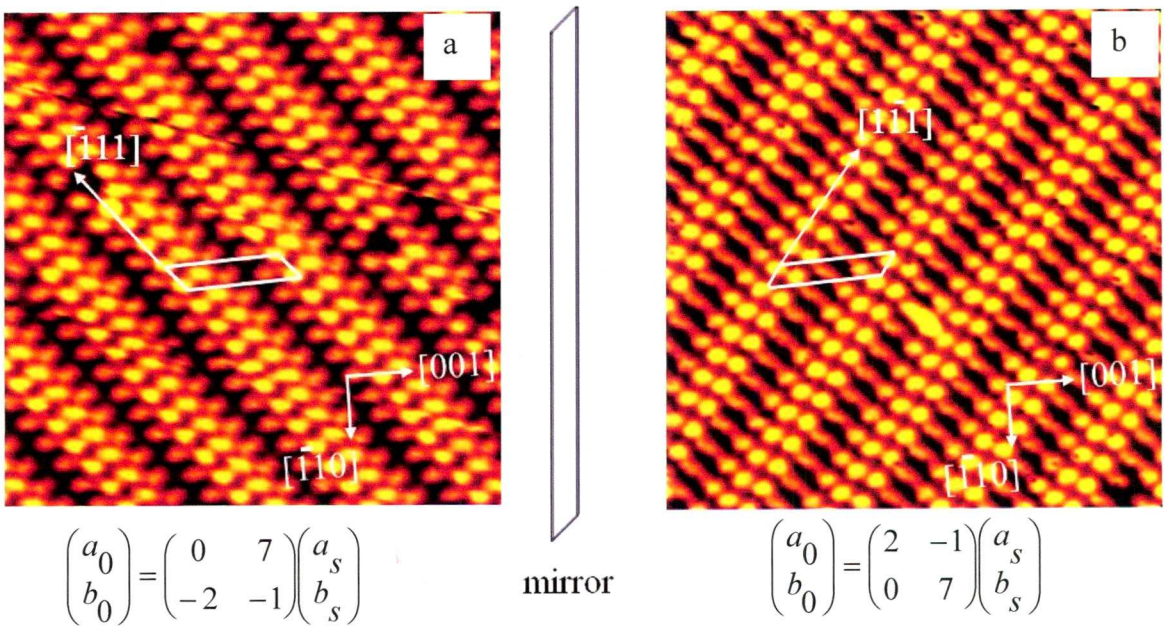

Figure 4.41. STM images (136 Å × 136 Å [V_t = -0.88 V; I_t =-0.37 nA] showing the a. *S*-Val (0 7, -2 -1) and b. (2 -1, 0 7) *R*-Val adlayers at 313 K

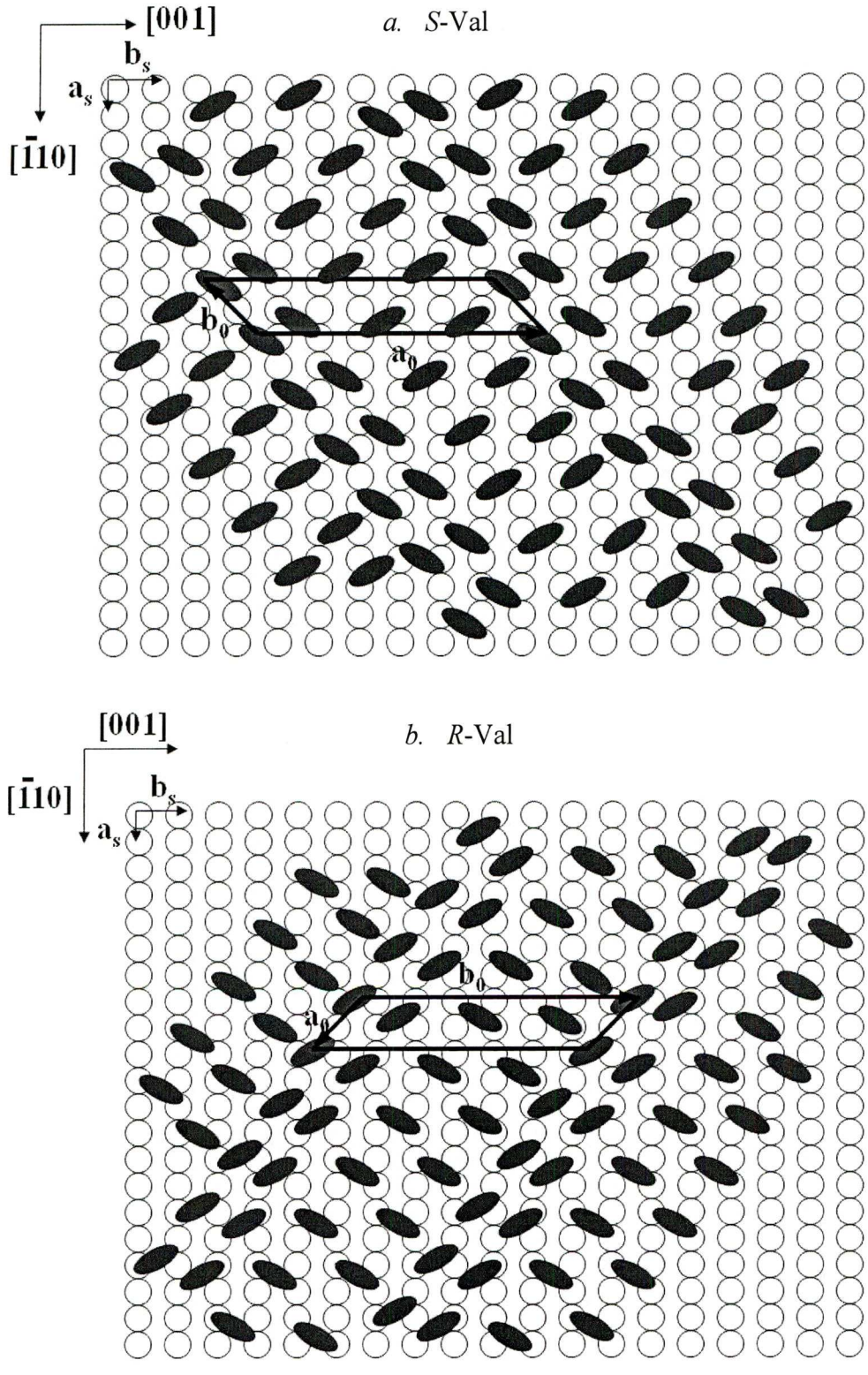

Figure 4.42. Structural model of *S*- and *R*-Val on Cu(110). Vectors a_0 an b_0 show the orientation of the respective unit cells

Preliminary DFT modelling of the room temperature adlayers points towards molecules of Val orienting differently within the unit cell. According to the simulation, the less bright molecules in the STM images still bond to Cu(110) via a three point interaction, but the oxygen atoms of the carboxylate bond diagonally to Cu atoms along the <112> direction (Figure 1.18 shows this direction on the Cu(110) lattice). This could possibly explain why molecules of Val seem to orientate differently with respect to each other inside the unit cell outlined in Figure 4.40. In Figure 4.42 positioning of *S*- and *R*-Val on the Cu(110) lattice is indicated by the orientation of the ovals which represent a triangular footprint considering that Val probably binds via the carboxyl and amino group (see Figures 4.32 and 4.43) in agreement with the RAIRS interpretation.

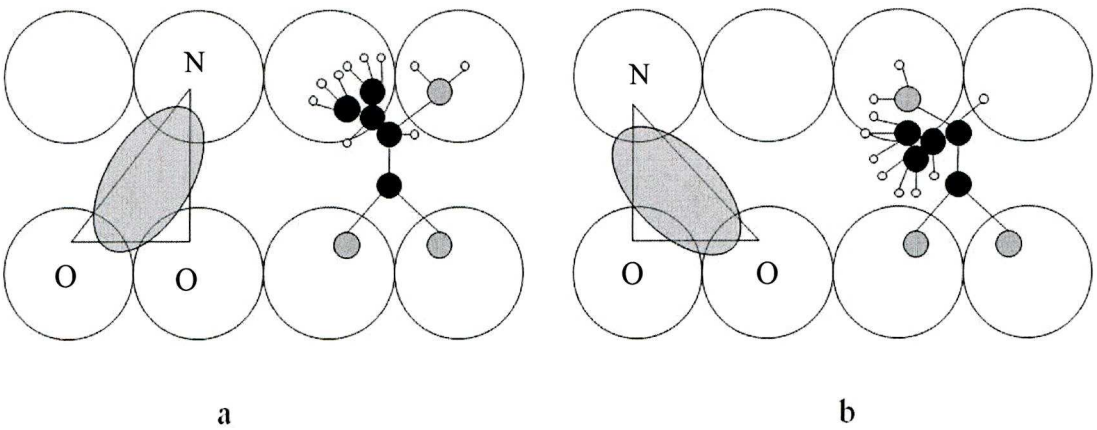

Figure 4.43. Possible footprint chirality of *S*-Valinate adsorbed on Cu(110) created by rotation around the chiral carbon. Image adapted from that of Ala footprint on Cu(110) [91]

DFT calculations have shown that the most stable adsorption geometry for *S*-Ala is the one shown in Figure 4.43 b[162]. In this figure, oxygen (O) and nitrogen (N) atoms are located at the vertices of the triangle. Even though the isopropyl side chain group of Val is directed away from the surface as in the case of the methyl group of Ala, further investigation is needed to confirm which is the preferred adsorption geometry of Val on Cu(110). Stabilization of the chiral self-assembled adlayers occurs as a result of hydrogen bonding interactions between electron rich atoms mainly oxygen (O) of the carboxylate group and hydrogen belonging either to the chiral carbon or to the amino (NH_2) group.

Annealing of the enantiopure adlayers of Val to temperatures above 473 K resulted in $c(4 \times 2)$ achiral structures. STM images of the annealed *S*- and *R*-Val adlayers illustrate the achiral organization of the two systems (Figures 4.44-4.46).

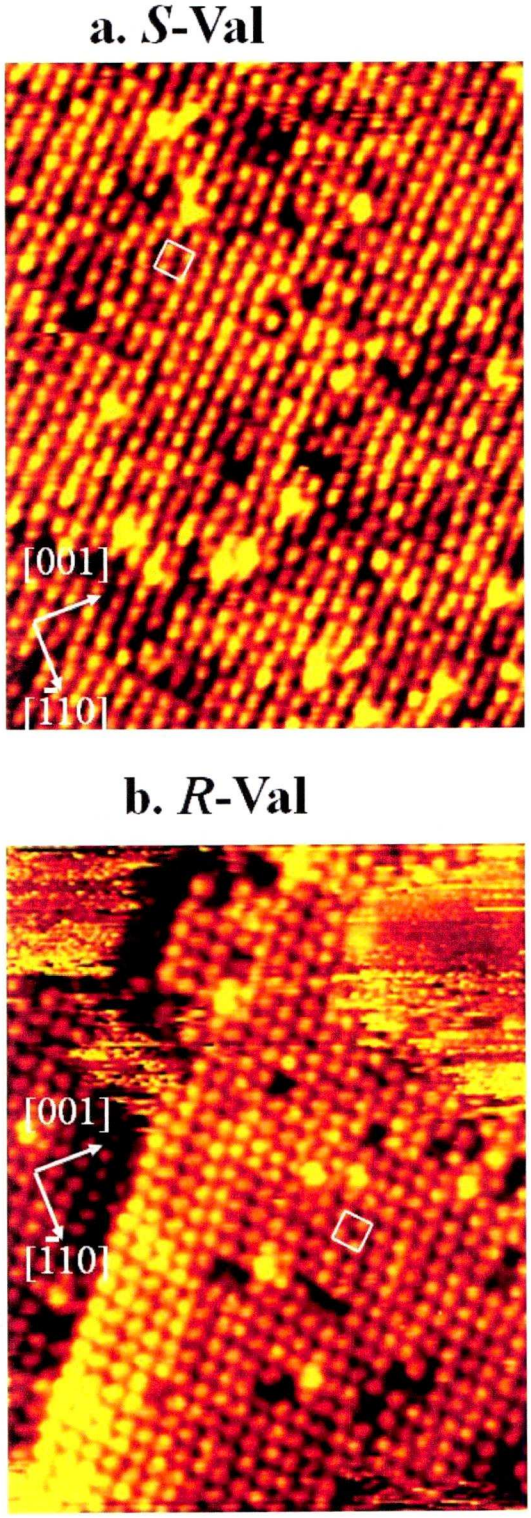

Figure 4.44. STM images (136 Å × 173 Å) [V_t = -0.88 V, I_t = -0.7 nA, Annealing temperature 473 K] showing the c(4 × 2) unit cells for a. *S*-Val and b. *R*-Val

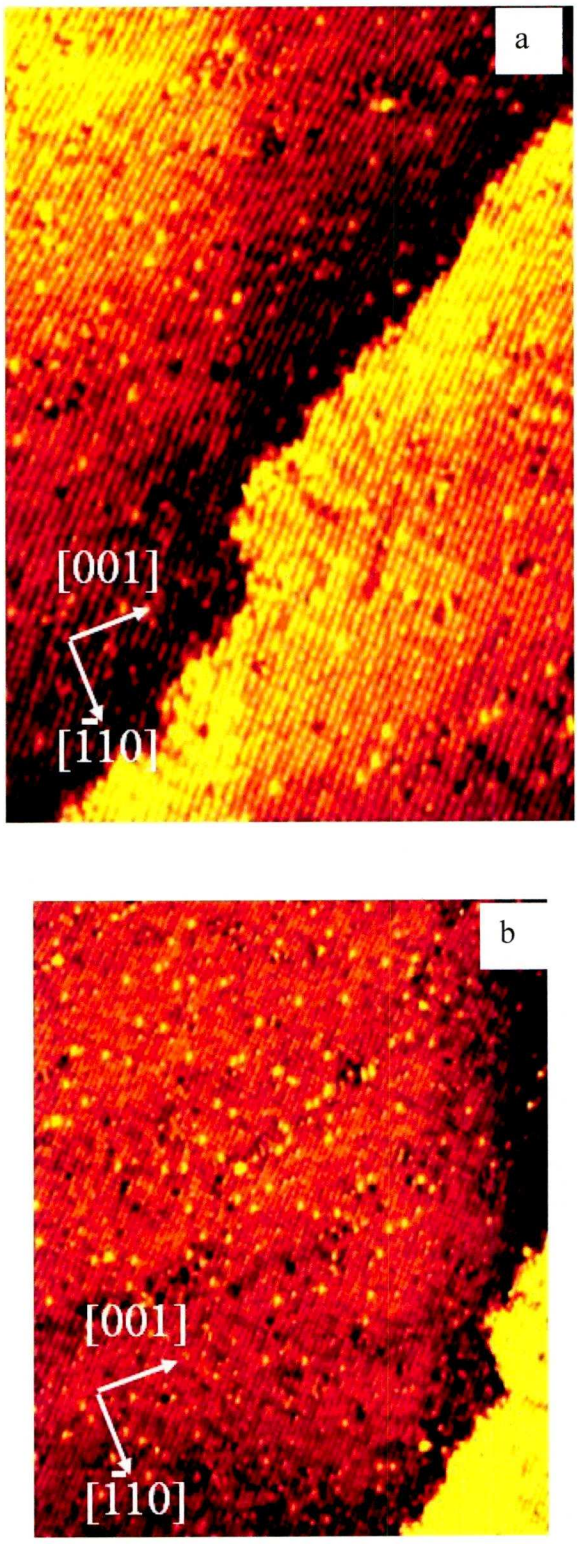

Figure 4.45. STM images of *S*-Val achiral phases: a. (314 Å × 443 Å) [V_t = -0.88 V, I_t = -0.56 nA, Annealing temperature 473 K], b. (445 Å × 547 Å) [V_t = -0.88 V, I_t = -0.56 nA, Annealing temperature 473 K]

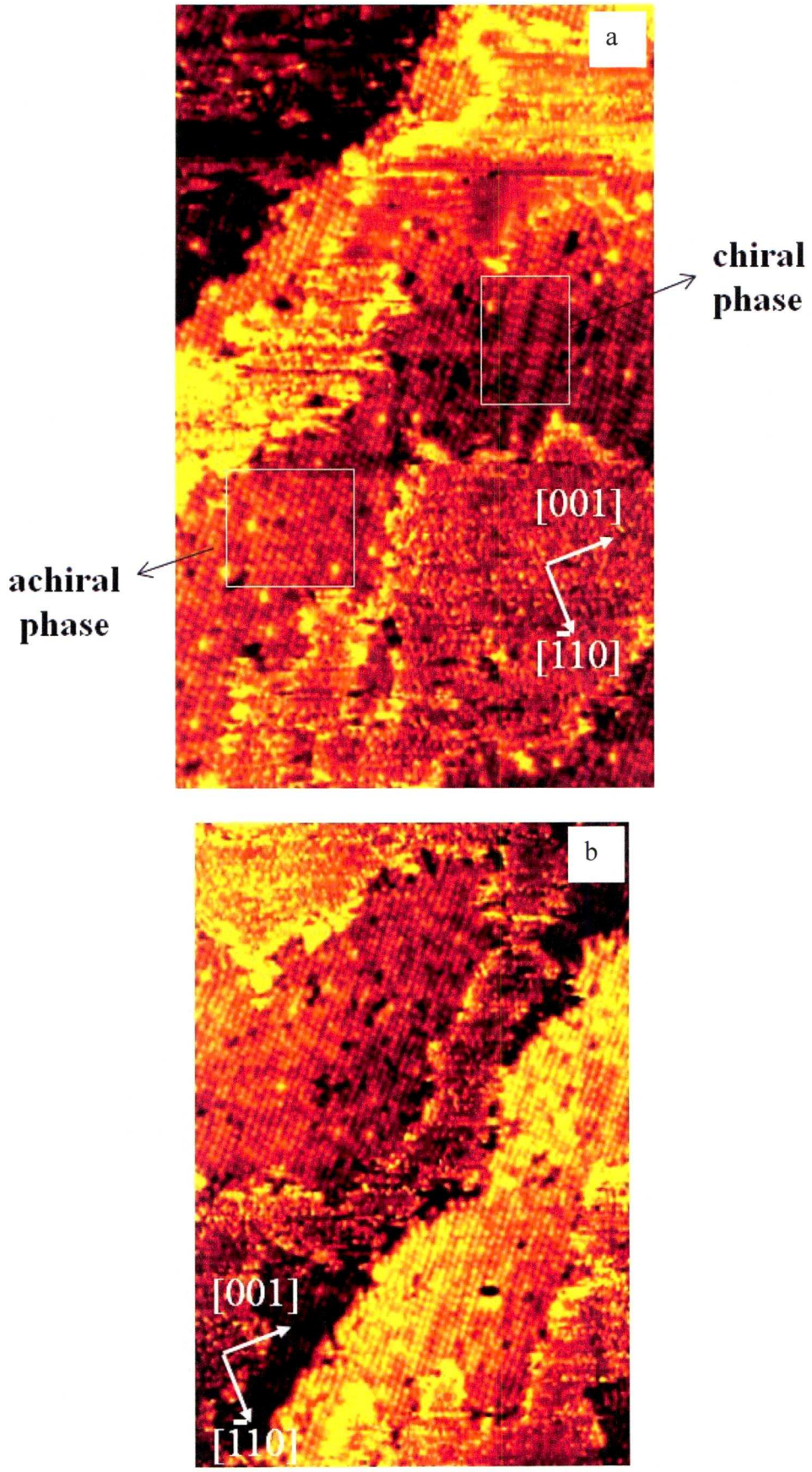

Figure 4.46. STM images of *R*-Val chiral/achiral phases: a. (309 Å × 496 Å) [V_t = -0.88 V, I_t = 0.42 nA, Annealing temperature 473 K], b. (310 Å × 457 Å) [V_t = -0.88 V, I_t= -0.53 nA, Annealing temperature 473 K]

The primitive unit cells of $c(4 \times 2)$ Val overlayers (refer to Figure 4.37 b for comparison) are depicted in Figure 4.44 a and b. The achiral phases for both *R*- and *S*-Val extended over the nanometre scale although in some areas of the images the unit cell appeared to be distorted from a true $c(4\times2)$ in agreement with the findings for enantiopure Ala on Cu(110) at temperatures above 400 K[91]. This can be due to Val adopting two possible chiral footprints inside the unit cell. In this respect, Rankin and Sholl's[162] DFT calculations have shown that the (3×2) unit cell of enantiopure Ala adlayers is made up of Ala molecules possessing opposite adsorption footprints as seen in Figure 4.43, which might also be the case for Val. Figure 4.45 shows a step edge feature of the surface for the *S*-Val achiral phase. In general, there exists long range order for this system, but there are instances of interrupted chains represented by black spots in the images. In addition, bright spots that can be due to molecules in the second layer can be observed in Figure 4.45.

The achiral *R*-Val phase is interesting because in selected images both chiral and achiral domains appear to coexist at the annealed temperature (Figure 4.46a). This suggests that the transition from the chiral to the achiral phase is via a first order transition.

4.3.3.2. STM of Racemic Val Adsorbed on Cu(110)

Adsorption of a racemic mixture of *S*- and *R*-Ala onto Cu(110) at room temperature was studied by STM. Overall, both enantiomers seemed to form a random mixture on the surface lacking order. Patchy areas illustrating this observation can be seen in Figure 4.47a. However, Figures 4.47 b and c show images that contain small areas of localized *R*- and *S*-Val domains. This suggests that phase separation of the enantiomers occurs to some extent possibly because like-like interactions between molecules of the same chirality are preferred, resulting in enantiopure domains of each chirality coexisting at the surface[91]. In these images the left and right-handed nanochannels form an angle of *ca* 78°C. Annealing of the racemic adlayer to 473 K produced a quasiperiodic structure that tends to possess a $c(4\times2)$ periodicity (Figures 4.48a and b). The resulting adlayer is mostly achiral and extends over a large area of the surface as illustrated in Figure 4.48 a. The purpose of the grid in Figure 4.48b is to guide the eye in the visualization of the $c(4\times2)$ unit cell. Notice that there is a partial

lack of registry between a theoretical $c(4\times2)$ overlayer represented as the grid (refer to Figure 4.37b) and the real annealed *S*-Val adlayer depicted in Figure 4.48b. Chiral domains on the surface were observed in a few instances and are displayed in Figure 4.47.

In conclusion, the racemic mixture is probably adsorbed on the surface as a random mixture of *S*- and *R*-Val molecules that confer net achirality to the surface perhaps similar to the behaviour of racemic Ala mixtures on Cu(110) [91, 162]. The orientation of the molecules in the unit cell cannot be predicted with the available information[91]. Further LEED and X-ray photoelectron diffraction studies as well as DFT calculations might be needed to address this question.

In summary, enantiomers of Val chemisorbed onto Cu(110) at room temperature forming mirror image stable adlayers that exhibited long-range order. A model was proposed for the self-assembly of the molecules based on combined RAIRS, LEED, and STM data. One of the main results was that molecules within the unit cell possibly adsorb on different sites as STM suggested it. Modelling of the Val-Cu(110) system is underway to look into this possibility.

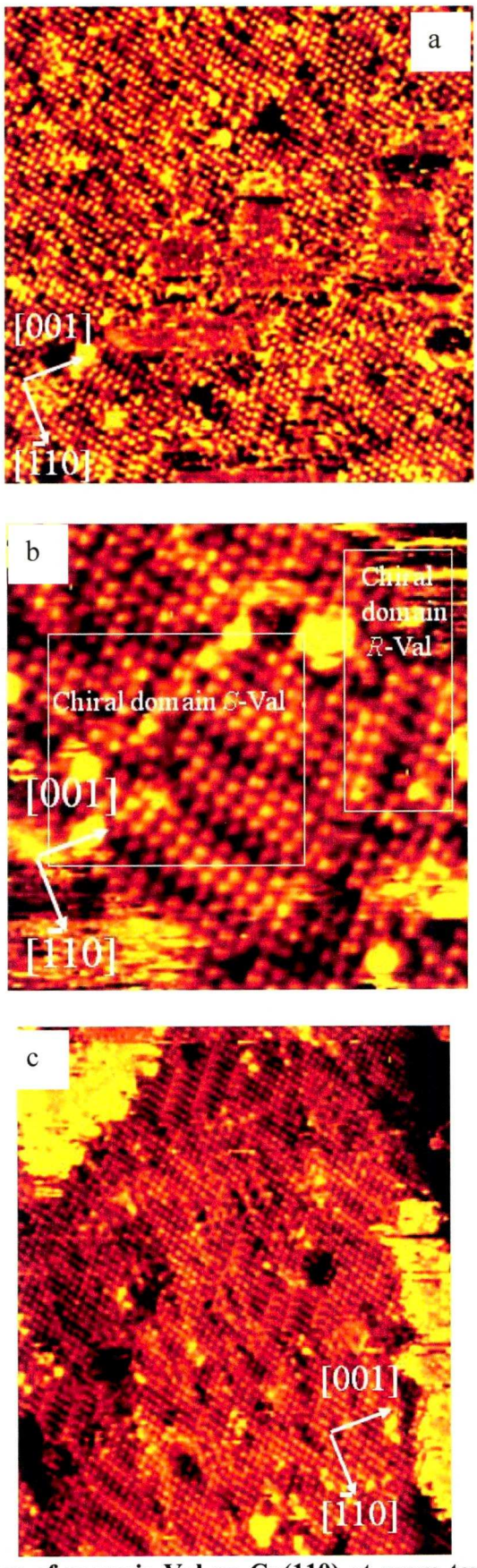

Figure 4.47. STM images of racemic Val on Cu(110) at room temperature. a. (311 Å × 311 Å) [V_t= -0.88 V, I_t= -0.42 nA], b. (133 Å × 133 Å) [V_t= -0.88 V, I_t= -0.49 nA], c. (312 Å × 381 Å) [V_t = -0.88 V, I_t = -0.49 nA]

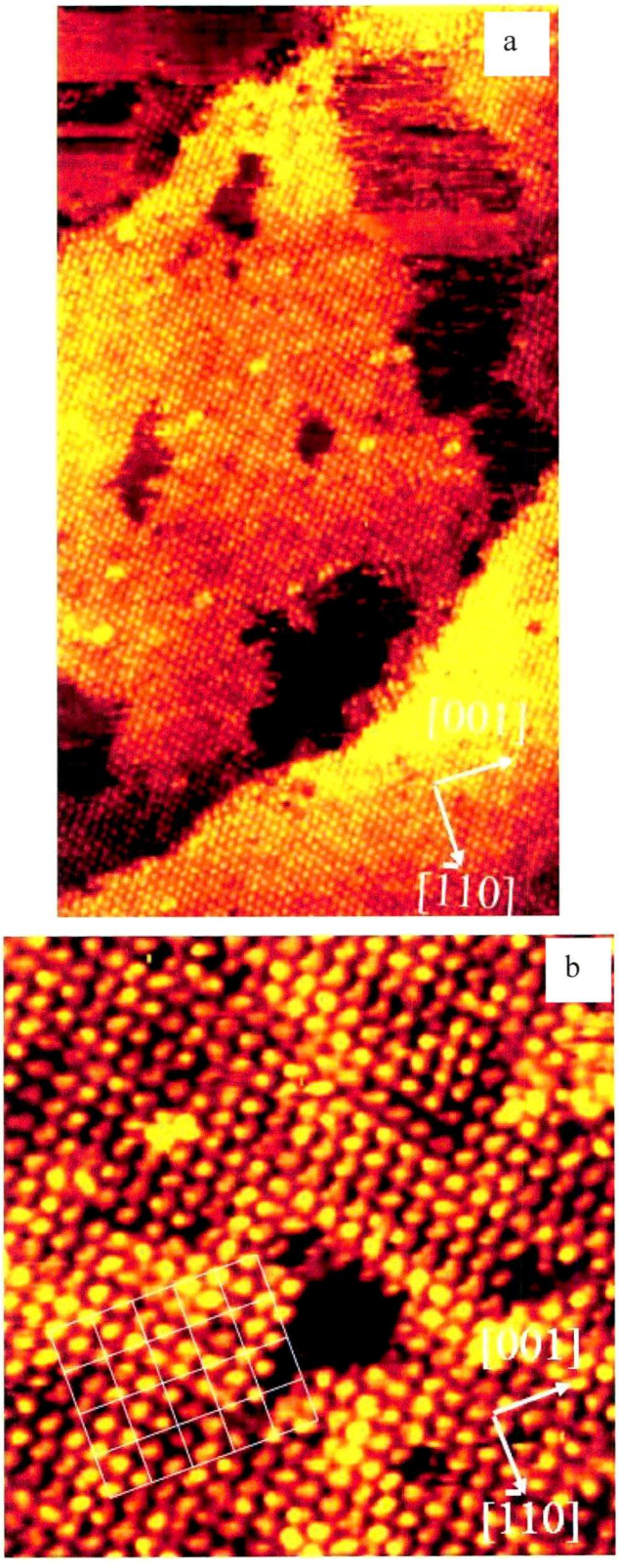

Figure 4.48. STM images of racemic Val on Cu(110). a. (314 Å× 769 Å) [V_t= -0.88 V, I_t= 0.39 nA, Annealing temperature 473 K], b. (136 Å× 136 Å) [V_t = -0.88 V, I_t = 0.51 nA, Annealing temperature 473 K]

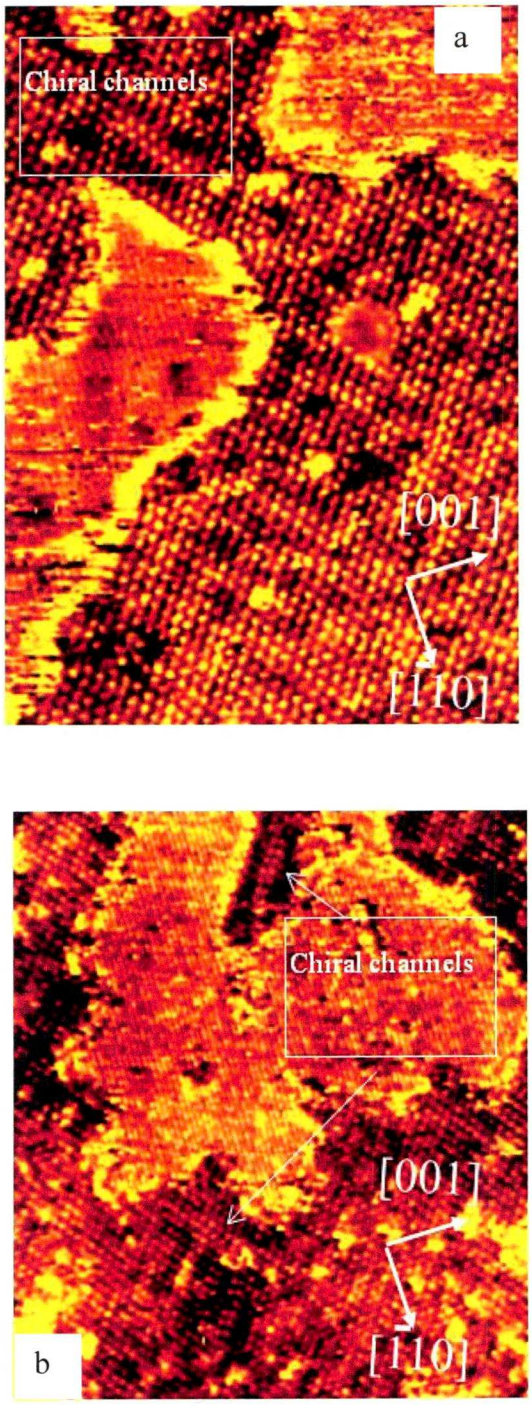

Figure 4.49. STM images of racemic Val on Cu(110). a. (223 Å × 305 Å) [V_t = -0.88 V, I= 0.52 nA, Annealing temperature 473 K], b. (312 Å × 354 Å) [V= -0.88 V, I_t = 0.50 nA, Annealing temperature 473 K]

CHAPTER 5 CONCLUSIONS AND RECOMMENDATIONS

This work examined the adsorption of a suite of chiral AAs on mineral surfaces in aqueous solution and of Val on a Cu(110) single crystal under UHV conditions. The main objective of the work was to study potential enantioselective adsorption of one AA enantiomer over the other on different minerals of prebiotic relevance. Evaluation of the extent of adsorption of AAs on minerals in aqueous systems was conducted in batch experiments by measuring AA concentrations before and after adsorption using HPLC with chiral thiol derivatisation. Assessment of selective adsorption was undertaken by carrying out statistical analysis of the data based on hypothesis testing for the equality of the means of the mineral-AA system and the standard AA solution.

Conditions for quantifiable adsorption of diluted AAs on several quartz substrates were determined. It was found that Arg displays affinity for quartz surfaces over a wide pH range and that under acidic conditions Asp binds onto quartz. Enantioselective adsorption of D-Arg and D-Asp on quartz sand occurred at high and low pH, respectively; this selectivity might have arisen due to specific interactions (i.e. hydrogen bonding) between the AA and the surface because electrostatic interactions rarely result in chiral discrimination. There were other instances of selective adsorption of Hist on powdered enantiomorphic quartz wafers. The selectivity was not correlated with the handedness of the wafers because in both cases the L-isomer appeared to be adsorbed preferentially. Selective adsorption on natural and synthetic single quartz crystal systems was not observed with the methods employed in this research even in systems where adsorption could be measured. Further investigation is needed to address whether the purity of enantiomorphic single quartz crystal surfaces influences preferential adsorption; for instance, using synthetic vs. natural quartz crystallographic planes. Molecular level techniques such as microarray analysis coupled with time of flight secondary ion mass spectroscopy (ToF-SIMS) can provide insight into this question as proposed by Hazen[58]. Evidence suggests that natural *d*- and *l*-quartz crystal faces adsorb fluorescent tagged L- and D-Lys[58], respectively, but since tagging alters the structure of the the unmodified AA, there is still the need to reconsider this issue. Molecular modelling of the interaction of chiral AAs at hydrated silica surfaces in

particular relevant crystallographic planes of quartz such the $(10\bar{1}0)$ might help understand the mechanism of a presumed selectivity of quartz.

Enantioselective effects were noted in the adsorption of racemic AAs on a commercial clay (montmorillonite K10), commonly used as a solid acid catalyst in organic synthesis. XRD characterisation of the material showed that quartz and mica were also present. The high surface area of the material along with a crude estimation of its composition suggested that montmorillonite was the main constituent of the mineral. Preferential adsorption of 5 μM D-Asp and D-Ser, and 500 μM L-Arg on K10 is reported. The Ser-K10 system was studied in greater detail because it gave the highest enantioselective signal at 5 μM. It is concluded that the interaction of Ser with K10 involves mainly physical adsorption. At higher concentrations, selectivity changed so that the L-isomer of Ser appeared to be adsorbed preferentially over the D-isomer. At present, the reason for this selectivity reversal remains unclear. The finding that charged (Asp and Arg) and polar (Ser) AAs displayed enantioselective behaviour with K10 indicates that the side chain must play a role in the observed discrimination. Although K10 is a heterogeneous material, it is hypothesized that a third interaction of the enantiomers of Ser via the hydroxyl group (-OH) with the siloxane cavity inside the interlamellar space of the clay might explain the selectivity. To clarify this, it is recommended that further adsorption experiments of racemic Ser be conducted with the < 2 μm size fraction of K10 which is mostly montmorillonite. There remains the question of whether the clay edges are enantioselective. It is suggested that parallel adsorption could be conducted with the unmodified < 2 μm fraction and with endcapped <2 μm material that eliminates the contribution of the silanol groups at the edges.

Adsorption of racemic Val on K10 and CuK10 was studied under various aqueous conditions. Adsorption was independent of pH because of the constant acidic pH of the K10-AA solution at a value of 3. High ionic strength decreased the adsorption of Val which can be interpreted as an indication for an adsorption mechanism involving the formation of an outer sphere complex between Val and K10. There was just one case of preferential adsorption of L-Val on CuK10 at pH 9, but gross adsorption on Cu-K10 was comparable to that on K10. It was speculated that the selectivity stemmed from stereoselective hydroxo Cu complexes. Val is a non-polar hydrophobic AA so it

lacks the favourable hydrogen bonding properties displayed by the side chains of Asp, Arg, and Ser lending support to the hypothesis that this extra interaction plays a role in chiral discrimination.

Kaolinite was similarly used as an adsorbent for Val. Experimental evidence suggests that the edges of the clay are the reactive sites since adsorption of Val on Cu-exchanged kaolinite decreased in comparison to the untreated kaolinite. Selective adsorption of D-Val on Cu-Kaolinite occurred at pH 9. Preliminary experiments indicated that the perfect cleavage plane of gypsum tended to be enantioselective towards L-AAs. River Mersey sediments were not enantioselective towards any of the AA enantiomers examined under the experimental conditions of this work.

Another important contribution of this project is the finding that divaline is formed from monomeric Val during wet-dry cycle experiments using CuK10 as a mineral catalyst. These cycles intended to simulate processes that might have happened to aqueous AAs under environmental conditions of the early Earth. Possibly, during this time shallow ponds, lined with aluminosilicate minerals, were replenished by rainfall and dried by the Sun under cyclic conditions. An alternative scenario for these cycles could have taken place at the seashore of a primitive Ocean due to tidal effects. Besides divaline, Val diketopiperazine was also tentatively identified as a reaction product. The yields of divaline dipeptide were small but significant and of the same magnitude as the yields reported for the formation of divaline by the SIPF reaction[130]. It is recommended that replicate experiments be conducted to assess the statistical significance of the data, particularly whether the yield of divaline depends on the chirality of Val (L- or D-) and also the effect of the starting concentration of Val on the reaction yield.

The adsorption of Val on Cu(110) in a ultra-high vacuum system was undertaken to understand how this AA bonds to a well-prepared, flat crystallographic plane in the absence of water. Enantiomers of Val chemisorbed on Cu(110) via a three point interaction. The molecule anchored to the surface via the two oxygens atoms of the carboxylate group and the nitrogen atom of the amino group. Enantiomers of Val self-assembled on Cu(110) at room temperature. The resulting adlayers are mirror images of each other, stable up to 373 K, and possess long-range order as determined from LEED and STM. A structural model for the orientation of Val within the unit cell

is proposed. From the STM images it is speculated that molecules within the unit cell might adopt more than one adsorption geometry and preliminary molecular modelling of the system (work in progress) points to support this conjecture.

Finally, there has been debate as to the most abundant secondary minerals on the early Earth that could have participated in prebiotic chemistry. Modelling has shown that phases such as iron oxides and iron (oxy)-hydroxides, green rust, sulphides (FeS, MnS), all of which possess photochemical activity, might have been involved in redox-reactions such as the photoreduction of CO_2 or N_2[165]. Products of these photocatalytic reactions include organic species (i.e. aldehydes and ammonia) that later underwent reactions of the Strecker synthesis type to form AAs. The selective and catalytic potential of the aforementioned minerals needs to be addressed. For example, Ferrihydrite, an iron oxide hydroxide, found in a wide range of environments on Earth and on extraterrestrial materials (e.g. Antartic micrometeorites, interplanetary dust particles) was found to adsorb a variety of amino acids (polar, non-polar, basic and acidic) by more than 60% and promoted peptide bond formation[166], but its prospective enantioselective capacity deserves further study. In the search for symmetry-breaking mechanisms, intrinsically chiral minerals with photocatalytic properties (i.e. cinnabar, HgS) represent model candidate surfaces for detailed molecular studies on the interaction of optically active molecules with chiral surfaces[167].

REFERENCES

[1] G. C. Barret, *Chemistry and Biochemistry of the Amino Acids*, Chapman and Hall, London, **1985**.

[2] I. H. Suh, K. H. Park, W. P. Jensen, D. E. Lewis, *Journal of Chemical Education* **1997**, *74*, 800.

[3] J. Clayden, N. Greeves, S. Warren, P. Wothers, *Organic Chemistry*, Oxford University Press, **2001**.

[4] A. Mannschreck, R. Kiesswetter, *Journal of Chemical Education* **2005**, *82*, 1034.

[5] L. E. Smart, E. A. Moore, Third ed., Taylor and Francis, Boca Raton, Florida, **2005**.

[6] R. M. Hazen, D. S. Sholl, *Nature Materials* **2003**, *2*, 367.

[7] R. M. Hazen, in *Progress in Biological Chirality* (Eds.: G. Pályi, C. Zucchi, L. Caglioti), Elsevier Ltd, Oxford **2004**, p. 429.

[8] C. Frondel, *The System of Mineralogy, Vol. III*, Seven ed., John Wiley & Sons, **1962**.

[9] A. M. Langer, *Quarterly Reviews of Biophysics* **1978**, *11*, 543.

[10] A. M. Cody, R. D. Cody, *Journal of Crystal Growth* **1991**, *113*, 508.

[11] T. A. Jackson, *Chemical Geology* **1971**, *7*, 295.

[12] A. Julg, *Comptes Rendus de l'Académie des Sciences Series II* **1986**, *303*, 1773.

[13] A. Julg, *Comptes Rendus de l'Académie des Sciences Series II* **1988**, *306*, 1153.

[14] K. Nakanishi, T. Sakiyama, K. Imamura, *Journal of Bioscience and Bioengineering* **2001**, *91*, 233.

[15] N. N. Vlasova, L. P. Golovkova, *Colloid Journal* **2004**, *66*, 657.

[16] V. A. Basiuk, *Adsorption of biomolecules at silica*, **2002**.

[17] A. Mellersh, A. Wilkinson, *Origins of Life and Evolution of the Biosphere* **2000**, *30*, 3.

[18] W. A. Bonner, P. Kavasmaneck, F. Martin, *Science* **1974**, *186*, 143.

[19] S. Furuyama, M. Sawada, K. Hachiya, T. Morimoto, *Bulletin of the Chemical Society of Japan* **1982**, *55*, 3394.

[20] G. G. Hammes, *Spectroscopy for the Biological Sciences*, Jonh Wiley and Sons, **2005**.

[21] G. Sposito, *The Chemistry of Soils*, Oxford University Press, New York, **1989**.

[22] W. Stumm, Morgan, J.J. , *Aquatic Chemistry*, Third Edition ed., John Wiley & Sons, Inc, **1996**.

[23] G. E. Brown, *Science* **2001**, *294*, 67.

[24] H. A. Al-Abadleh, V. H. Grassian, *Surface Science Reports* **2003**, *52*, 63.

[25] G. Attard, Barnes, C., *Surfaces*, Oxford University Press, **1998**.

[26] H. Churchill, H. Teng, R. M. Hazen, *American Mineralogist* **2004**, *89*, 1048.

[27] J. I. Hedges, P. E. Hare, *Geochimica et Cosmochimica Acta* **1987**, *51*, 255.

[28] S. M. Henrichs, S. F. Sugai, *Geochimica et Cosmochimica Acta* **1993**, *57*, 823.

[29] B. K. G. Theng, *The Chemistry of Clay-Organic Reactions.*, The Institute of Physics, **1974**.

[30] J. Bujdak, B. M. Rode, *Reaction Kinetics and Catalysis Letters* **1997**, *62*, 281.

[31] J. Bujdak, B. M. Rode, *Journal of Molecular Evolution* **1997**, *45*, 457.

[32] J. Bujdak, B. M. Rode, *Journal of Molecular Catalysis a-Chemical* **1999**, *144*, 129.

[33] J. Bujdak, H. Slosiarikova, N. Texler, M. Schwendinger, B. M. Rode, *Monatshefte Fur Chemie* **1994**, *125*, 1033.
[34] T. L. Porter, M. P. Eastman, M. E. Hagerman, J. L. Attuso, E. D. Bain, *Journal of Vacuum Science & Technology a-Vacuum Surfaces and Films* **1996**, *14*, 1488.
[35] S. D. Jang, R. A. Condrate, *American Mineralogist* **1972**, *57*, 494.
[36] M. F. Brigatti, S. Colonna, D. Malferrari, L. Medici, *Geochimica et Cosmochimica Acta* **2004**, *68*, 781.
[37] L. O. B. Benetoli, C. M. D. de Souza, K. L. da Silva, I. G. D. Souza, H. de Santana, A. Paesano, A. C. S. da Costa, C. Zaia, D. A. M. Zaia, *Origins of Life and Evolution of Biospheres* **2007**, *37*, 479.
[38] A. Gupta, G. H. Loew, J. Lawless, *Inorganic Chemistry* **1983**, *22*, 111.
[39] J. Ikhsan, B. B. Johnson, J. D. Wells, M. J. Angove, *Journal of Colloid and Interface Science* **2004**, *273*, 1.
[40] J. Bebié, M. A. A. Schoonen, *Geochemical Transactions* **2000**, *1*, 47.
[41] J. F. Lambert, *Origins of Life and Evolution of Biospheres* **2008**, *38*, 211.
[42] E. Friebele, A. Shimoyama, P. E. Hare, C. Ponnamperuma, *Origins of Life and Evolution of the Biosphere* **1981**, *11*, 173.
[43] W. A. Bonner, P. R. Kavasmaneck, *Journal of Organic Chemistry* **1976**, *41*, 2225.
[44] W. A. Bonner, P. R. Kavasmaneck, *Journal of the American Chemical Society* **1977**, *99*, 44.
[45] W. A. Bonner, P. R. Kavasmaneck, F. S. Martin, J. J. Flores, *Origins of Life and Evolution of the Biosphere* **1975**, *6*, 367.
[46] J. J. Flores, W. A. Bonner, *Journal of Molecular Evolution* **1974**, *3*, 49.
[47] P. R. Kavasmaneck, W. A. Bonner, *Journal of the American Chemical Society* **1977**, *99*, 44.
[48] S. Furuyama, H. Kimura, M. Sawada, T. Morimoto, *Chemistry Letters* **1978**, 381.
[49] R. M. Hazen, T. R. Filley, G. A. Goodfriend, *Proceedings of the National Academy of Sciences of the United States of America* **2001**, *98*, 5487.
[50] V. Ostroverkhov, G. A. Waychunas, Y. R. Shen, *Chemical Physics Letters* **2004**, *386*, 144.
[51] E. T. Degens, J. Matheja, T. A. Jackson, *Nature* **1970**, *227*, 492.
[52] T. A. Jackson, *Experientia* **1971**, *27*, 242.
[53] W. A. Bonner, J. Flores, *Currents in Modern Biology* **1973**, *5*, 103.
[54] A. Julg, A. Favier, Y. Ozias, *Surface Science* **1986**, *165*, L53.
[55] B. Siffert, A. Naidja, *Clay Minerals* **1992**, *27*, 109.
[56] H. Hashizume, B. K. G. Theng, A. Yamagishi, *Clay Minerals* **2002**, *37*, 551.
[57] B. Kahr, B. Chittenden, A. Rohl, *Chirality* **2006**, *18*, 127.
[58] R. M. Hazen, *American Mineralogist* **2006**, *91*, 1715.
[59] M. Sajewicz, H. E. Hauck, G. Drabik, E. Namyslo, B. Glod, T. Kowalska, *Journal of Planar Chromatography-Modern TLC* **2006**, *19*, 278.
[60] H. Hashizume, *Origins of Life and Evolution of the Biosphere* **2006**, *36*, 279.
[61] C. Dryzum, Y. Mastai, A. Shvalb, D. Avnir, *Journal of Materials Chemistry* **2009**, *19*.
[62] A. Mannschreck, R. Kiesswetter, E. von Angerer, *Journal of Chemical Education* **2007**, *84*, 2012.
[63] V. A. Davankov, *Chirality* **1997**, *9*, 99.

[64] P. Ebbesen, *European Journal of Cancer Prevention : the Official Journal of the European Cancer Prevention Organisation (ECP)* **1991**, *1*, 39.
[65] K. Soai, S. Osanai, K. Kadowaki, S. Yonekubo, T. Shibata, I. Sato, *Journal of the American Chemical Society* **1999**, *121*, 11235.
[66] J. J. McCullough, R. M. Lemmon, *Journal of Molecular Evolution* **1974**, *3*, 57.
[67] T. Ikeda, H. Amoh, T. Yasunaga, *Journal of the American Chemical Society* **1984**, *106*, 5772.
[68] C. H. Yu, S. Q. Newton, D. M. Miller, B. J. Teppen, L. Schafer, *Structural Chemistry* **2001**, *12*, 393.
[69] F. Bergaya, B. K. G. Theng, G. Lagaly, in *Developments in Clay Science, Vol. 1*, Elsevier, **2008**, p. 1224.
[70] H. Bruckner, R. Wittner, H. Godel, *Chromatographia* **1991**, *32*, 383.
[71] D. S. Kaufman, W. F. Manley, *Quaternary Science Reviews* **1998**, *17*, 987.
[72] G. Subramanian, *Chiral Separation Techniques. A Practical Approach*, Second ed., Wiley-VCH, Verlag GmbH, **2001**.
[73] W. Amelung, X. Zhang, *Soil Biology & Biochemistry* **2001**, *33*, 553.
[74] H. Bruckner, M. Lupke, *Chromatographia* **1991**, *31*, 123.
[75] A. V. Kunnas, T. P. Jauhiainen, *Journal of Chromatography* **1993**, *628*, 269.
[76] T. L. Porter, M. P. Eastman, R. Whitehorse, E. Bain, K. Manygoats, *Scanning* **2000**, *22*, 1.
[77] J. Bujdak, B. M. Rode, *Origins of Life and Evolution of the Biosphere* **1999**, *29*, 451.
[78] N. Lahav, D. White, S. Chang, *Science* **1978**, *201*, 67.
[79] J. G. Lawless, N. Levi, *Journal of Molecular Evolution* **1979**, *13*, 281.
[80] H. Le Son, Y. Suwannachot, J. Bujdak, B. M. Rode, *Inorganica Chimica Acta* **1998**, *272*, 89.
[81] T. L. Porter, M. P. Eastman, E. Bain, S. Begay, *Biophysical Chemistry* **2001**, *91*, 115.
[82] K. Plankensteiner, H. Reiner, B. M. Rode, *Origins of Life and Evolution of the Biosphere* **2005**, *35*, 411.
[83] A. H. Eder, S. Saetia, B. M. Rode, *Inorganica Chimica Acta* **1993**, *207*, 3.
[84] J. R. Collins, G. H. Loew, B. T. Luke, D. H. White, *Origins of Life and Evolution of the Biosphere* **1988**, *18*, 107.
[85] B. M. Rode, *Peptides* **1999**, *20*, 773.
[86] N. M. Nagy, J. Konya, *Applied Clay Science* **2004**, *25*, 57.
[87] T. L. Porter, M. P. Eastman, M. E. Hagerman, L. B. Price, R. F. Shand, *Journal of Molecular Evolution* **1998**, *47*, 373.
[88] J. C. Vickerman, *Surface Analysis-The Principal Tecniques*, John Wiley & Sons, **1997**.
[89] S. M. Barlow, R. Raval, *Surface Science Reports* **2003**, *50*, 201.
[90] S. M. Barlow, S. Louafi, D. Le Roux, J. Williams, C. Muryn, S. Haq, R. Raval, *Surface Science* **2005**, *590*, 243.
[91] S. Haq, A. Massey, N. Moslemzadeh, A. Robin, S. M. Barlow, R. Raval, *Langmuir* **2007**, *23*, 10694.
[92] M. Bieri, T. Burgi, *Journal Of Physical Chemistry B* **2005**, *109*, 10243.
[93] D. Wang, S. B. Lei, L. J. Wan, C. Wang, C. L. Bai, *Journal of Physical Chemistry B* **2003**, *107*, 8474.
[94] A. Lesarri, E. J. Cocinero, J. C. Lopez, J. L. Alonso, *Angewandte Chemie-International Edition* **2004**, *43*, 605.

[95] S. Barlow, *Fundamentals of Catalysis and Surface science (CHEM 911).Department of Chemistry. University of Liverpool*, **2004**.
[96] K. Soai, S. Osanai, K. Kadowaki, S. Yonekubo, T. Shibata, I. Sato, *Journal Of The American Chemical Society* **1999**, *121*, 11235.
[97] M. Wedyan, M. R. Preston, *Environmental Science & Technology* **2005**, *39*, 2115.
[98] K. Evgenii, T. Wolfram, *Origins of Life and Evolution of the Biosphere* **2000**, *30*, 431.
[99] C. Frondel, *The System of Mineralogy. Vol. III. Silica Minerals*, Seventh ed., John Wiley and Sons, Inc, **1962**.
[100] G. G. Lemmlein, *Collections of the Mineralogical Society. USSR* **1944**, *73*, 94.
[101] G. G. Lemmlein, *The Morphology and Genesis of Crystals*, **1973**.
[102] A. B. Vistelius, *Collections of the Mineralogical Society USSR* **1950**, *79*, 191.
[103] C. Frondel, *American Mineralogist* **1978**, *63*, 17.
[104] J. Walker, *Introduction to Probability and Statistics*, Fourmilab, **2009**.
[105] A. Nasreen, *Synlett* **2001**, 1341.
[106] T. Erbe, H. Bruckner, **2000**, *881*, 81.
[107] A. Braithwaite, F. J. Smith, *Chromatographic Methods*, 5th Edition ed., Kluwer Academic Publishers, London, **1996**.
[108] D. A. Skoog, D. M. West, *Fundamentals of Analytical Chemistry*, 4th Edition ed., Saunders College Publishing, Philadelphia, **1982**.
[109] V. Humblot, University of Liverpool (Liverpool), **2002**.
[110] SPECS, **2009**.
[111] D. A. M. Zaia, H. J. Vieira, C. Zaia, *Journal of the Brazilian Chemical Society* **2002**, *13*, 679.
[112] A. Rimola, M. Sodupe, P. Ugliengo, *The Journal of Physical Chemistry C* **2009**, *113*, 5741.
[113] Y. Ota, T. Sato, S. Tamaura, *Geochimica et Cosmochimica Acta* **2007**, *71*, A744.
[114] R. P. Schwarzenbach, P. M. Gschwend, D. M. Imboden, *Environmental Organic Chemistry*, Second ed., Wiley-Interscience, Hoboken, New Jersey, **2003**.
[115] M. Kosmulski, *Journal of Colloid and Interface Science* **2006**, *298*, 730.
[116] J. W. Han, J. N. James, D. S. Sholl, *Surface Science* **2008**, *602*, 2478.
[117] L. Stievano, L. Y. Piao, I. Lopes, M. Meng, D. Costa, J. F. Lambert, *European Journal of Mineralogy* **2007**, *19*, 321.
[118] J. D. Morton, J. D. Semrau, K. F. Hayes, *Geochimica et Cosmochimica Acta* **2001**, *65*, 2709.
[119] L. Ammann, F. Bergaya, G. Lagaly, *Clay Minerals* **2005**, *40*, 441.
[120] C. R. Reddy, Y. S. Bhat, G. Nagendrappa, B. S. Jai Prakash, *Catalysis Today, In Press, Corrected Proof.*
[121] C. Cativiela, J. M. Fraile, J. I. Garcia, J. A. Mayoral, E. Pires, F. Figueras, L. C. Demenorval, *Tetrahedron* **1992**, *48*, 6467.
[122] J. M. Fraile, J. I. Garcia, J. A. Mayoral, T. Tarnai, P. J. Alonso, *Chemical Communications* **1996**, 1981.
[123] R. A. S. Villegas, J. L. D. Santo, M. C. S. de Mattos, M. de Aguiar, A. W. S. Guarino, *Journal of the Brazilian Chemical Society* **2005**, *16*, 565.
[124] J. Q. Jiang, Z. Q. Zeng, *Chemosphere* **2003**, *53*, 53.
[125] A. Naidja, P. M. Huang, *Applied Clay Science* **1994**, *9*, 265.
[126] M. Frenkel, L. Hellerkallai, *Chemical Geology* **1977**, *19*, 161.

[127] J. T. Kloprogge, E. Mahmutagic, R. L. Frost, *Journal of Colloid and Interface Science* **2006**, *296*, 640.
[128] F. Tsvetkov, U. Mingelgrin, *Clays and Clay Minerals* **1987**, *35*, 391.
[129] K. Plankensteiner, A. Righi, B. M. Rode, R. Gargallo, J. Jaumot, R. Tauler, *Inorganica Chimica Acta* **2004**, *357*, 649.
[130] K. Plankensteiner, H. Reiner, B. A. Rode, *Peptides* **2005**, *26*, 1109.
[131] V. Humblot, C. Methivier, C. M. Pradier, *Langmuir* **2006**, *22*, 3089.
[132] A. Kuhnle, T. R. Linderoth, B. Hammer, F. Besenbacher, *Nature* **2002**, *415*, 891.
[133] M. Graff, J. Bukowska, *Journal of Physical Chemistry B* **2005**, *109*, 9567.
[134] D. W. Deamer, R. Dick, W. Thiemann, M. Shinitzky, *Chirality* **2007**, *19*, 751.
[135] M. R. Warne, N. L. Allan, T. Cosgrove, *Physical Chemistry Chemical Physics* **2000**, *2*, 3663.
[136] M. Alkan, B. Kalay, M. Dogan, Ö. Demirbas, *Journal of Hazardous Materials* **2008**, *153*, 867.
[137] A. Julg, A. Favier, Y. Ozias, *Structural Chemistry* **1990**, *1*, 137.
[138] S. M. Le Roux, A. Turner, G. E. Millward, L. Ebdon, P. Appriou, *Journal of Environmental Monitoring* **2001**, *3*, 37.
[139] X. C. Wang, C. Lee, *Marine Chemistry* **1993**, *44*, 1.
[140] C. Huber, G. Wächtershäuser, *Science* **1998**, *281*, 670.
[141] M. Pontes-Buarque, A. C. Tessis, J. A. P. Bonapace, M. B. M. Monte, F. De Souza-Barros, A. Vieyra, *Anais Da Academia Brasileira De Ciencias* **2000**, *72*, 317.
[142] U. Meierhenrich, *Amino Acids and the Asymmetry of Life*, Springer, **2008**.
[143] N. N. Nair, E. Schreiner, D. Marx, *Journal of the American Chemical Society* **2006**, *128*, 13815.
[144] N. Kitadai, T. Yokoyama, S. Nakashima, *Journal of Colloid and Interface Science* **2009**, *329*, 31.
[145] Z. Paszti, T. Keszthelyi, O. Hakkel, L. Guczi, *Journal of Physics-Condensed Matter* **2008**, *20*.
[146] A. Aubrey, H. J. Cleaves, J. H. Chalmers, A. M. Skelley, R. A. Mathies, F. J. Grunthaner, P. Ehrenfreund, J. L. Bada, *Geology* **2006**, *34*, 357.
[147] C. Estrada, C. L. Jonsson, C. M. Jonsson, in *Carnegie Summer Scholars Program Symposium*, **2008**.
[148] D. A. Sverjensky, C. M. Jonsson, C. L. Jonsson, H. J. Cleaves, R. M. Hazen, *Environmental Science & Technology* **2008**, *42*, 6034.
[149] R. G. Cooks, D. X. Zhang, K. J. Koch, F. C. Gozzo, M. N. Eberlin, *Analytical Chemistry* **2001**, *73*, 3646.
[150] A. Parbhakar, J. Cuadros, M. A. Sephton, W. Dubbin, B. J. Coles, D. Weiss, *Colloids and Surfaces a-Physicochemical and Engineering Aspects* **2007**, *307*, 142.
[151] D. Fox, in *New Scientist*, **2009**, p. 5.
[152] D. Deamer, S. Singaram, S. Rajamani, V. Kompanichenko, S. Guggenheim, *Philosophical Transactions of the Royal Society of London Series B Biological Sciences* **2006**, *361*, 1809.
[153] N. Moslemzadeh, M. Tamara, R. Raval, D. Prior, M. R. Preston, *Surface and Interface Analysis* **2009**, *41*, 1.
[154] J. Napier, J. Yin, *Peptides* **2006**, *27*, 607.
[155] F. Li, D. Fitz, D. G. Fraser, B. M. Rode, *Journal of Inorganic Biochemistry* **2008**, *102*, 1212.

[156] A. H. Eder, B. M. Rode, *Journal of the Chemical Society-Dalton Transactions* **1994**, 1125.
[157] L. O. B. Benetoli, C. M. D. de Souza, K. L. da Silva, I. G. D. Souza, H. de Santana, A. Paesano, A. C. S. da Costa, C. Zaia, D. A. M. Zaia, *Origins of Life and Evolution of Biospheres* **2007**, *37*, 479.
[158] B. Barbier, A. Chabin, D. Chaput, A. Brack, *Planetary and Space Science* **1998**, *46*, 391.
[159] S. G. Stepanian, I. D. Reva, E. D. Radchenko, L. Adamowicz, *Journal of Physical Chemistry A* **1999**, *103*, 4404.
[160] I. Nakagawa, R. J. Hooper, J. L. Walter, T. J. Lane, *Spectrochimica Acta* **1965**, *21*, 1.
[161] S. M. Barlow, K. J. Kitching, S. Haq, N. V. Richardson, *Surface Science* **1998**, *401*, 322.
[162] R. B. Rankin, D. S. Sholl, *Surface Science* **2005**, *574*, L1.
[163] N. P. Kryukova, V. Y. Frolov, F. A. Kolokolov, S. N. Bolotin, V. T. Panyushkin, *Russian Journal of General Chemistry* **2005**, *75*, 503.
[164] S. Blankenburg, W. G. Schmidt, *Nanotechnology* **2007**, *18*.
[165] M. Schoonen, A. Smirnov, C. Cohn, *Ambio* **2004**, *33*, 539.
[166] G. Matrajt, D. Blanot, *Amino Acids* **2004**, *26*, 153.
[167] B. Pal, S. Ikeda, B. Ohtani, *Inorganic Chemistry* **2003**, *42*, 1518.
[168] R. G. Greenler, *Journal of Chemical Physics* **1969**, *50*, 1963.
[169] M. A. Chesters, *Journal of Electron Spectroscopy and Related Phenomena* **1986**, *38*, 123.
[170] A. Foster, W. Hofer, *Scanning Probe Microscopy. Atomic Scale Engineering by Forces and Currents*, Springer, New York, **2006**.
[171] M. A. Geday, A. M. Glazer, *Journal of Applied Crystallography* **2002**, *35*, 185.

APPENDIX 1. ULTRA HIGH VACUUM SPECTROSCOPIC TECHNIQUES

This Appendix was adapted mainly from the books by Vickerman[88] and Attard and Barnes[25]. Therefore the reader is referred to these references for further details on the techniques.

1. Reflection-Absorption Infrared Spectroscopy (RAIRS).

This technique is particularly suited for investigating adsorbed layers on metal surfaces. A typical experiment involves focusing an infrared beam through an IR-transparent window on to the sample surface at grazing incidence; a geometry that has been proven to enhance absorption of IR radiation by the adsorbate overlayer. The sample acts as a mirror reflecting beam out of a second vacuum-sealed window, where it is recollimated on to a photoconductive semiconductor detector such as mercury cadmium telluride (MCT) (detection range 5000-800 cm^{-1}) (Figure A1.1)[25].

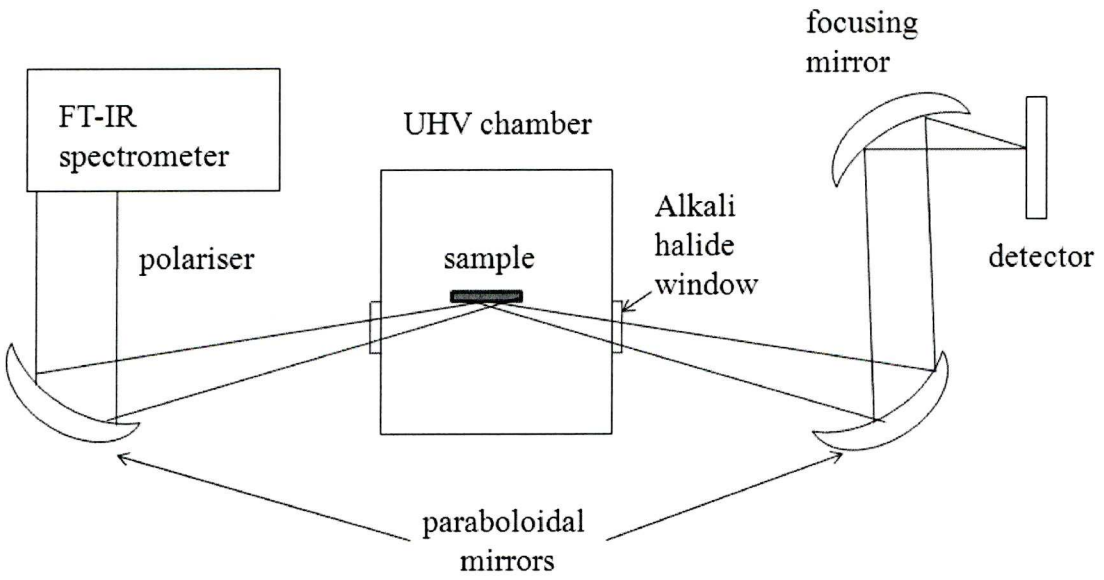

Figure A1.1 Setup of a RAIRS experiment

Only one polarisation of the light effectively interacts with the surface. Figure A1.2 illustrates the incident and reflected electric vectors of the *s* and *p* components of the radiation. *p* refers to parallel polarised radiation and *s* to perpendicular polarised radiation with respect to the plane of incidence. Greenler[168] showed that at the point of contact with the surface, the *p*-polarised radiation has a net combined amplitude that is almost twice that of the incident radiation as indicated by the vector summation of E_p^i and E_p^r. In contrast, the incident and reflected electric vectors of the *s*-polarised

radiation undergo a 180° phase shift with respect to each other so that the net amplitude of the IR radiation parallel to the surface is zero[88].

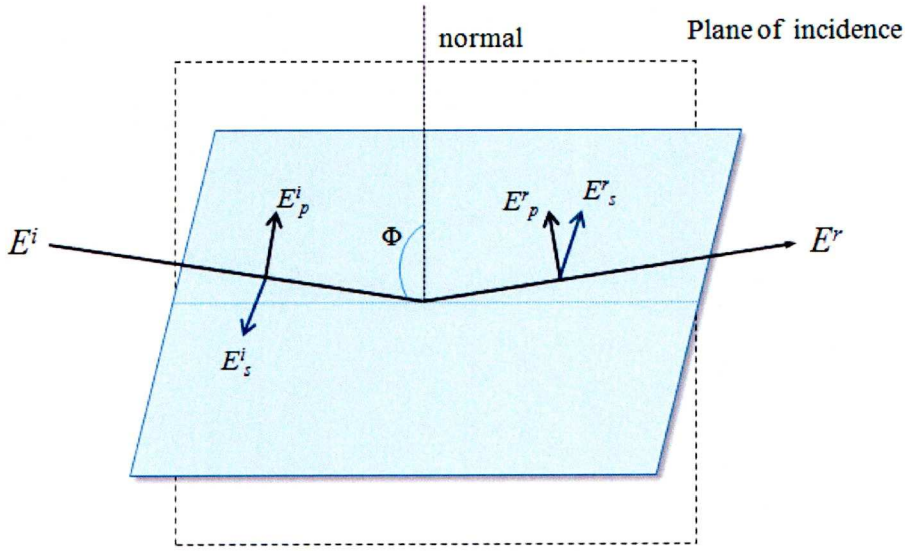

Figure A1.2. Schematic diagram of the *s*- and *p*-polarisation of incident (E_i) and reflected (E_r) IR radiation

This implies that only *p*-polarised radiation can interact with the surface leading to the following selection rule: "Only vibrational modes with a dipole moment change normal to the surface will be observed." Near grazing incidence IR beams result in enhanced excitement of the vibrational modes of the adsorbate [169] and therefore higher changes in reflectivity ($\Delta R = (R_0-R)$) and absorption intensity (Figures A1.3 and A1.4).

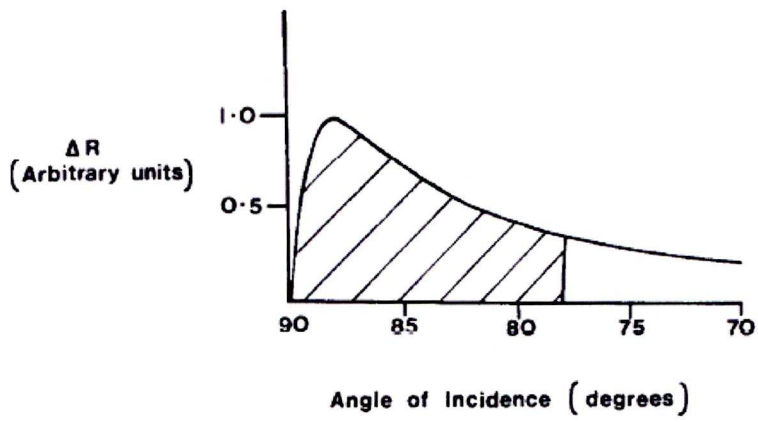

Figure A1.3. Schematic representation of the variation in band intensity with angle of incidence[169]

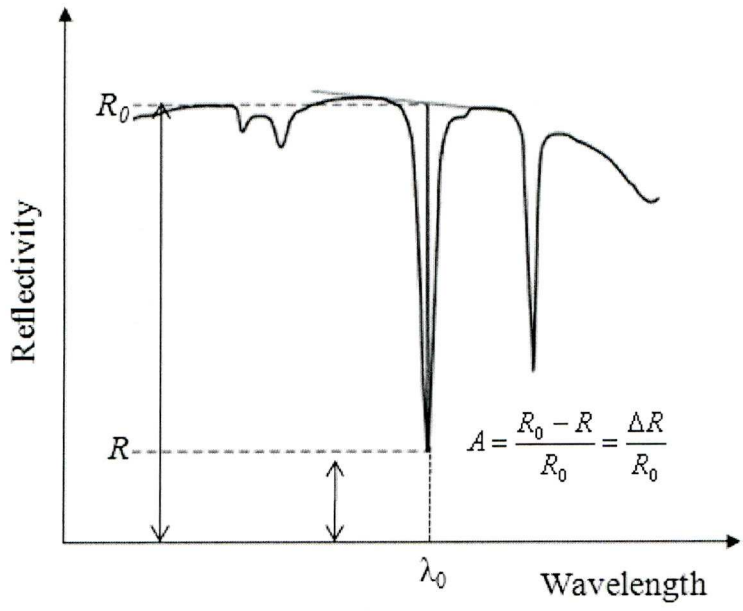

Figure A1.4. Absorption of IR by an adsorbate, illustrating the calculation of absorbance (A) based on the change in reflectivity

The selection rule can also be explained by considering the response of the valence electrons of the substrate (i.e. metal) to the molecular vibrations of an adsorbate. For example, carbon monoxide (CO) induces image charges in the substrate (Figure A1.5). When CO is upright, the dipole moments of both substrate and molecule reinforce each other. Therefore, enhanced IR absorption occurs upon vibration. In contrast, when CO lies down on the surface, the molecule and image dipole cancel resulting in no IR signal[25].

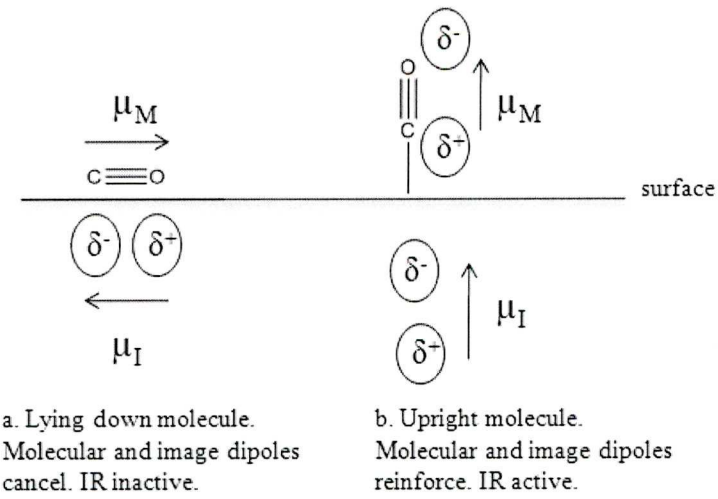

Figure A1.5. Illustration of surface selection rule for observation of RAIRS in terms of molecular and image dipoles[25]

Thus, the optimum conditions for measuring the RAIR spectra of species adsorbed at metallic surfaces require *p*-polarised light with plane of incidence perpendicular to the surface at grazing incidence (85-89°) (see Figure A1.3).

The chemical groups of the adsorbate molecule that are involved in bonding, the adsorption geometry of the adsorbate, and the adsorption site can be investigated by RAIRS due to the frequency of internal vibrations that can be excited. RAIRS is particularly useful in determining adsorbate geometry on metals due to the RAIRS metal selection rule. Finally, high resolution spectra (1-5 cm^{-1}) and fast data collection using a FTIR spectrometer can be obtained by RAIRS, thus allowing monitoring the adsorption of a target molecule with time[25].

2. Low-Energy Electron Diffraction (LEED)

In a LEED experiment, a beam of electrons with energy range 20-1000 eV is fired at a crystal surface. Then, the positions of the electrically reflected backscattered electrons (i.e. electrons that have not lost energy) are recorded. These electrons are diffracted by atoms or molecules at the crystal surface.

Electrons in the 20-1000 eV energy range have inelastic mean free paths of between 5 and 20 Å and therefore may travel a few atomic layers into the surface. Considering this, electrons in this energy range are excellent probes of surface structure because they possess de Broglie wavelengths that are of the same order of magnitude as the interatomic spacing between atoms/molecules at surfaces. Thus, incident electrons may undergo diffraction if the atoms in the surface are arranged periodically[25].

Figure A1.6 shows a typical setup of a LEED experiment[25]. Essentially, an electron beam of variable energy produced by an electron gun is fired at the sample. Then, the electrons are backscattered from the sample to a system of grids G1-G4. The backscattered electrons are of two types: elastically scattered electrons giving rise to a set of diffracted beams which create the LEED pattern, and inelastically scattered electrons, which make up 99% of the flux. The elastically scattered electrons are accelerated towards the fluorescent screen S. Thus the electrons in the diffracted beam possess high energy to excite the fluorescence in the screen S, generating a pattern of bright LEED spots. The grids G2 and G3 are subjected to an adjustable negative

potential which serves the purpose of rejecting the majority of the electric flux that is made up of inelastically scattered electrons that would otherwise contribute to a diffuse background on the LEED screen. The LEED pattern can be either viewed by eye or recorded using a video camera if quantitative intensity measurements are required[25].

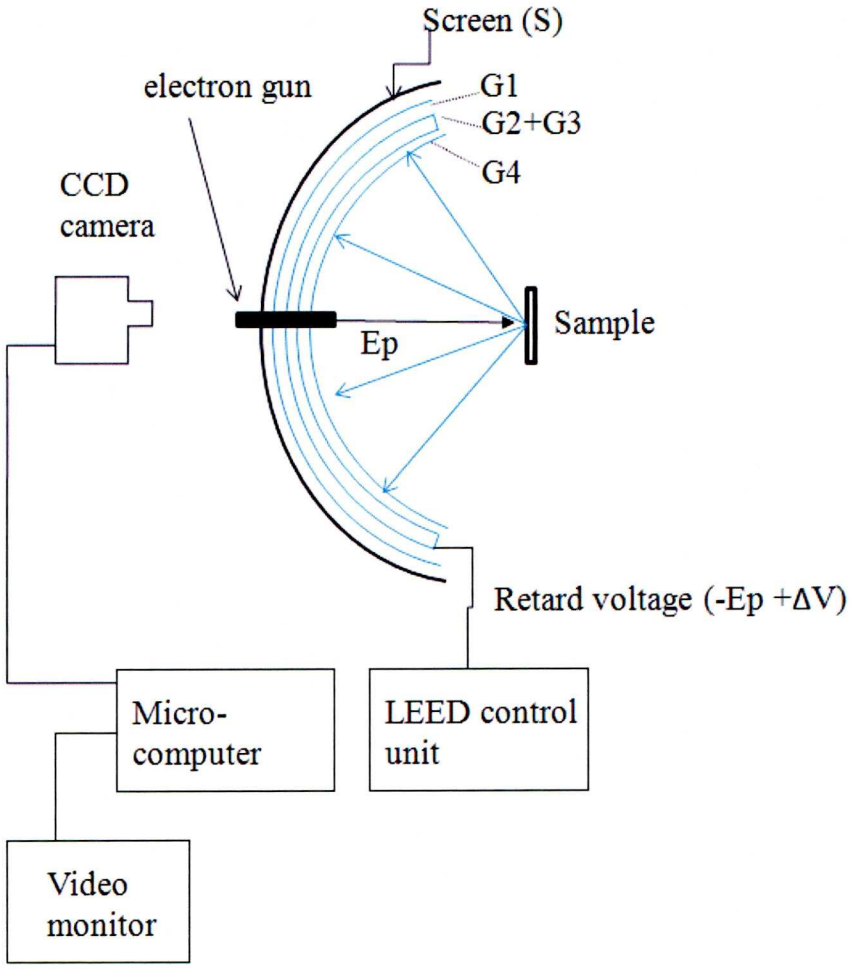

Figure A1.6. Schematic showing a LEED apparatus. Electrons of kinetic energy E_p are directed at the sample from an electron gun[25]

From the LEED pattern, the two-dimensional periodicity of the surface unit cell can be determined as well as the variation in unit cell size. The variation of spot intensities with beam energy provides information on surface geometry i.e. bond lengths and bond angles. LEED is generally used to evaluate surface order as well as the cleanliness of a substrate before conducting an experiment on it[25].

The wavelength of the electrons can be determined from the de Broglie equation:

$$\lambda = \left(\frac{150.6}{E(eV)} \right)^{1/2}$$ *Equation A1.1*

Thus, electron of energies of 20-200 eV correspond to wavelengths of 2.74-0.87 Å that are similar to atomic spacing. In order to understand the LEED process, consider the conditions for electron diffraction for a primary beam of electrons at normal incidence by a row of lattice points with separation *a* in a one-dimensional chain of atoms (Figure A1.7).

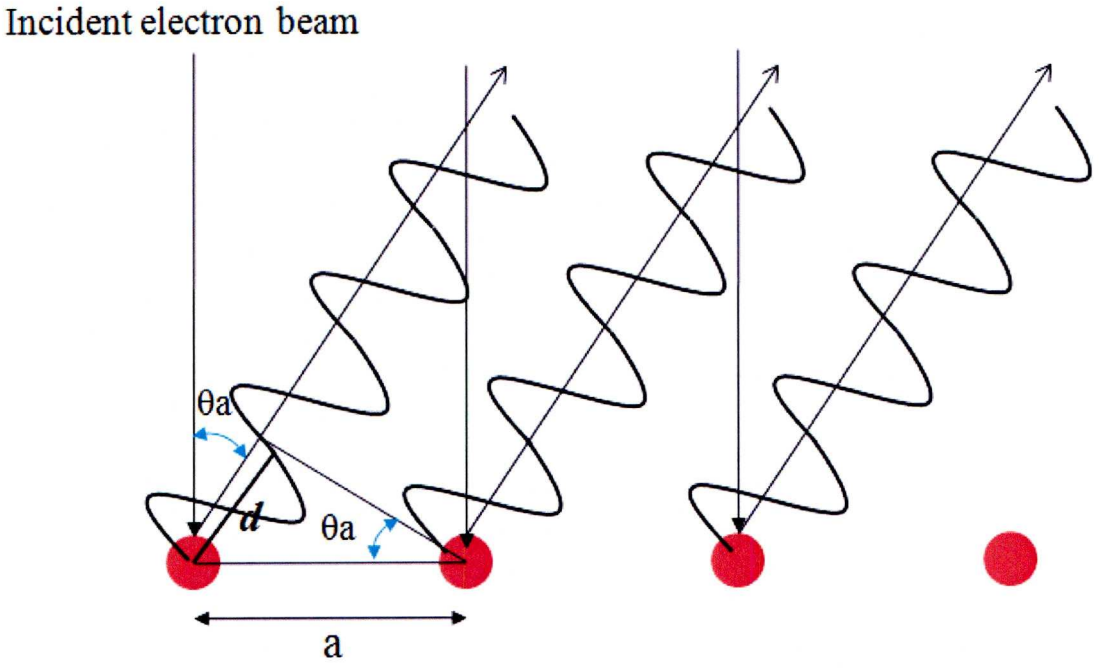

Figure A1.7. Schematic diagram of diffraction of a primary beam of electrons at normal incidence to the sample surface[25]

Bragg's law states that for constructive interference the path difference (*d*) between two adjacent beams should be an integral number of wavelengths according to:

$$d = a \sin\theta = n\lambda$$ *Equation A1.2*

Where n can take values of 0, ±1, ±2, ±3

Rearrangement of equation A1.2 gives

$$\sin\theta_a = \frac{n\lambda}{a}$$ *Equation A1.3*

Therefore for a fixed wavelength λ and lattice spacing *a*, only well-defined values of θ_a are allowed for which constructive interference will be observed corresponding to integer values of *n*. Moreover, for a fixed lattice constant *a*, an increase in the incident energy (E) results in a smaller wavelength and hence decreased θ_a, meaning that the diffracted beams move closer together.

The distance between the observed spots on the LEED screen can be calculated geometrically as illustrated in Figure A1.8. The distance observed (*y*) is proportional to *l*/a, indicating that the observed LEED pattern is a picture of the reciprocal surface net. This means that the distance between adjacent points in the LEED pattern reflecting the reciprocal lattice is inversely proportional to the distance between points in the corresponding direction of the real surface unit mesh (the direct lattice).

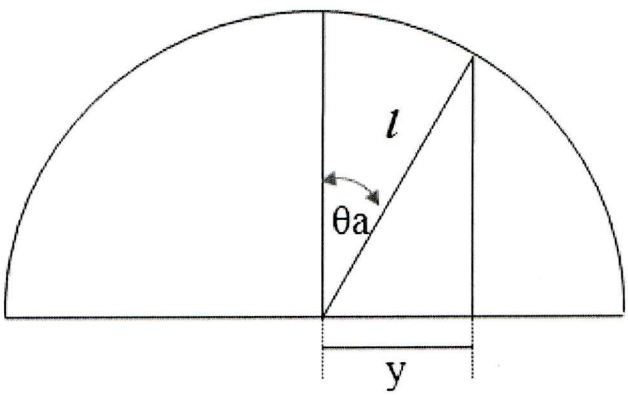

Figure A1.8. Schematic representation of distance *y* at which LEED spots are seen on the screen

Quantitative interpretation of LEED patterns requires an understanding of the relationship between real space and reciprocal space surface nets. The real space surface net can be generated from a translation vector:

$t = ma + nb$ *Equation A1.4*

where *m* and *n* are integers and a and b are the unit mesh vectors. A reciprocal surface net is generated by a reciprocal translation vector:

$G = h\mathrm{A} + k\mathrm{B}$ *Equation A1.5*

where h and k are integers and A and B are the unit mesh vectors in reciprocal space.

The real space and reciprocal space vectors are related by:

$A.a=2\pi$, $B.b=2\pi$, $A.b=0$, $B.a=0$ *Equation A1.6*

with the lengths related by

$$|A| = \frac{2\pi}{|a|} \text{ and } \qquad |B| = \frac{2\pi}{|b|} \qquad \textit{Equation A1.7}$$

If a and b are perpendicular.

A.b=0 and B.a means that A is perpendicular to b and B is perpendicular to a.

Similarly to the reciprocal unit cell vectors, the wavelength of the incident beam λ can be represented by its reciprocal, the wave vector, k

$$|k| = \frac{2\pi}{\lambda} \qquad \textit{Equation A1.8}$$

The Ewald sphere construction used in 3D diffraction can be applied to diffraction from a surface. The surface plane can be imagined as a raft of atoms pulled away from the bulk so that the distance between raft and bulk tends to infinity. Consequently, the reciprocal lattice becomes a set of infinitely long rods normal to the plane of atoms since the distance in reciprocal space are inversely proportional to the distances in real space. In the Ewald sphere construction, the wave vector k represents the incident radiation. k is drawn at the correct angle of incidence of θ and length $2/\lambda$ and with its head at the origin 0 as in the case of Figure A1.9. To finish the Ewald sphere construction a circle of radius $2\pi/\lambda$ is drawn with its centre at the other end A of the vector. The circle satisfies the law conservation of energy: $|k'|=|k_0|$. Thus, every lattice point cut by the circle represents a diffracted beam satisfying the equation $k'_{//} = k_{0//} + G$ and amounts to the conservation of the component of momentum parallel to the surface, where G is a translation vector. If the circle passes through no points, then diffraction does not occur i.e. $\lambda > 2a$.

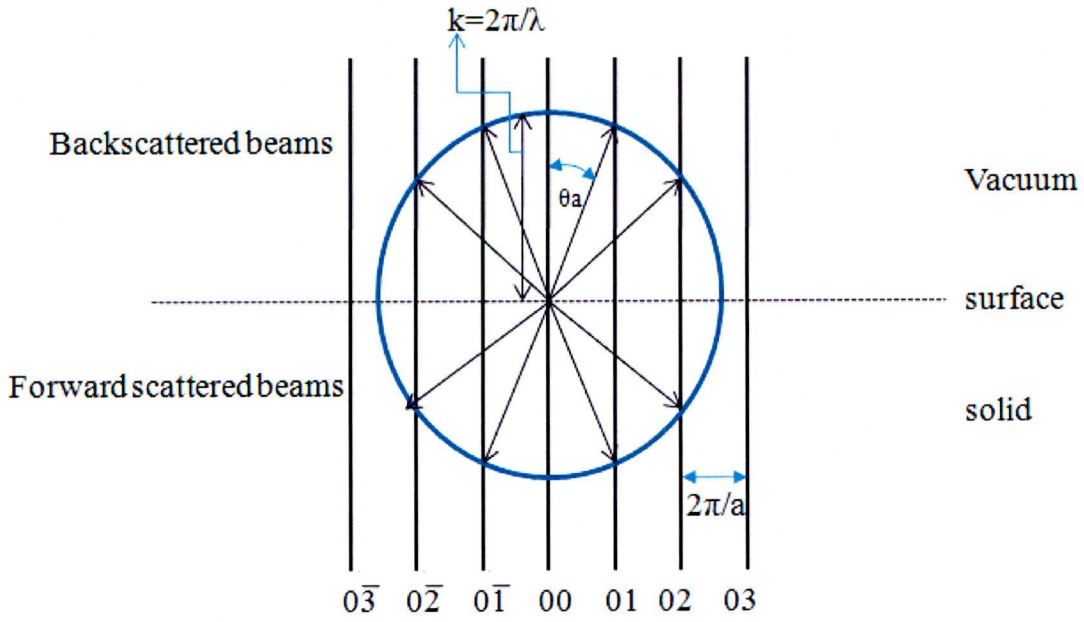

Figure A1.9. Ewald sphere construction for diffraction into a particular direction. The diagram corresponds to normal incidence of the wavevector *k* at 00

When molecules adsorb on surfaces, LEED allows determination of whether the overlayer has an ordered structure. However, the observed unit cell is recorded in reciprocal space, and it needs to be converted back to real space to see the actual structure of the surface. The matrix notation (M) is useful to relate the overlayer with reciprocal space unit vectors A_0, B_0 to the substrate with reciprocal space unit vectors A_s, B_s according to,

$$A_0 = M_{11}^{*} A_s + M_{12}^{*} B_s$$
$$B_0 = M_{21}^{*} A_s + M_{22}^{*} B_s \qquad \textit{Equation A1.9}$$

Thus, in reciprocal space:

$$\begin{pmatrix} A_0 \\ B_0 \end{pmatrix} = M^{*} \begin{pmatrix} A_s \\ B_s \end{pmatrix} \qquad \textit{Equation A1.10}$$

and in real space

$$\begin{pmatrix} a_0 \\ b_0 \end{pmatrix} = M \begin{pmatrix} a_s \\ b_s \end{pmatrix} \qquad \textit{Equation A1.11}$$

The subscripts *0* and *s* refer to the overlayer and the susbtrate, respectively. Lowercase a and b correspond to the real space unit cell vectors. The real space and reciprocal space matrices can be related by,

$M^* = (M^{-1})^T$ i.e. M^* is the inverse transpose of M *Equation A1.12*

or

$M = (M^{*-1})^T$ i.e. M is the inverse transpose of M^* *Equation A1.13*

Inspection of the LEED pattern provides the coefficients M_{11}^*, M_{12}^*, M_{21}^*, M_{22}^* in reciprocal space. The inverse transpose of M^* can be calculated by

$$(M^{*-1})^T = \frac{1}{\det M^*}\begin{pmatrix} M_{22}^* & -M_{21}^* \\ -M_{12}^* & M_{11}^* \end{pmatrix} = M = \begin{pmatrix} M_{11} & M_{12} \\ M_{21} & M_{22} \end{pmatrix} \qquad \textit{Equation A.1.14}$$

This matrix M can be replaced into equation 11 to give the overlayer structure in real space. Note the following conventions for the unit cell vectors. In both reciprocal and real space a right-handed system is adopted, meaning a anticlockwise movement from A_s (a_s) to B_s (b_s) and from A_0 (a_0) to B_0 (b_0). A_s points down and B_s to the right of A_s. In addition $|A_s| \geq |B_s|$ and the angle between A_s and B_s is $\leq 90°$. The angle between A_0 and B_0 is also $\leq 90°$. The opposite conventions hold for the real space vectors.

In summary, LEED can display if a surface is ordered. Moreover, the overlayer structures of an adsorbate can be determined. The two-dimensional periodicity of an overlayer with respect to the substrate can be obtained from LEED, but not necessarily the adsorption site of the molecule. Nevertheless, insight into the adsorption site and bond lengths may be obtained from quantitative LEED where the intensity of the diffracted beams is measured as a function of energy.

3. Scanning Tunelling Microscopy (STM).

Binnig and Rohrer invented the scanning tunnelling microscope in the early 1980s and were awarded the Nobel Prize in physics for their work. In a typical STM experiment, a sharp metallic tip prepared by etching a wire to a very fine point (as small as 20 nm) is brought to within 5-10 Å of a conducting or semiconducting surface[88]. A voltage V_t is applied between the tip and the sample, and the tip is scanned across the

surface, producing a tunnelling current (I_t) usually measured in nanoamperes. If the tip is biased positively relatively to the sample, a current originates when electrons from the surface travel through the tip due to quantum mechanical tunnelling. The principle of tunelling relies on the small distance between tip and sample. Otherwise, electrons would not hop from sample to the tip because of an energetic barrier for electron transfer. Thus, tunnelling is better illustrated by the energy level diagram shown in Figure A1.10.

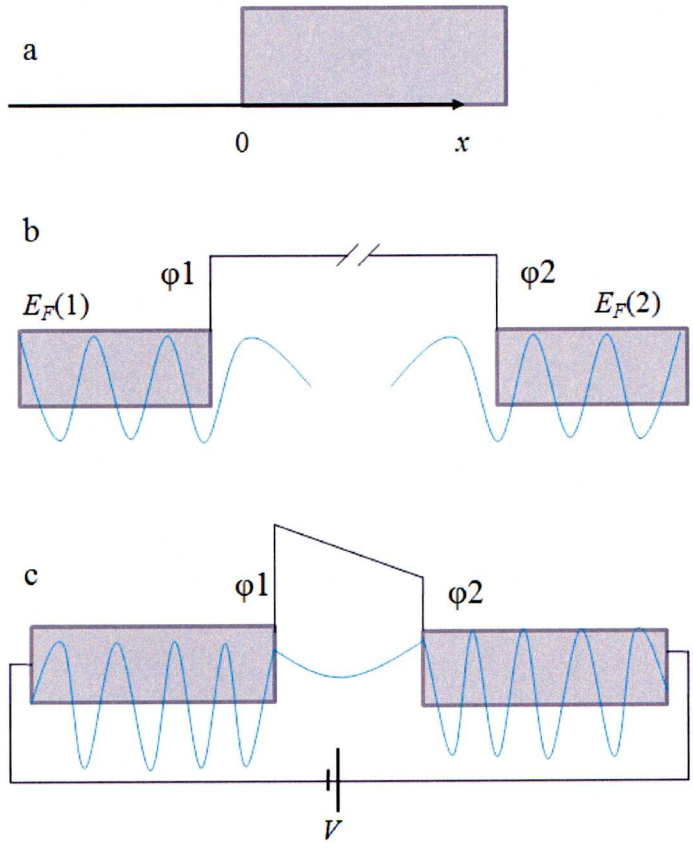

Figure A1.10. a. An infinitely thick potential barrier. Potential =V for x>0 and 0 for x<0. b. Two potential wells that are spatially separated. c. Two potential wells separated by a small distance, and with an applied potential difference[88]

In Figure A1.10a, the electron is incident upon an infinitely thick potential barrier of height V. The Schrödinger equation demonstrates a mechanism to understand tunnelling. It has two components:

For x<0: $$\boldsymbol{H} = -(\boldsymbol{h}^2/2\boldsymbol{m})(\boldsymbol{d}^2/\boldsymbol{dx}^2)$$ *Equation A.1.15*

And inside the barrier (x>0): $$\boldsymbol{H} = -(\boldsymbol{h}^2/2\boldsymbol{m})(\boldsymbol{d}^2/\boldsymbol{dx}^2) + \boldsymbol{V}$$ *Equation A1.16*

The solutions to these equations are:

$\varphi = Ae^{ikx} + Be^{-kx}$ with $k = (2mE/h^2)$ inside the well, *Equation A1.17*

and $\varphi = Ce^{ik'x} + Be^{-k'x}$ with $k = (2m(E-V)/h^2)^{1/2}$ inside the barrier *Equation A1.18*

The real part of equation A1.18 tells us that the wavefunction decreases exponentially with distance inside the barrier. As a result, it is probable than an electron can be found inside a barrier. Now, consider two potential wells close together, i.e. only separated by a potential barrier of finite thickness (Figure A1.10c). If the potential barrier is small, it is probable than an electron might penetrate it and hop from one well to another. In other words, overlapping Fermi level wavefunctions make tunnelling possible and if a voltage is applied, the generated current can then be measured[88]. The magnitude of the tunnelling current is a measure of the overlap of the two wave functions and varies exponentially with the separation between the tip and sample (equation A1.19). Thus, a topographic image of the surface can be obtained by moving the tip across the surface.

$I(W) = C\exp(-W\sqrt{\phi})$ *Equation A1.19*

where C is a constant, W is the sample to tip gap, and the sample work function Φ. Scanning the tip at constant height results in high tunnelling current in areas having protrusions where W decreases. Equation A1.19 suffices to understand the principle of STM. However, a more detailed expression of the tunnelling current, including the effects of the tip geometry is given by

$$I = 32\pi^3 h^{-1} e^2 V \phi_0^2 D_t(E_F) W^2 \kappa^{-4} e^{-2\kappa W} \sum |\varphi_v(r_0)| 2\delta(E_v - E_F) \qquad \textit{Equation A1.20}$$

where ϕ_0 is the work function, $D_t(E_F)$ is the density of states at the Fermi level per volume of the tip, E_F is the Fermi energy,and φ_v is the wavefunction of the sample. Equation A1.20 indicates that the tunnelling current is proportional to the local density of states at the Fermi level and at the centre of the STM tip.

The main components of an STM are shown in Figure A1.11. The tip is mounted in the STM head on a piezoelectric tube scanner. Applying a voltage to the

piezoelectric material results in contraction or expansion of the material so that fine motion of the tip is accomplished with piezodrives X, Y, and Z.

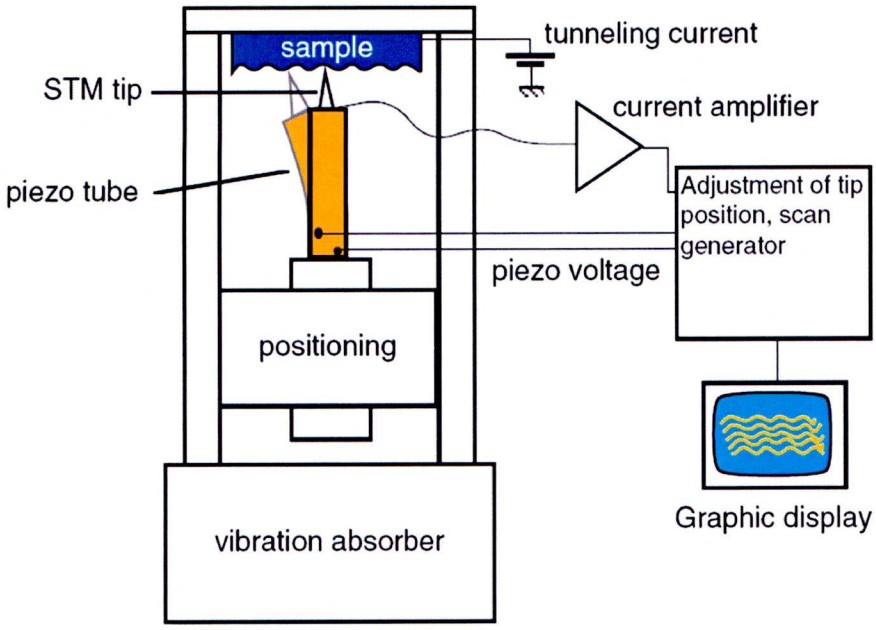

Figure A1.11. Typical STM setup. The tip is mounted on a piezoelectric tube that can be deformed by applied electric fields. Thus, the tip can be manipulated vertically and laterally. The position of the tip is adjusted according to the tunnelling current via an electronic feedback loop if operating in the constant current mode, generating a two-dimensional current contour[170]

There are two modes of imaging a surface with STM: the constant current mode and the constant height mode. In the constant current mode, the value of W is fixed by moving the tip in the *z*-direction while scanning the *xy* plane. Thus, a topographic image of the surface can be obtained by plotting the *z*-piezo electric voltage vs. lateral position (Figure A1.12a). In contrast, in the constant height mode, the tip is scanned in the *xy* plane of the surface, but it does not move in the *z*-direction (Figure A1.12b). Consequently, the tip-sample distance (W) changes, resulting in varying tunnelling current. The recorded image of surface topography is obtained from a plot of tunnelling current vs. position in the surface plane. The constant current mode is preferred for rough surfaces because potential tip-sample collisions which can damage the tip are avoided. Conversely, the constant height mode is preferred for atomically flat surfaces[25]. It is important to keep in mind that an STM image is a map of the density of electronic states at the surface. This means that each bump in the image does not necessary corresponds to a surface atom position. However, when interpreted correctly

the STM image provides data on the structure and bonding of atoms at surfaces. The resolutions of STM are 1 Å in the plane of the surface and less than 0.1 Å perpendicular to the surface whilst tunneling currents range from 100 pA to 30 nA. One of the advantages of this technique is that it is not restricted to vacuum since it can be applied in liquid and air environments. Moreover, STM can be used to move atoms and molecules across a surface and to make molecules react.

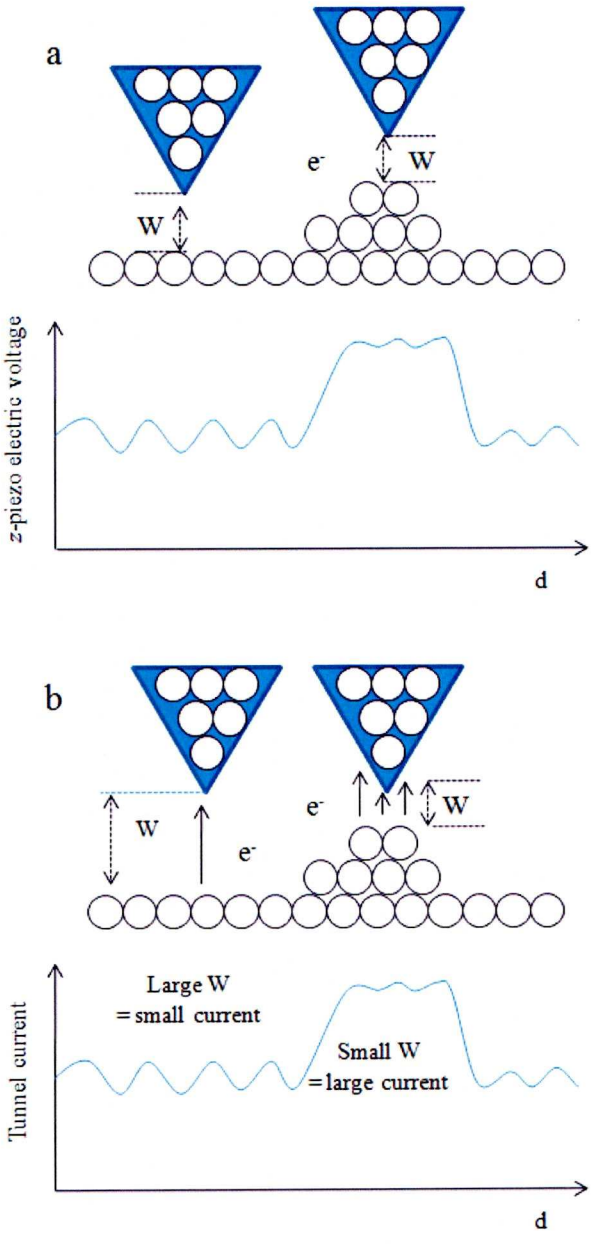

Figure A1.12. STM operating modes. a. constant current, b. constant height[25]

APPENDIX 2. DETERMINATION OF THE HANDEDNESS OF A SYNTHETIC QUARTZ SPECIMEN

The handedness of a synthetic quartz crystal used in adsorption experiments was determined by two methods described below. First of all, a thin slab of quartz, (Size= 25 mm ×13 mm; thickness = 2 mm) was cut perpendicular to the *c*-axis, which is the optical axis of the crystal. The slab surfaces were then subjected to manual rough grinding with carborundum (silicon carbide, SiC) of 400, 600, and 800-mesh. Next, the surfaces were polished on a Kent 3 automatic lapping and polishing unit (Engis Ltd) by using Metadi II Diamond Polishing Compounds (Büehler Science) with particle size 0.25, 1, 3 and to 6 μm. The slab surfaces were successively polished with each diamond paste for 30 min, starting with the 6 μm diamond paste. After each polishing step with a given diamond paste, the holder and slab were cleaned by ultrasonication for 10 min. A final chemical-mechanical polishing was conducted with Syton polishing fluid for 4 hours. The resulting 2 mm thick slab was deemed to be well-prepared for optical measurements.

Quartz is an optically active mineral because it lacks a centre of symmetry. Therefore when light passes through a thin section of the crystal orientated perpendicular to the *c*-axis, the plane of polarization is rotated to either the left or right, depending on whether the crystal is left or right-handed. Monochromatic light of a Na lamp (589 nm) usually produces a rotation of 22°/mm for quartz. Another way to visualize optical activity is to acquire interference figures which are obtained using a λ/4 compensator lense in conjunction with the optical microscope (see Figure A2.1). This setup is called a conoscope. The 2 mm thick slab was studied and a spiral (so called Airy's spiral) was observed and photographed with a digital camera. The sense of the spiral dictates the handedness of the crystal. Figure A2.2 shows that for both faces of the quartz slab the spirals coil to the right (clockwise) indicating that the crystal is right-handed.

Unambiguous determination of the optical rotation of a crystal was reported by Glazer and Geday[171]. In their method, conoscopic illumination was used in a microscope equipped with a rotating polarizer-circular analyser system and monochromatic light. The resulting interference pattern was separated into its constituent parts: the sign of the optical indicatrix and birefringency. In addition, simulated Airy's spiral images reproduced quite well the observed images. The synthetic quartz slab was analysed with Geday and Glazer's technique at Oxford University. The images are presented in Figure A2.3. The φ image corresponds to the Airy's spiral and it can be concluded that the synthetic quartz specimen is right-

handed (positive rotation) because the spiral increases in a clockwise sense from the centre of the image outwards.

Figure A2.1. Optical microscope setup for optical activity measurement

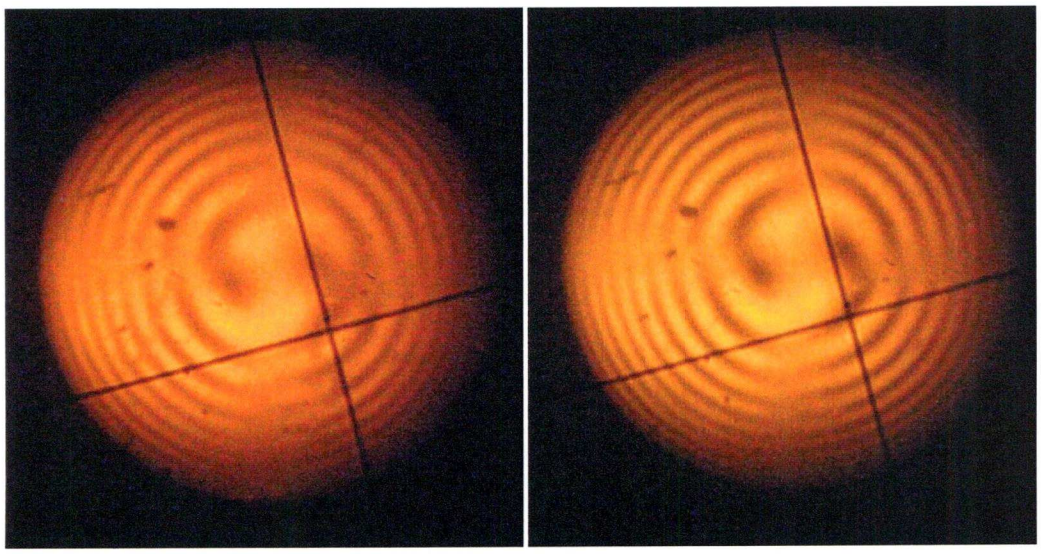

Figure A2.2. Airy's spiral images obtained with conoscopic method. Quartz slab thickness=2 mm

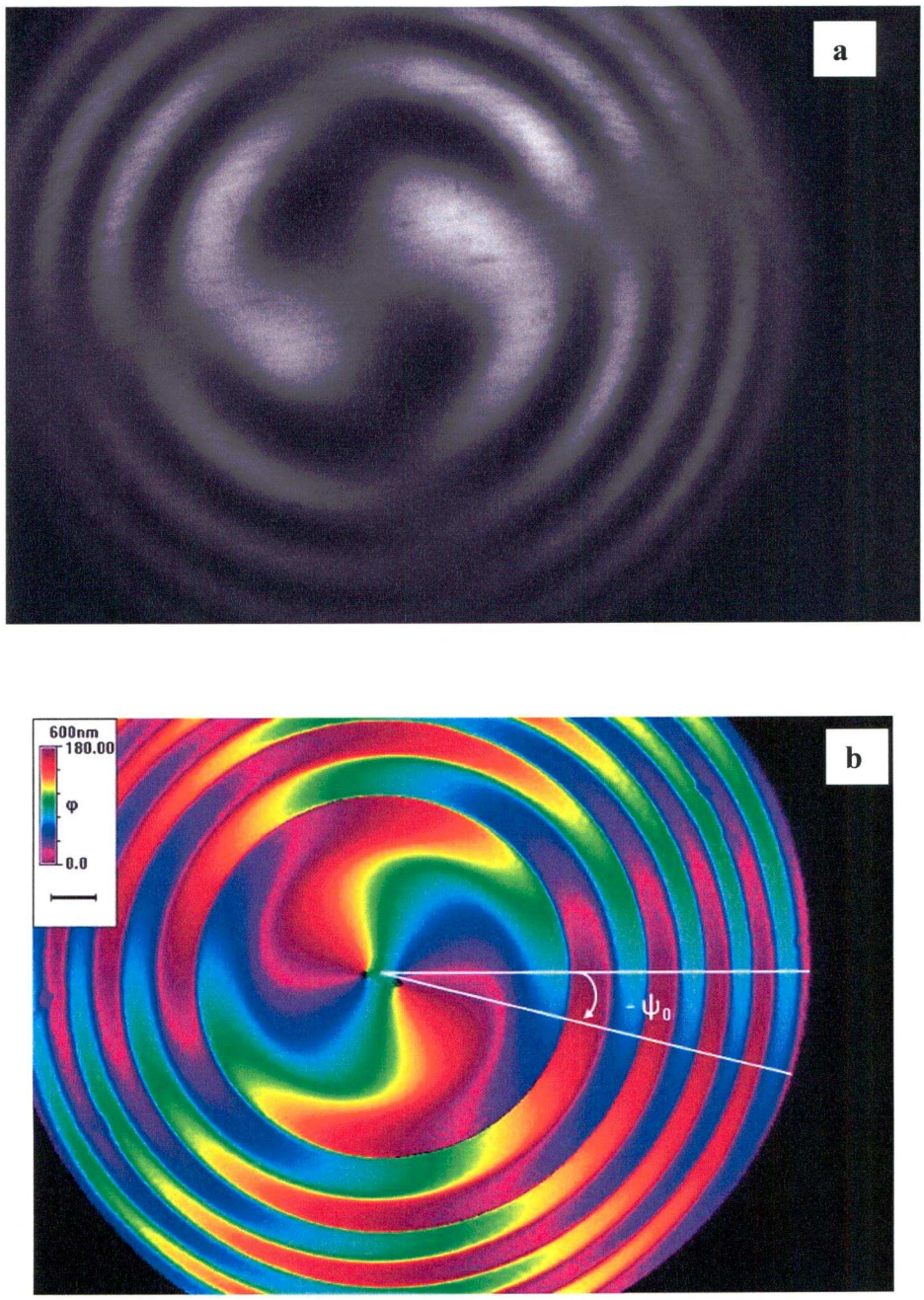

Figure A2.3. Conoscopic images of a *2* mm thick slice of quartz cut on (001): (a) unprocessed image in the rotating-polarizer system; (b) separated φ image

APPENDIX 3. X-RAY DIFFRACTION OFMONTMORILLONITE K10

1. Sample preparation

Approximately 10 g of dry K10 was transferred to a glass beaker and hydrated for 48 hr in 100 mL of distilled water. The component particles were then suspended by gentle stirring with a glass rod and separated by ultrasonic dispersion for a period of 15 min. The dispersed particles were then size separated to produce <2 μm, 2-20 μm and >20 μm fractions (equivalent spherical diameter) using standard particle size separation techniques (gravity settling and centrifugation). The resultant size fractions were suspended in distilled water and quickly frozen with liquid nitrogen prior to removal of water by freeze-drying. Once dry, each size fraction was allowed to equilibrate (24 hr) at ambient temperature (*ca* 20°C) and humidity (*ca* 30 % relative humidity) and then transferred to a side-loading aluminium cavity mount to produce a randomly orientated sample for X-ray diffraction analysis.

In addition to the size-fractionated samples, an untreated sample of the stock K10 (as supplied) and a sample of heat-treated K10 were also analysed as randomly orientated specimens for comparison purposes.

2. X-ray diffraction analysis

Randomly oriented samples were analysed in step scan mode from 3 to 65° 2θ with step increments of 0.02° 2θ and a counting time of 2 seconds per step using a Siemens 500D X-ray diffractometer (fitted with a graphite monochromator, 1° divergence and anti-scatter slits, 0.15° detector slit), and Cu Kα (λ= 1.5419 Å) radiation generated at 40 kV and 30 mA.

3. Estimation of the Mineral Content of K10

The chemical analysis of the Sigma-Aldrich K10 analysed by X-ray Fluorescence[124] was: SiO_2 (69.21%), Al_2O_3 (16.61%), Fe_2O_3 (4.67%), MgO (2.06%), Na_2O(0.12%), K_2O(1.55%), TiO_2 (0.47%), P_2O_5 (0.03), MnO (0.02%). Total: 94.64%.

Since the main crystalline phases identified by K10 were quartz, smectite, and muscovite, the percentages of SiO_2, Al_2O_3, and K_2O were adjusted accordingly assuming that only these three oxides were present in the bulk material. On a weight basis, this is equivalent to 79% SiO_2, 19%, Al_2O_3, and 1.77% K_2O. Muscovite was

assumed to have the structural formula: $KAl_3Si_3O_{10}(OH)_2$ (MW=398.3 g/mol). It was further assumed that all potassium (K) is incorporated in the muscovite.

One formula weight of muscovite contains approximately 10% K:

% K in muscovite = (39 g K/398.3 g muscovite) = 0.098%

The oxide percentages of SiO_2, Al_2O_3, and K_2O were converted to elemental composition of Si, Al, and K by:

base =100 g of K10

Si = (28.08 g Si/60.08 g SiO_2) *79 g = 36.93 g Si
Al = (53.96 g Al/101.96 g Al_2O_3)*19 g = 10.05 g Al
K = (78 g K/ 94 g K_2O)*1.77 = 1.468 g K

therefore K10 must contain 14.68 g of muscovite: 1.468g K/(0.1 g K/ g muscovite).

Knowing this, the amounts of Al and Si in muscovite were calculated by

Al = (14.68 g)* (80.94 g Al/398.3 g muscovite) = 2.98 g
Si = (14.84 g)*(84.24 g Si/398.3 g muscovite) = 3.10 g

Substracting the amounts of Al and Si in muscovite from the initial amounts:

$(Al)_{remaining}$ = 10.05 g -2.98 g = 7.07 g
$(Si)_{remaining}$ = 36.96 g -3.10 g = 33.86 g

Now, assuming that the remaining Al is associated with smectite, the % of smectite in K10 can be estimated. The smectite formula used for this purpose was $½\ (Na)_{0.3}(Al_{1.7}Mg_{0.3})Si_4O_{10}(OH)_2$ (MW=183.188 g/mol)

$(\%Al)_{smectite}$ = (0.5*1.7*26.98)/(183.188 g) = 0.125

Thus,

smectite = 7.07 g/0.125 = 56.48 g

quartz= 100g - 56.5g - 15g = 28.5 g